1989

Transducer effects on ultrasonic attenuation measurements

Mary A. Paul
Iowa State University

PMA-002

Transducer effects on ultrasonic attenuation measurements

by

Mary A. Paul

A Thesis Submitted to the

Graduate Faculty in Partial Fulfillment of the

Requirements for the Degree of

MASTER OF SCIENCE

Department: Engineering Science and Mechanics
Major: Engineering Mechanics

Signature redacted for privacy

Iowa State University
Ames, Iowa
1989

TABLE OF CONTENTS

LIST OF TABLES

LIST OF FIGURES

ACKNOWLEDGEMENTS

This work has been supported by the Center for Non Destructive Evaluation, Ames Laboratory. Dr. Anna Pate's support and guidance during this work is greatly appreciated. Also greatly appreciated is the technical support and advice of David Bennink, Sam Wormley, Frank Margetan, and numerous others at the Center.

The support and encouragement of my parents, Mr. and Mrs. Eugene Paul, has been invaluable to me. Special thanks also to Alan Dona for his support, understanding, and patience.

1 INTRODUCTION

Ultrasonic nondestructive evaluation can be used to quantitatively interpret received electrical signals from ultrasonic measurements. In order to preform this interpretation, several techniques have been used. Two of these techniques are the standard procedure and the measurement model. The standard procedure compares the waves reflected from the flawed specimen with the waves reflected from many specimens of the same host material with different known flaws in the interior. By matching reflections, the approximate size of the flaw can be estimated by comparison with the response from the known standard flaw model; however, this method requires a large number of known, standard flaw models, which makes it a difficult procedure to use. In addition, different flaw shapes of different sizes can result in the same overall peak-to-peak response. Therefore, precise flaw sizing can not be obtained with this technique.

To obtain more quantitative results based on the received electrical signals from ultrasonic measurements, mathematical models can be used. An example of a mathematical model used for flaw characterization in ultrasonic nondestructive evaluation is the measurement model which is derived and discussed in detail by Thompson and Gray in reference [1]. In this model, the relationship between the received voltage from an ultrasonic experiment and the complex scattering amplitude

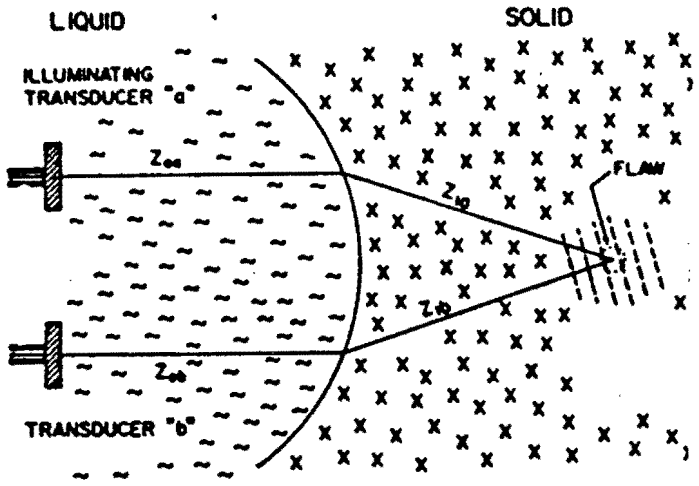

Figure 1.1: Schematic of Measurement Set-up for Immersion Testing

of the flaw is written as

$$\Gamma = \Upsilon\beta\Psi e^{j[k_o(z_{oa}-z_{ob})-k_a z_{1a}+k_b z_{1b}]-[\alpha_o(z_{oa}+z_{ob})+\alpha_a z_{1a}-\alpha_b z_{1b}]} \tag{1.1}$$

where :

$\Psi = \beta T_a T_b C_a C_b$

$\Upsilon = \dfrac{2A^* \rho_1 v_b}{jk_b a^2 \rho_o v_o}$

A^* = the complex scattering amplitude of the flaw

Γ = the received signal from the ultrasonic measurement

β = the measurement system efficiency factor

$z_{oa}, z_{ob}, z_{1a}, z_{1b}$ = distances defined in Figure 1.1

T_a, T_b = the transmission coefficients

C_a, C_b = measure of the diffraction induced deviations from the initial plane-wave condition (z dependent)

$j = \sqrt{-1}$

k_o, k_a, k_b = wave numbers in the liquid and solid

$\alpha_o, \alpha_a, \alpha_b$ = the ultrasonic attenuation per unit length for the waves in the liquid and solid

ρ_1 = density of the solid

v_b = the ultrasonic velocity in the solid determined by transducer "b"

a = radius of the transducer

ρ_o = density of the liquid

v_o = wavespeed in the liquid

The received signal, Γ, is what measured by the ultrasonic experiment; and the scattering amplitude, A^*, is the quantity which is to be calculated from Equation 1.1. Once A^* is calculated, scattering theory can be applied to find the characteristics of the flaw present in the specimen.

As can be seen from Equation 1.1, the relationship between the received signal, Γ, and the scattering amplitude of the flaw, A^*, requires the knowledge of several ultrasonic quantities. These quantities can be found from theoretical calculations and from independent measurements. The system efficiency factor, β, and the attenuation of the ultrasonic wave in the materials, α, are both found from independent measurements. Transmission coefficients, T_a and T_b, and diffraction

corrections, C_a and C_b, can be calculated as shown in reference [1], based on the assumption that the transducer is a circular, rigid piston radiating through planar and cylindrical interfaces at either normal or oblique incidences.

The need for accurate estimation of the ultrasonic attenuation of the solid, as required in Equation 1.1, provided the motivation for this thesis. Specifically, the research focussed on experimental methods for ultrasonic wave attenuation measurement. In particular, consistency of experimental results obtained with different methods and different transducers was investigated.

In the course of the research, it was discovered that transducers' properties have significant effect on the results of the attenuation measurements, especially in materials with low attenuation. In order to investigate these effects, the radiation patterns of all transducers used in the experiments were studied. Specifically, radial and axial pressure profiles of the transducers were measured and compared to the theoretical model of the planar piston source. Results of the transducer characterizations were then used to decrease the transducer dependence of the attenuation measurements.

It is anticipated that the results of this thesis will improve the accuracy of ultrasonic nondestructive evaluations based on the measurement model. Specifically, more accurate calculation of the scattering amplitude of the flaw can be obtained using the developments of this thesis which lead to measurements of the host material's attenuation that are more consistent and less dependent on individual transducer properties.

2 ATTENUATION MEASUREMENTS

2.1 Measurement Scope and Objectives

To use the measurement model of Equation 1.1, the ultrasonic wave attenuation in the sample must be known. However, researchers have found it difficult to measure the attenuation of ultrasonic waves in solids, especially for low attenuating materials.

The ultrasonic wave attenuation of two types of aluminum, both having low values of attenuation, were measured. One of the samples was 7075 aluminum, which has a large grain size and therefore few boundaries for the ultrasonic wave to be scattered from. The other sample was A357 aluminum, which has high porosity and therefore many boundaries for the ultrasonic wave to be reflected from. These two aluminum samples were chosen to see if they would yield results with similar transducer dependence and method bias.

The 7075 aluminum has an extremely low attenuation value which is very difficult to measure. Figure 2.1 shows the spread of the maximum and minimum attenuation values obtained over 81 different measurements (three different methods and three nominally identical 10 MHz transducers) of the attenuation in this aluminum. The difficulty of measuring the attenuation can be seen in the large spread of values which were obtained.

The measurement of the attenuation of A357 aluminum, which is a higher attenuating aluminum because of the increased number of boundaries, was found to be more consistent across the three different methods and three different 10 MHz transducers than the 7075 aluminum.

The ultrasonic wave attenuation values for the two samples was measured by three different methods and five different transducers to study the effects of both the measurement method and the transducer on the experimental evaluation of attenuation. The following quantities were examined based on the results of the attenuation tests:

1) repeatability: scatter in results can be caused by experimental errors in data acquisition, signal processing, probe and specimen positioning, and probe orientation, which was attempted to be kept normal to the tested specimen's surface for all tests;

2) bias in each method: caused by different modeling used for each technique and different distances involved in each method due to different block sizes and echoes required; and

3) dependence on transducers: caused by differences between individual transducers, which are all characterized by the producers as nominally identical and modeled by researchers with the rigid piston theory using the stated nominal diameters and frequencies.

2.2 Theory

Attenuation is the decrease in wave amplitude as the wave travels through a specimen. If A_O is the incident amplitude and A is the amplitude after traveling a

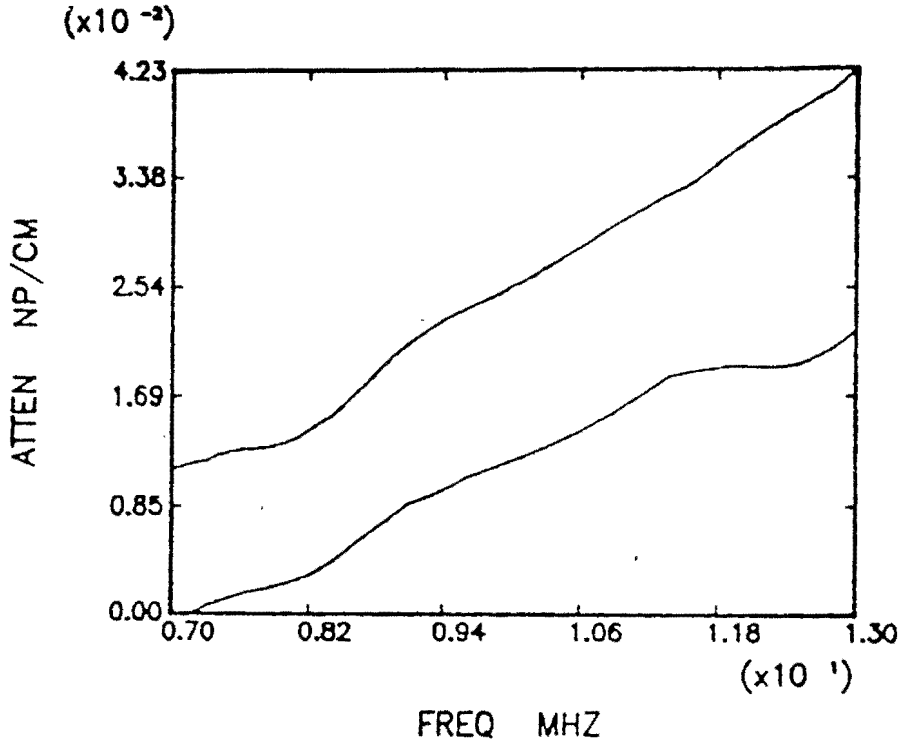

Figure 2.1: Maximum and Minimum Attenuation Values Obtained from all Measurements Performed for 7075 Aluminum (all Transducers all Methods)

distance, z, a relation can be written which describes the decay or attenuation of the wave

$$A = A_o e^{-\alpha z} \tag{2.1}$$

where α is the attenuation constant. This attenuation in a metal specimen can be attributed to two effects, absorbtion and scattering. Absorbtion can mainly be attributed to internal friction or viscosity and elastic hysteresis. The absorbtion in solids is usually a linear function in frequency. The scattering is due mainly to grain boundaries. The frequency dependence, f, of the attenuation constant, α, resulting from the scattering can be divided into three ranges depending on the ratio of the wavelength, λ, to the average grain size diameter, $\overline{D}$ [2]:

1) Rayleigh Scattering ($\lambda >> \overline{D}$)

Attenuation constant is proportional to $\overline{D}^3 f^4$

2) Random Phase (Stochastic Scattering) ($\lambda \approx \overline{D}$)

Attenuation constant is proportional to $\overline{D} f^2$

3) Diffusion Scattering ($\lambda \leq \overline{D}$)

Attenuation constant is proportional to $\frac{1}{\overline{D}}$

The transition between the ranges is gradual and is affected by the larger-than-mean-size grains present in the specimen [2].

2.3 Attenuation Measurement Techniques

Two types of waveforms that can be used to determine the attenuation of the solid material are the pulse-type and harmonic-type waveforms. In the pulse system, a pulsed signal of a given frequency is converted by means of a transducer into a pulsed ultrasonic wave. The pulse travels through the sample and is reflected

between the sample boundaries decaying exponentially at a rate proportional to the attenuation constant. The harmonic techniques are associated with steady-state conditions. A continuous wave of some frequency travels through the specimen; and by evaluation of the received waveform, the attenuation in the specimen at that frequency can be obtained.

A number of methods for measuring attenuation are known. These methods include contact methods [3], [4], [5], [6], [7], [8] and immersion methods [9], [10], which use multiple echoes in various configurations with appropriate correction factors applied to find the attenuation in materials.

In many attenuation measurement techniques, it is required that beam divergence be accounted for. As the ultrasonic wave propagates, it spreads out. This phenomenon is called diffraction. Diffraction results in a decay of the wave amplitude as it propagates away from the transducer. Errors in modeling of a transducer's diffraction properties will result in errors in the measured attenuation of the specimen.

Since the following methods were convenient for an immersion set-up with the type of laboratory equipment available for the project, the following three methods were chosen for the attenuation measurements in this thesis:

a) Multiple Thickness [11]

b) Multiple Echo [9]

c) Multiple Echo II [5]

In all three measurement methods, the same theory regarding the ultrasonic wave attenuation, transmission through interfaces, and reflection from planar boundaries was used.

periment, $V_o^{(n)}(f)$, schematically shown in Figure 2.2, is related to the magnitude of the spectrum of the input voltage, $V_i(f)$, as follows:

$$|V_o^{(n)}(f)| = |V_i(f)||\mathcal{Z}(f)\gamma||D(z_o, z_1^{(n)}, f)|e^{(-2\alpha_1(f)z_1^{(n)} - 2\alpha_o(f)z_o)} \qquad (2.2)$$

where

(n) = an integer corresponding to the reflection number (not an exponent)

$z_1^{(n)}$ = the distance travelled in the specimen for the n^{th} reflection

z_o = the distance travelled in the liquid

f = frequency

$V_i(f)$ = the input voltage

$V_o(f)$ = the received voltage

$\mathcal{Z}(f)$ is a measure of the efficiency of the measurement system, including the transducer, and must be calculated experimentally, since the performance of the measurement system is often quite different from predictions of theoretical models [1]; γ includes two factors: transmission, (T), and reflection, (R), which can be calculated from

$$R = \frac{|\rho_o v_o - \rho_1 v_1|}{|\rho_o v_o - \rho_1 v_1|} \qquad (2.3)$$

and

$$T = \frac{2(\rho_1 v_1)}{|\rho_o v_o - \rho_1 v_1|} \qquad (2.4)$$

where

ρ_o = density of the water

ρ_1 = density of the material

v_o = velocity of the ultrasonic wave in water

v_1 = velocity of the ultrasonic wave in the material

$D(z_o, z_1^{(n)}, f)$ is the frequency dependent correction for the spreading of the beam as it travels through the specimen or, in other words, the diffraction correction. The diffraction must be accounted for or else it could be mistaken for attenuation. Assuming that a transducer has a field of a rigid vibrating piston, the diffraction corrections can be calculated as [1]

$$D(z_o, z_1^{(n)}, f) = e^{\frac{-j2\pi}{s_e}}[J_o(\frac{2\pi}{s_e}) + jJ_1(\frac{2\pi}{s_e})] \tag{2.5}$$

where

$$s_e = 2(\frac{z_o\lambda_o}{a^2} + \frac{z_1\lambda_1}{a^2}) \tag{2.6}$$

where

λ_o = wavelength in the water

λ_1 = wavelength in the solid

J_o = Bessel function of the first kind of order zero

J_1 = Bessel function of the first kind of order one

a = radius of the transducer

Equations 2.5 and 2.6 assume that the transducer is radiating as a planar piston source. Therefore, to insure correct compensation for the diffraction, the assumption of a planar piston source needs to be confirmed for each transducer.

A pulse-echo configuration was used in this work with non-focused, immersion transducers, and during the measurements, all signals were taken at normal incidence upon liquid-material interfaces. The material interfaces were all smooth, flat and parallel as shown in Figure 2.2. Digital equipment was used for the measurements with 512 points of the time domain signal being averaged 64 times and

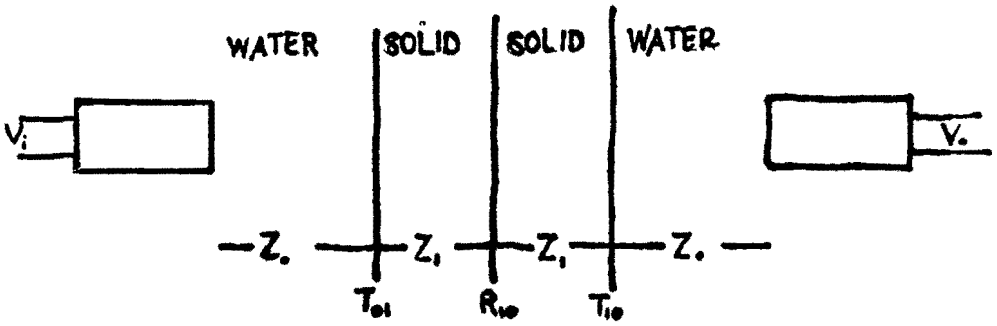

Figure 2.2: Experimental Schematic for a General Attenuation Measurement

then Fast Fourier Transformed into the frequency domain during the data acquisition. The frequency domain signals were used in the equations for the attenuation calculations.

2.3.1 Multiple Thickness Technique (MT)

In this technique [11], three blocks of different thicknesses of the same material are used. A back surface reflection from each specimen is measured as shown in Figure 2.3. In the calculation of the attenuation constant, one of the back surface reflections is used as the reference signal by normalizing back scattered signals

received from the other two specimens as follows:

$$\frac{V_o^{(n)}(f)}{V_o^{(1)}(f)} = \frac{R(z_o,f)}{R(z_o,f)} \frac{|D(z_o,z_1^{(n)},f)|}{|D(z_o,z_1^{(1)},f)|} e^{-2\alpha_1(f)(z_1^{(n)}-z_1^{(1)})} \tag{2.7}$$

where n= 2,3 are echo numbers, $V_o^{(1)}(f)$, $D(z_o,z_1^{(1)},f)$, and $z_1^{(1)}$ refer to the back scattered voltage spectrum, diffraction corrections, and block distance involved in the reference measurement, while $V_o^{(n)}(f)$, $D(z_o,z_1^{(n)},f)$, and $z_1^{(n)}$ refer to the respective quantities involved in the measurements of the other two specimens. $R(z_o,f)$ refers to the combined effect of the measurement system efficiency factor and the reflection characteristics of the interfaces. The value of $R(z_o,f)$ remains constant for the three measurements if the water path is held constant, therefore the term $R(z_o,f)$ cancels out in Equation 2.7. However, the diffraction corrections, $D(z_o,z_1^{(n)},f)$, need to be calculated. These corrections are dependent on the transducer. In this study, a rigid piston model was assumed and the diffraction corrections were calculated as stated in Equations 2.5 and 2.6. Thus, from Equation 2.7, the attenuation was calculated from:

$$2\alpha_1(f)(z_1^{(1)} - z_1^{(n)}) = \ln \frac{V_o^{(1)}(f)}{V_o^{(n)}(f)} \frac{|D(z_o,z_1^{(n)},f)|}{|D(z_o,z_1^{(1)},f)|} \tag{2.8}$$

where a straight line fit passing through the origin was used to find the value of the attenuation for each frequency within the transducer bandwidth (see Figure 2.4).

2.3.2 Multiple Echo Technique (ME)

In this method [9], one material specimen is used with three consecutive back surface echoes being measured (see Figure 2.5). Similarly to the previously discussed

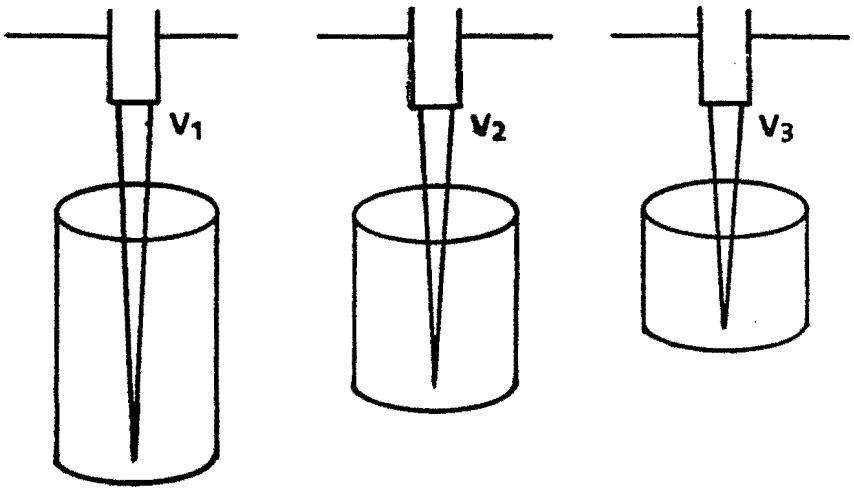

Figure 2.3: Reflections Used for the Multiple Thickness Test

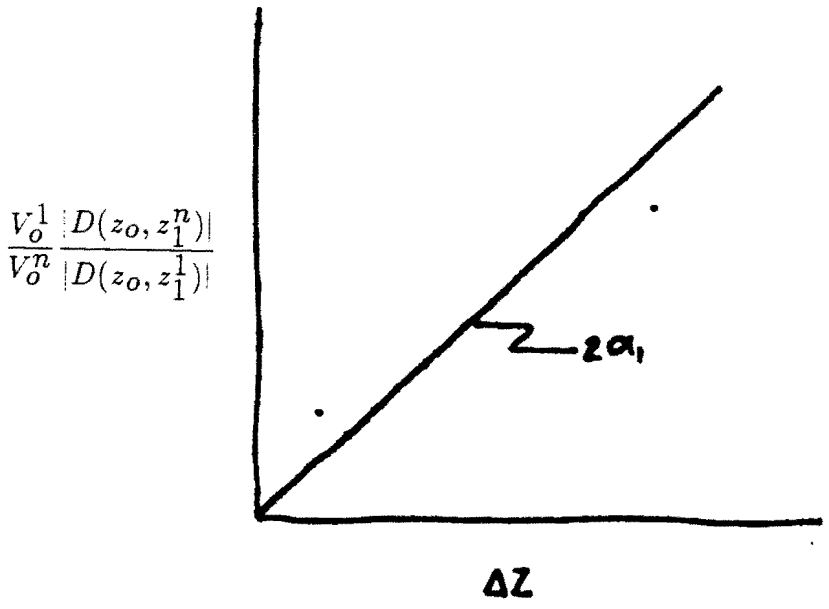

Figure 2.4: Graph Used at Each Frequency to Find the Attenuation Constant at that Frequency

method, one reflection is used as the reference echo and ratios between this echo and the other two echoes are calculated as:

$$\frac{V_o^{(1)}(f)}{V_o^{(n)}(f)} = \frac{R^{(1)}(z_o)}{R^{(n)}(z_o)} \frac{|D(z_o, z_1^{(1)}, f)|}{|D(z_o, z_1^{(n)}, f)|} \frac{e^{-2\alpha_1(f) z_1^{(1)}}}{e^{-2\alpha_1(f) z_1^{(n)}}} \tag{2.9}$$

where n is an echo number, n= 2,3. In this case, the reflection coefficients, $R^{(n)}(z_o)$, are not equal, when n= 2,3, as they were in the multiple thickness test (see Figure 2.3); therefore, Equation 2.9 becomes:

$$\frac{V_o^{(1)}(f)}{V_o^{(n)}(f)} = \frac{R(z_o)}{R(z_o)^{2n-1}} \frac{|D(z_o, z_1^{(n)}, f)|}{|D(z_o, z_1^{(n)}, f)|} \frac{e^{-2\alpha_1(f) z_1^{(1)}}}{e^{-2\alpha_1(f) z_1^{(n)}}} \tag{2.10}$$

The value used for the reflection coefficient where plane waves and normal incidence are assumed is:

$$R(z_o) = \frac{|\rho_o v_o - \rho_1 v_1|}{|\rho_o v_o + \rho_1 v_1|} \tag{2.11}$$

where ρ_o and ρ_1 are the densities and v_o and v_1 are the velocities of the ultrasonic wave in the liquid (water) and the solid, respectively. The diffraction must still be accounted for and it is taken into account by again using Equations 2.5 and 2.6. The attenuation can be solved for by using:

$$2\alpha_1(f)(z_1^{(1)} - z_1^{(n)}) = \ln \frac{V_o^{(1)}(f)}{V_o^{(n)}(f)} R(z_o)^{2(n-1)} \frac{|D(z_o, z_1^{(n)}, f)}{|D(z_o, z_1^{(1)}, f)|} \tag{2.12}$$

and a straight line fit of the expression $\frac{V_o^{(1)}(f)}{V_o^{(n)}(f)} [R(z_o)]^{2(n-1)} \frac{|D(z_o, z_1^{(n)}, f)|}{|D(z_o, z_1^{(1)}, f)|}$ versus $(z_1^{(n)} - z_1^{(1)})$ as in the multiple thickness method.

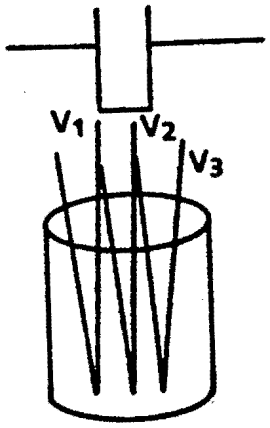

Figure 2.5: Reflections Used in the Multiple Echo Test

2.3.3 Multiple Echo II Method (MEII)

In this method [5], one specimen with two, flat, parallel surfaces is used with the front surface reflection, the first back surface, and the second back surface reflection being measured (see Figure 2.6). The block must have an air interface at the back to simulate the perfect reflection with the back surface reflection coefficient equal to one. At the front surface the following notation is used for the magnitude of the pressure spectrum:

$$\text{incident pressure} = I(f) = 1 \tag{2.13}$$

$$\text{reflected pressure} = R(f) = A(f) \tag{2.14}$$

$$\text{transmitted pressure} = T(f) \tag{2.15}$$

When the first back surface echo reaches interface 1 then,

$$\text{incident pressure} = (1 - R(f))\epsilon^{-2l\alpha(f)} \tag{2.16}$$

$$\text{reflected pressure} = R(f)[(1 - R(f))\epsilon^{-2l\alpha(f)}] \tag{2.17}$$

$$\text{transmitted pressure} = B(f) \tag{2.18}$$

where

l = the distance travelled in the specimen

Therefore

$$B(f) + R(f)(1 + R(f))\epsilon^{-2l\alpha(f)} = (1 + R(f))\epsilon^{-2l\alpha(f)} \tag{2.19}$$

or

$$B(f) = (1 - R(f)^2)\epsilon^{2l\alpha(f)} \tag{2.20}$$

In a similar way, when the second back surface echo reaches interface 2 it is found that

$$\text{second back surface reflection} = C'(f) = R(f)(1 - R(f)^2)\epsilon^{-4l\alpha(f)} \tag{2.21}$$

The front scattered signal, $A(f)$, and backscattered signals, $B(f)$ and $C'(f)$, which are measured, must all individually be corrected for diffraction effects using Equations 2.5 and 2.6 before they are normalized and used to calculate $\alpha(f)$. If all the echoes are normalized by $B(f)$:

$$\frac{A(f)}{B(f)} = M_1(f) = \frac{R(f)}{1 - R^2(f)}\epsilon^{-2l\alpha(f)} \tag{2.22}$$

$$\frac{C'(f)}{B(f)} = M_2(f) = R(f)\epsilon^{-2l\alpha(f)} \tag{2.23}$$

and from Equations 2.22 and 2.23,

$$R(f) = \left(\frac{M_1(f)M_2(f)}{1 + M_1(f)M_2(f)}\right)^{\frac{1}{2}} \tag{2.24}$$

and

$$\alpha(f) = \frac{\ln\left(\frac{R(f)}{M_2(f)}\right)}{2l} \tag{2.25}$$

The normalized signals, $M_1(f)$ and $M_2(f)$, are frequency dependent and were used for the calculations of attenuation at each frequency within the bandwidth of the transducer. A graph of attenuation over these frequencies was made.

2.4 Experimental Apparatus

Instruments used include the Panametrics pulser-receiver model 5052 PR, Alan Industries Inc. external attenuator, Textronics model 7912 programmable digitizer,

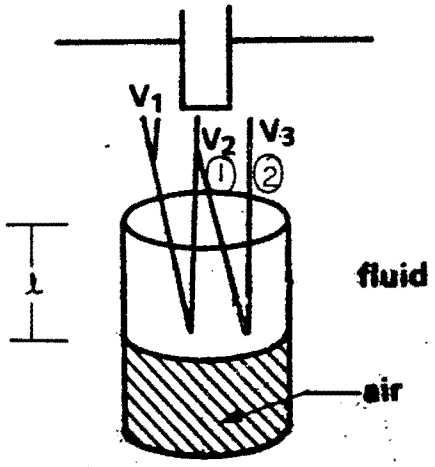

Figure 2.6: Multiple Echo II Technique Set-up

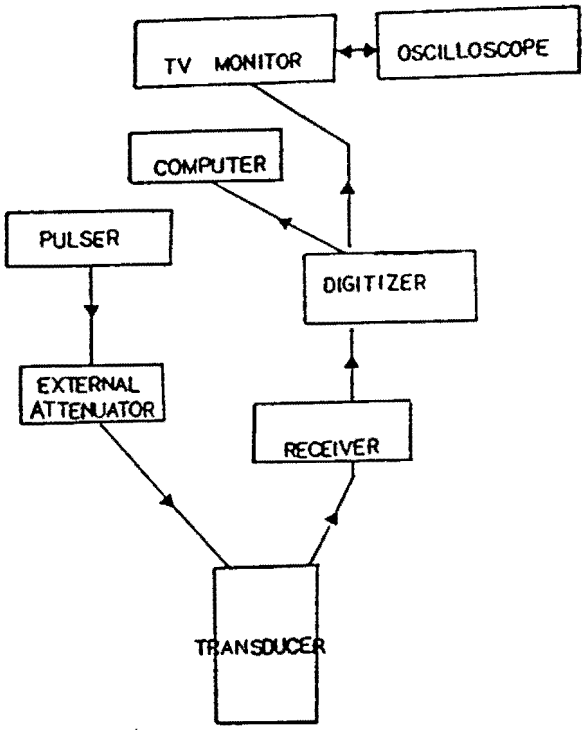

Figure 2.7: Block Diagram of the Equipment Used in the Measurements

Textronics 4052 computer, and Textronics 7A16P-7B92A oscilloscope with NEC character display TV monitor as shown in Figure 2.7. The same set-up was used for all experiments, making the measurements, with the exception of the transducers, independent of the equipment. Transducers used for the attenuation experiments included three 10 MHz and two 15 MHz, .25 inch nominal diameter, V312, unfocused, immersion probes.

2.5 Measurement Procedures

2.5.1 7075 Aluminum

For the multiple thickness technique, 3 inch, 1.5 inch, and .5 inch thick, cylindrical, two inch diameter, 7075 aluminum blocks were used in the experiments which involved measuring the back surface reflection for each block. The water path distance was kept constant at 3 cm for the 10 MHz transducers and 4 cm for the 15 MHz transducers. The test was run nine times for each transducer. Attenuation coefficients were calculated according to Equation 2.8.

For the multiple echo technique, the same 1.5 inch aluminum block was used as in the multiple thickness technique, and the first, second, and third back surface reflections were measured. The water path distance was kept constant at 3 cm for the 10 MHz transducers and 4 cm for the 15 MHz transducers. The test was run nine times for each transducer. Equation 2.12 was used to calculate the attenuation coefficients.

For the multiple echo II technique, the same 1.5 inch aluminum block was used with the front surface reflection, first back surface echo, and second back surface echo being measured. The test was run with a constant water path of 3 cm for the 10 MHz transducers and 4 cm for the 15 MHz transducers. The attenuation coefficients were calculated according to Equation 2.25.

For all three measurement techniques, the attenuation constants were calculated at frequency intervals of 0.1 MHz. A curve was then drawn through the individual data points to obtain a graph of the frequency dependent attenuation for each experiment.

2.5.2 A357 Aluminum

For the multiple thickness technique rectangular A357 aluminum blocks were used with thicknesses of .974 inches, .811 inches, and .343 inches. The back surface reflection for each block was measured. The water path distance was kept constant at 3 cm for the 10 MHz transducers used in the measurements. The test was run five times per transducer, and the attenuation constants were calculated at each frequency according to Equation 2.8.

For the multiple echo technique, the same .974 inch A357 aluminum block was used as in the multiple thickness method. The first, second, and third back surface echoes were measured, and the water path distance was kept constant at 3 cm. The test was run five times for each transducer. Equation 2.12 was used to calculate the attenuation coefficients at each frequency.

For the multiple echo II technique, the same .974 inch A357 aluminum block was used with the front surface reflection, first back surface echo, and second back surface echo being measured. The test was run with a constant water path distance of 3 cm. The attenuation coefficient was calculated according to Equation 2.25.

Similarly to the 7075 aluminum attenuation versus frequency graphs, a frequency interval of 0.1 MHz was used in obtaining the graphs.

2.6 Results and Discussion

2.6.1 Measured Attenuation in 7075 Aluminum

The measured, frequency dependent attenuation was examined to check 1) the repeatability of the measurement for the same transducer and same method, 2)

the bias towards a particular method, and 3) the consistency of the measurements across transducers.

2.6.1.1 10 MHz Results Repeatability of the attenuation measurements for nine tests at 10 MHz (the nominal frequency of the transducers) can be seen by looking at the deviations between the high and low values of attenuation. In general, these values are under or equal to $\pm$ 20 % as shown in Table 2.1. It should be noted that these results, even though they contain significant experimental scatter, are acceptable for use in the measurement model of Equation of 1.1, because they were obtained with extremely small values of measured attenuation. Therefore, the attenuation contribution is relatively insignificant compared to other quantities which must be accounted for in the model. Consequently, the large experimental scatter in the attenuation results contributes very little error in the calculation of the scattering amplitude of the flaw. Typical attenuation measurement results are presented in Figures 2.8 through 2.10. These data are shown for transducer 3, however, they are typical results in that the multiple thickness test shows the greatest consistency of all three methods over all nine tests. This could be explained by the fact that precise attenuation measurements depend on the blocks having parallel sides. Note that the error due to the lack of parallel sides accumulates due to the consecutive echoes being measured in the ME and MEII techniques; however, in the MT technique, since only one echo is taken per block, these parallel sides are not as critical.

Bias of a particular method can be examined by looking at Figures 2.11 through 2.13. These graphs show the average attenuation over the nine tests per transducer per

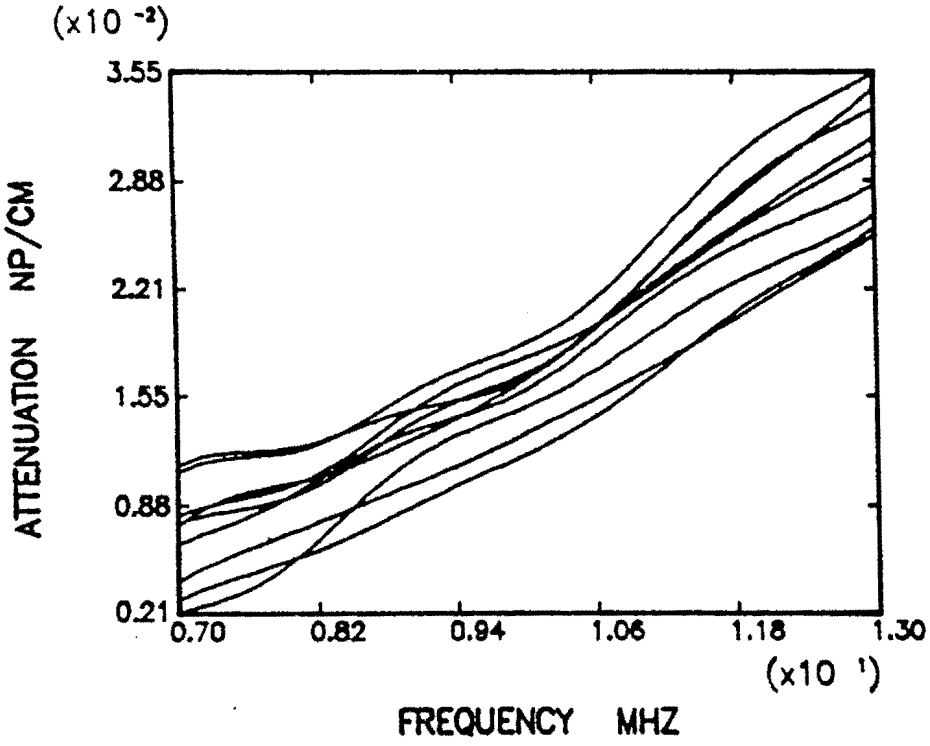

Figure 2.8: Attenuation in 7075 Aluminum Measured with Transducer 3 using the MEII Method

Table 2.1: Spread Between Minimum and Maximum Values of Attenuation Measured at 10 MHz (Nine Tests per 10 MHz Transducer per Method)

Method	Transducer Number	Spread($\frac{Np}{cm}$)	Spread %
ME	1	.7245234(10^-2)	35.03
MT	1	.3717692(10^-2)	18.56
MEII	1	.3987275(10^-2)	1.93
ME	2	.8366453(10^-2)	42.525
MT	2	.2985893(10^-2)	14.20
MEII	2	.4581881(10^-2)	24.239
ME	3	.4478911(10^-2)	28.414
MT	3	.1764437(10^-2)	13.562
MEII	3	.6760299(10^-2)	42.628

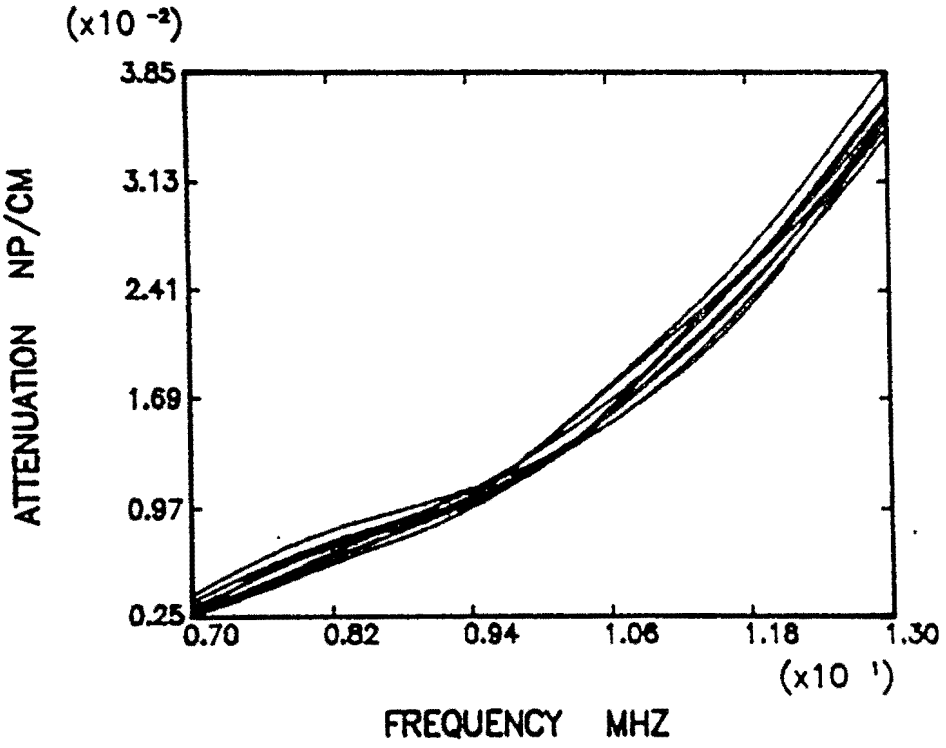

Figure 2.9: Attenuation in 7075 Aluminum Measured with Transducer 3 using the MT Method

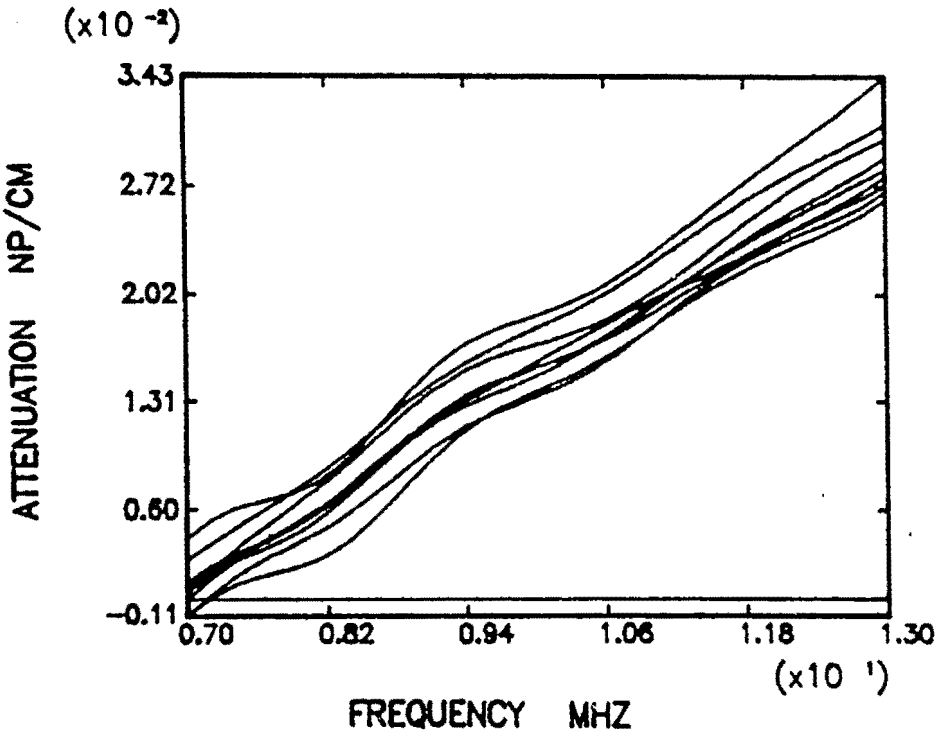

Figure 2.10: Attenuation in 7075 Aluminum Measured with Transducer 3 using the ME Method

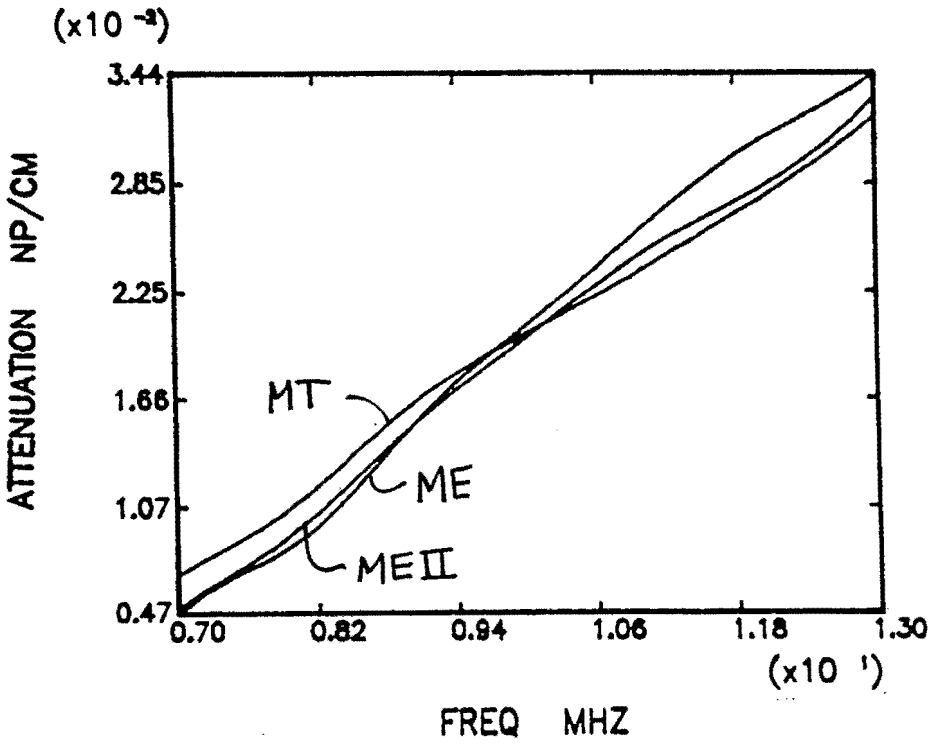

Figure 2.11: Attenuation in 7075 Aluminum Measured with Transducer 1 using MT, ME, and MEII Methods

method. The data are graphed individually for each transducer. By examination of these graphs, it can be seen that for each transducer, there is some scatter in results across measurement techniques, however, no one particular method seems to give consistently higher than average or lower than average results. In order to calculate experimental scatter in attenuation results, deviations were defined according to the equation:

$$\epsilon(f) = \frac{\alpha(f)_{experimental} - \alpha(f)_{average}}{\alpha(f)_{average}} \tag{2.26}$$

For all three transducers, the attenuation deviations obtained with three dif-

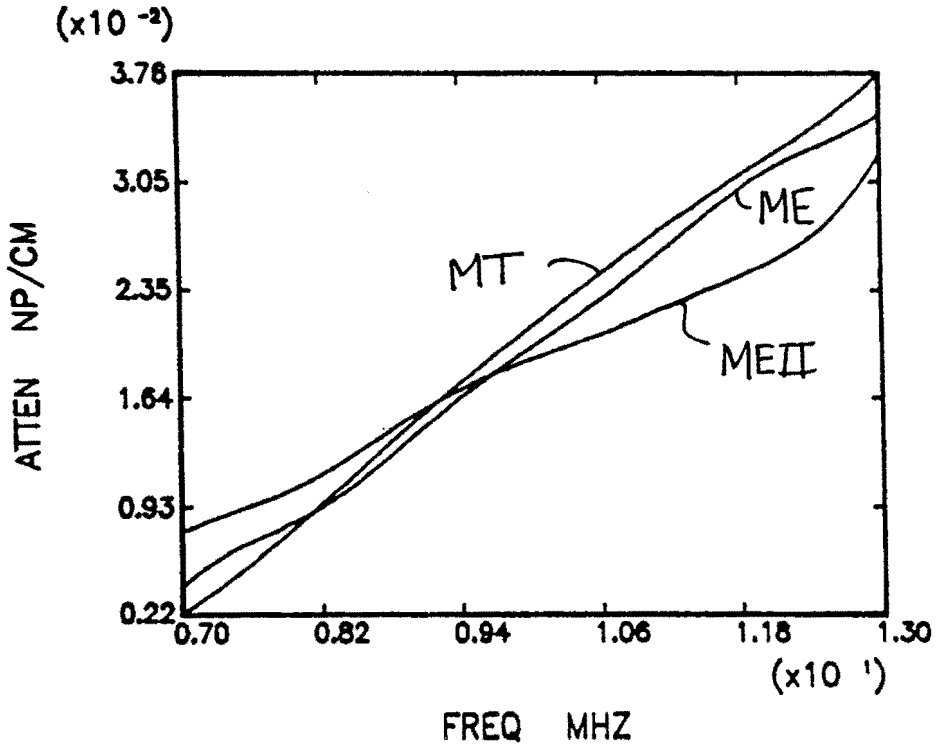

Figure 2.12: Attenuation in 7075 Aluminum Measured with Transducer 2 using MT, ME, and MEII Methods

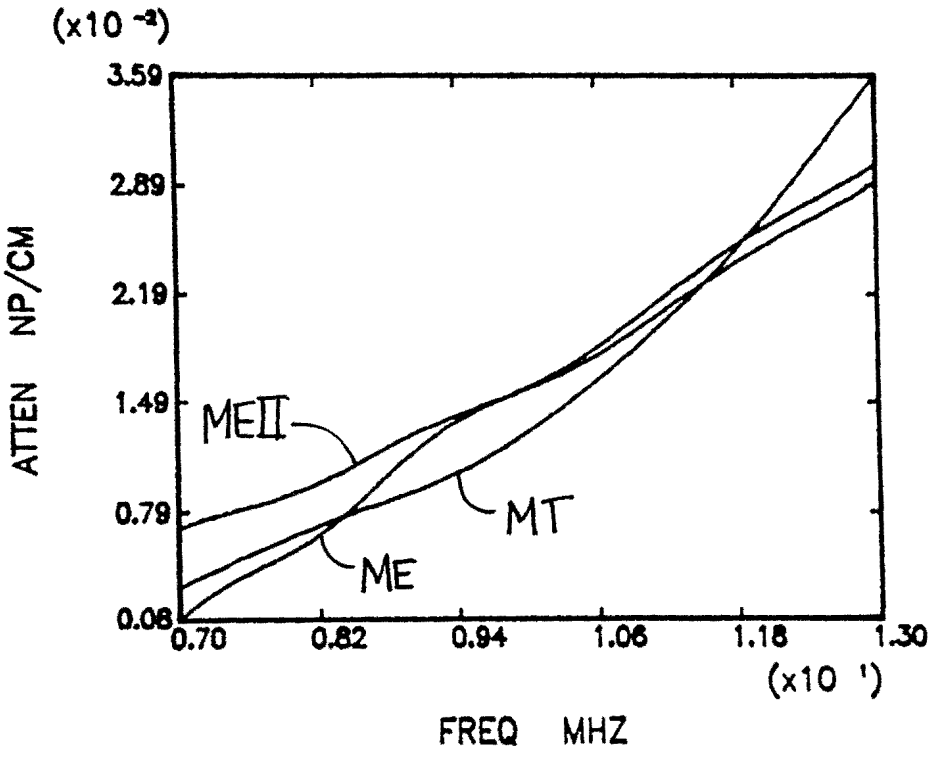

Figure 2.13: Attenuation in 7075 Aluminum Measured with Transducer 3 using MT, ME, and MEII Methods

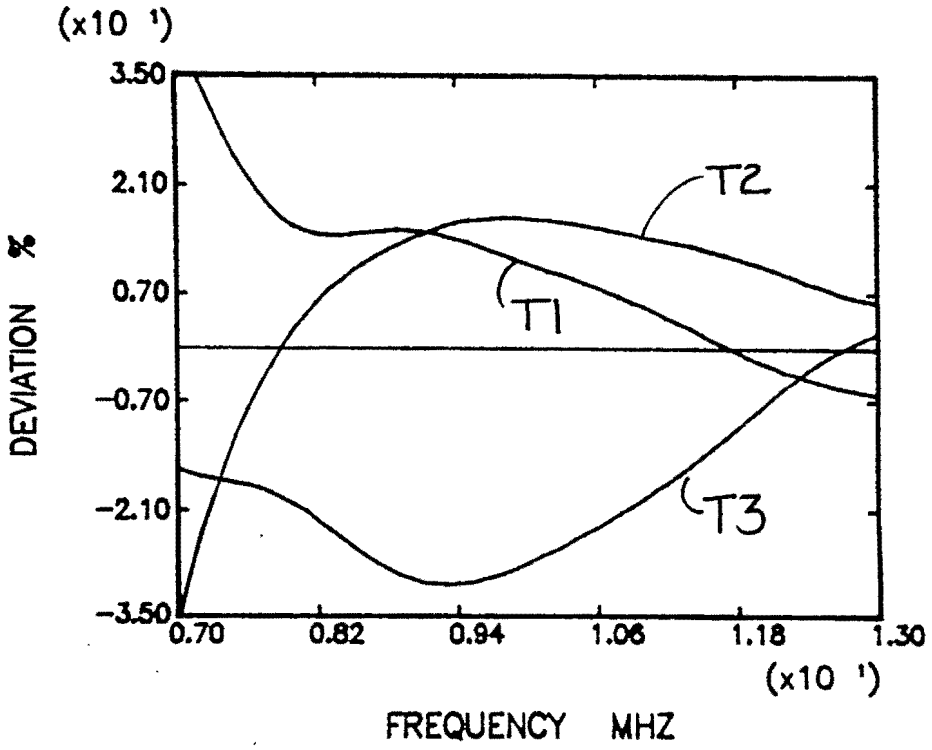

Figure 2.14: Deviation of 7075 Aluminum Attenuation Measured with the MT Technique (Transducers 1, 2, 3)

ferent transducers for each particular method have values within $\pm$ 20 %, showing once again consistency and no bias between methods. It must be noted, however, that the multiple thickness technique, although very consistent for only one transducer, is the most inconsistent across transducers; consequently, this method is very dependent on transducer characterization. The multiple echo II method, however, is the least transducer dependent. Figures 2.14 through 2.16 show the deviations obtained for all three methods.

It is known that source characterization is important at rather small distances from a source, and at very large distances, all fields resemble an amplitude decay

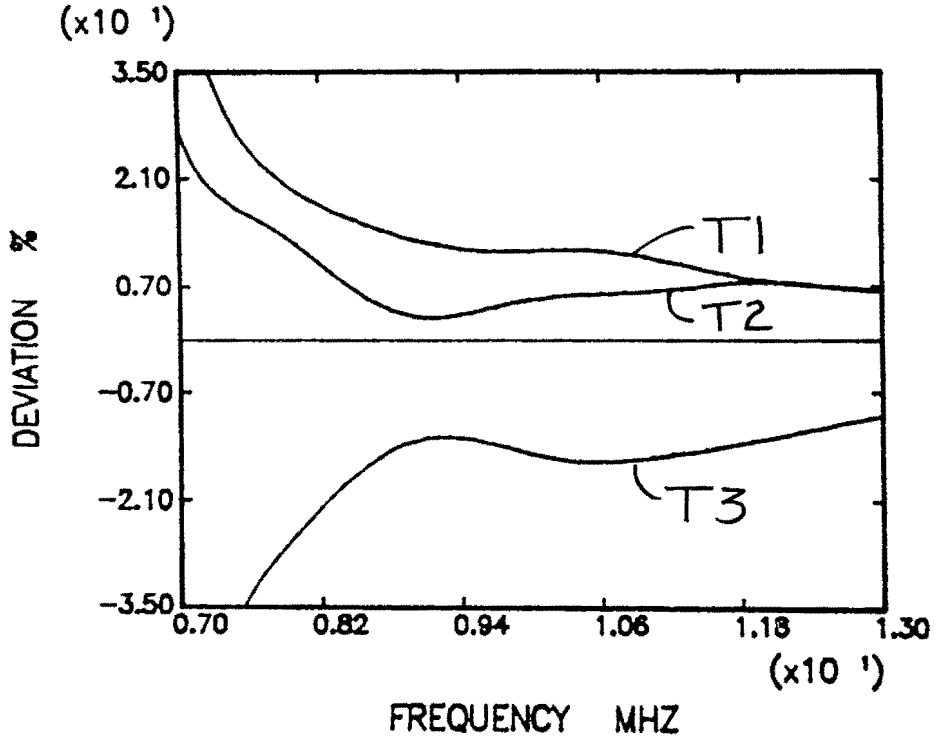

Figure 2.15: Deviation of 7075 Aluminum Attenuation Measured with the ME Technique (Transducers 1, 2, 3)

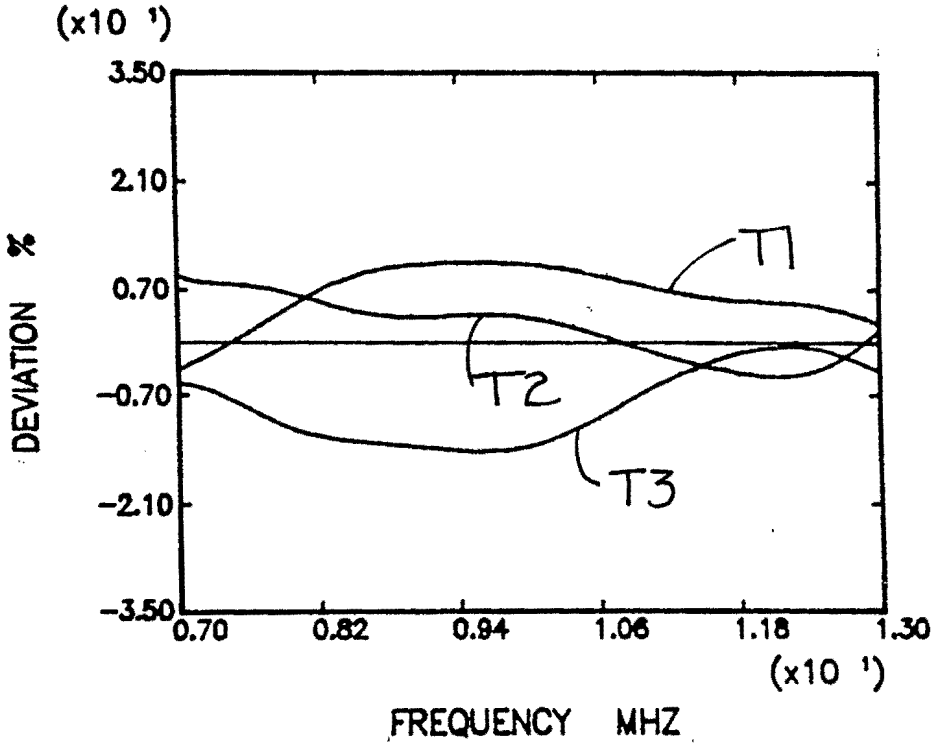

Figure 2.16: Deviation of 7075 Aluminum Attenuation Measured with the MEII Technique (Transducers 1, 2, 3)

Table 2.2: s Parameters for the Different Attenuation Measurement Methods (s= $\frac{z\lambda}{a^2}$)

Measurement Method	Frequency MHz	s Parameter Value			
		echo 1	echo 2	echo 3	average
MT	10	2.477	5.672	10.465	6.205
ME	10	5.672	10.465	15.257	10.465
MEII	10	0.880	5.672	10.465	5.672

which is inversely proportional to the distance. A dimensionless parameter describing the distance from the piston source is the s parameter. It is defined according to the equation [12]:

$$s = \frac{z\lambda}{a^2} \tag{2.27}$$

where

z= the distance from the transducer of radius a

λ = the wavelength

The s parameters for the different methods can be seen in Table 2.2. If scatter in measured attenuation is caused by inaccurate modeling of individual transducers, then one would expect that the higher the s value is, the lower should be the experimental scatter, however in looking at Figures 2.14 through 2.16, this tendency does not seem to be followed. Results obtained with the MEII method show the smallest deviations between transducers although this method uses the smallest distances (the lowest average s value). However, scatter in results obtained with the ME method are smaller than with the MT method's which do follow the expected tendency.

The consistency of the measurements across transducers can be examined by looking at the results of the individual methods averaged for the three transducers

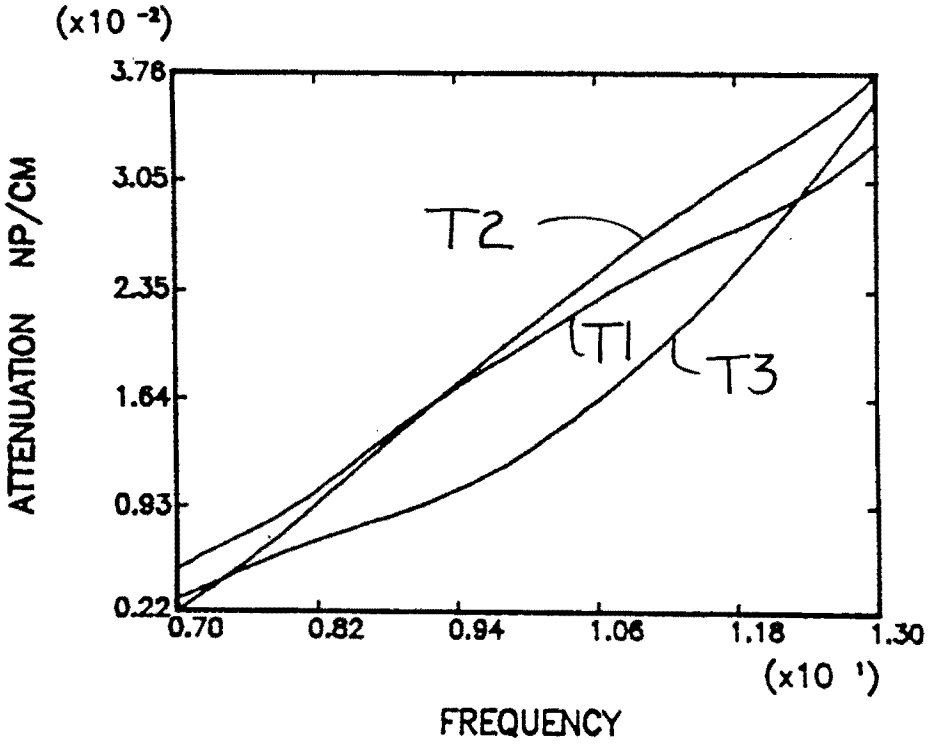

Figure 2.17: Attenuation in 7075 Aluminum Measured with the Multiple Thickness Technique (Transducers 1, 2, 3)

separately. Results can be seen in Figures 2.17 through 2.19. For all methods, transducer 3 gives consistently the lowest attenuation values, while the results for transducers 1 and 2 show no particular bias and are in general closer in value to each other than to results obtained with transducer 3. All transducers - except transducer 3 - give deviations under 20 % for each test with the same averaging technique being followed as before. Figures 2.20 through 2.22 illustrate this result.

2.6.1.2 15 MHZ Results Repeatability of nine attenuation measurements for each transducer and each method was better than the results for the 10 MHz transducers. The spread between the values of the measured attenuation is shown

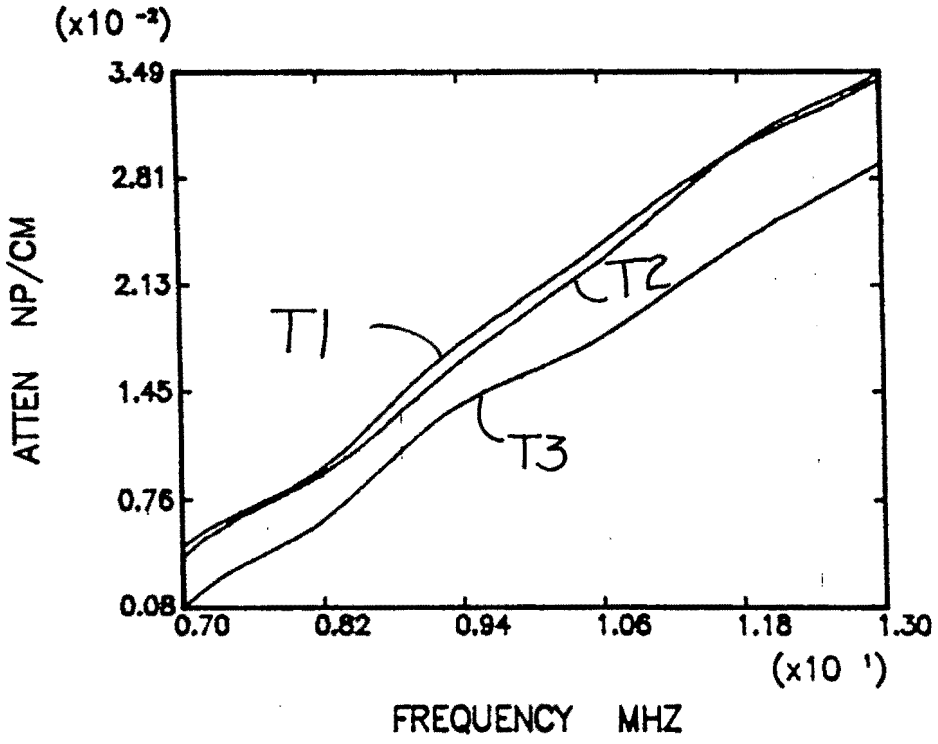

Figure 2.18: Attenuation in 7075 Aluminum Measured with the Multiple Echo Technique (Transducers 1, 2, 3)

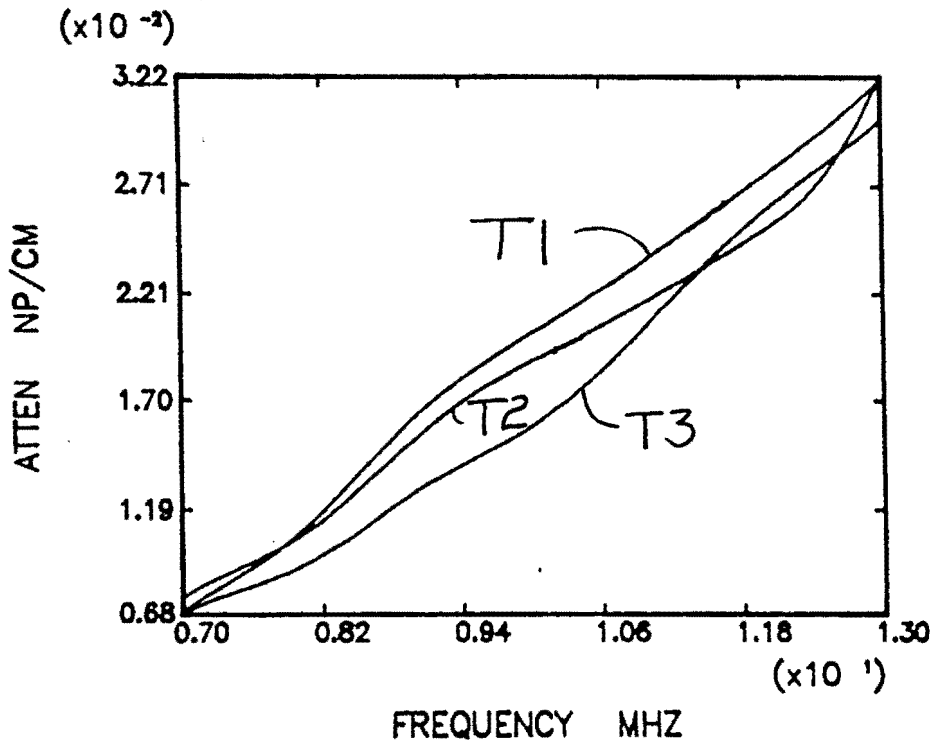

Figure 2.19: Attenuation in 7075 Aluminum Measured with the Multiple Echo II Technique (Transducers 1, 2, 3)

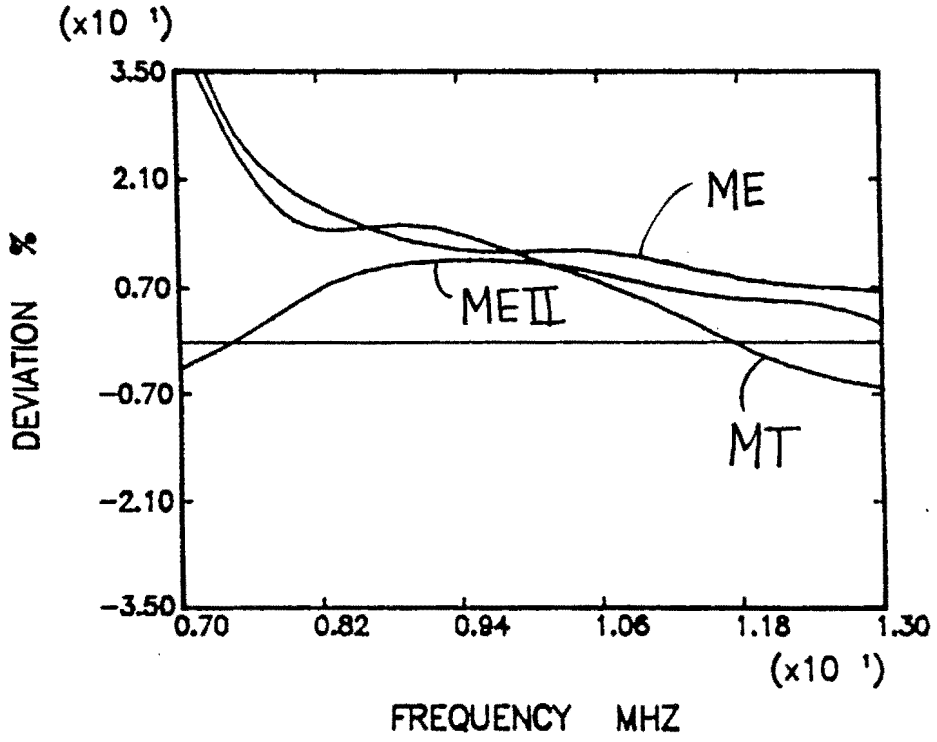

Figure 2.20: Deviation of the Results of ME, MT, and MEII Attenuation Tests for 7075 Aluminum (Transducer 1)

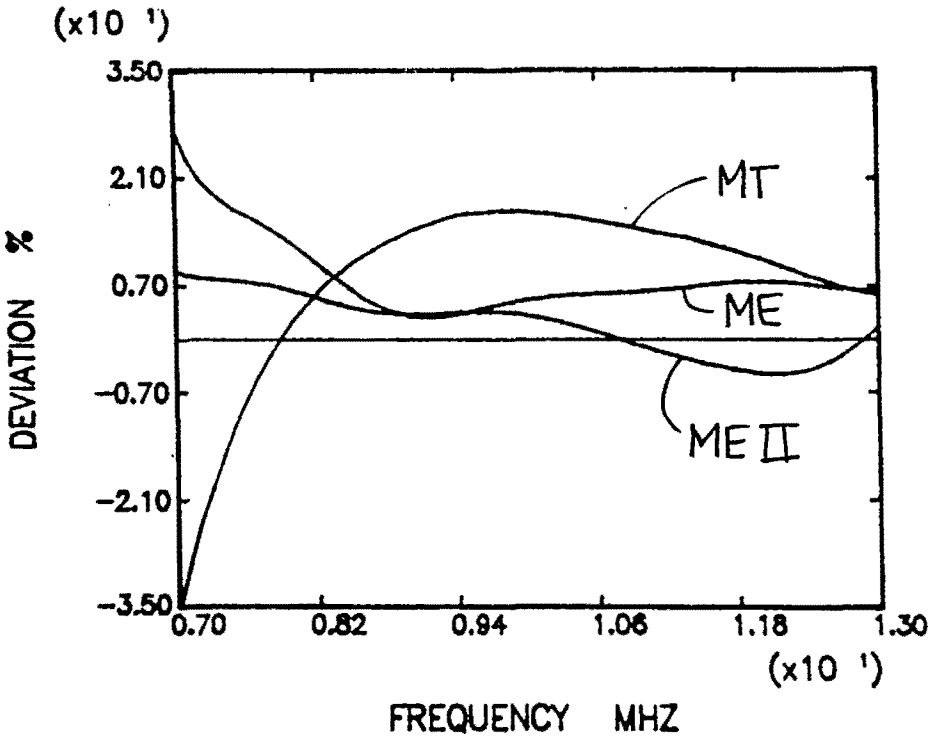

Figure 2.21: Deviation of the Results of ME, MT, and MEII Attenuation Tests for 7075 Aluminum (Transducer 2)

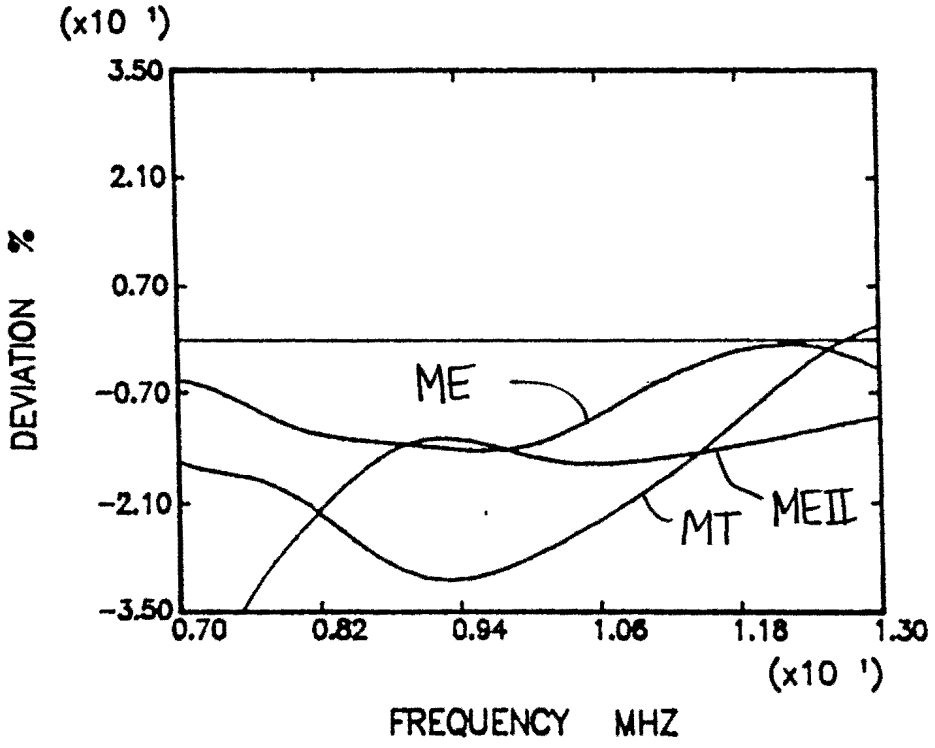

Figure 2.22: Deviation of the Results of ME, MT, and MEII Attenuation Tests for 7075 Aluminum (Transducer 3)

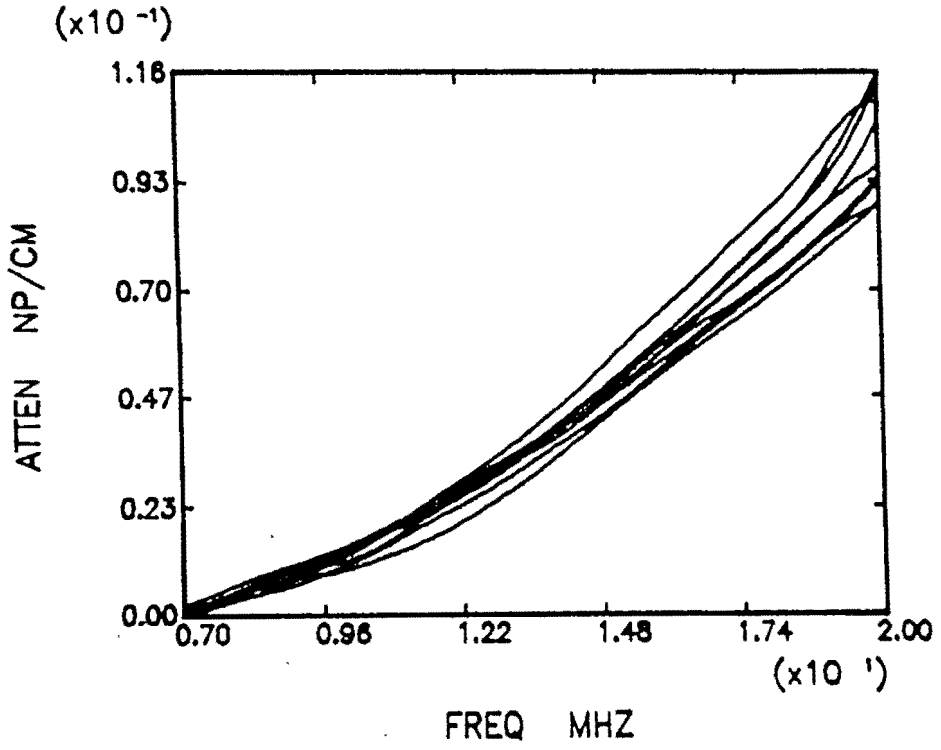

Figure 2.23: Attenuation in 7075 Aluminum using the MT Technique with 15 MHz Transducer 1

in Table 2.3. In this case, with the 15 MHz transducers, no conclusion can be made for one method being more consistent than any of the other methods. Results for transducer 1 with the multiple thickness technique can be seen in Figure 2.23.

Differences between attenuation values measured with a particular method can be examined from results shown in Figures 2.24 and 2.25. These graphs show no bias toward any one particular method, and in looking at the deviations (which were calculated according to Equation 2.26), it is seen that the scatter in the results obtained with all methods, ME, MT, and MEII, stay under 6%, within the transducer frequency bandwidth, as shown in Figures 2.26 through 2.28.

Table 2.3: Spread Between Highest and Lowest Values of Attenuation Measured at 15 MHz (Nine Tests per 15 MHz Transducer per Method)

Method	Transducer Number	Spread (Np/cm)	Spread %
ME	1	.8473967(10)$^{-2}$	22.457
MT	1	1.1543546(10)$^{-2}$	23.942
MEII	1	.9522852(10)$^{-2}$	24.455
ME	2	1.0809563(10)$^{-2}$	26.857
MT	2	1.0625124(10)$^{-2}$	23.634
MEII	2	.7505517(10)$^{-2}$	1.773

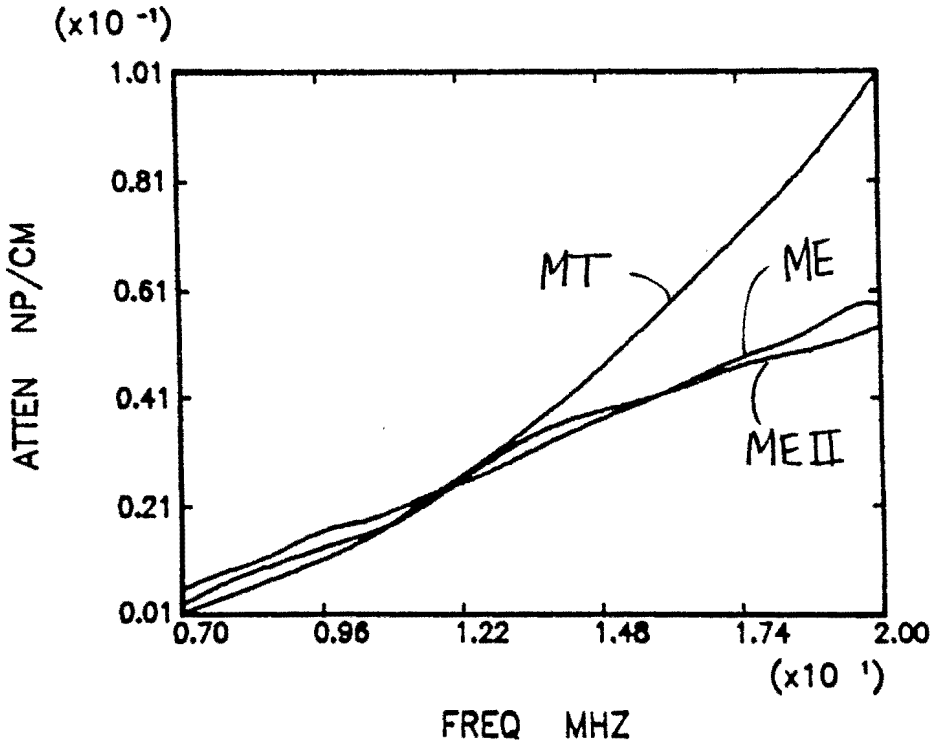

Figure 2.24: Attenuation in 7075 Aluminum using the ME, MEII, and MT Techniques with 15 MHz Transducer 1

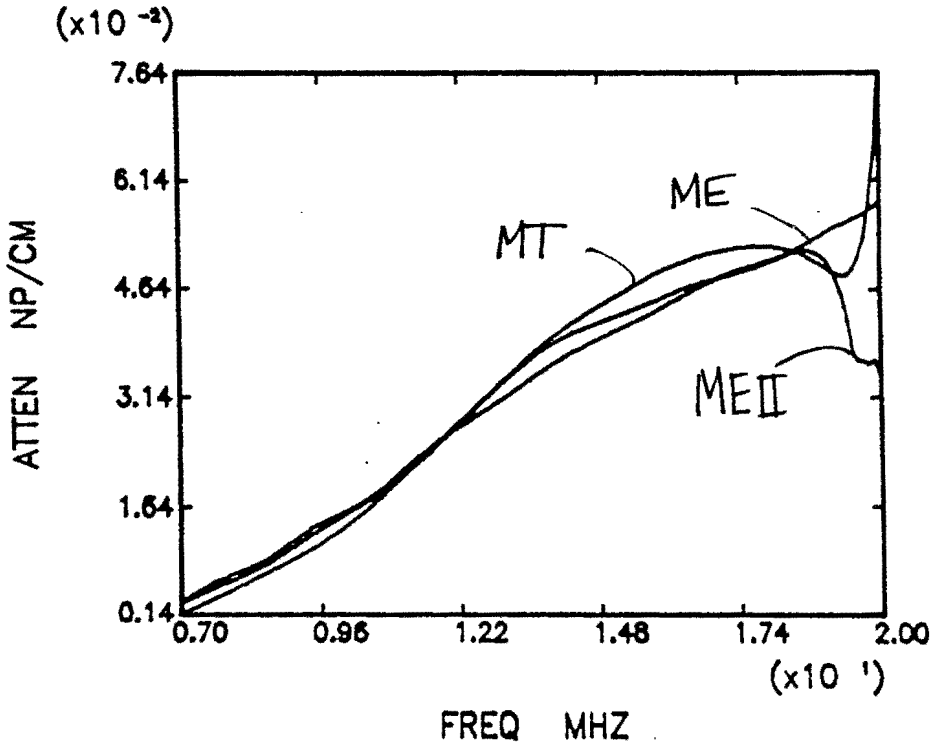

Figure 2.25: Attenuation in 7075 Aluminum using the ME, MEII, and MT Techniques with 15 MHz Transducer 2

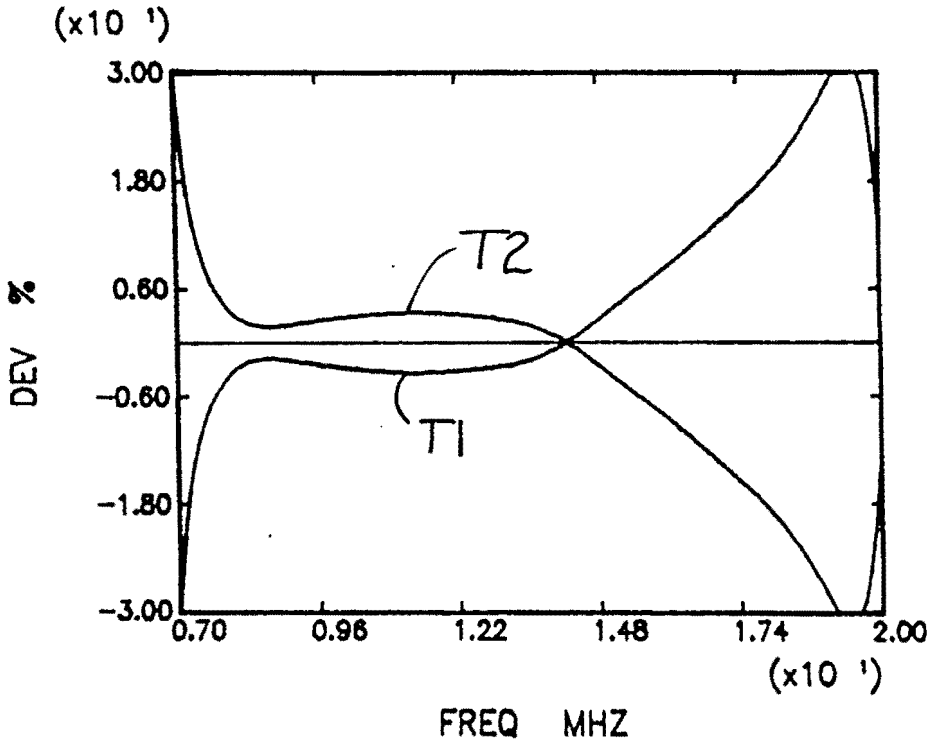

Figure 2.26: Deviation of 7075 Aluminum Attenuation Measured with the MT Technique for 15 MHz Transducers 1 and 2

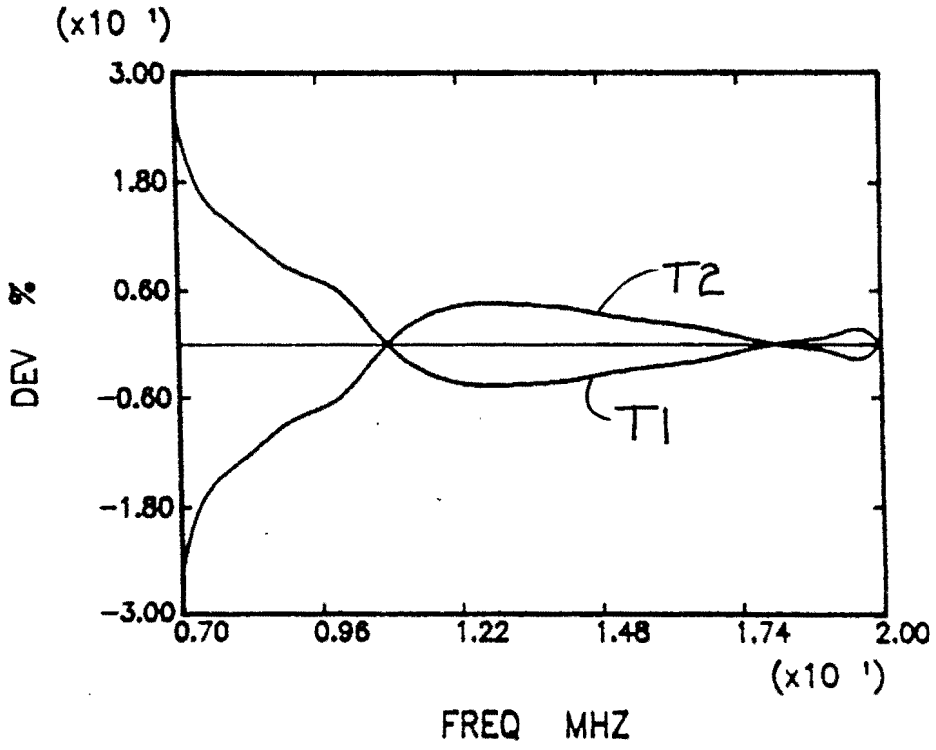

Figure 2.27: Deviation of 7075 Aluminum Attenuation Measured with the ME Technique for 15 MHz Transducers 1 and 2

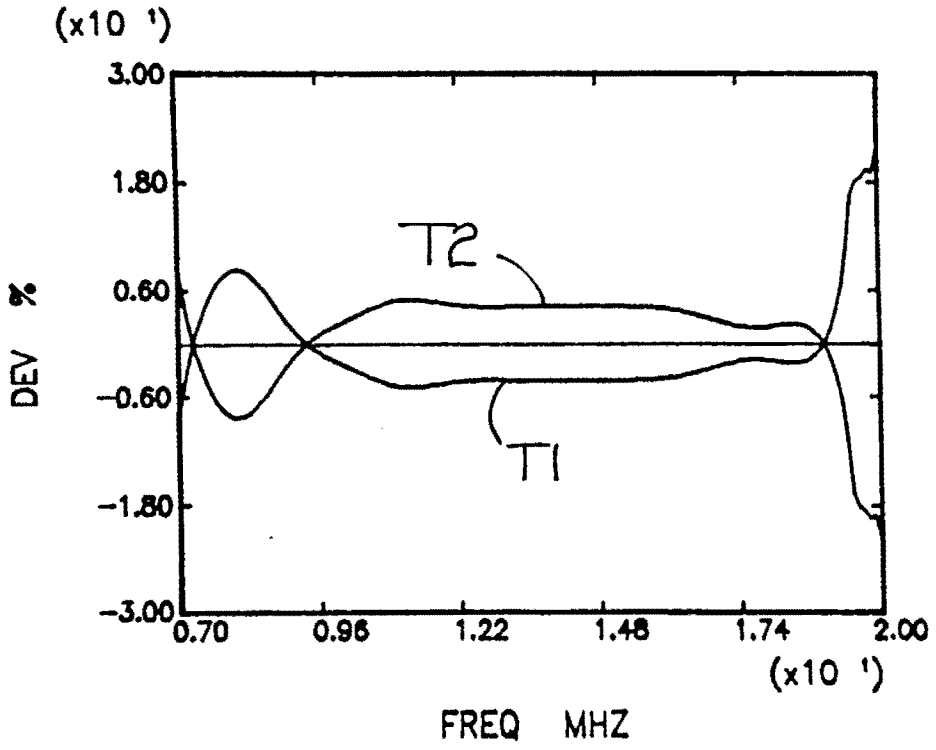

Figure 2.28: Deviation of 7075 Aluminum Attenuation Measured with the MEII Technique for 15 MHz Transducers 1 and 2

The s parameters for the three methods can be seen in Table 2.4. All deviations in attenuation results obtained with the 15 MHz transducers are lower than with the 10 MHz transducers, even though the 10 MHz results had higher s values. This could be due to the fact that at 15 MHz, the material attenuation value is significantly higher than at 10 MHz. Thus the effect of characterizing the transducers (diffraction correction estimations) becomes less important. Another way of considering the attenuation versus diffraction importance is to note that as the material attenuation becomes larger, it is the main cause of decreasing the propagating wave amplitude

Table 2.4: s Parameter for the Different Attenuation Measurement Methods

Measurement Method	Frequency MHz	s Parameter Value			
		echo 1	echo 2	echo 3	average
MT	15	1.847	3.977	7.172	6.498
ME	15	3.977	7.172	10.367	7.172
MEII	15	.782	3.977	7.172	3.977

with the wave diffraction (beam spread) being the secondary factor.

Differences between transducers are minimal, with transducer 2 giving slightly higher values of attenuation than transducer 1 for all methods as shown in Figure 2.29. The deviations in attenuation measured with different transducers for the three methods were smaller than $\pm$ 6 %, as shown in Figure 2.30.

2.6.2 Measured Attenuation in A357 Aluminum

Repeatability of the attenuation measurements for five tests per transducer was much better than with the 7075 aluminum. The A357 aluminum attenuation values were five times higher than the attenuation values obtained for the 7075 aluminum. This increase made the attenuation much easier to measure since the diffraction did not play a significant role in the experimental results. It must be noted, however, that when the values of the attenuation increase, in order to use the measurement model successfully, more accuracy in the attenuation measurements is required.

Figures 2.31 through 2.33 can be examined to find the bias between methods, and from these graphs, it is evident that no particular method gives consistently high or low values for the attenuation. The deviations (which were calculated according to Equation 2.26) stay under $\pm$ 9 %, as seen in Figures 2.34 through 2.36, for all methods.

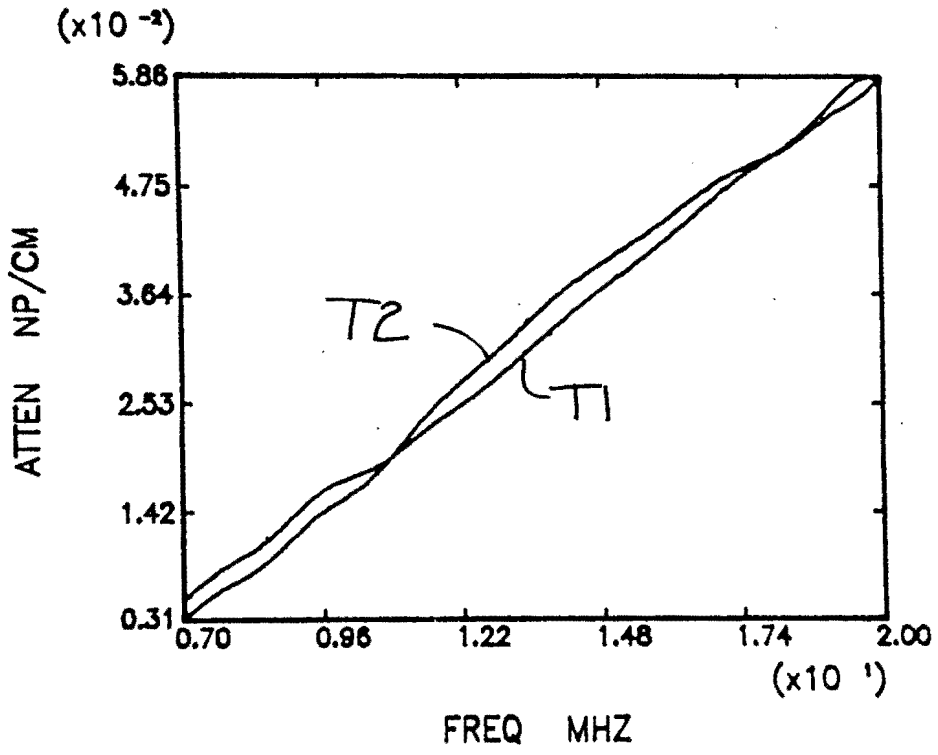

Figure 2.29: Attenuation in 7075 Aluminum with the ME Technique for 15 MHz Transducers 1 and 2

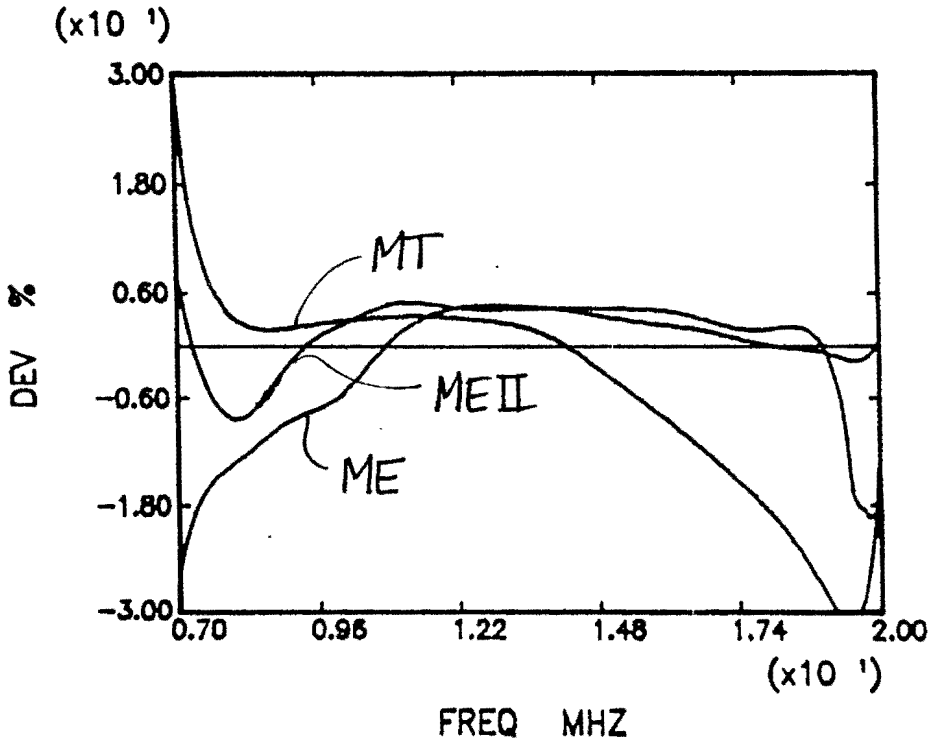

Figure 2.30: Deviation of the 7075 Aluminum Attenuation Measured with the MT, ME, and MEII Techniques for Transducer 2

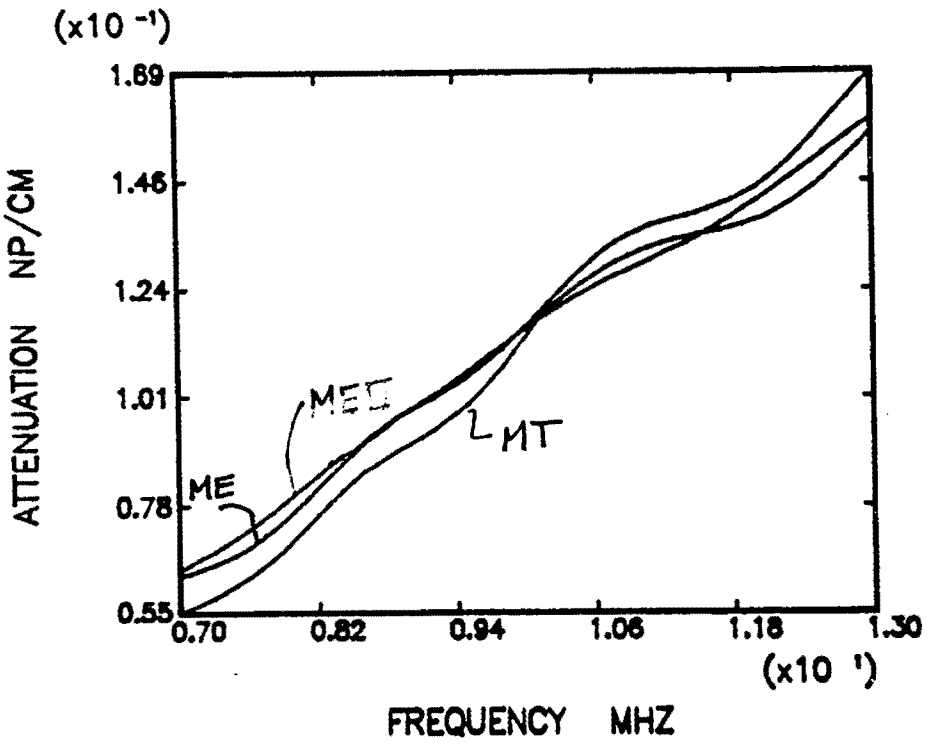

Figure 2.31: Attenuation in A357 Aluminum Measured with Transducer 1 using the MT, ME, and MEII Methods

Differences between transducers are minimal as can be seen in Figures 2.37 through 2.39. The deviations between transducers for the three methods stayed within $\pm$ 9 %, and these results can be seen in Figures 2.40 through 2.42.

2.7 Conclusions

Three experimental techniques, the multiple echo, multiple echo II, and the multiple thickness technique, have been used to measure the ultrasonic wave attenuation in 7075 and A357 aluminum. Measurements were performed with non-focused, immersion type transducers: three of 10 MHz and two of 15 MHz nominal

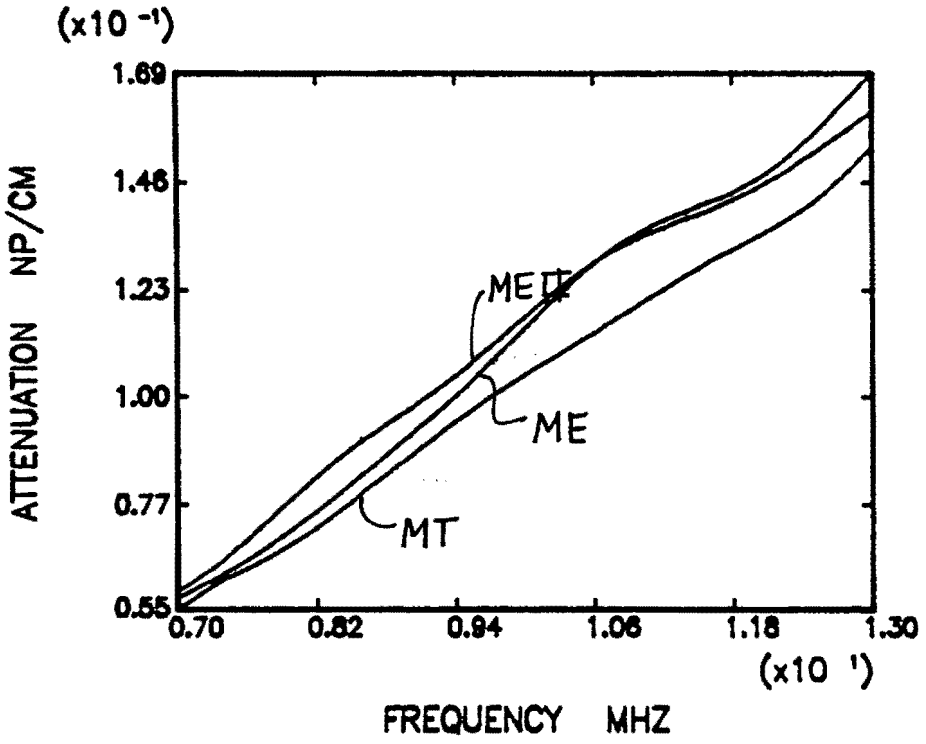

Figure 2.32: Attenuation in A357 Aluminum Measured with Transducer 2 using the MT, ME, and MEII Methods

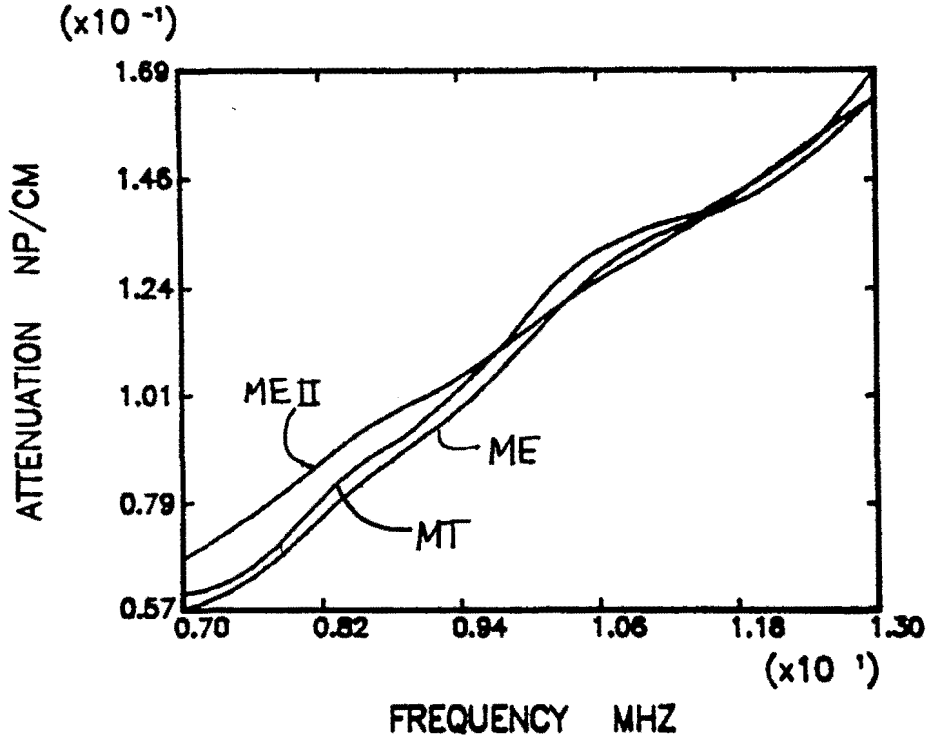

Figure 2.33: Attenuation in A357 Aluminum Measured with Transducer 3 using the MT, ME, and MEII Methods

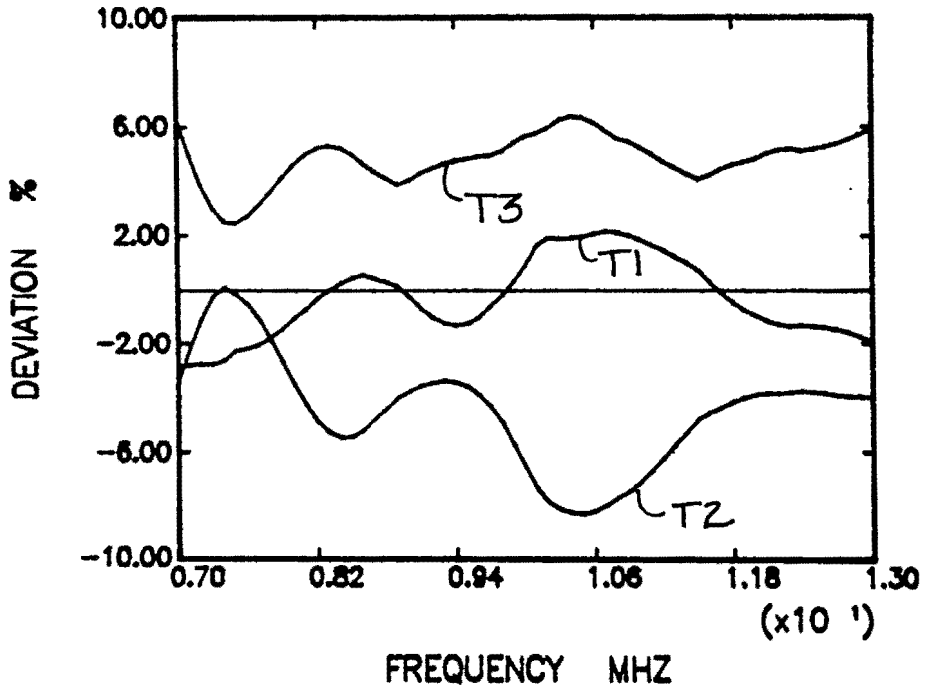

Figure 2.34: Deviation of A357 Aluminum Attenuation Measured with the MT Technique (Transducer 1, 2, 3)

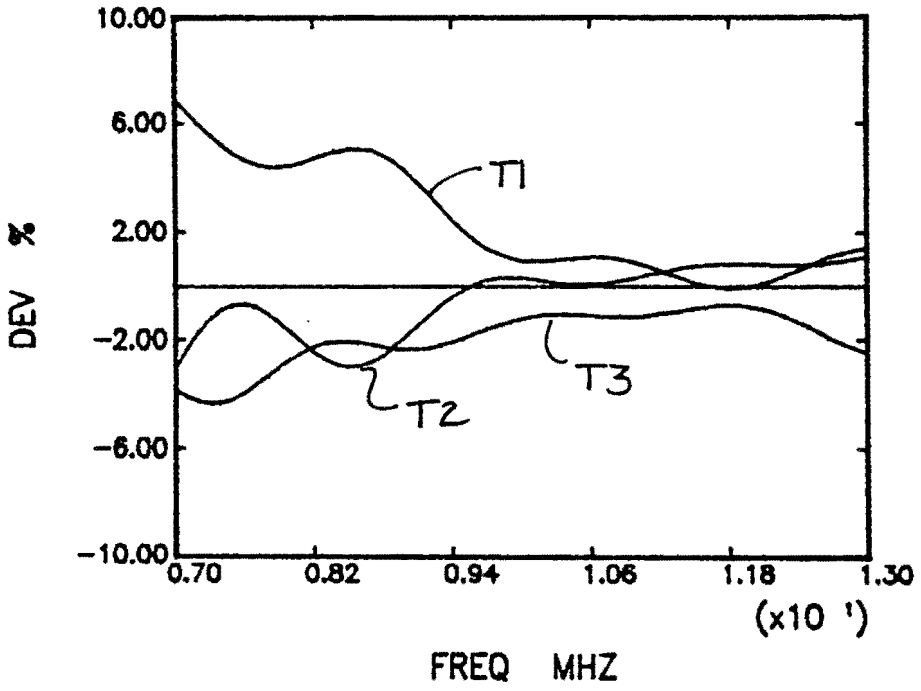

Figure 2.35: Deviation of A357 Aluminum Attenuation Measured with the ME Technique (Transducer 1, 2, 3)

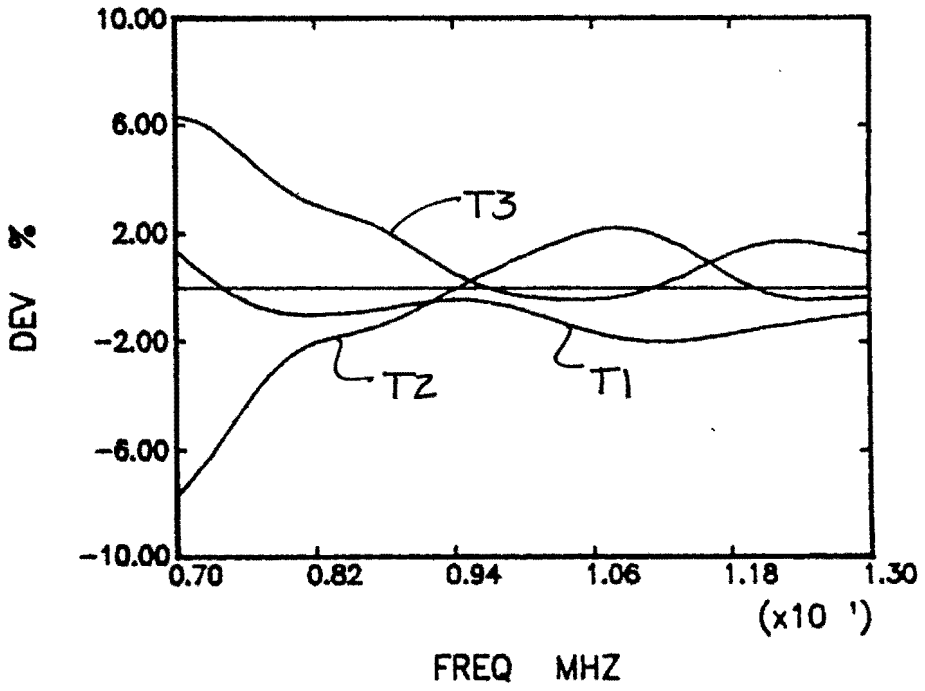

Figure 2.36: Deviation of A357 Aluminum Attenuation Measured with the MEII Technique (Transducer 1, 2, 3)

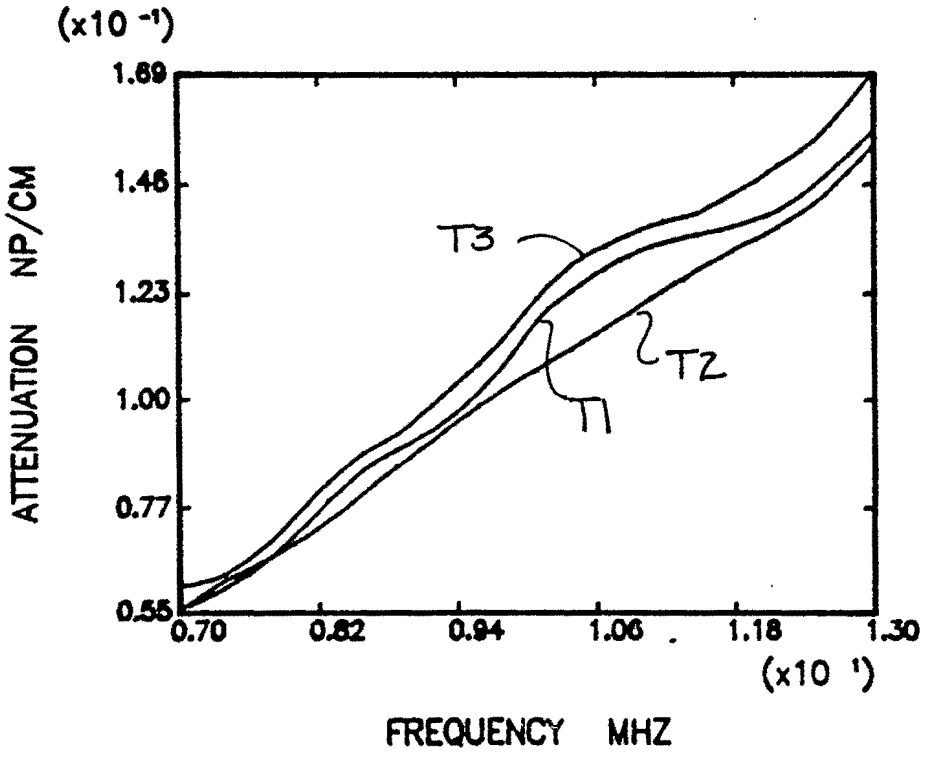

Figure 2.37: Attenuation of A357 Aluminum Measured with the MT Technique (Transducer 1, 2, 3)

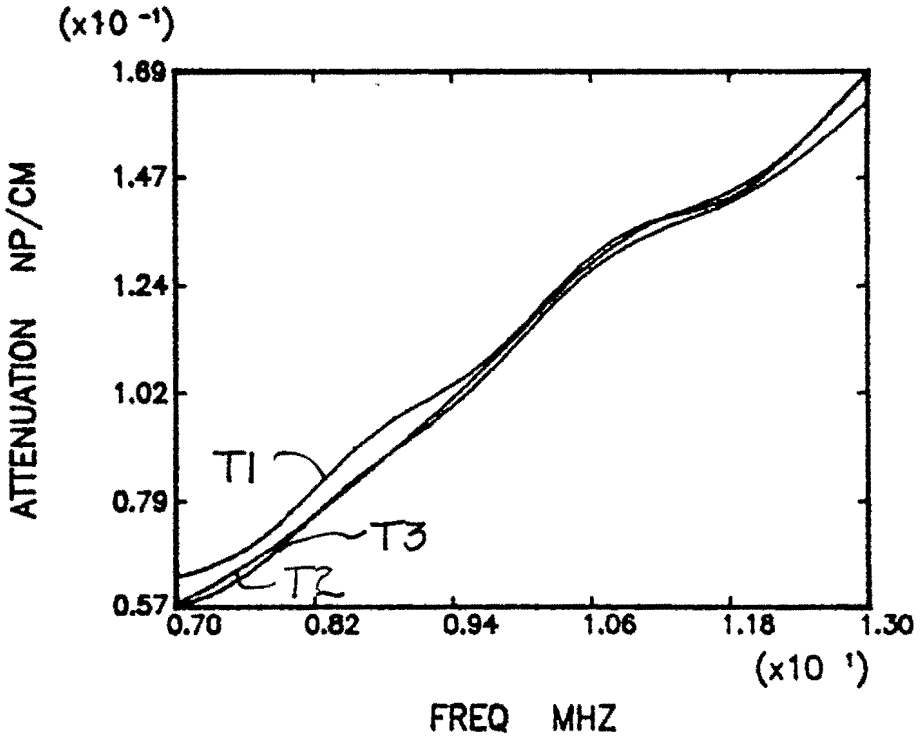

Figure 2.38: Attenuation of A357 Aluminum Measured with the ME Technique (Transducer 1, 2, 3)

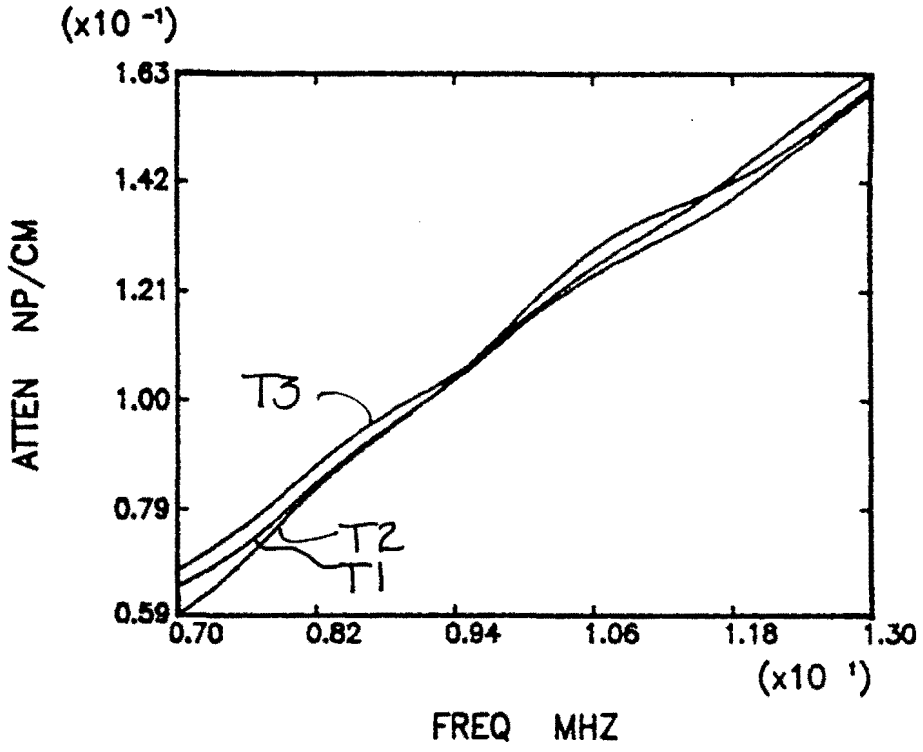

Figure 2.39: Attenuation of A357 Aluminum Measured with the MEII Technique (Transducer 1, 2, 3)

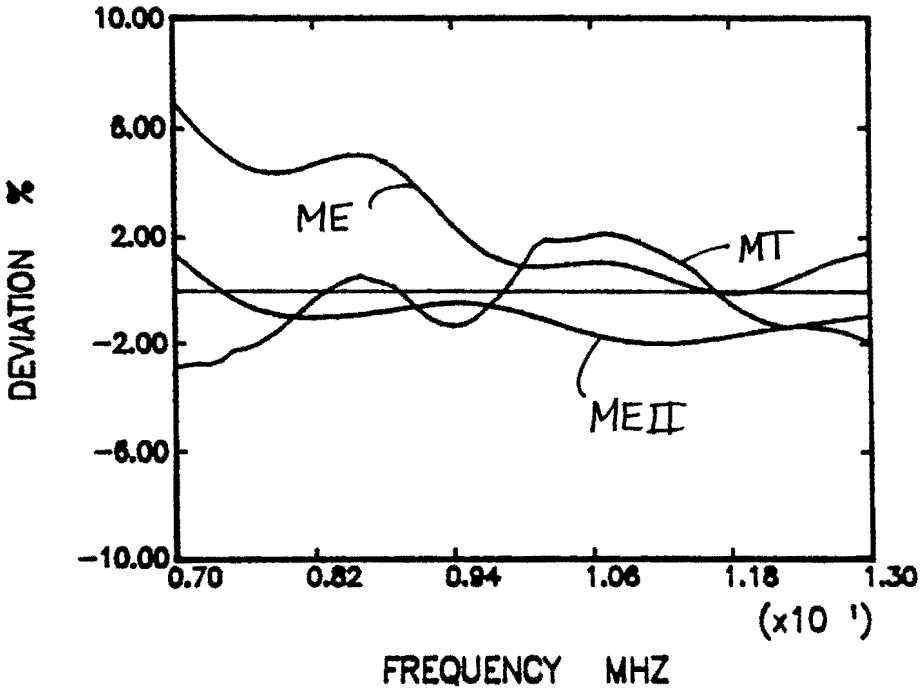

Figure 2.40: Deviation of the Results of the MT, ME, and MEII Attenuation Tests for A357 Aluminum (Transducer 1)

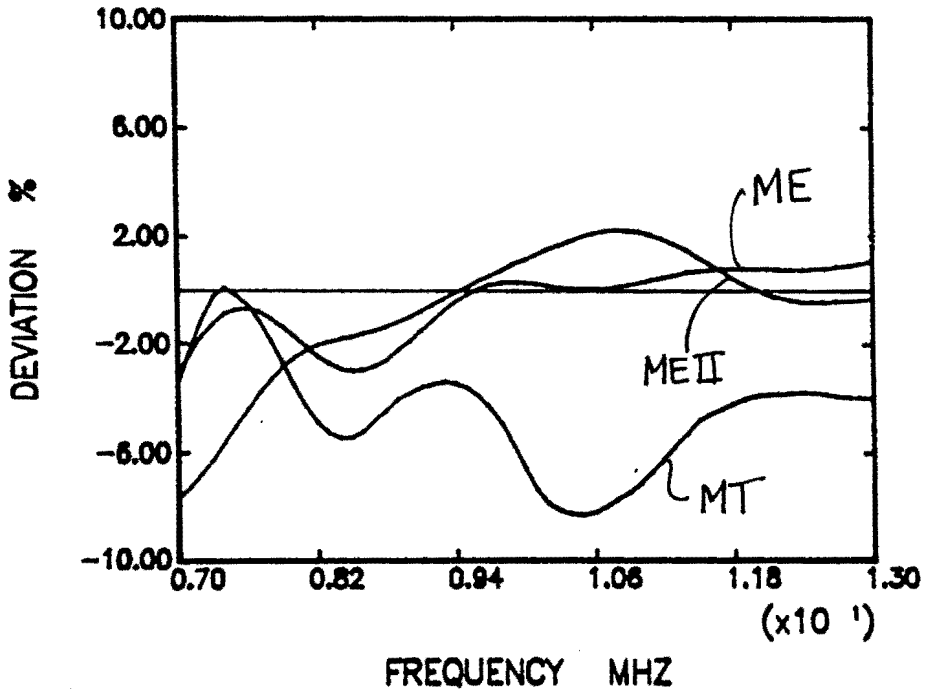

Figure 2.41: Deviation of the Results of the MT, ME, and MEII Attenuation Tests for A357 Aluminum (Transducer 2)

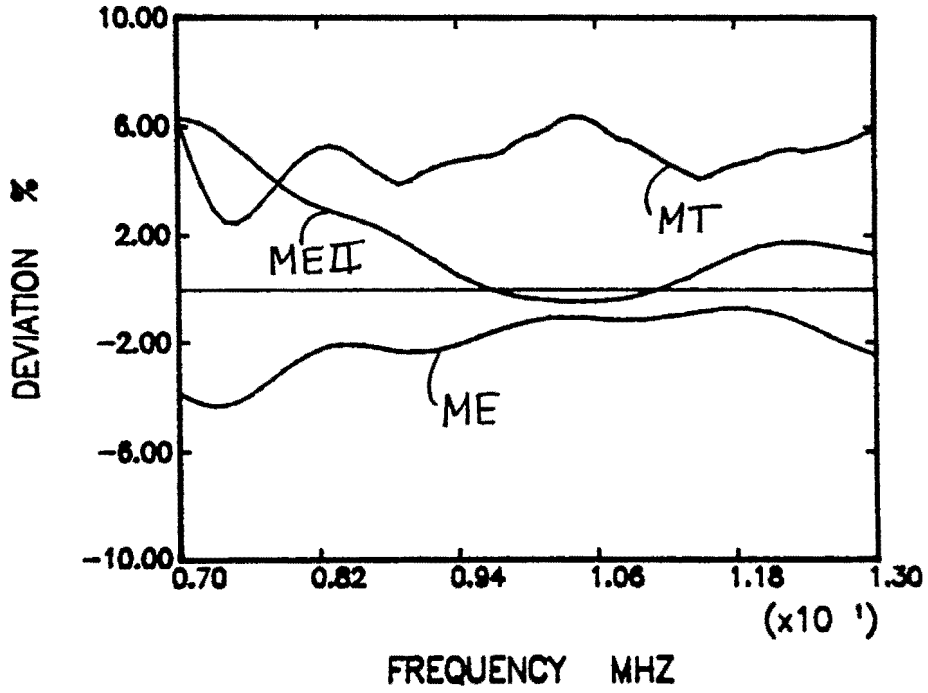

Figure 2.42: Deviation of the Results of the MT, ME, and MEII Attenuation Tests for A357 Aluminum (Transducer 3)

frequency. The frequency dependent attenuation was measured and checked for repeatability of the measurement for the same transducer and same method, the bias toward a particular method, and the consistency of the measurements across transducers. The conclusions reached can be stated as follows:

1) The multiple thickness method of measurement is the most repeatable when compared to the other two methods of measurement, however, it is also the most transducer dependent.

2) No one particular method gives consistently higher than average or lower than average results.

3) More accurate characterization of transducers is needed to make attenuation measurements less transducer dependent by improving estimations of diffraction corrections for the probes involved.

4) At higher frequencies, attenuation measurements become more consistent even when the same methods are used, because the attenuation increases with frequency, and the diffraction effects associated with the probe's beam become less important.

5) Dealing with materials of high attenuation, it is possible to measure the attenuation more consistently, using the same methods and transducers, than for materials with extremely low attenuation. This feature can be attributed to the fact that the diffraction corrections, and, therefore the transducer characterization, are less important when material attenuation is rather high. However, it is important to note that methods tested in this thesis are not suitable for extremely high attenuating materials.

In summary, it is evident that individual transducer characteristics are the

most significant factors causing scatter in attenuation measurements, especially for low attenuating materials such as aluminum alloys.

3 TRANSDUCER CHARACTERIZATION

3.1 Introduction

In order to quantitatively interpret received electrical signals from ultrasonic measurements, the ultrasonic transducers used in the measurements must be characterized such that their properties can be compensated for. It is common practice in modeling of experiments, including attenuation measurements, to assume that transducers radiate acoustic waves as planar piston sources. However, there is evidence, in the literature, based on a variety of transducers' field investigations (on-axis pressure studies, c-scan profiles, and surface motion imaging) that individual transducers of the same diameter and nominal frequency can generate considerably different fields. Therefore, by correlating vibrating piston theory with experimental results, analysis and comparisons of the transducers can be made.

It has been demonstrated in the previous chapter of this thesis that individual transducer characteristics can cause scatter in attenuation results. In this chapter, the 10 MHz transducers used in previously performed attenuation tests are experimently investigated, and their results are compared with rigid piston theory. Specifically, axial and radial pressure amplitude profiles are measured. Using the axial profile, an active diameter of each transducer is calculated. The radial profiles are used to gain insight into the symmetry of the individual transducers.

As a result, differences between fields generated by the transducers involved in the measurements and the rigid piston theory predictions are investigated.

The goal of reported research in this section is to identify transducers that behave most closely to the rigid piston theoretical predictions. Next, these results will be used to attempt to decrease the scatter in attenuation results caused by inaccuracies in transducer characterization.

3.2 Axial Profiles

3.2.1 Theory

Based on the assumption that the transducer radiates as a planar circular piston, the pressure amplitude on axis of the transducer is [12]

$$P(r,0) = 2\rho_O c u_O \left| \sin \frac{1}{2} kr \left[\sqrt{1 + \left(\frac{a}{r}\right)^2} - 1 \right] \right| \tag{3.1}$$

where

ρ_O = fluid density

c = acoustic velocity in the fluid

u_O = surface velocity amplitude

k = wave number

r = axial distance from the transducer

a = radius of the transducer

If any technique of measuring the pressure amplitude of the ultrasonic wave is used along the axis of the piston, and this axial-distance-dependent amplitude is compared to the theoretical profile, an active diameter can be calculated for

the transducer which makes the theoretical profile correlate most closely with the experimental profile.

3.2.2 Axial Profile Measurements

The transfer function for a transmitting-receiving transducer system can be defined as

$$H(f,z) = \frac{V_r(f,z)}{V_t(f,z)} \tag{3.2}$$

where

$V_r(f,z)$ = voltage at the receiving transducer

$V_t(f,z)$ = voltage at the transmitting transducer

This transfer function can also be written in terms of transducer characterization equations and the Green's function. To determine the transducer parameters from the measurement of $H(f,z)$ at various transducer locations, z, a convenient form of the Green's function can be obtained if a 'quasi point' reflector located on the acoustic axis of the transducer, in the same fluid medium is used [13]. In this thesis, a small spherical reflector method was used for the purpose of transducer characterization. In this method, the impulse response at locations along the axis is measured using the experimental setup shown in Figure 3.1. From the transfer function derived, which assumes a 'quasi point' reflector located on the acoustic axis of the transducer, the measured profile can be compared to the theoretical profile with use of the following two Equations [13]:

$$|c(f,z)|_E = |\beta(f)|\sqrt{|V_r(f,z)|}e^{\alpha(f)z} \tag{3.3}$$

where

$\mathcal{J}(f)$ = frequency dependent complex scale factor (measurement system efficiency factor)

$V_r(f,z)$ = the received frequency dependent voltage when the scatterer is at axial distance z

$\alpha(f)$ = the attenuation of the signal in water

and

$$|c(f,z)| = 2|\sin[\frac{1}{2}k(\sqrt{z^2+a^2(f)}-z]| \tag{3.4}$$

where

k= wave number

z= small scatter axial distance

$a(f)$ = active radius of the transducer

The parameter of variation between Equations 3.3 and 3.4 is the frequency dependent radius, $a(f)$, which can be varied until the least accumulated error between the theoretical and measured values of $c(f,z)$ is arrived at where the accumulated error is

$$\tilde{E}(f_j) = \frac{1}{N}\sqrt{\sum_{i=1}^{N}(V_{th}(f_j,z_i)-Vm(f_j,z_i))^2} \times 100 \qquad j=1,2.....M \tag{3.5}$$

where

N= number of positions included in the curve fitting procedure

M = the number of frequencies in the pressure spectrum

$V_{th}(f_j,z_i)$ = the theoretical pressure magnitude of the on axis profile at frequency, f_j, and distance, z_i

$Vm(f_j,z_i)$ = the scaled experimental pressure magnitude of the on axis profile at frequency, f_j, and distance, z_i

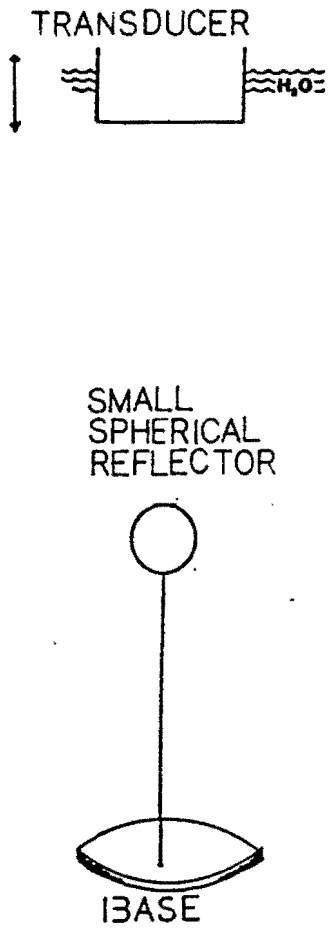

Figure 3.1: Schematic of the Set-up used for Axial Profile Measurements

In fitting the theoretical profile to the experimental profile, knowledge of the attenuation constant of the water is necessary. This value can either be entered as a known value or it can be calculated in the curve fitting procedure. Calculation of it takes place at the same time as the calculation of the frequency dependent complex scale factor, $\mathcal{B}(f)$, by a least squares fit of

$$\ln \frac{|V(f_j,z)|}{|c(f_j,z)|} = \ln \mathcal{B}(f_j) - \alpha(f_j)z \qquad j = 1,2,.....M \tag{3.6}$$

where $V(f_j,z)$ is measured, $c(f_j,z)$ is calculated from the choice of the diameter, and z is known. If the attenuation is entered as a textbook value, $\mathcal{B}(f)$ is calculated similarly by a least squares fit, however, in this case, the attenuation constant is known, so there is only one parameter to determine in the fitting procedure.

The frequency dependent radius arrived at by use of the least accumulated error is called the active radius which can be used for evaluating ultrasonic attenuation measurements in such a way that the results become less transducer dependent.

3.2.3 Experimental Apparatus

The electronic equipment used for the transducer characterization was the same as that previously used in the attenuation measurements. The schematic of the apparatus can be seen in Figure 2.7. The same equipment was used for all experiments making the measurements, with the exception of the transducers, independent of the equipment. Transducers used for the axial profile experiments include the same three, 10 MHz, .25 inch nominal diameter, model V312 unfocused, immersion probes which were used in the attenuation tests. The serial numbers and corresponding transducer numbers (which correlate to the numbers used in the attenuation tests) are shown in Table 3.1.

Table 3.1: Serial Numbers of the Transducers

Transducer Number	Serial Number
1	44689
2	58498
3	44686

3.2.4 Procedure

An approximately .2 cm spherical reflector was used (see Figure 3.1), and the impulse response at each location, from .5 cm to 11 cm at .5 cm intervals, was measured. The Fast Fourier Transform was performed on the time domain wave forms of the received voltage. The axial profiles were then extracted from the resulting frequency domain data within the range of 9 to 11 MHz with a spacing of 0.125 MHz. The external and internal attenuation values and time/division settings on the oscilloscope were kept constant throughout all measurements. By maximizing the output signal at the beginning of every experiment, the transducer was positioned so that it's acoustic axis was normal to the spherical reflector. The measurement was run twice per transducer.

3.2.5 Results and Discussion

The experimental versus theoretical results were examined in a number of different ways. First, the active diameter was found by fitting the experimental data with the theoretical data for all s values including both the nearfield and farfield data (Case 1). In doing this, the attenuation coefficient in water was both entered as a known value, and calculated in the fitting procedure. Second, the active diameter was found by fitting the theoretical data for s values greater than 1 thus including

Table 3.2: Active Diameters

Transducer Number	Active Diameter, a_1
1	.234
2	.237
3	.244

only the farfield data (Case 2). In this case, the attenuation was calculated in the fitting procedure. Finally, the active diameters were found by fitting the theoretical data for s values greater than 1, however, in this case, an assumed value of the attenuation was used in the fitting procedure (Case 3). From these three cases, three active diameters for three different ways of fitting the data were found which are denoted by a_i, where $i = 1, 2, 3$.

3.2.5.1 Case 1 The results were quite similar whether a text book value of .0265 $\frac{Np}{cm}$ was used for the attenuation or whether the attenuation was calculated during the fitting procedure. The resulting active diameters can be seen in Table 3.2 for the three transducers. The graphs of the axial profiles can be seen in Figures 3.2 through 3.4, and the ERMS, or accumulated error in percentage, can be seen for each transducer in Figures 3.5 through 3.7. As can be seen in these graphs, the fit between the experimental and theoretical data matches better for transducers 1 and 2 than for transducer 3. This leads to the assumption that transducer 3 does not follow the planar piston model as well as transducers 1 and 2, and in looking at the attenuation measurement results for aluminum, it can be noted that transducers 1 and 2 gave similar results while the results for transducer 3 were not as close.

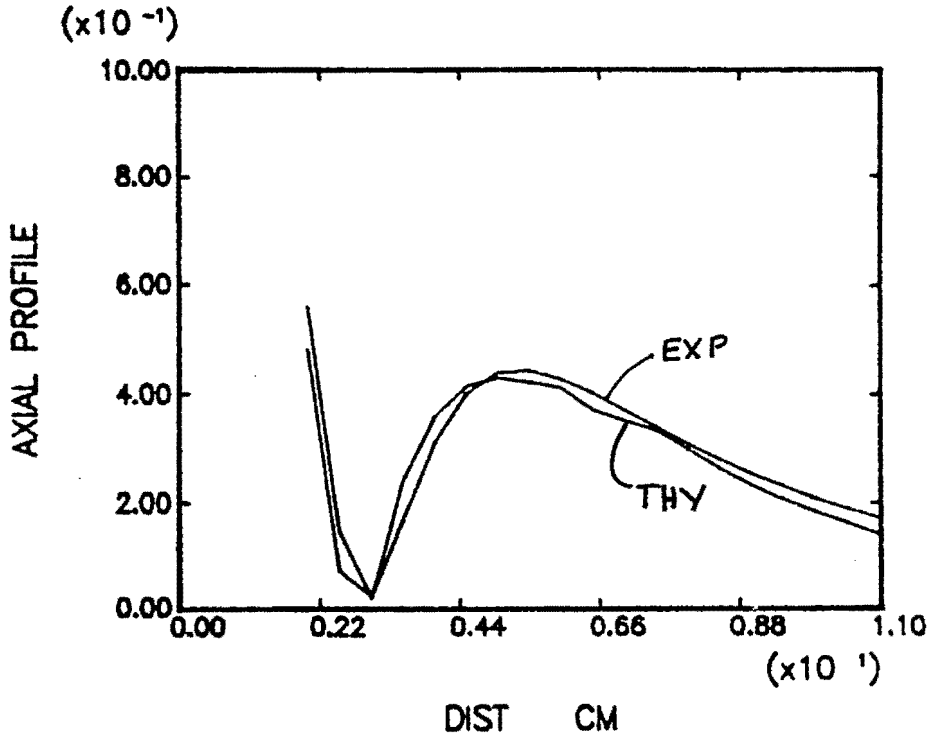

Figure 3.2: Axial Profile for Transducer 1 (Experimental and Theoretical)

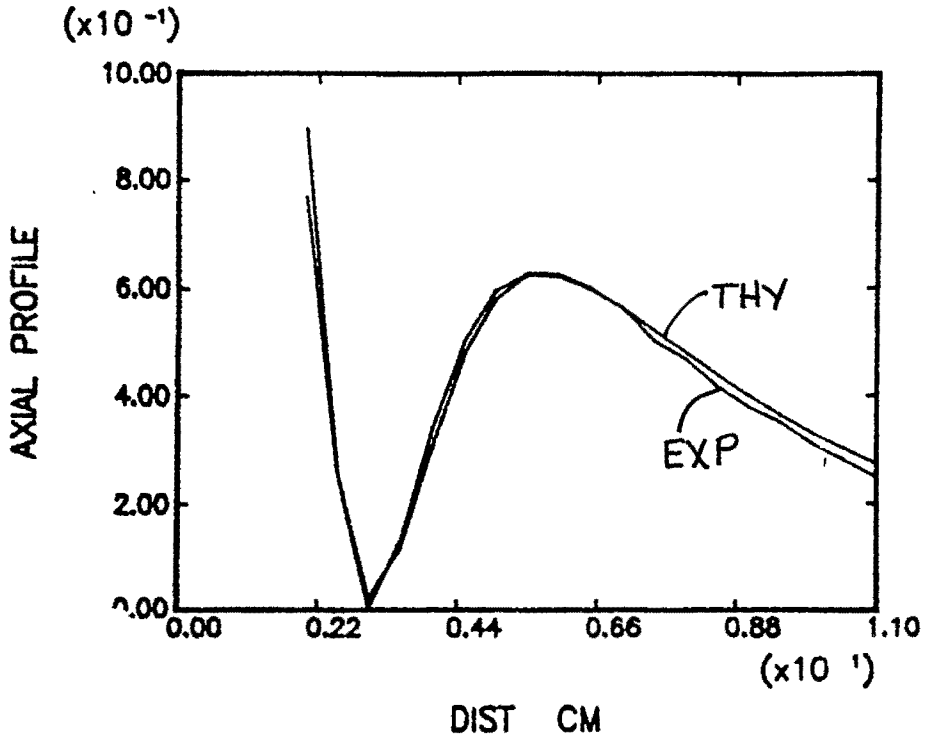

Figure 3.3: Axial Profile for Transducer 2 (Experimental and Theoretical)

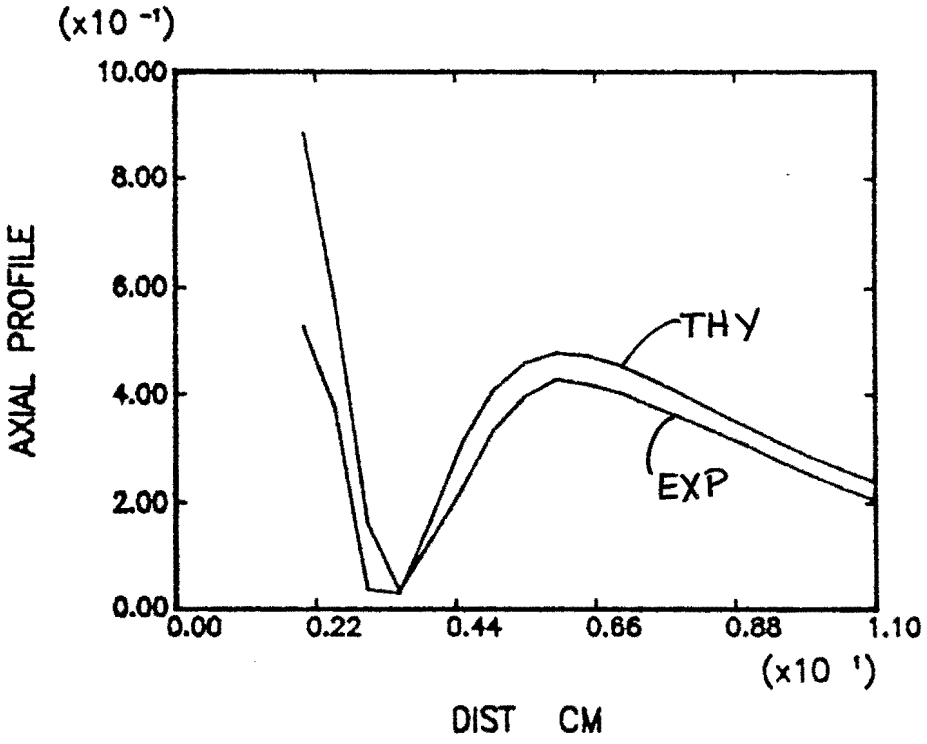

Figure 3.4: Axial Profile for Transducer 3 (Experimental and Theoretical)

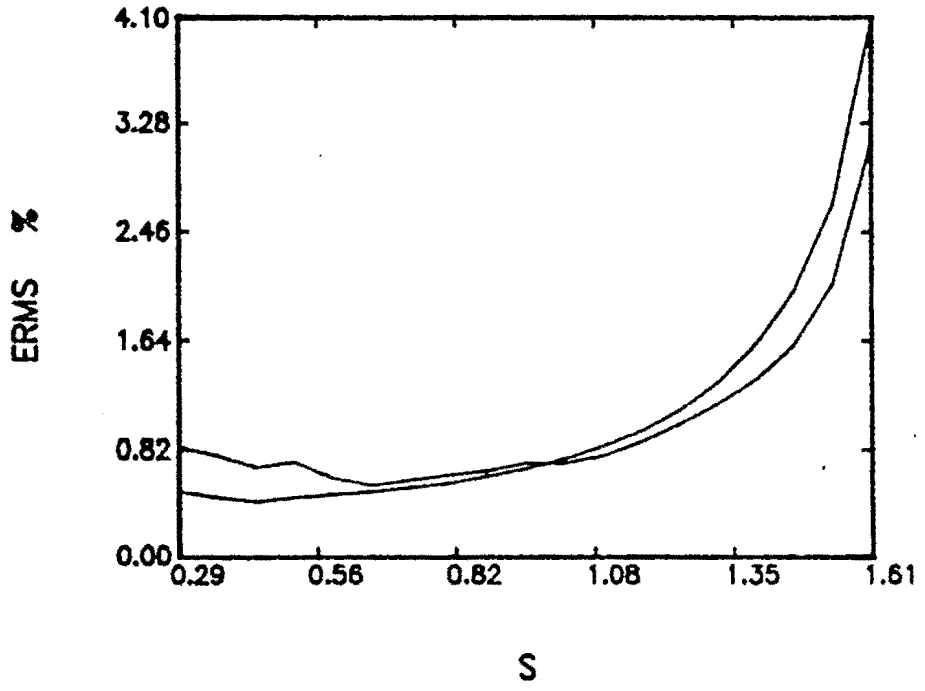

Figure 3.5: Accumulated Error Between Theoretical and Experimental Axial Profiles for Transducer 1

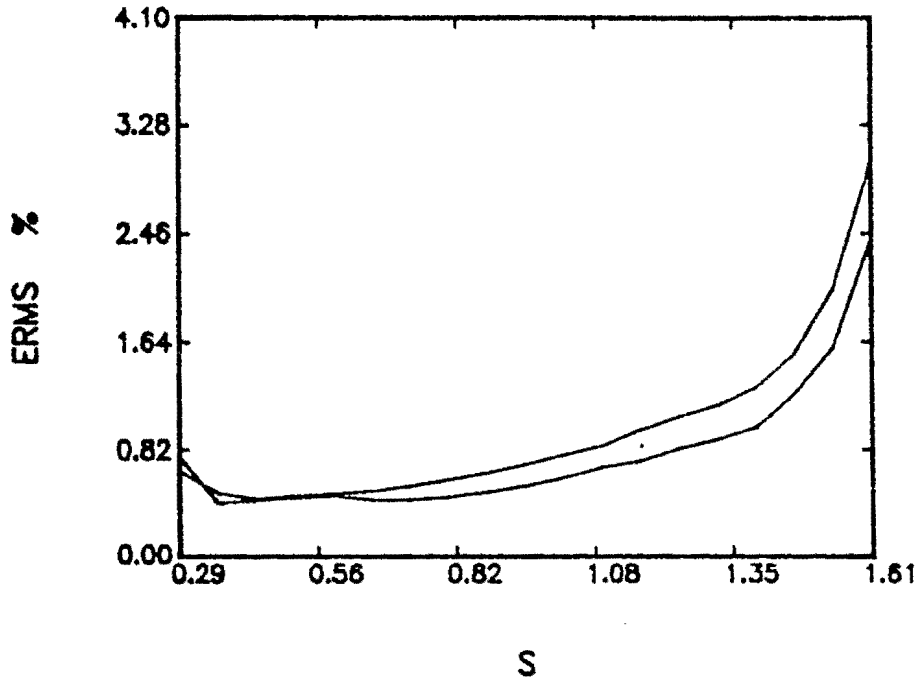

Figure 3.6: Accumulated Error Between Theoretical and Experimental Axial Profiles for Transducer 2

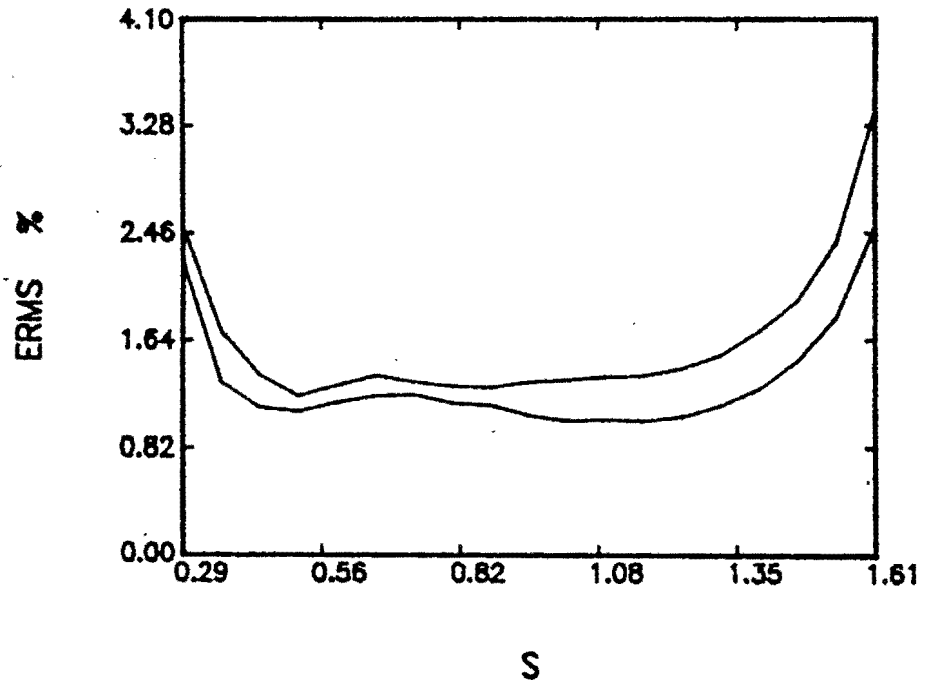

Figure 3.7: Accumulated Error Between Theoretical and Experimental Axial Profiles for Transducer 3

3.2.5.2 Case 2 Looking at the accumulated error for Case 1, it can be seen that the theoretical and experimental curves fit better in the nearfield. This is due to an evaluation of the data which has much more emphasis on the nearfield data than on the farfield data. Therefore, this section is devoted to seeing how the farfield emphasis effects the results.

The fitting procedure in Case 2 was designed such that the error over all data decreases as the s value increases, or in other words, the fit of theoretical to experimental data improves in the farfield. In this case, the fitting procedure calculated the water attenuation rather than assuming a known value. The results for fitting the data only over the farfield can be seen in Table 3.3. As can be seen from these results, fitting the data only over the farfield locations creates some difficulties especially for transducers 1 and 3. Both of these transducers obtain active diameters greater than the nominal diameters - a result which suggests error. Also, the calculated water attenuation, when this active diameter was used to evaluate the farfield and nearfield data, acquires values over 3.5 times the given textbook value, and the accumulated errors over the nearfields and farfields rise to extremely high values as compared to the previous case. Figures 3.8 through 3.10 show the the theoretical and experimental axial profiles for all three transducers. As can be seen by the graphs, the fits are not as good as in Case 1. This can also be seen by looking at the results of the accumulated errors in Figures 3.11 through 3.13.

3.2.5.3 Case 3 It can be observed that transducer 2 gives consistent results whether the data is fit over the nearfield and farfield (Case 1) or whether the data

Table 3.3: Results for Fitting Axial Data Over s>1 with a Calculated Attenuation Value being used for the Fit

Transducer Number	Active Diameter a_2	Calculated Attenuation (Np/cm)		Accumulated Error (%)	
		s>1	All s	s>1	All s
1	.269	.094414	.116854	.337202	36.279
1	.258	.079586	.101699	.325463	24.226
2	.238	.038407	.035561	.388188	1.883
2	.229	.030304	.029444	.437427	6.278
3	.256	.043579	.101270	.212050	17.665
3	.254	.042978	.128600	.190073	31.163

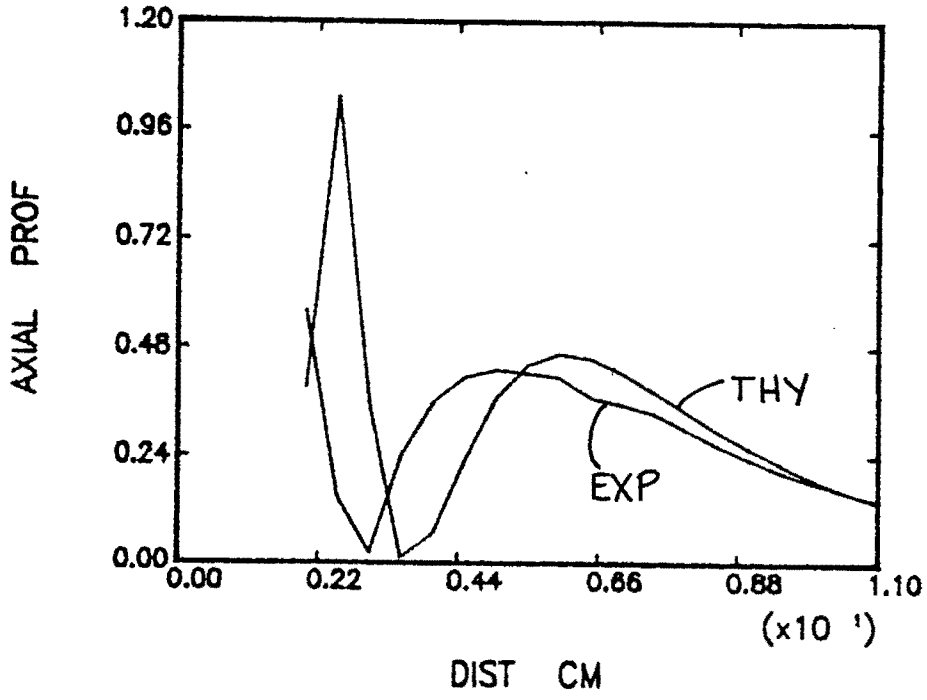

Figure 3.8: Axial Profile for Transducer 1 (Data Fit with Calculated Value of Water Attenuation for s > 1)

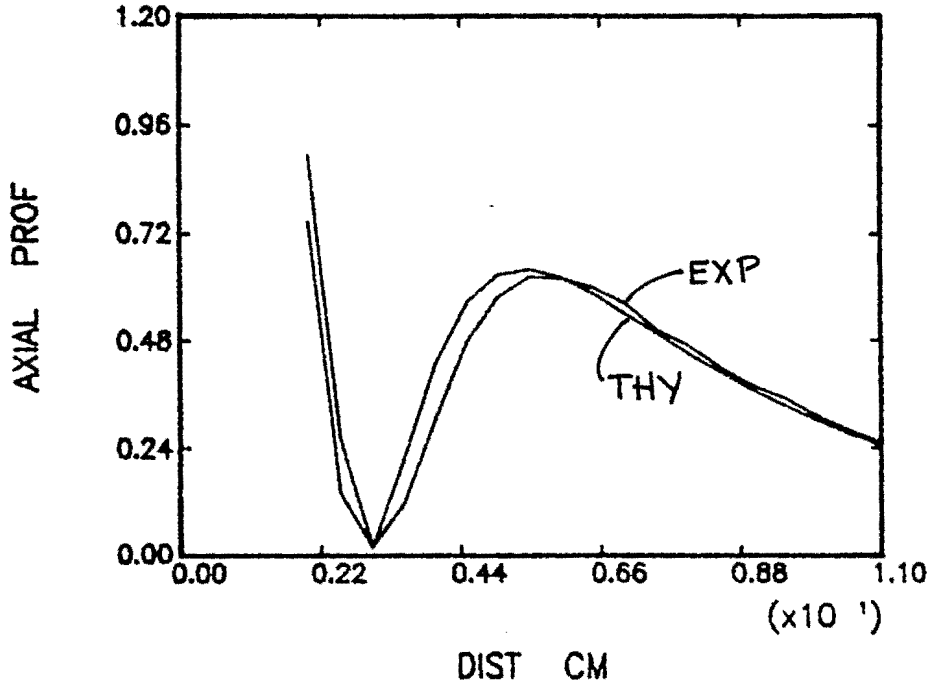

Figure 3.9: Axial Profile for Transducer 2 (Data Fit with Calculated Value of Water Attenuation for s > 1)

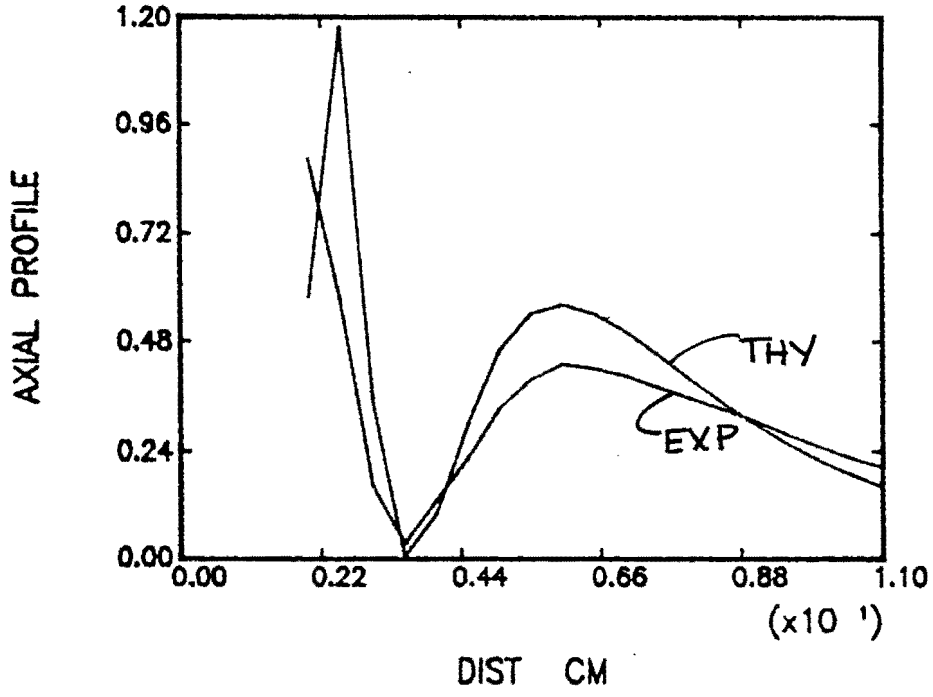

Figure 3.10: Axial Profile for Transducer 3 (Data Fit with Calculated Value of Water Attenuation for $s > 1$)

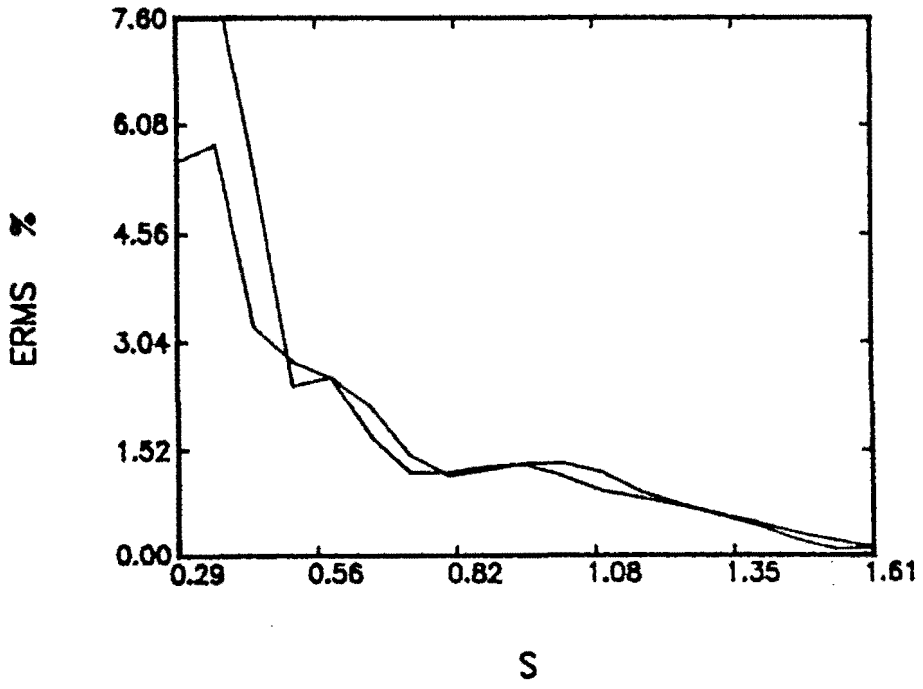

Figure 3.11: Accumulated Error Between Experimental and Theoretical Data Obtained with Transducer 1 (Data Fit with Calculated Value of Water Attenuation for $s > 1$)

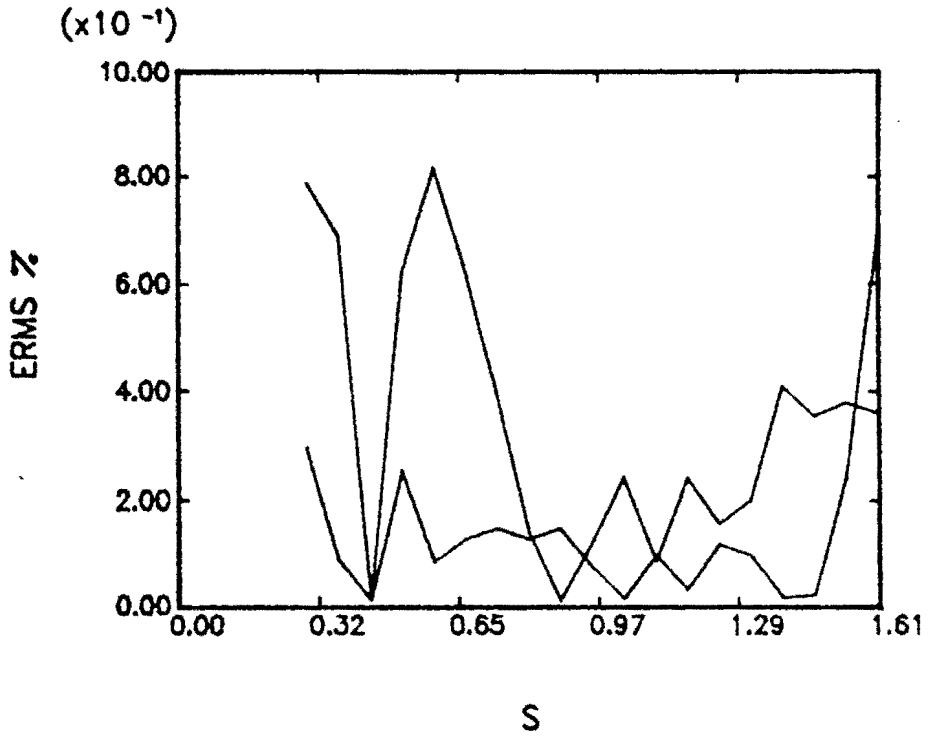

Figure 3.12: Accumulated Error Between Experimental and Theoretical Data Obtained with Transducer 2 (Data Fit with Calculated Value of Water Attenuation for s > 1)

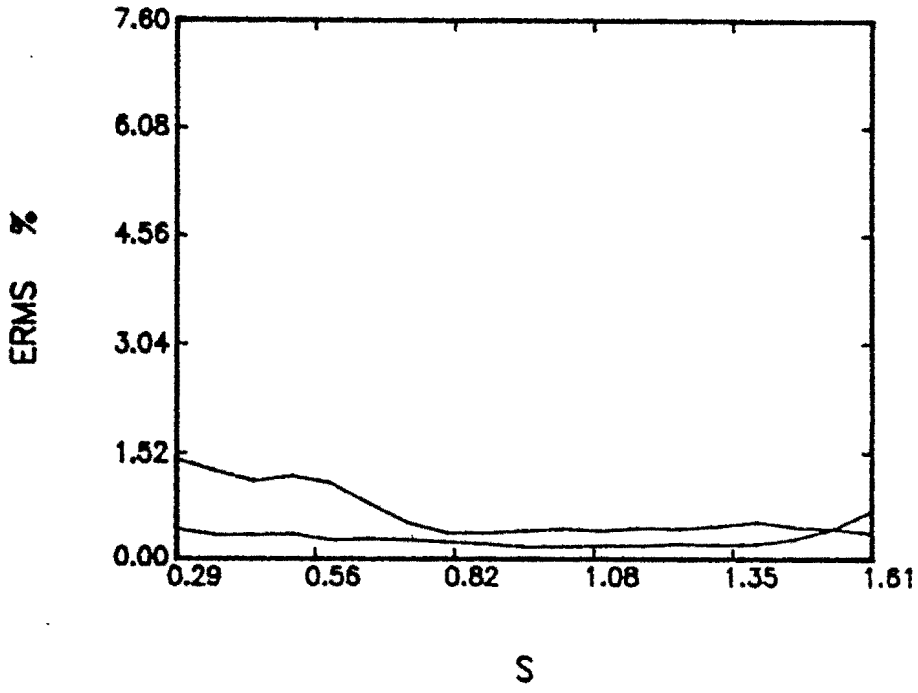

Figure 3.13: Accumulated Error Between Experimental and Theoretical Data Obtained with Transducer 3 (Data Fit with Calculated Value of Water Attenuation for $s > 1$)

Table 3.4: Results for Fitting Data Over s>1 with Attenuation equal to .038407 Np/cm

Transducer Number	Active Diameter, a_3	Accumulated Error (%)	
		s>1	All s
1	.227	.85539	4.3309
1	.222	.63015	4.1129
2	.238	.38818	1.2854
2	.237	.48916	2.2170
3	.252	.22767	11.7863
3	.251	.19815	11.9805

are just fit in the farfield (Case 2). In addition, the calculated water attenuation for this transducer stays very constant whether the data is run over all s values or only over s>1. Therefore, in Case 3, the attenuation value from the Case 2 results (.038407 Np/cm) was used in the fitting procedure and the data were fitted for s>1. These results can be seen in Table 3.4. Transducers 1 and 2 give reasonable results, but transducer 3 has slightly higher accumulated error, than transducers 1 and 2, and the calculated active diameters are larger than the nominal diameter by .8%. Table 3.5 shows the difference between the active diameters calculated in this case for s>1 and for all the data. The new active diameters calculated by this method are slightly smaller for transducers 1 and 2 and slightly larger for transducer 3.

The graphs of the axial profiles obtained for this case can be seen in Figures 3.14 through 3.16, and the accumulated error can be seen in Figures 3.17 through 3.19. As expected, in this case the accumulated error decreases as s increases showing the emphasis, in this fitting procedure, being placed more heavily on the farfield data in comparison to the nearfield data.

Table 3.5: Differences in Calculated Active Diameters for Case 1 and Case 3

Transducer Number	$\frac{a_1-a_3}{a_1} \times 100$
1	3.81%
1	2.20%
2	.85%
2	.85%
3	-3.28%
3	-4.15%

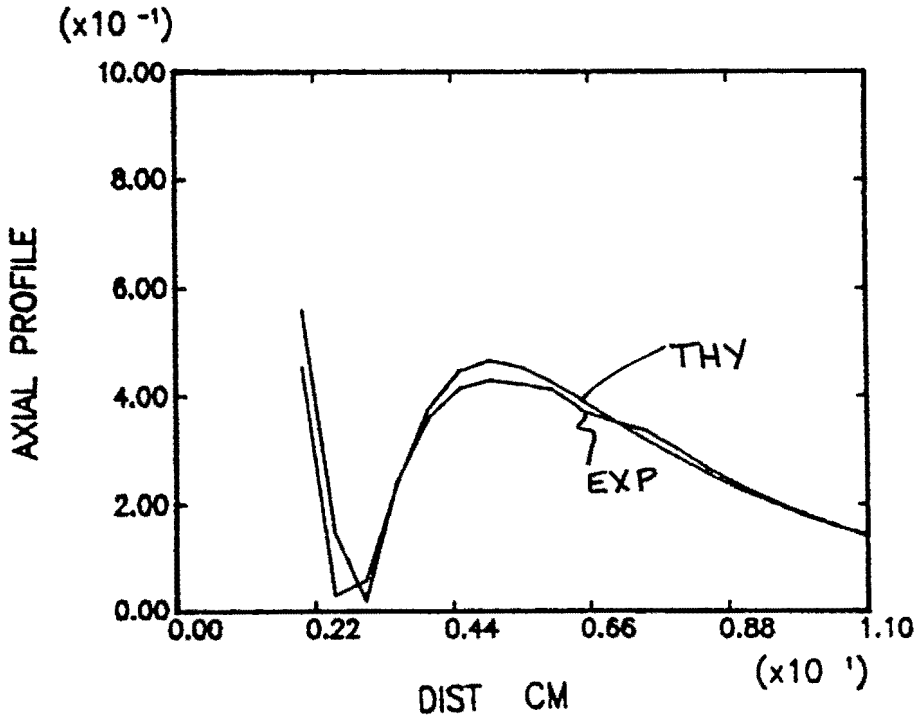

Figure 3.14: Axial Profile of Transducer 1 with Experimental and Theoretical Fit for s > 1 with Water Attenuation = .038407 Np/cm

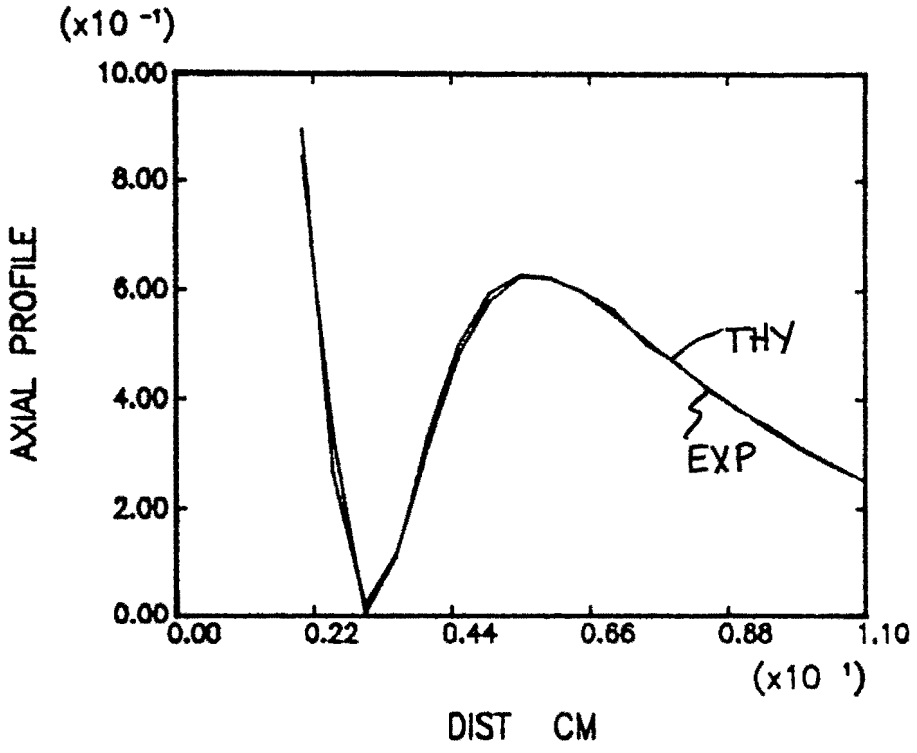

Figure 3.15: Axial Profile of Transducer 2 with Experimental and Theoretical Fit for s > 1 with Water Attenuation = .038407 Np/cm

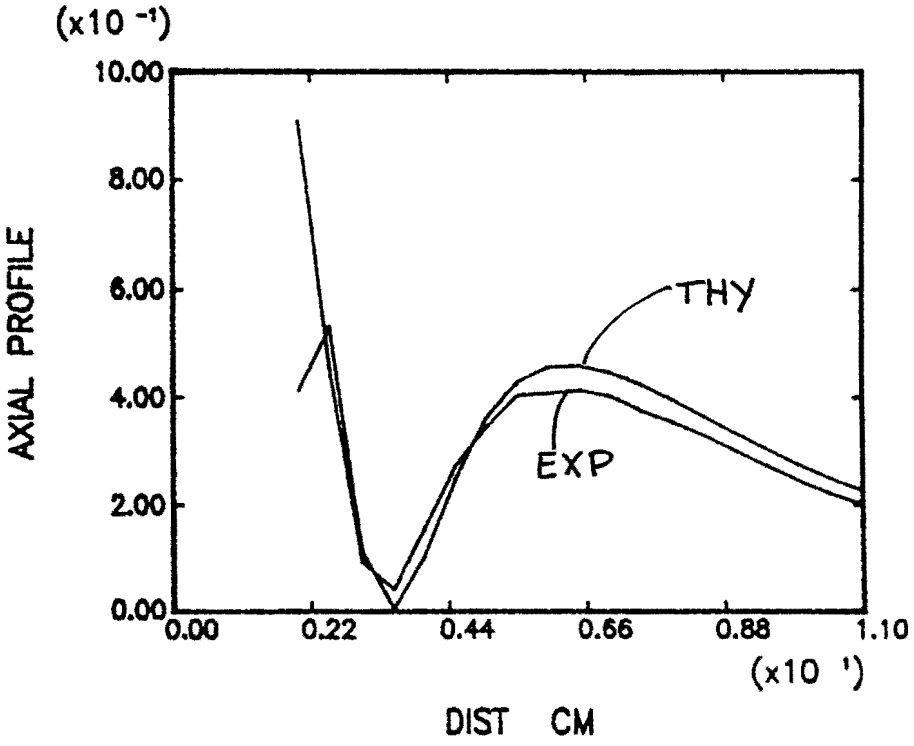

Figure 3.16: Axial Profile of Transducer 3 with Experimental and Theoretical Fit for s > 1 with Water Attenuation = .038407 Np/cm

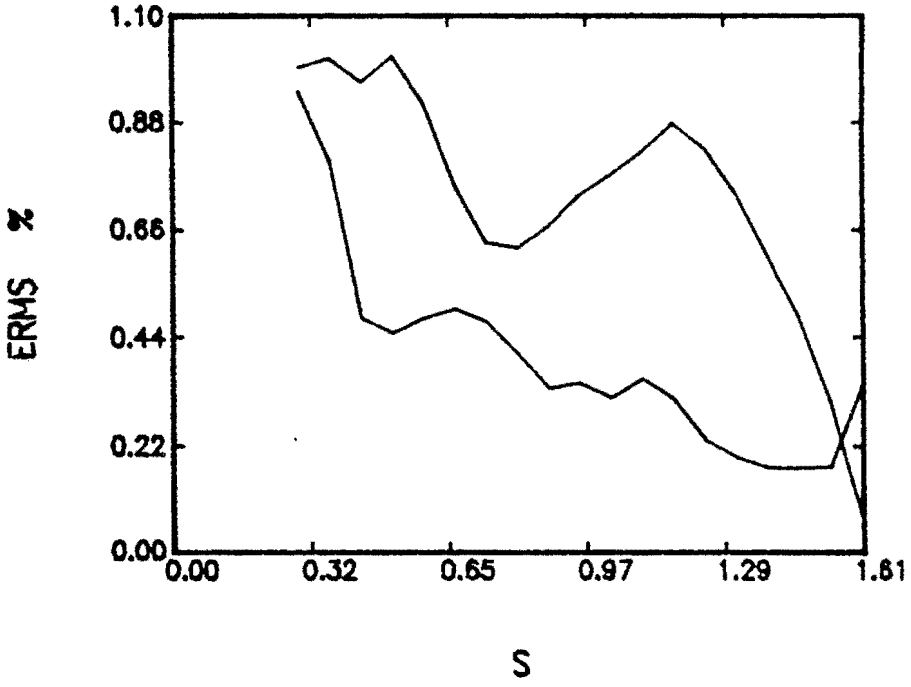

Figure 3.17: Accumulated Error in the Axial Profile of Transducer 1 when Fit for $s > 1$ with Water Attenuation = .038407 Np/cm

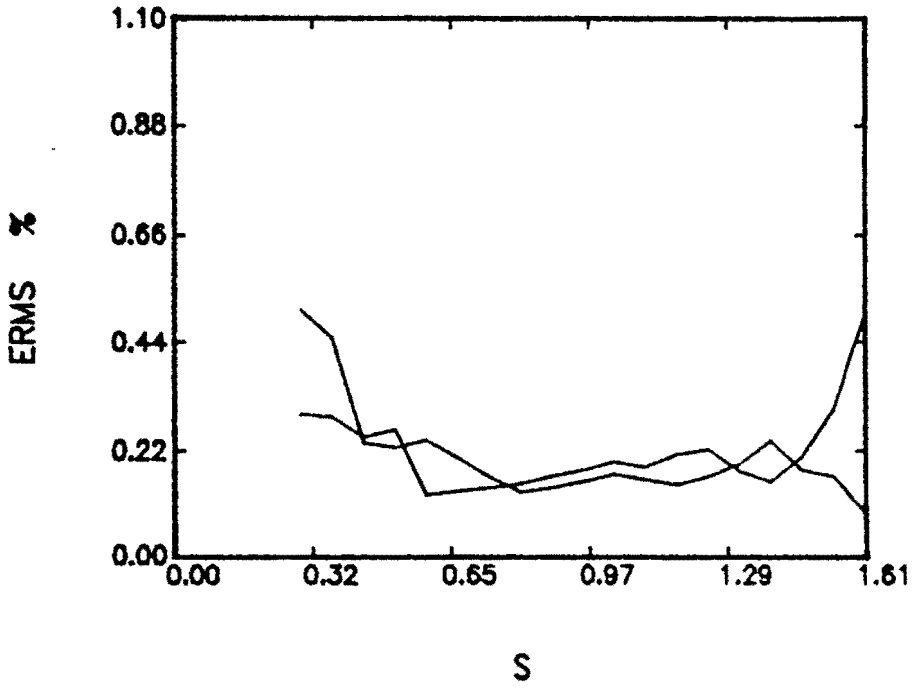

Figure 3.18: Accumulated Error in the Axial Profile of Transducer 2 when Fit for $s > 1$ with Water Attenuation = .038407 Np/cm

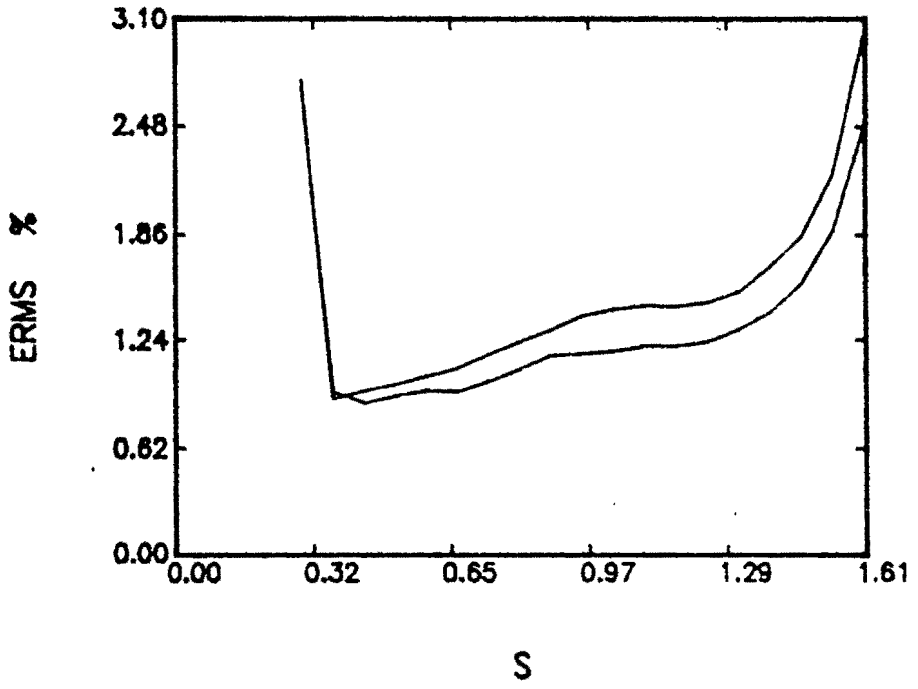

Figure 3.19: Accumulated Error in the Axial Profile of Transducer 3 when Fit for $s > 1$ with Water Attenuation = .038407 Np/cm

3.2.6 Conclusions

The axial profile can be used to characterize transducers as planar piston sources with the calculation of an active diameter. However, care must be taken when calculating these active diameters to 1) evaluate the effect of incorporating both the nearfield data and the farfield data in calculating the accumulated error necessary in finding the active diameter, and 2) to properly account for the attenuation of the ultrasonic wave in water during the calculations of the active diameters.

3.3 Radial Profiles

3.3.1 Theory

If the pressure amplitude is measured at a fixed distance, z, a c-scan of the transducer can be taken, enabling the radial profile of the transducer to be examined. The symmetry of the transducer can be evaluated by looking at the consistency of the pressure at a given radial distance. Also, the average radial pressure can be compared to the theoretical radial pressure which can be calculated by the Rayleigh integral performed over the surface of the transducer.

3.3.2 Radial Profile Measurements

In this measurement, the same method previously discussed for the axial profiles was used, and the impulse response at locations at a fixed distance, z, was measured using the setup shown in Figure 3.20.

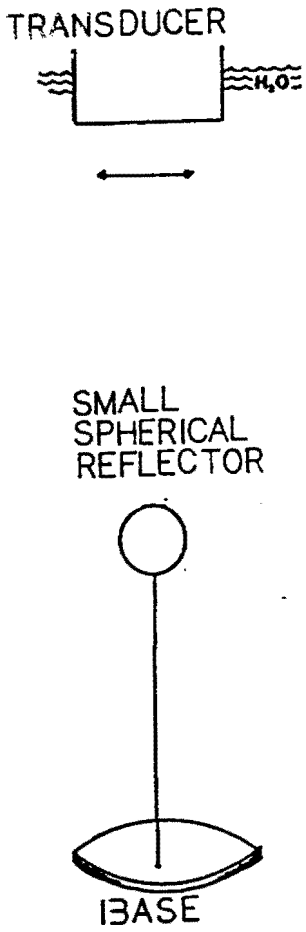

Figure 3.20: Set-up used for the Radial Profile Measurements

3.3.3 Experimental Apparatus

The experimental apparatus used in the radial profile measurements is the same as the equipment used in the axial profile measurements with the addition of an automated scanner. This scanner did cause some difficulty when attempting to find the maximum output signal (the center of the probe radiation), also the signal amplitude was noticeably decreased when the scanner was turned on for the measurement.

3.3.4 Procedure

An approximately .2 cm spherical reflector was used, and the data was taken for a frequency of 10 MHz. The measurements were taken at distances of 6 cm (s= .88) and 8 cm (s= 1.17). The scan was run in an .21 inch by .21 inch square grid of .015 inch intervals for the test run at 6 cm and a .27 by .27 inch square grid of .015 inch intervals for the test run at 8 cm. At the beginning of each scan, the transducer was normalized and centered above the spherical reflector by maximizing the output signal.

3.3.5 Results and Discussion

The results of the c-scans were examined for two features, 1) the symmetry of the profile, and 2) the agreement with the theoretical radial profile when s $<$ 1 and when s$>$ 1.

3.3.5.1 Symmetry The radial symmetry was calculated by

$$\mathrm{Dev}(r) = \frac{P(r_i, z_o)_{MAX} - P(r_i, z_o)_{MIN}}{P(r_i, z_o)_{AVG}} \tag{3.7}$$

where

$P(r_i, z_o)_{MAX}$ = maximum pressure magnitude at radius, r

$P(r_i, z_o)_{MIN}$ = minimum pressure magnitude at radius, r

$P(r_i, z_o)_{AVG}$ = average pressure magnitude at radius, r, which was calculated from

$$P(r_i, z_o) = \frac{1}{N} \sum_{j=1}^{N} P_j(r_i, z_o) \tag{3.8}$$

Figure 3.21 shows the points which would be used to calculate $P(r_i, z_o)_{MAX}$, $P(r_i, z_o)_{MIN}$, and $P(r_i, z_o)_{AVG}$ at $r = r_2$. The radial symmetry was calculated for $r = 1, 2, 3...N$, where N is the largest radial distance for which the pressure magnitude was measured. Figures 3.22 through 3.24 demonstrate the radial symmetry of the profiles which were measured in the nearfield. As can be seen by these figures, none of the three transducers have very good symmetry. In fact, the deviations were up to 1000 % at a radial distance equal to .80 of the radius of the probe. However, the high deviations at this distance could be due to noise contributions at the edge of the radiated field. The scans were much more symmetric near the center of the transducer with deviations less than 100 % for a radial distance equal to .20 of the radius of the probe. Figures 3.25 through 3.30 show the measured c-scans, which are also lacking symmetry, for the three 10 MHz transducers.

3.3.5.2 Nearfield Radial Profiles For z= 6 cm (s = .88), the radial profiles were compared with the theoretical profiles. The theoretical profiles were normalized to the radial profiles by minimizing the accumulated error between the theoretical and experimental profiles. When this was done, for all transducers, it was found that near the center of the transducer, there was more consistency with

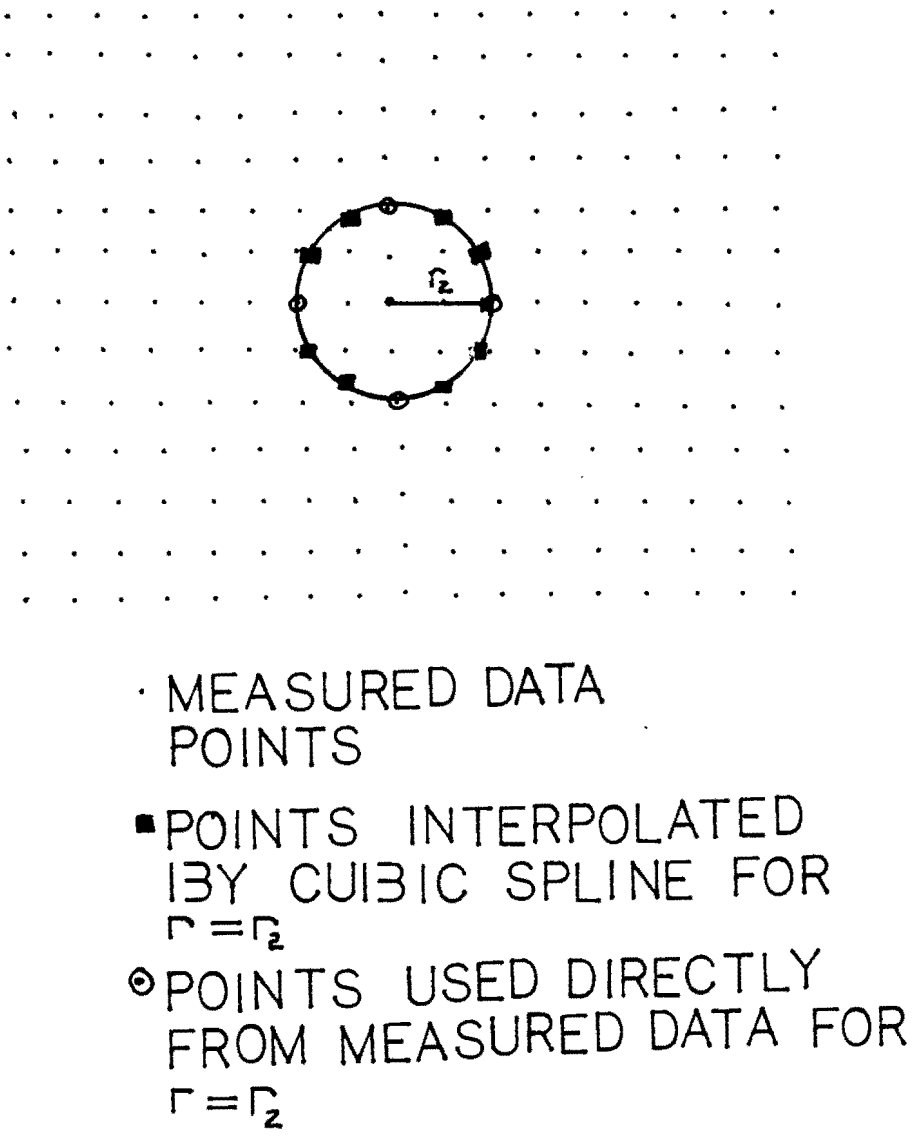

Figure 3.21: Points used to Calculate the Radial Symmetry for $r = r_2$

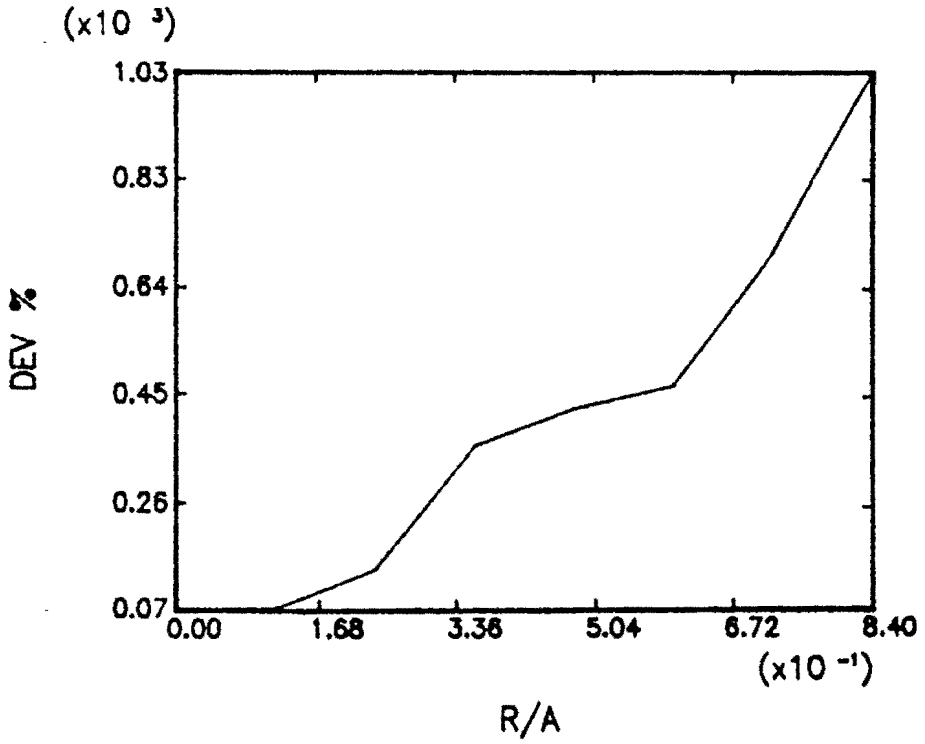

Figure 3.22: Radial Symmetry of the Transverse Pressure Profile Measured for Transducer 1 at 6 cm or s = .88

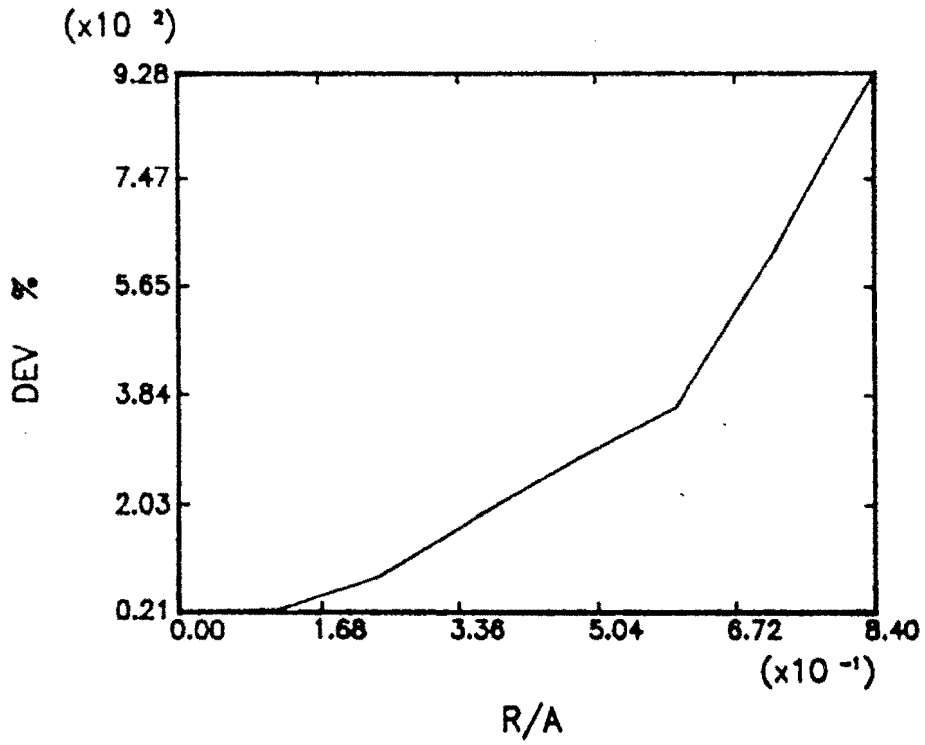

Figure 3.23: Radial Symmetry of the Transverse Pressure Profile Measured for Transducer 2 at 6 cm or s = .88

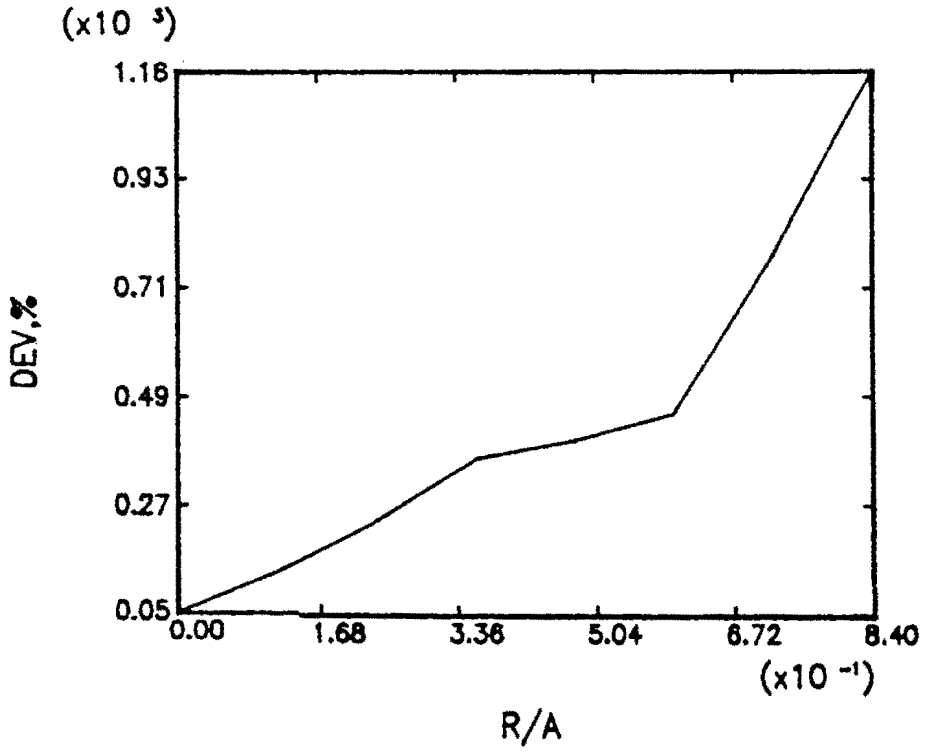

Figure 3.24: Radial Symmetry of the Transverse Pressure Profile Measured for Transducer 3 at 6 cm or s = .88

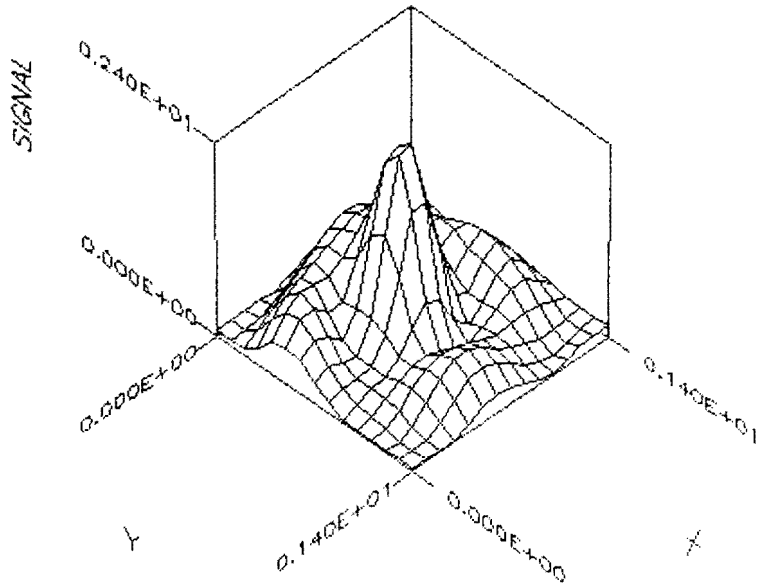

Figure 3.25: Radial Pressure Profile of Transducer 1 at 6 cm (s = .88)

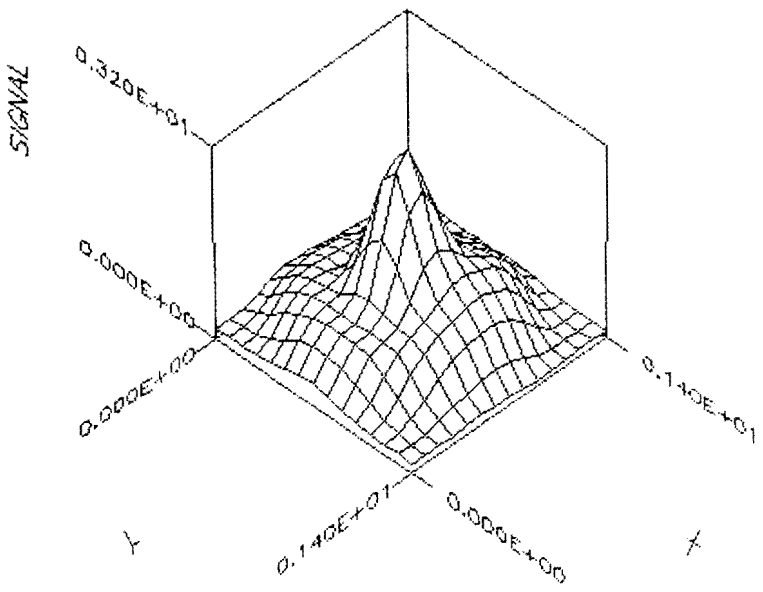

Figure 3.26: Radial Pressure Profile of Transducer 2 at 6 cm (s = .88)

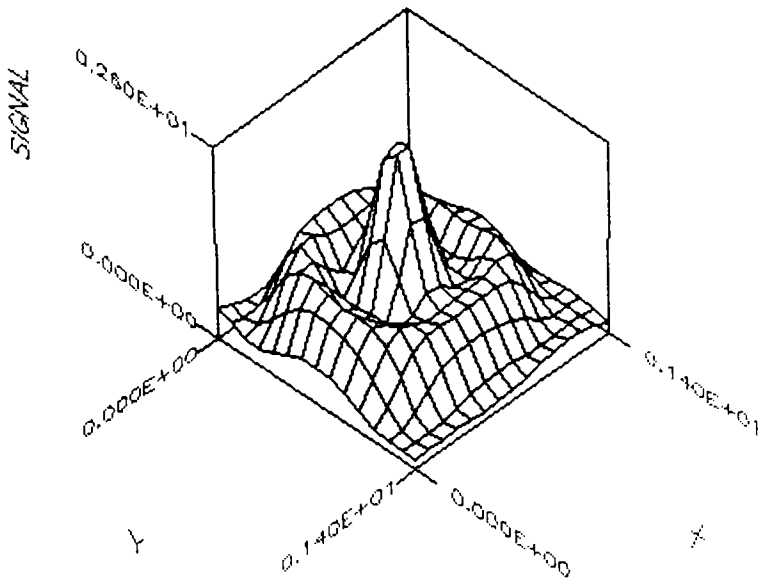

Figure 3.27: Radial Pressure Profile of Transducer 3 at 6 cm (s = .88)

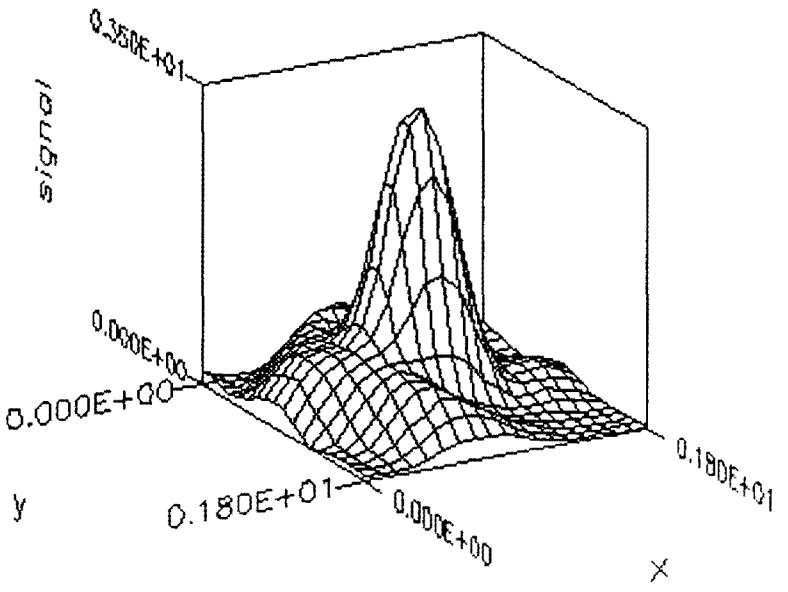

Figure 3.28: Radial Pressure Profile of Transducer 1 at 8 cm (s = 1.17)

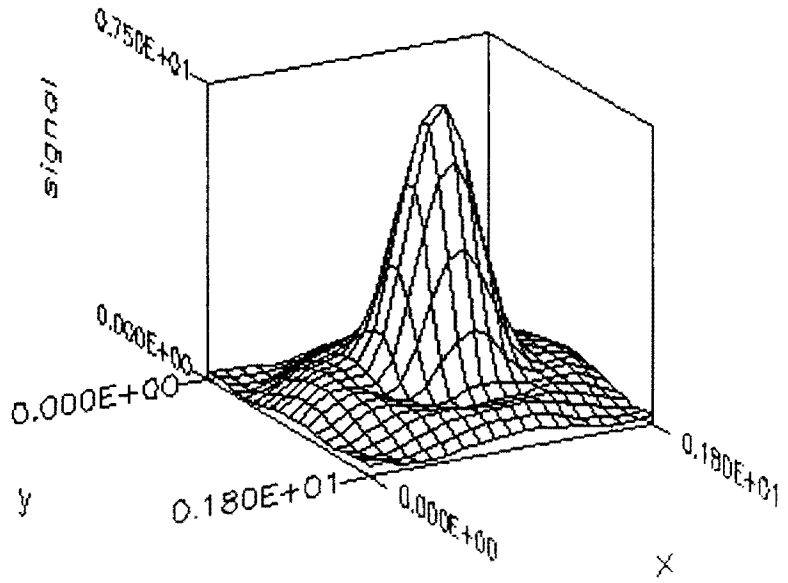

Figure 3.29: Radial Pressure Profile of Transducer 2 at 8 cm (s = 1.17)

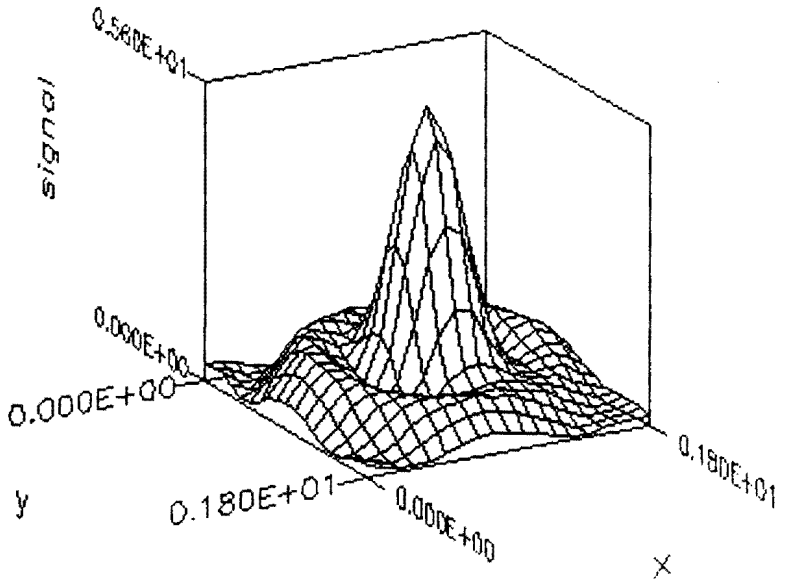

Figure 3.30: Radial Pressure Profile of Transducer 3 at 8 cm (s = 1.17)

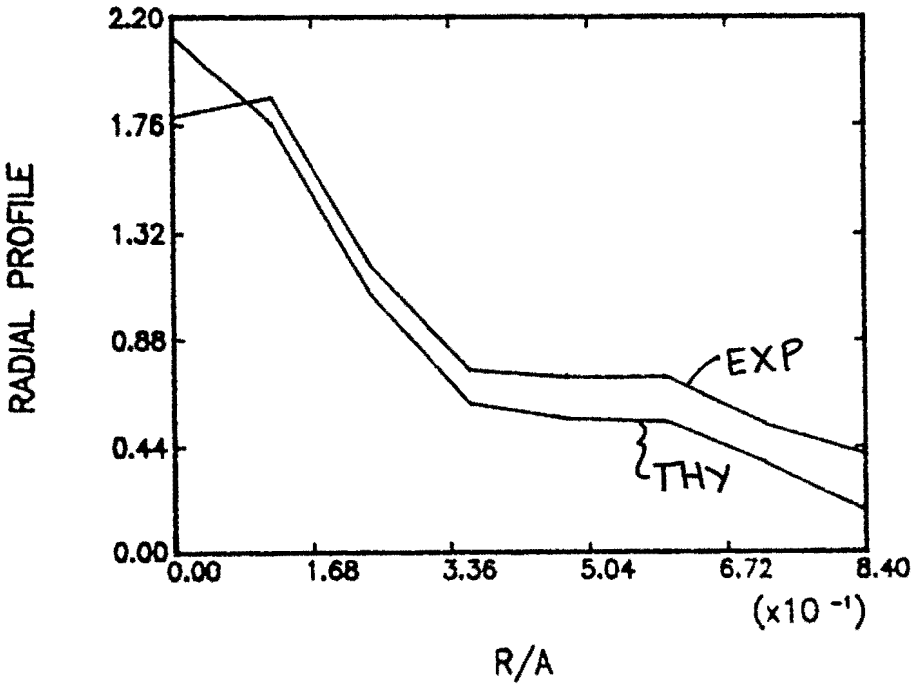

Figure 3.31: Radial Profile of Transducer 1 for s = .88; Theoretical and Experimental Data using Nominal Diameter

the theoretical profiles. Again, as in the axial profile case, transducer 3 had the greatest deviations from the theoretical profiles. These results are shown in Figures 3.31 through 3.33. Use of the active diameter in evaluation of the theoretical profile did not change results significantly. Figures 3.34 through 3.36 show this result.

3.3.5.3 Farfield Radial Profiles For z= 8 cm (s= 1.17), the theoretical profiles were again normalized to the experimental profiles by minimizing the accumulated error between the two. Again, in this case, for all transducers, there was more consistency with theory near the center of the transducer, and transducer 3

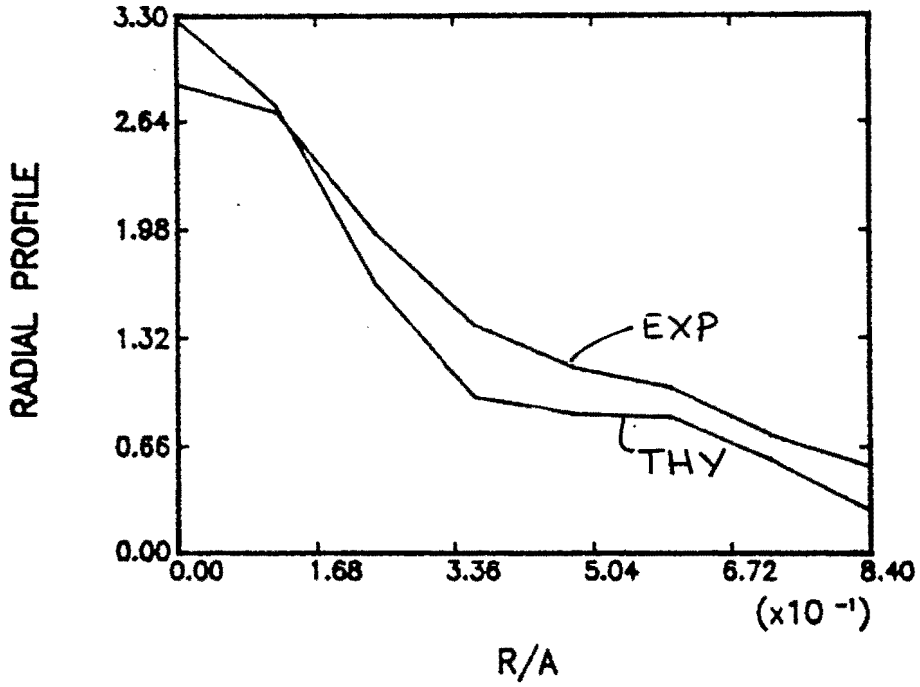

Figure 3.32: Radial Profile of Transducer 2 for s = .88; Theoretical and Experimental Data using Nominal Diameter

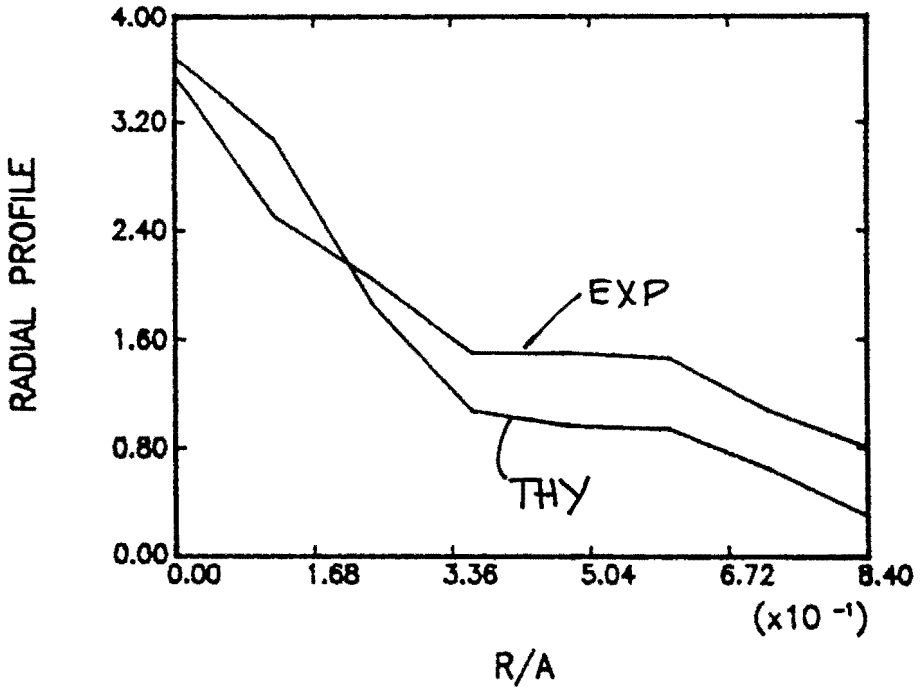

Figure 3.33: Radial Profile of Transducer 3 for s = .88; Theoretical and Experimental Data using Nominal Diameter

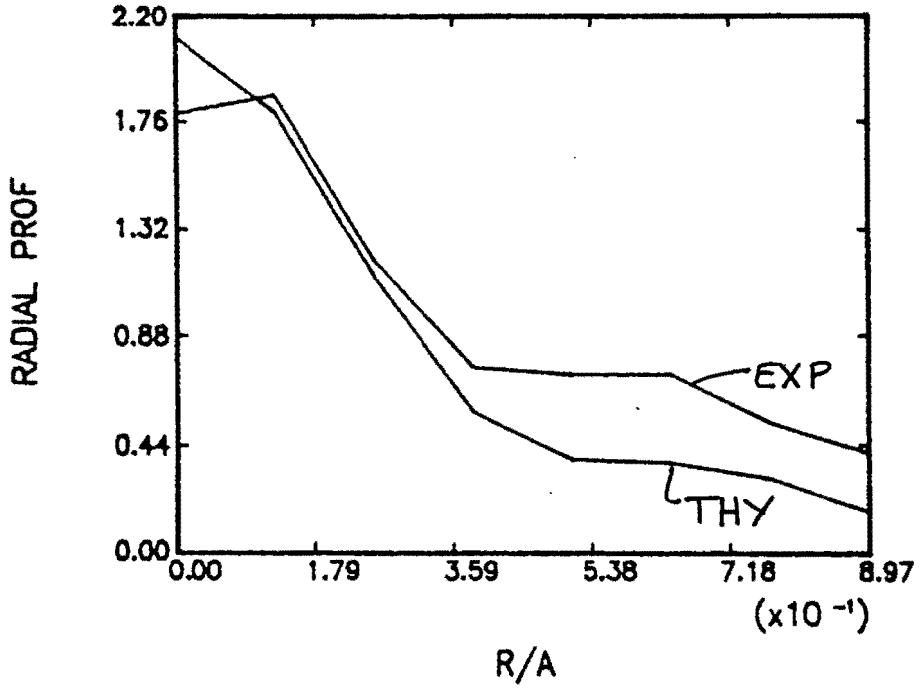

Figure 3.34: Radial Profile of Transducer 1 for s = .88; Theoretical and Experimental Data using Active Diameter

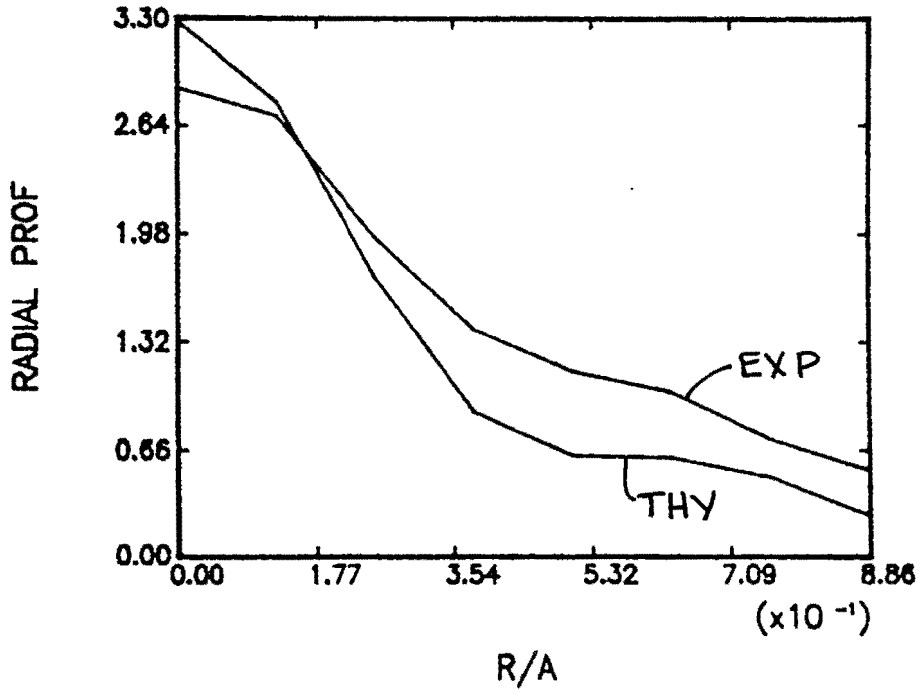

Figure 3.35: Radial Profile of Transducer 2 for s = .88; Theoretical and Experimental Data using Active Diameter

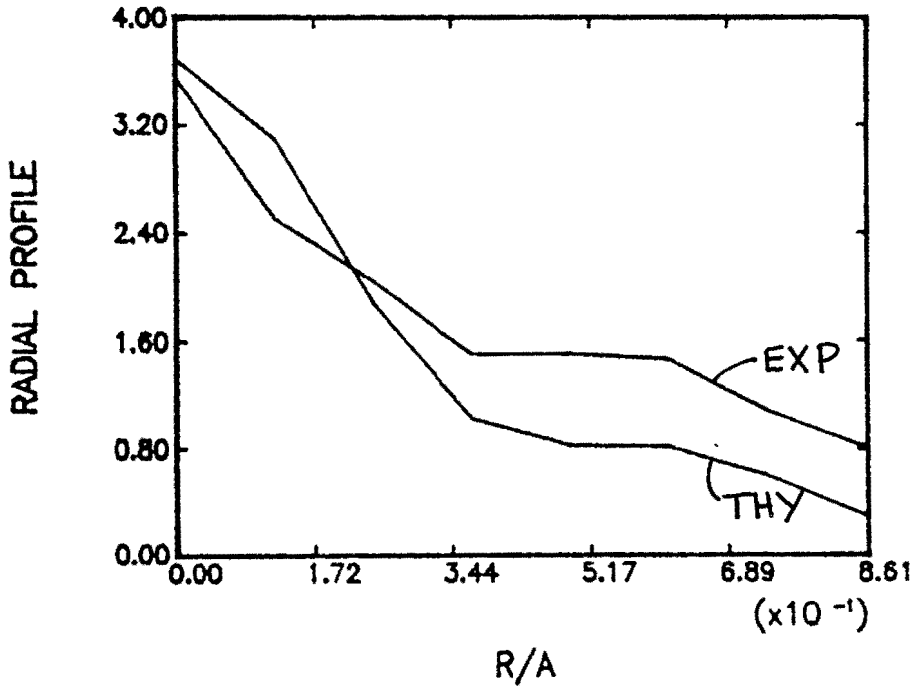

Figure 3.36: Radial Profile of Transducer 3 for s = .88; Theoretical and Experimental Data using Active Diameter

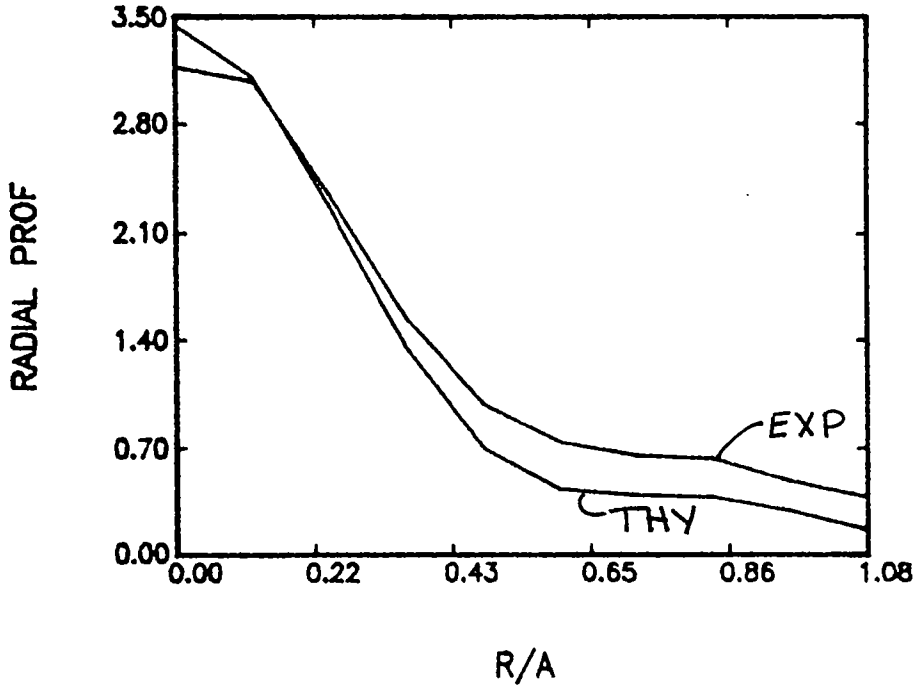

Figure 3.37: Radial Profile of Transducer 1 for s = 1.17; Theoretical and Experimental Data using Nominal Diameter

had the greatest deviations from theory. These results are graphed in Figures 3.37 through 3.39. Use of the active diameter had little significance. The results for active diameters can be seen in Figures 3.40 through 3.42.

3.3.6 Conclusions

The radial profile was used to analyze and compare the transducers for symmetry and agreement with planar piston theory. It was found that a) in general, the transducer profiles are not highly symmetric although symmetry is higher near the center of the transducer, b) the averaged radial profiles were very consistent

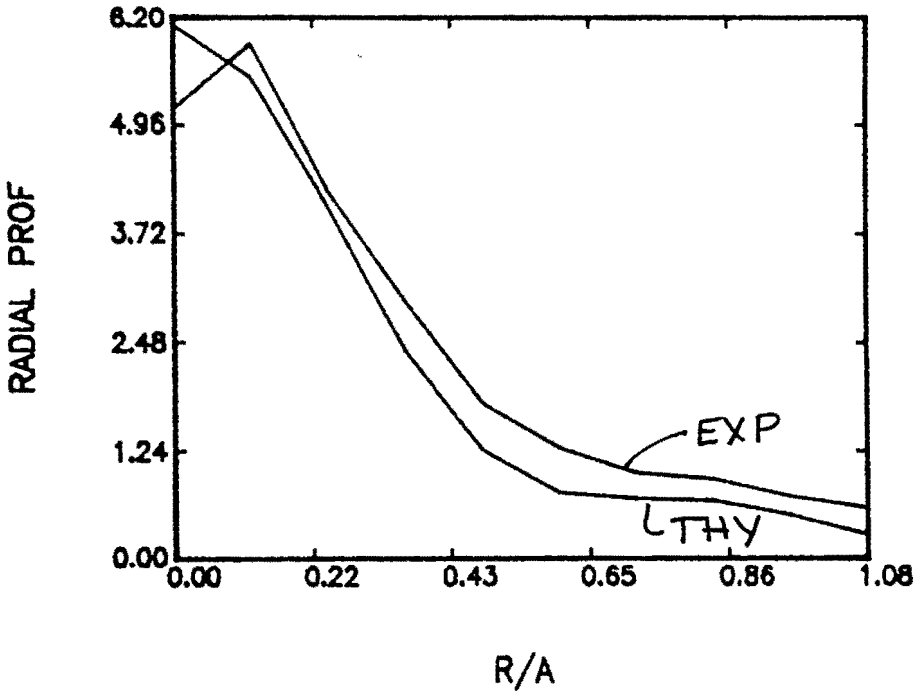

Figure 3.38: Radial Profile of Transducer 2 for s = 1.17; Theoretical and Experimental Data using Nominal Diameter

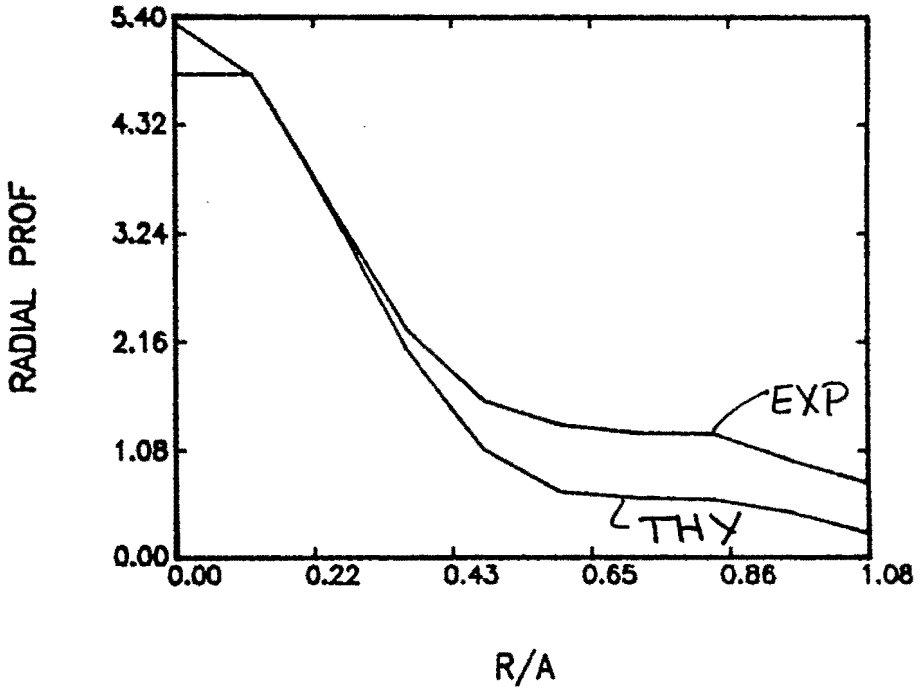

Figure 3.39: Radial Profile of Transducer 3 for s = 1.17; Theoretical and Experimental Data using Nominal Diameter

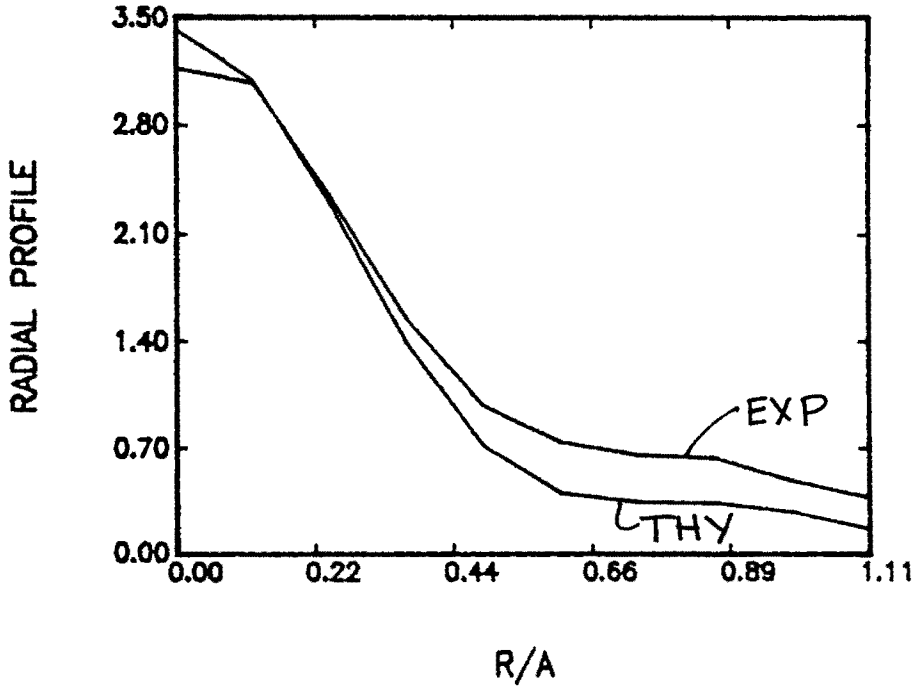

Figure 3.40: Radial Profile of Transducer 1 for s = 1.17; Theoretical and Experimental Data using Active Diameter

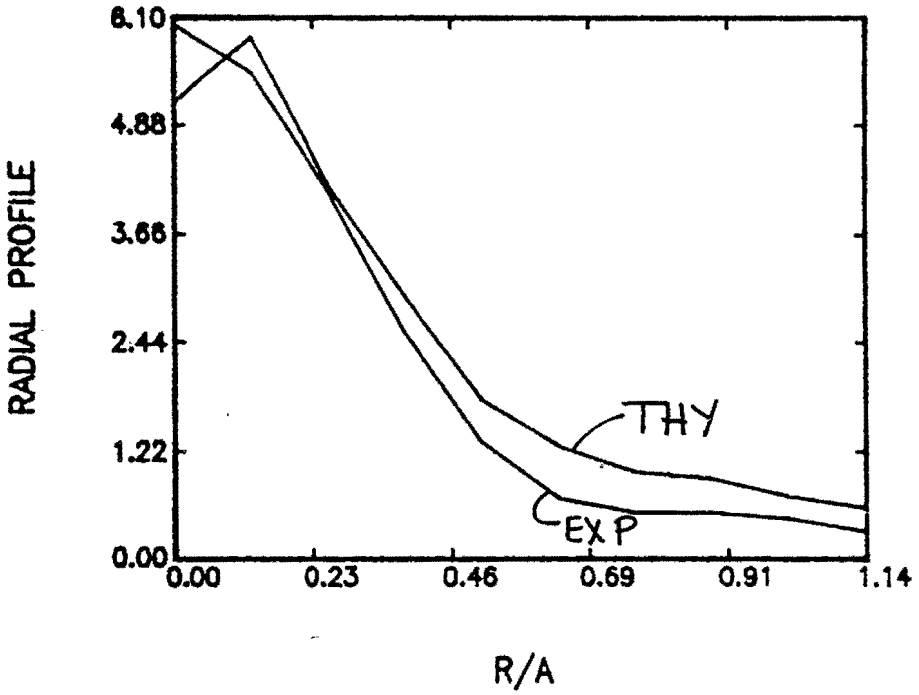

Figure 3.41: Radial Profile of Transducer 2 for s = 1.17; Theoretical and Experimental Data using Active Diameter

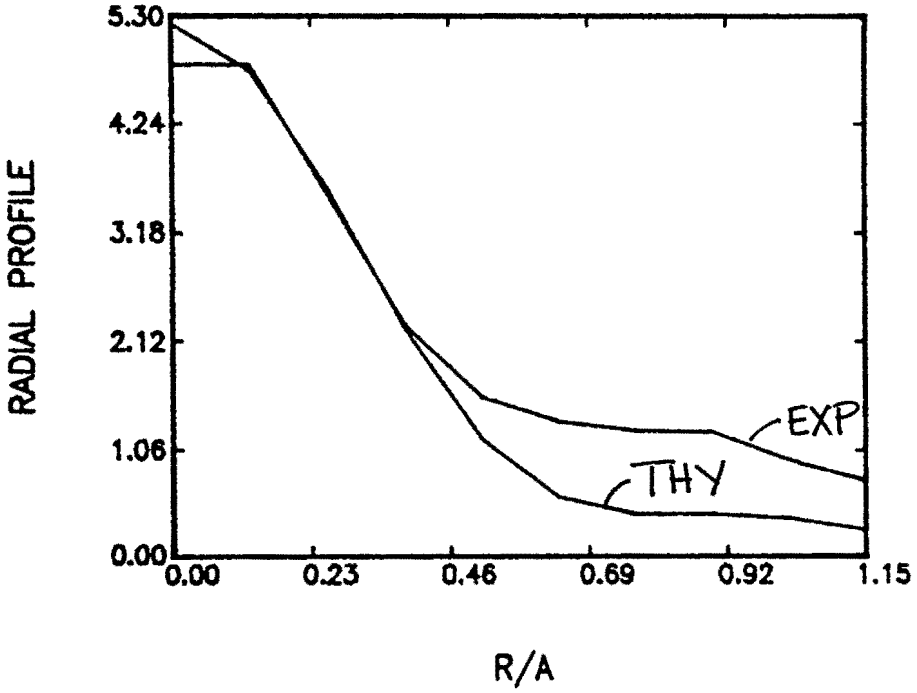

Figure 3.42: Radial Profile of Transducer 3 for s = 1.17; Theoretical and Experimental Data using Active Diameter

with the theory near the center of the transducer, c) both axial and radial profiles of transducers 1 and 2 are more similar to the rigid piston theoretical predictions than transducer 3, and d) use of the active diameter does not greatly influence the radial profiles.

3.4 Summary

The axial and radial profiles of a transducer can be used to analyze and compare transducer radiation patterns for their agreement with theory and for their over all symmetry. It was found, with the three 10 MHz transducers being used for the attenuation tests, that all involved transducer's behavior differed somewhat from theory, although transducers 1 and 2 followed theory more closely for both the axial profile and the radial profile results. In examining the symmetry of the transducers, it was found that the greatest symmetry occurred near the center of the transducer, with the outer edges of the radiation pattern being far from symmetric. The results of the transducer examination verify the results obtained for the attenuation measurements in that transducers 1 and 2 gave more similar results, and the results for transducer 3 were much different.

4 EFFECT OF TRANSDUCER CHARACTERIZATION ON ATTENUATION MEASUREMENTS

4.1 Introduction

The results of the previous chapter on transducer characterization can now be used to attempt to decrease the transducer dependence of the attenuation measurements which were presented in Chapter 2. The radial profile results can not be utilized at this time due to insufficient knowledge of how to use the information which was obtained, however the axial profile results (the active diameters) can be used directly in the calculation of the diffraction corrections, and therefore the attenuation measurements.

4.2 Effect of Errors in Diameter Estimation on Attenuation Measurements

The effect of error in the value for the probe's diameter on the results of the attenuation measurement was investigated for the three different methods. For a specific method, z_0 is the water path distance (constant) plus the distance to the first echo, and z is the water path distance (constant) plus the distance to the second or third echos necessary for the specific attenuation method in question. The received signal, $|V(z,f)|$, can be related to the system efficiency, reflection

coefficients, and transmission coefficients, $\beta(f)$, the diffraction corrections, $D(z,f)$, and the attenuation of the specimen, $\alpha(f)$, by [14]:

$$|V(z,f)| = |\beta(f)||D(z,f)|e^{-\alpha(f)z} \tag{4.1}$$

When a reference voltage is measured using the distance, z_o, one obtains,

$$|V(z_o,f)| = |\beta(f)||D(z_o,f)|e^{-\alpha(f)z_o} \tag{4.2}$$

The following ratios can then be written

$$e^{\alpha(f)(z-z_o)} = \frac{|D(z,f)|}{|D(z_o,f)|}\frac{|V(z_o,f)|}{|V(z,f)|} \tag{4.3}$$

and

$$\frac{V(z_o)|}{|V(z)|} = e^{\alpha(f)(z-z_o)}\frac{D(z_o,f)|}{D(z,f)|} \tag{4.4}$$

Using the incorrect value of the probe diameter, one obtains

$$e^{\alpha'(f)(z-z_o)} = \frac{|D'(z,f)|}{|D'(z_o,f)|}\frac{|V(z_o,f)|}{|V(z,f)|} \tag{4.5}$$

where the primed quantities refer to the quantities calculated with the incorrect value of the active diameters, and the corresponding unprimed quantities refer to the same quantities calculated with the correct probe diameters. Upon substitution of Equation 4.4 into Equation 4.5,

$$e^{\alpha'(f)(z-z_o)} = \frac{|D'(z,f)|}{|D'(z_o,f)|}\frac{|D(z_o,f)|}{|D(z,f)|}e^{\alpha(f)(z-z_o)} \tag{4.6}$$

and

$$\alpha'(f)(z-z_o) = \ln\frac{|D'(z,f)|}{|D'(z_o,f)|}\frac{|D(z_o,f)|}{|D(z,f)|} + \alpha(f)(z-z_o) \tag{4.7}$$

Therefore, the error in attenuation due to the error in transducer diameter is,

$$\Delta\alpha(f) = \alpha'(f) - \alpha(f) = \frac{1}{z - z_o} \ln \frac{|D'(z,f)|}{|D'(z_o,f)|} \frac{|D(z_o,f)|}{|D(z,f)|} \tag{4.8}$$

From Equation 4.8, it can be seen that the dependency of the experimental estimate of the attenuation constant on the probe diameter can be discussed in terms of the distance, $z - z_o$. The distance , $z - z_o$, is defined as the distance of travel between the first and second echo or the first and third echo. From Equation 4.8, it is evident that error in attenuation caused by errors in diameter estimation depends on: the distance, $z - z_o$, the diffraction correction at the true diameter and distance z_o and z, and the diffraction correction at the estimated diameter and distance z_o and z. From Figures 4.1 through 4.6, among all three attenuation measurement methods, the largest error in the diffraction correction occurs in the MT method for a given value of the error in the estimation of the probe's diameter. From this follows the largest error in measured attenuation. The second largest error occurs in the multiple echo II method.

Initially, z_o was 3 cm in the 10 MHz multiple thickness technique. However, if z_o is changed, the delta attenuation for a specific error in probe's diameter also changes. Therefore, a z_o can be found for the multiple thickness method which makes the attenuation error, $\Delta\alpha(f)$, approximately equal to the attenuation error in the results from the multiple echo and multiple echo II techniques at a 3 cm water path distance. The distance, z_o, which satisfies this condition is 8 cm (see Figure 4.7). The results across the three 10 MHz transducers obtained with the MT technique and the distance, z_o, equal to 8 cm can be seen in Figure 4.8.

The deviations of these results can be seen in Figure 4.9, and they are very

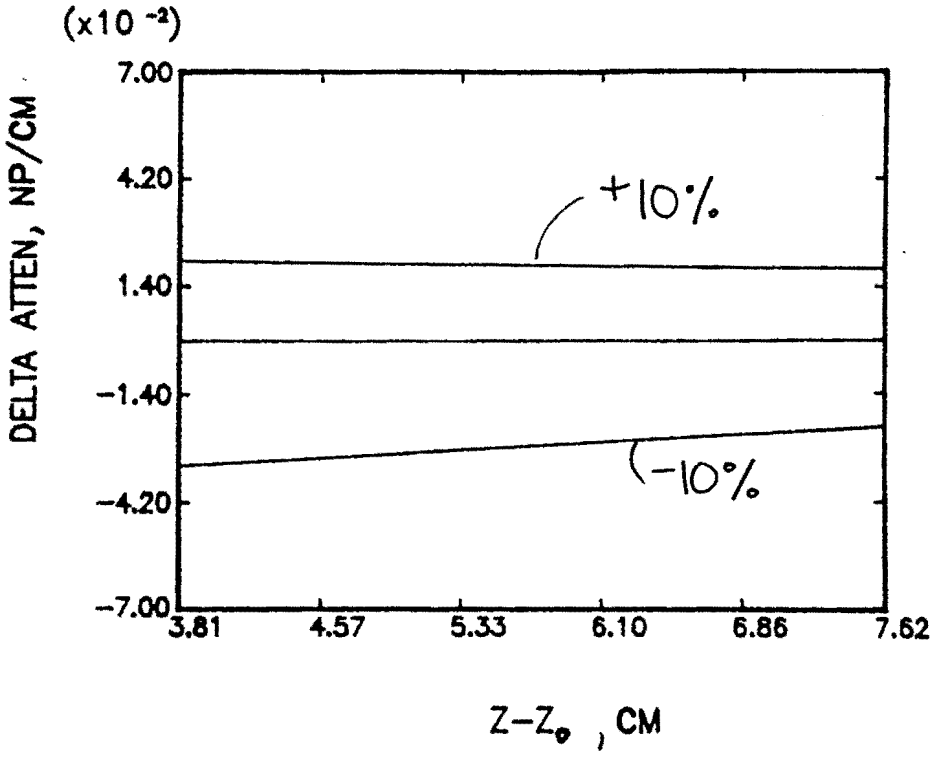

Figure 4.1: Change in Attenuation by the MT Attenuation Technique and a 10 MHz Probe Caused by $\pm$ 10 % Error in Probe Diameter Estimation

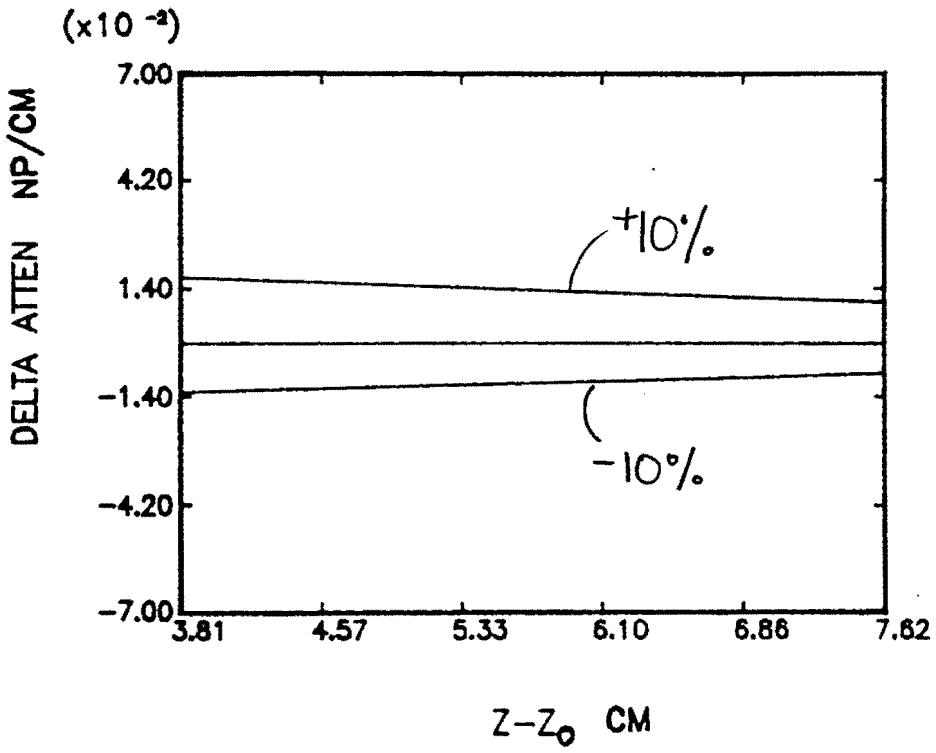

Figure 4.2: Change in Attenuation by the ME Attenuation Technique and a 10 MHz Probe Caused by $\pm$ 10 % Error in Probe Diameter Estimation

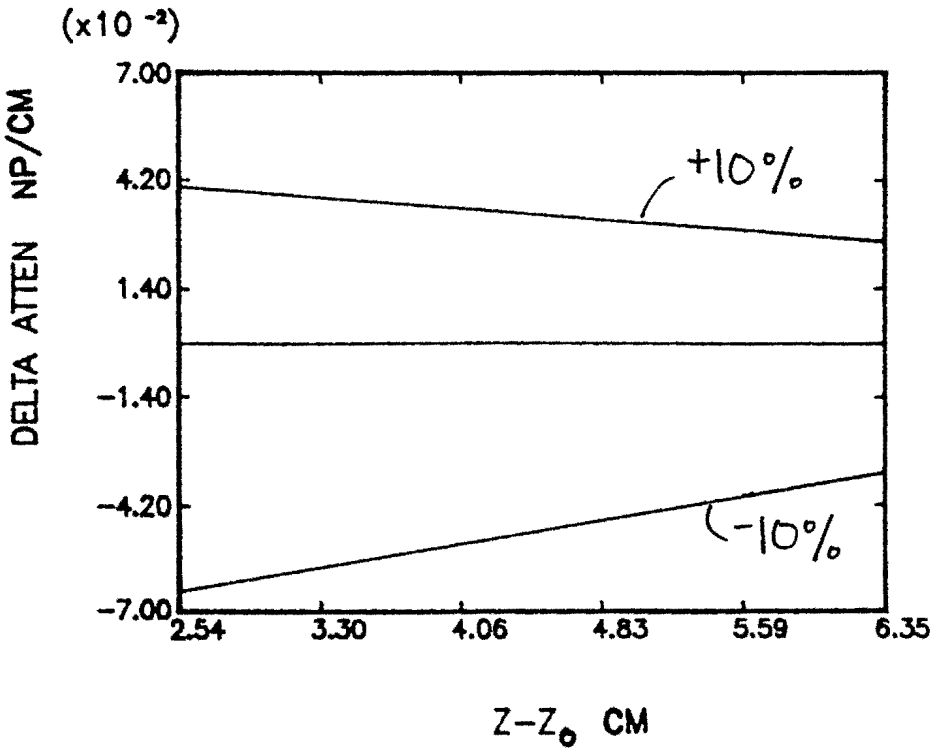

Figure 4.3: Change in Attenuation by the MEII Attenuation Technique and a 10 MHz Probe Caused by $\pm$ 10 % Error in Probe Diameter Estimation

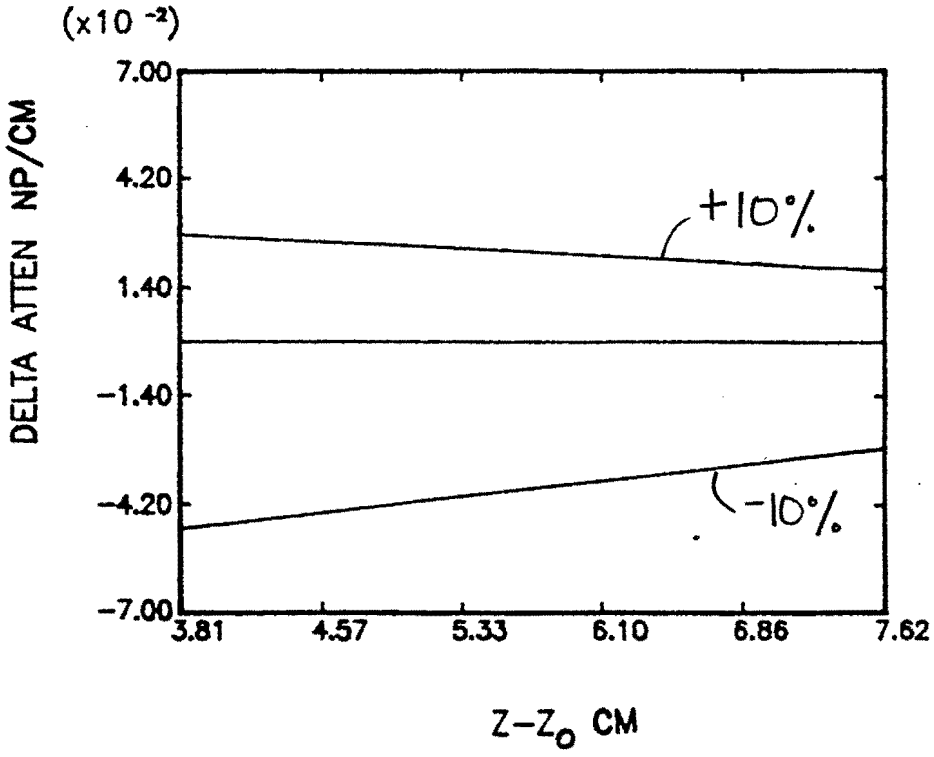

Figure 4.4: Change in Attenuation by the MT Attenuation Technique and a 15 MHz Probe Caused by $\pm$ 10 % Error in Probe Diameter Estimation

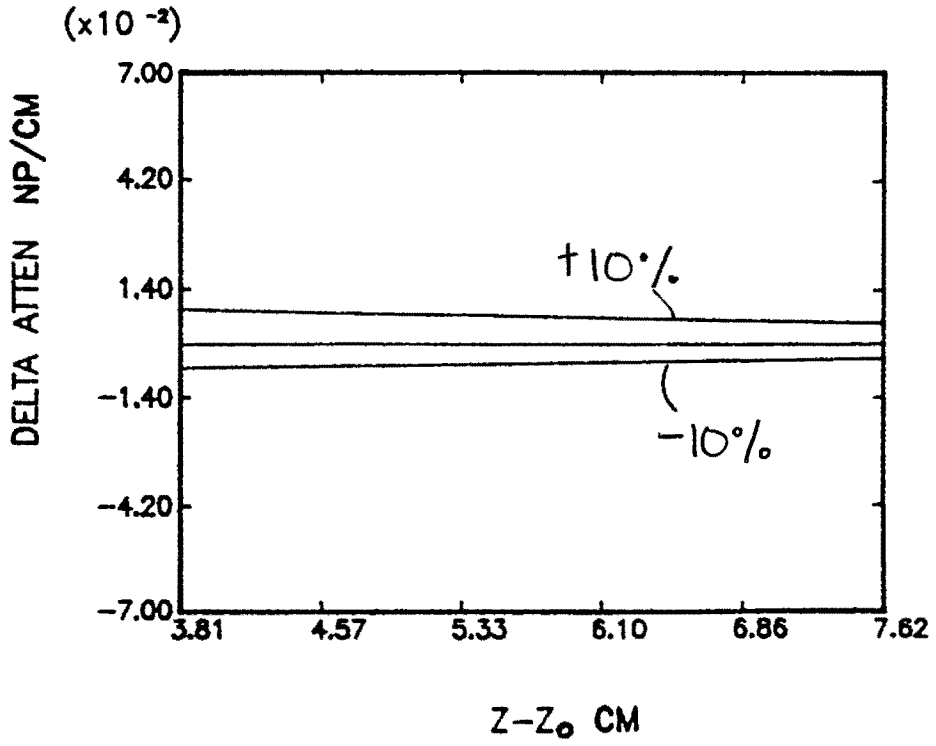

Figure 4.5: Change in Attenuation by the ME Attenuation Technique and a 15 MHz Probe Caused by $\pm$ 10 % Error in Probe Diameter Estimation

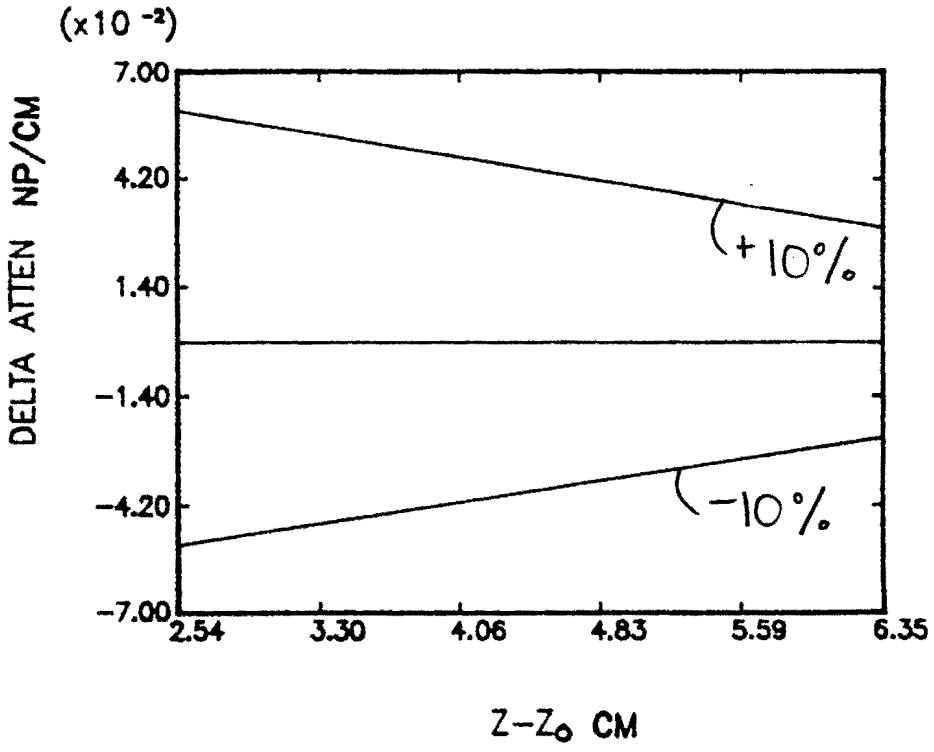

Figure 4.6: Change in Attenuation by the MEII Attenuation Technique and a 15 MHz Probe Caused by $\pm$ 10 % Error in Probe Diameter Estimation

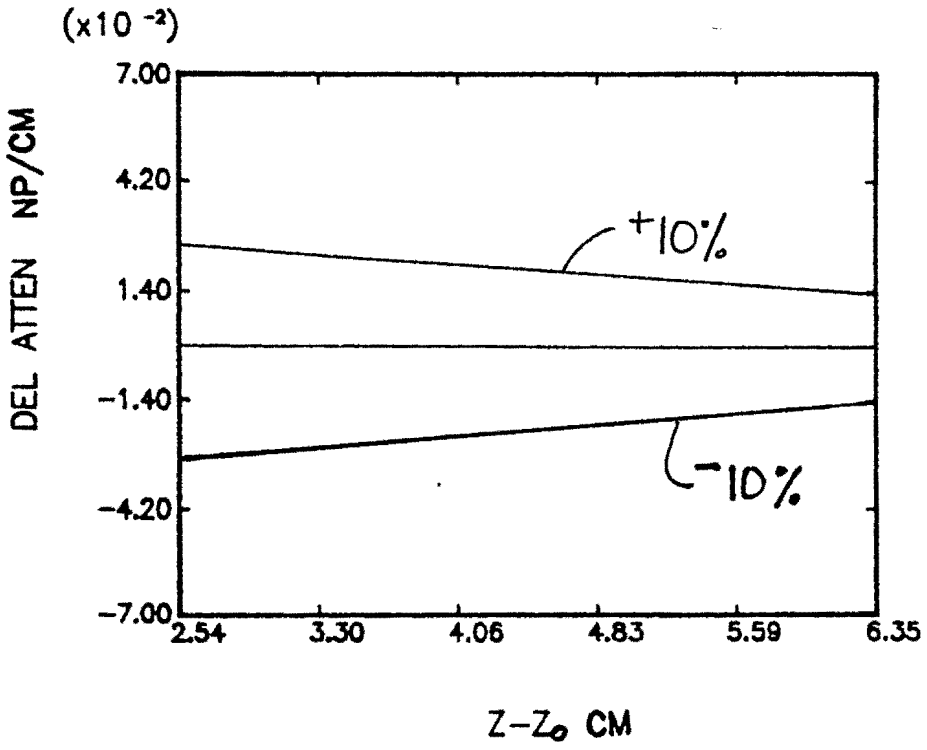

Figure 4.7: Change in Attenuation by the MT Attenuation Technique with z_o = 8 cm and a 10 MHz Probe Caused by a *pm* 10 % Error in Probe Diameter Estimation

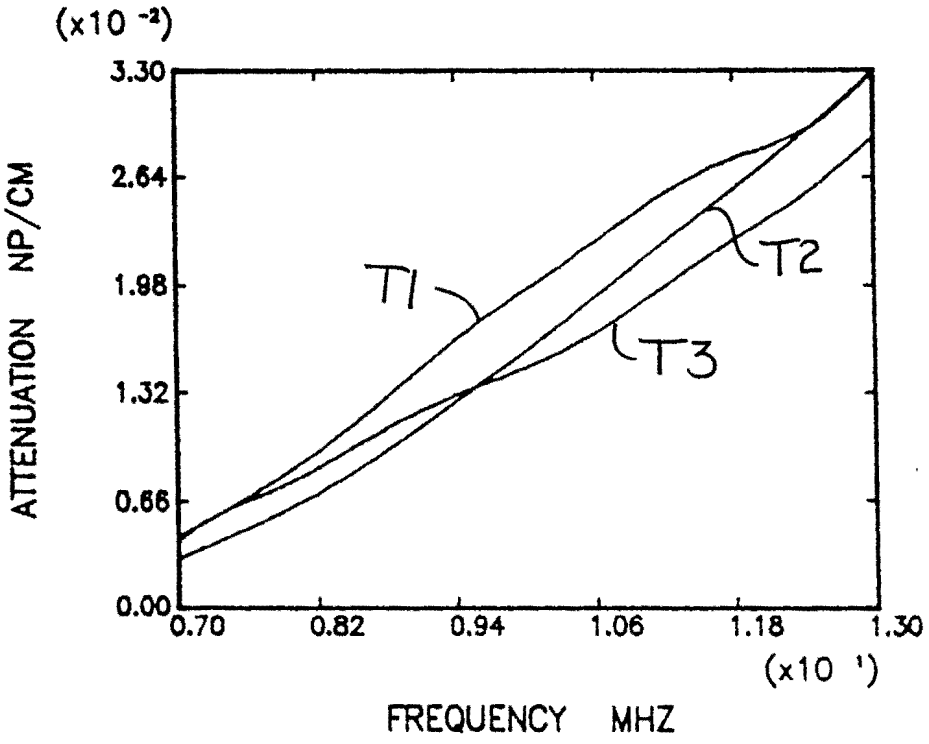

Figure 4.8: Attenuation in 7075 Aluminum Measured with the MT Technique at $z_o = 8$ cm using the Nominal Diameter (Transducers 1,2,3)

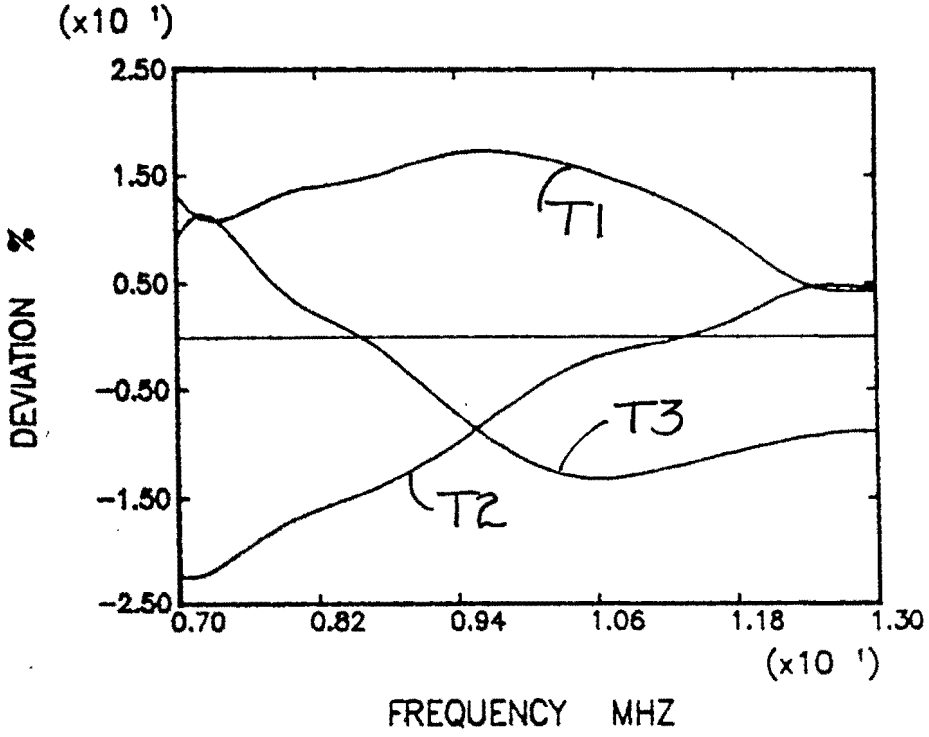

Figure 4.9: Deviation in Measured Attenuation for 7075 Aluminum with the MT Method at z_o = 8 cm using Transducers 1,2,3 with the Nominal Diameter

comparable to those for the multiple echo and the multiple echo II methods run at 3 cm. Figures 4.10 and 4.11 show the results when the active diameters are used, instead of the nominal diameters, and as expected, the deviations of the attenuation values between the transducers decrease. These results show the importance of the distance at which the measurement is performed in the attenuation measurement.

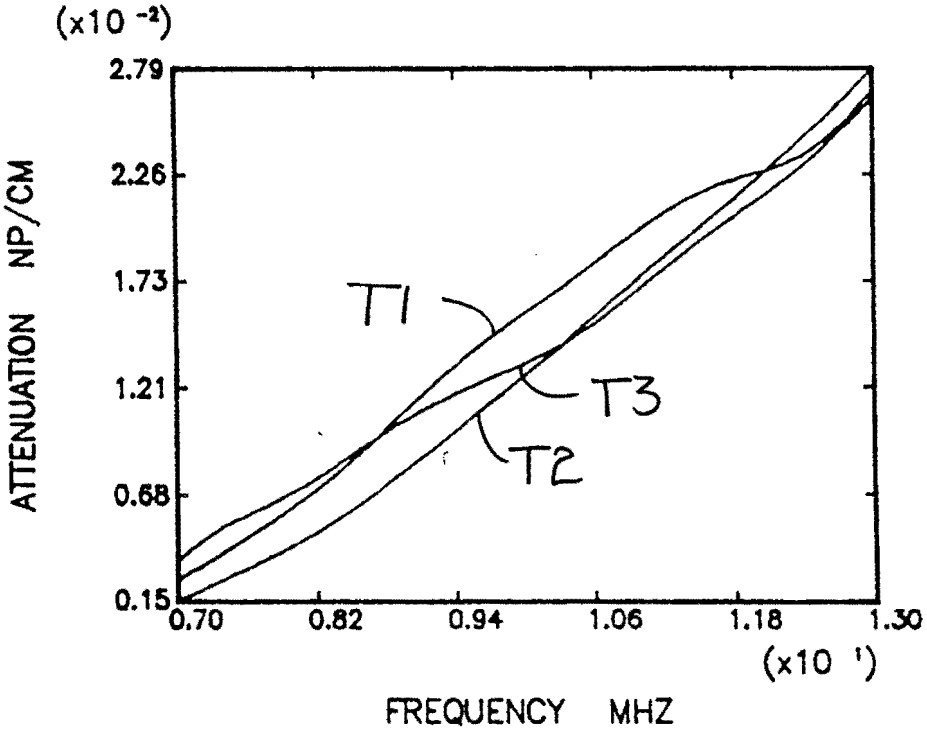

Figure 4.10: Attenuation in 7075 Aluminum with the MT Method at $z_o = 8$ cm using Transducers 1,2,3 and Their Respective Active Diameters

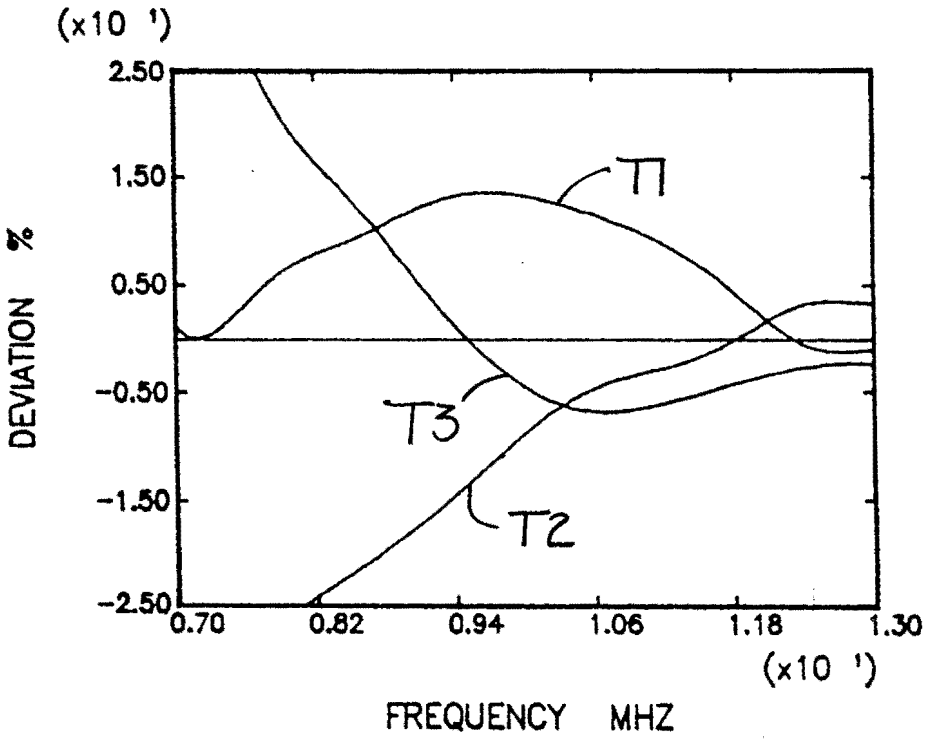

Figure 4.11: Deviation in Measured Attenuation for 7075 Aluminum with the MT Method at $z_o = 8$ cm using Transducers 1,2,3 with Their Respective Active Diameters

4.3 Attenuation Measurements of 7075 Aluminum with 10 MHz Transducers Using Active Diameters

In order to improve the consistency of the measurements across transducers, active diameters for each transducer were found assuming they behave as planar piston sources. These diameters were calculated based on measuring the backscattered signals from small spherical reflectors located along the main axis of the transducer, as described in detail in Chapter 3. In finding the active diameters, the fit between experimental and theoretical axial profiles was better with transducers 1 and 2, and active diameters of .234 inches and .237 inches, respectively were found. However for transducer 3, the fit between experimental and theoretical axial profiles was not as good leading to the conclusion that this transducer does not follow the planar piston model as well as the other two transducers. An active diameter of .244 inches was found for this transducer.

Bias of a particular method using the active diameters to calculate the attenuation can be seen in Figures 4.12 through 4.14. The multiple thickness method gives the lowest value for all transducers, and there is quite a bit of scatter across measurement techniques. The attenuation values obtained with the use of the active diameters are all lower than the results obtained with the nominal diameters. Deviations between transducers for each particular method stayed within $\pm$ 20 % with the MEII method giving the lowest deviations and the MT the highest. The deviations with the active diameters are lower than the values obtained with the nominal diameters for all methods. These results can be seen in Figures 4.15 through 4.17.

The consistency of the measurements across transducers can be examined by

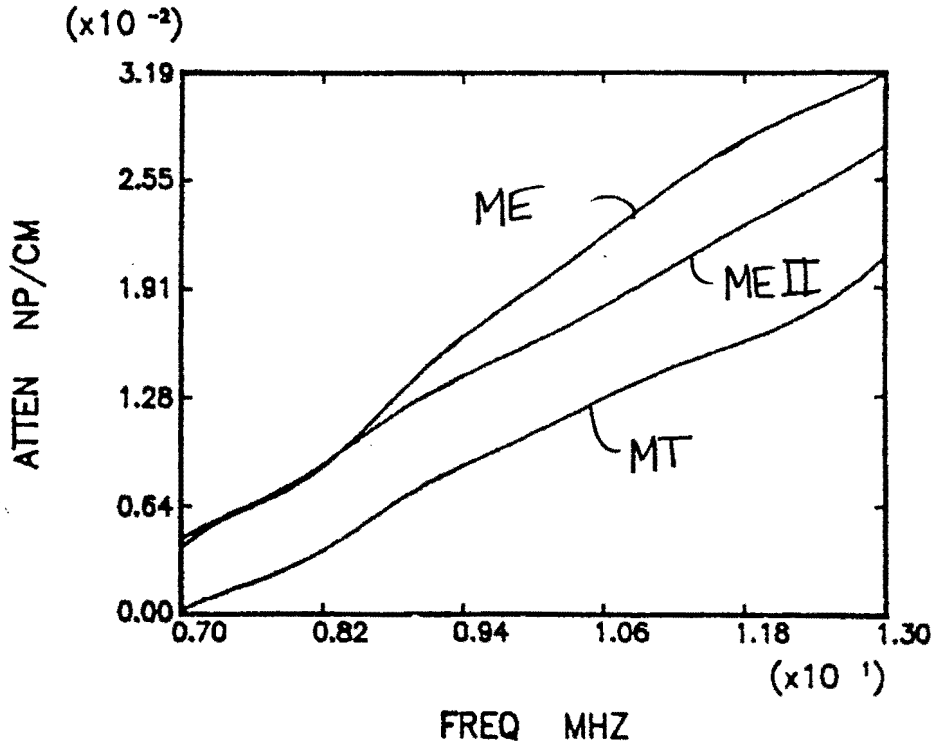

Figure 4.12: Attenuation in 7075 Aluminum with the ME, MT, and MEII Techniques using Transducer 1 with the Active Diameter

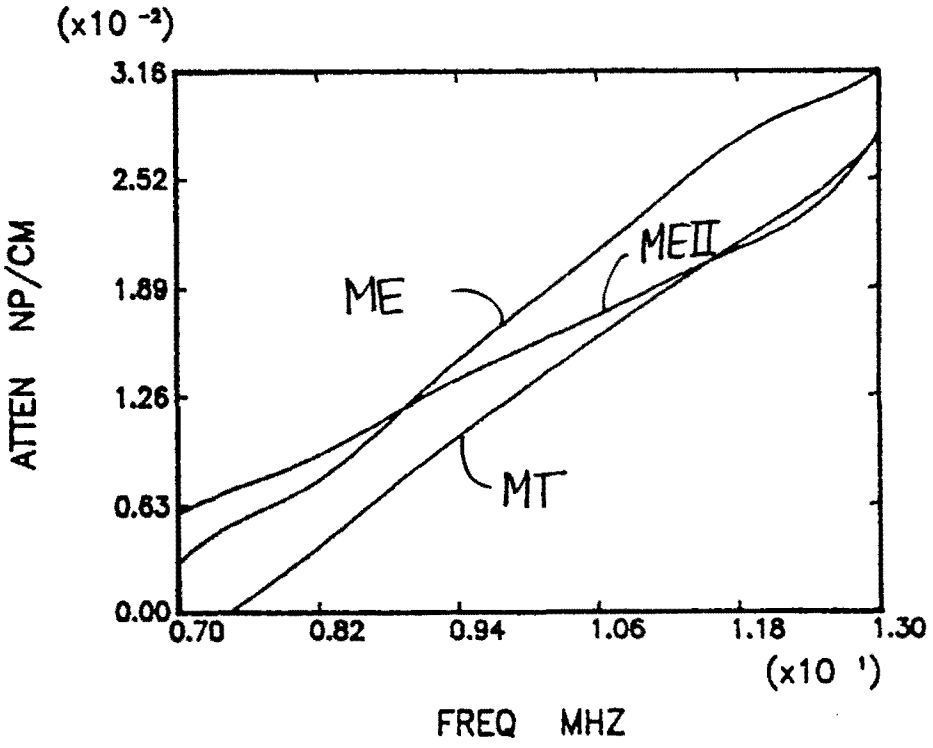

Figure 4.13: Attenuation in 7075 Aluminum with the ME, MT, and MEII Techniques using Transducer 2 with the Active Diameter

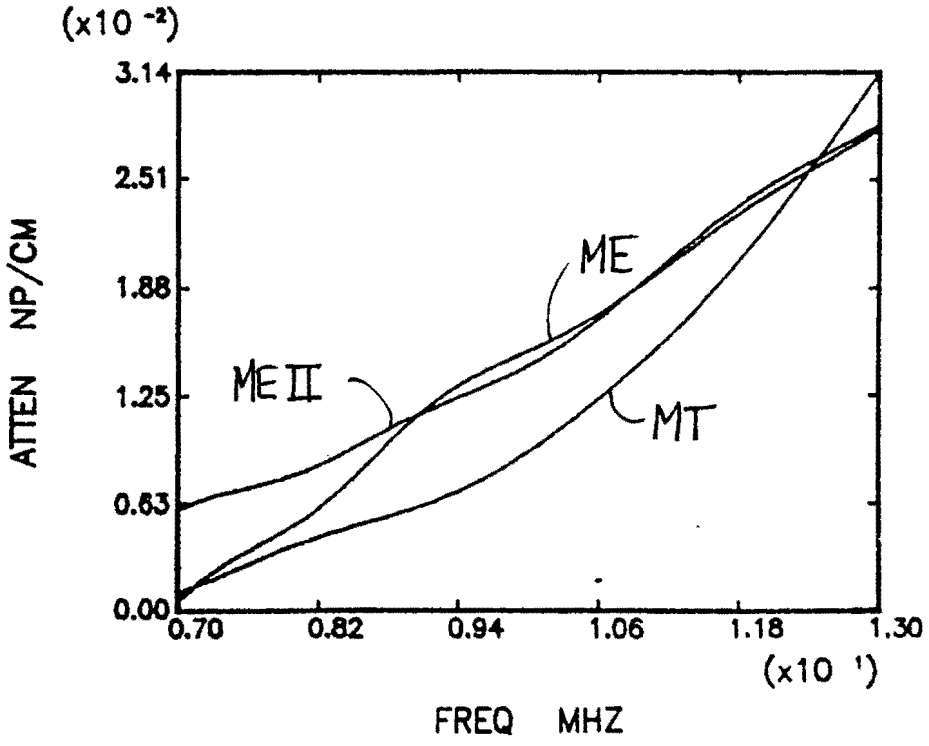

Figure 4.14: Attenuation in 7075 Aluminum with the ME, MT, and MEII Techniques using Transducer 3 with the Active Diameter

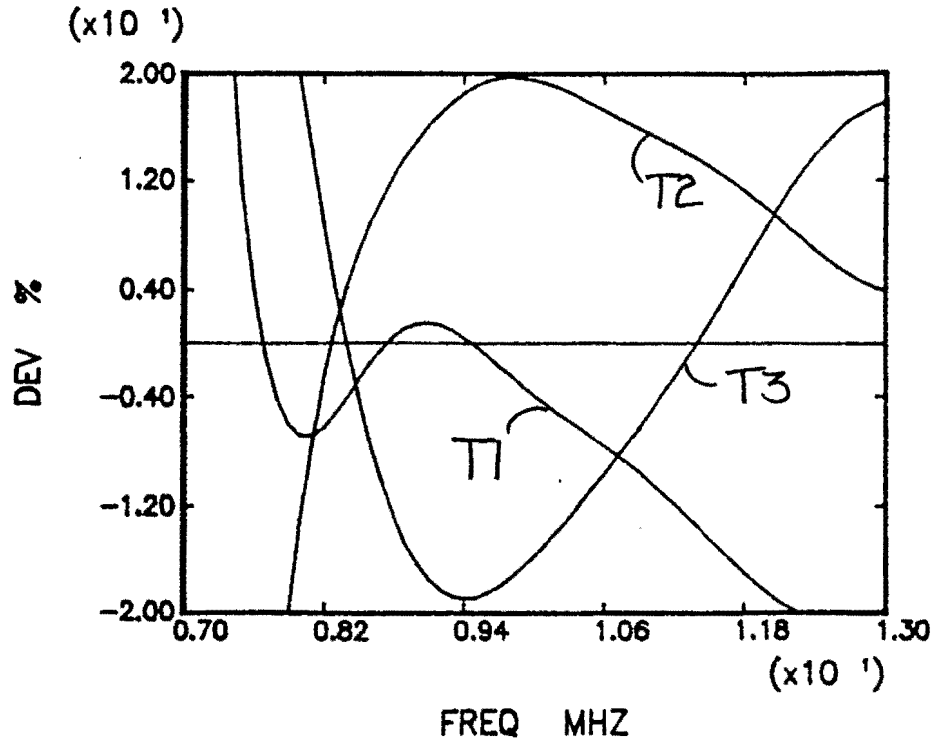

Figure 4.15: Deviation of the Measured Attenuation for 7075 Aluminum with the MT Method using Transducers 1,2,3

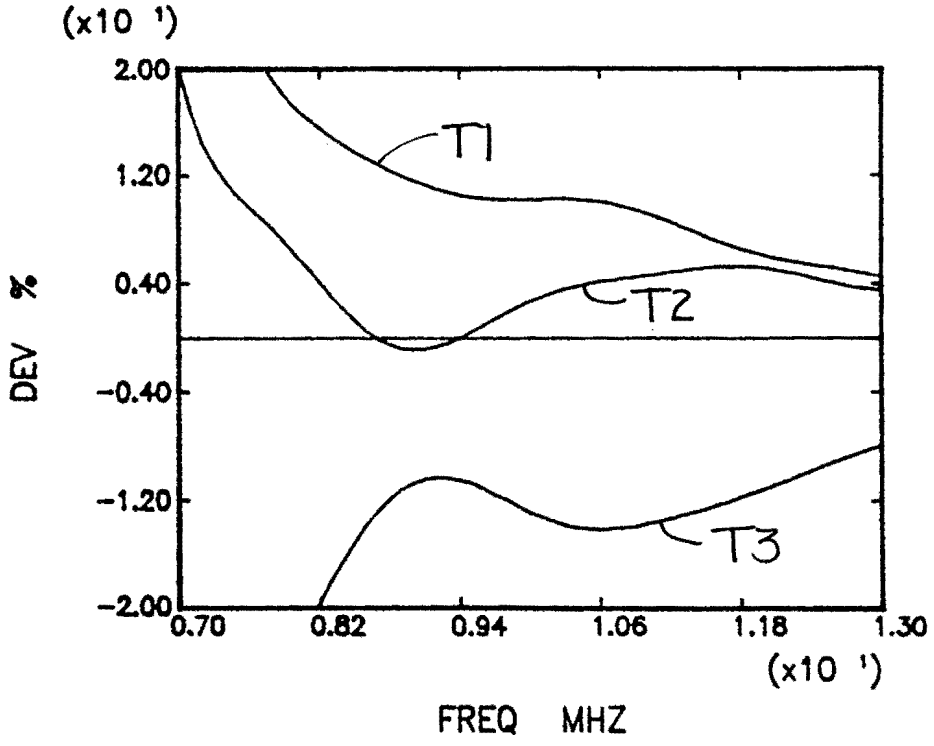

Figure 4.16: Deviation of the Measured Attenuation for 7075 Aluminum with the ME Method using Transducers 1,2,3 with the Active Diameters

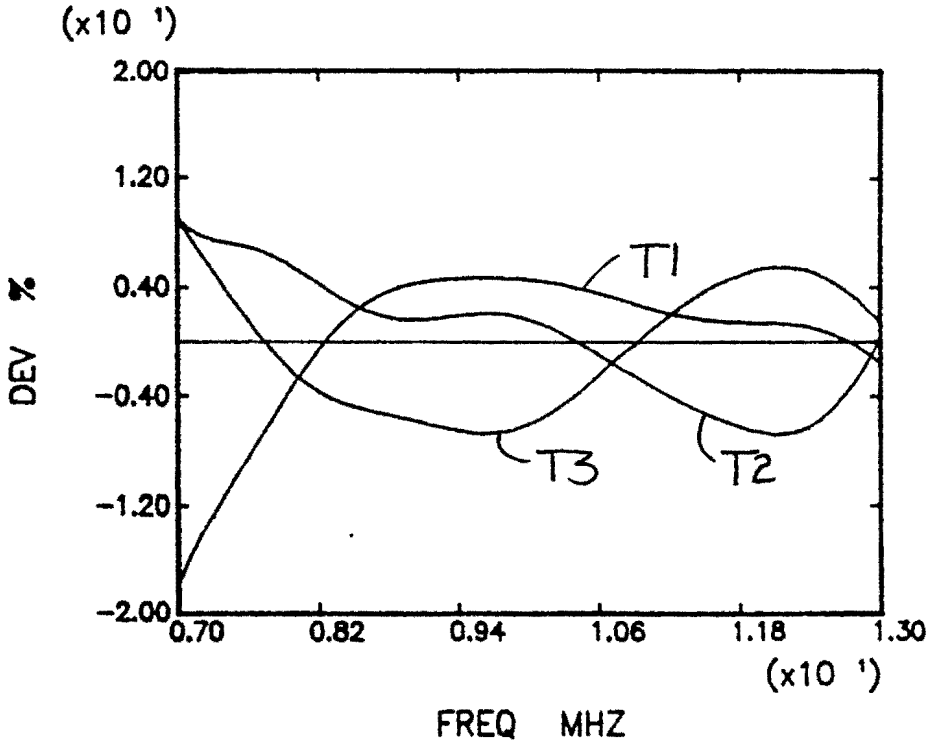

Figure 4.17: Deviation of the Measured Attenuation for 7075 Aluminum with the MEII Method using Transducers 1,2,3 with the Active Diameters

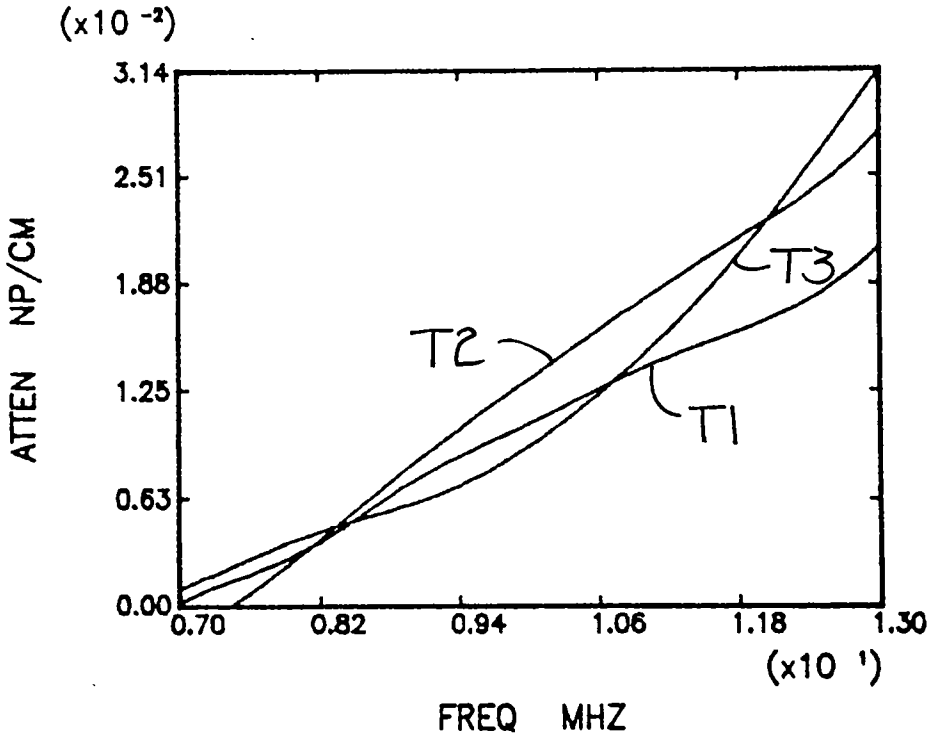

Figure 4.18: Attenuation of 7075 Aluminum with the Multiple Thickness Technique using Transducers 1,2,3 with the Active Diameters

looking at Figures 4.18 through 4.20. No one transducer shows bias with any particular method. Deviations are all within $\pm$ 20 % and are lower than the deviations for the nominal diameters. Results can be seen in Figures 4.21 through 4.23.

4.4 Scatter in Attenuation Results when Transducer not Obeying Piston Theory is Excluded

As was stated before, transducer 3 does not follow the planar piston model as well as transducers 1 and 2. Therefore, by eliminating transducer 3 from the

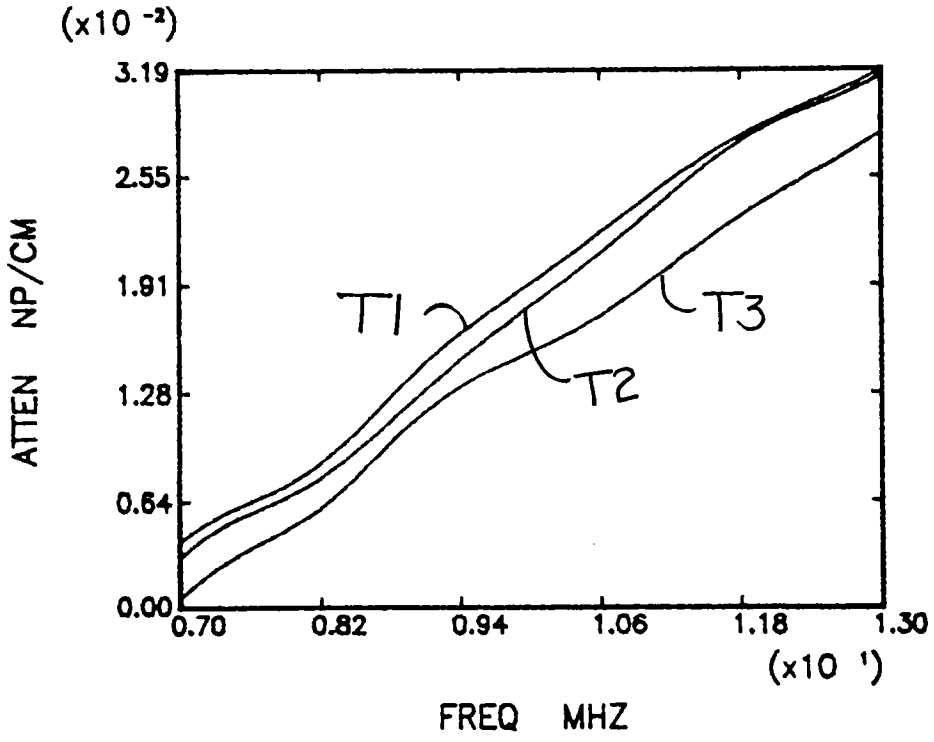

Figure 4.19: Attenuation of 7075 Aluminum with the Multiple Echo Technique using Transducers 1,2,3 with the Active Diameters

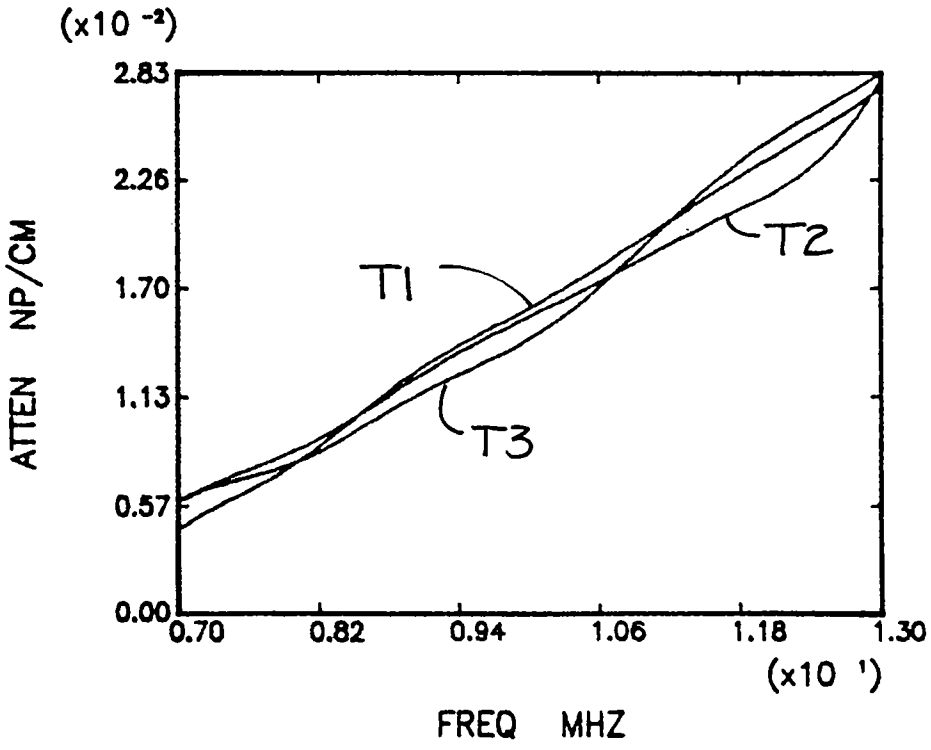

Figure 4.20: Attenuation of 7075 Aluminum with the Multiple Echo II Technique using Transducers 1,2,3 with the Active Diameters

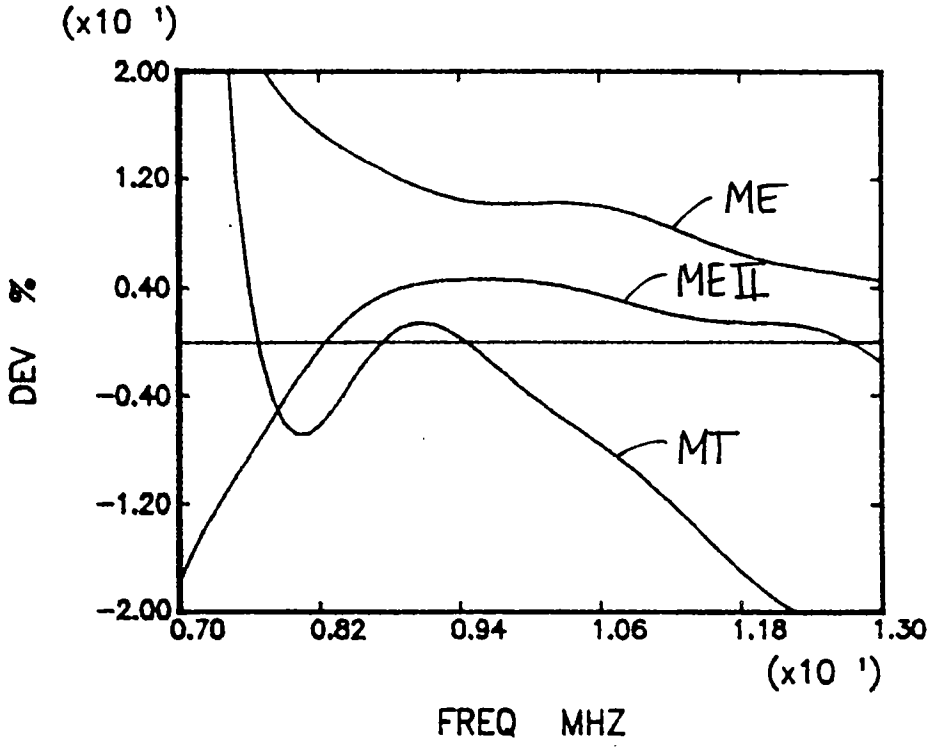

Figure 4.21: Deviation in the Measured Attenuation of 7075 Aluminum with the MT, ME, and MEII Techniques for Transducer 1 using the Active Diameter

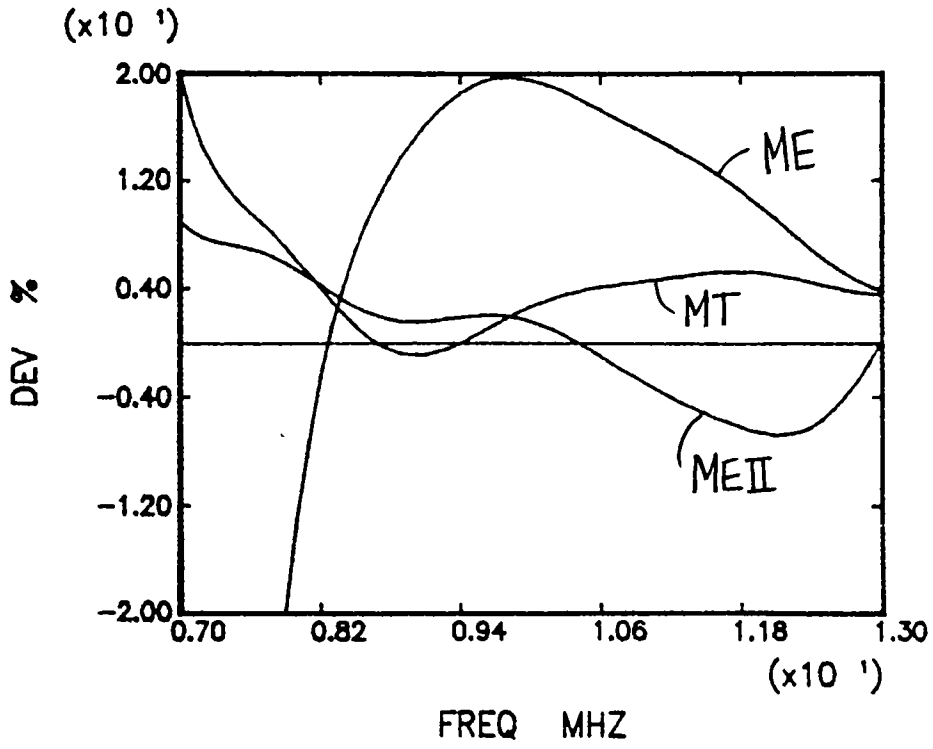

Figure 4.22: Deviation in the Measured Attenuation of 7075 Aluminum with the MT, ME, and MEII Techniques for Transducer 2 using the Active Diameter

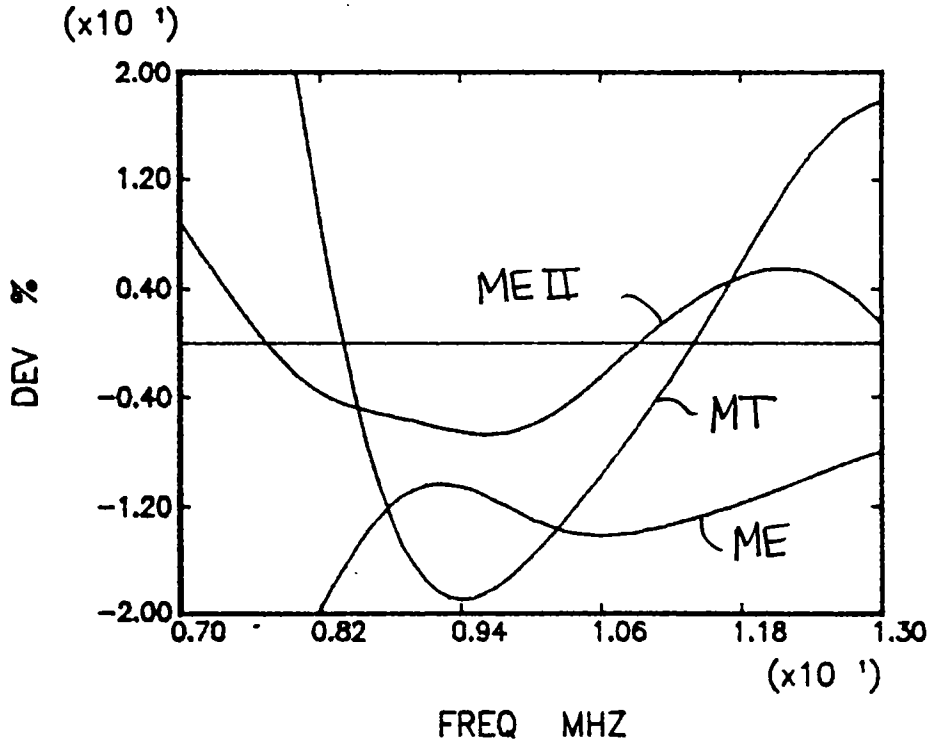

Figure 4.23: Deviation in the Measured Attenuation of 7075 Aluminum with the MT, ME, and MEII Techniques for Transducer 3 using the Active Diameter

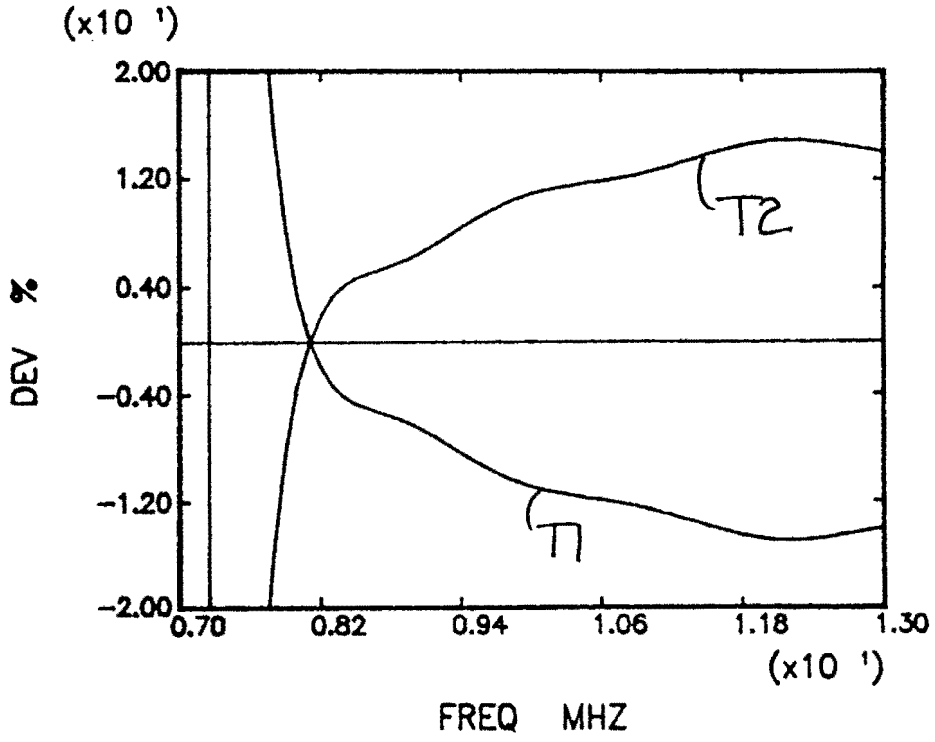

Figure 4.24: Deviation in the Measured Attenuation in 7075 Aluminum using the MT Attenuation Technique with Transducers 1 and 2 using Active Diameters (Transducer 3 Eliminated from the Results)

results, the deviations between the methods and the transducers should decrease. As can be seen by Figures 4.24 through 4.26, as predicted, the deviations between methods decrease, and, as seen in Figures 4.27 through 4.28, the deviations between transducers also decrease.

4.5 Conclusions

Transducer characterization by means of the active diameter can have significant effects on the attenuation measurements. The results of the research in this

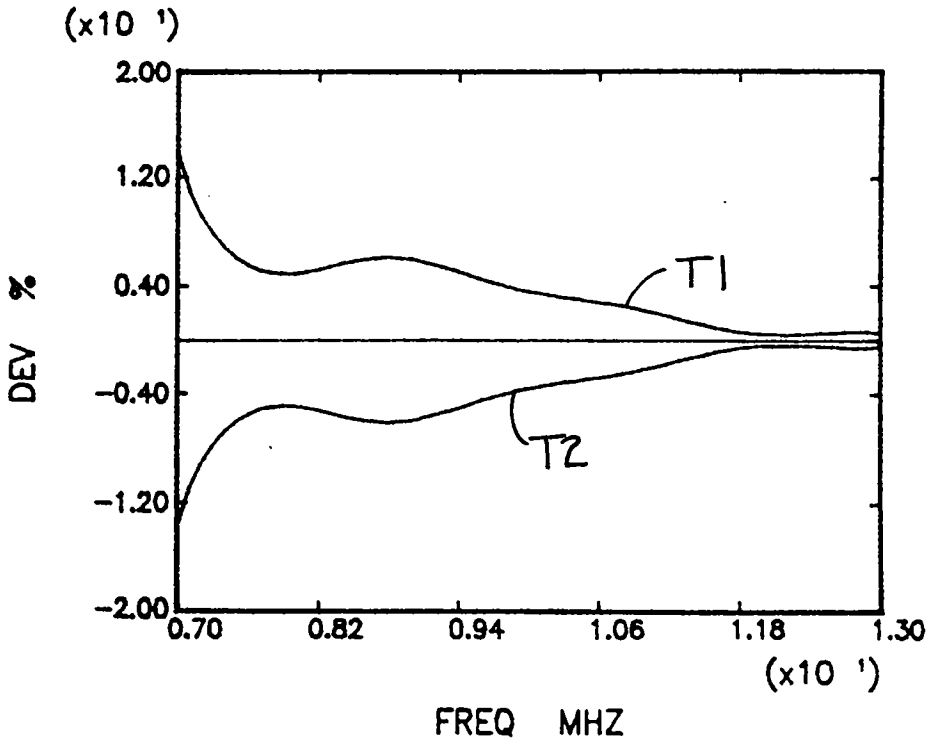

Figure 4.25: Deviation in the Measured Attenuation of 7075 Aluminum using the ME Attenuation Technique with Transducers 1 and 2 using Active Diameters (Transducer 3 Eliminated from the Results)

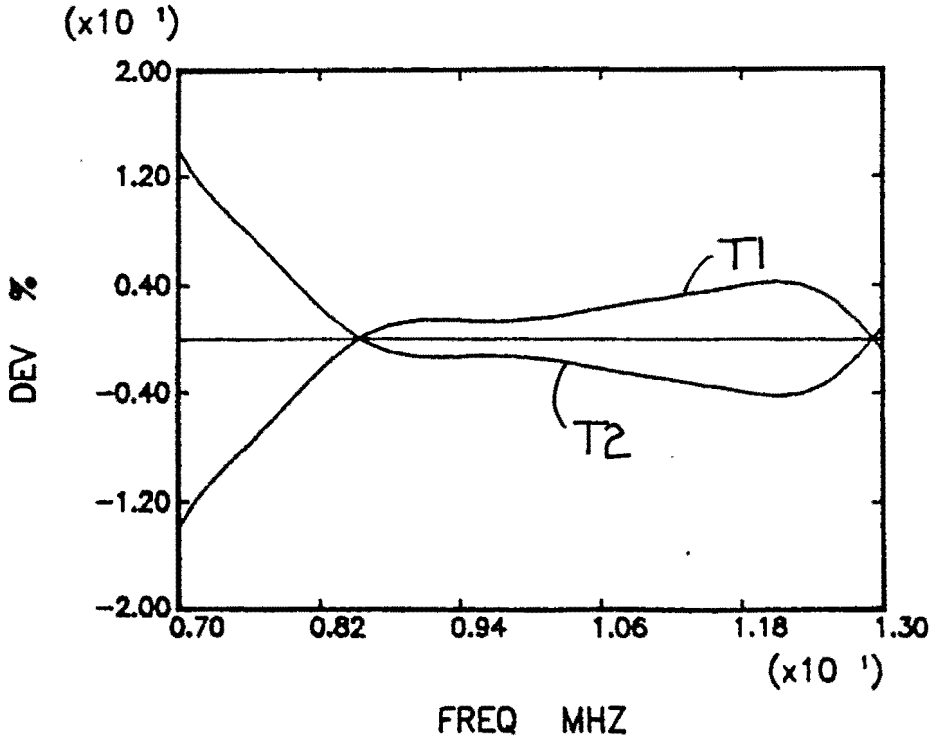

Figure 4.26: Deviation in the Measured Attenuation of 7075 Aluminum using the MEII Attenuation Technique with Transducers 1 and 2 using Active Diameters (Transducer 3 Eliminated from the Results)

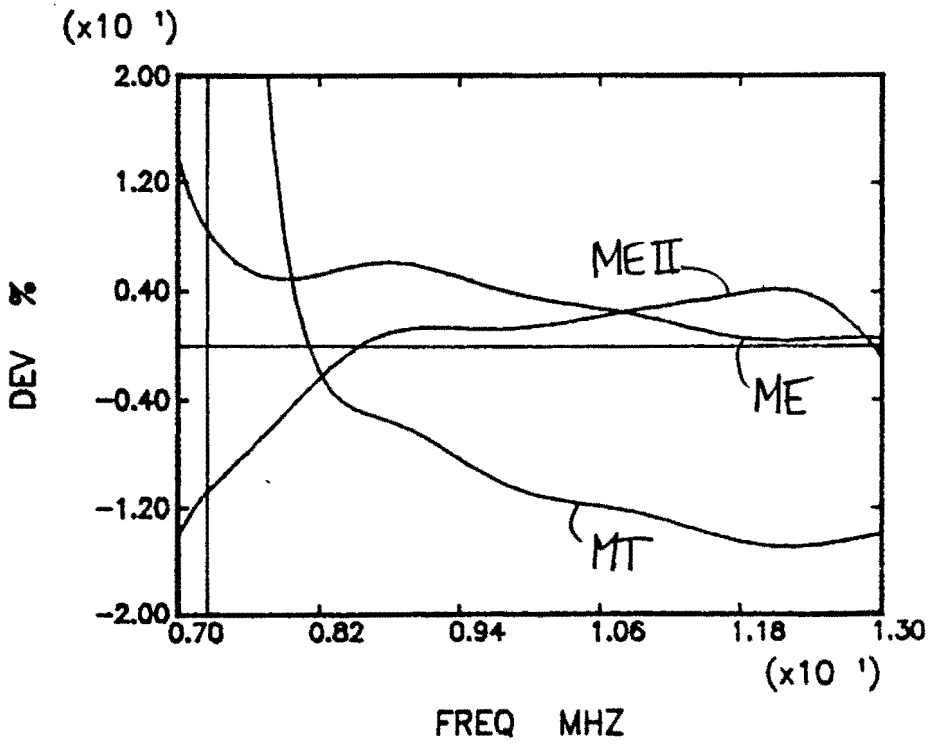

Figure 4.27: Deviation in the Measured Attenuation of 7075 Aluminum using the MT, ME, and MEII Attenuation Techniques with Transducer 1 with the Active Diameter (Transducer 3 Eliminated from the Results)

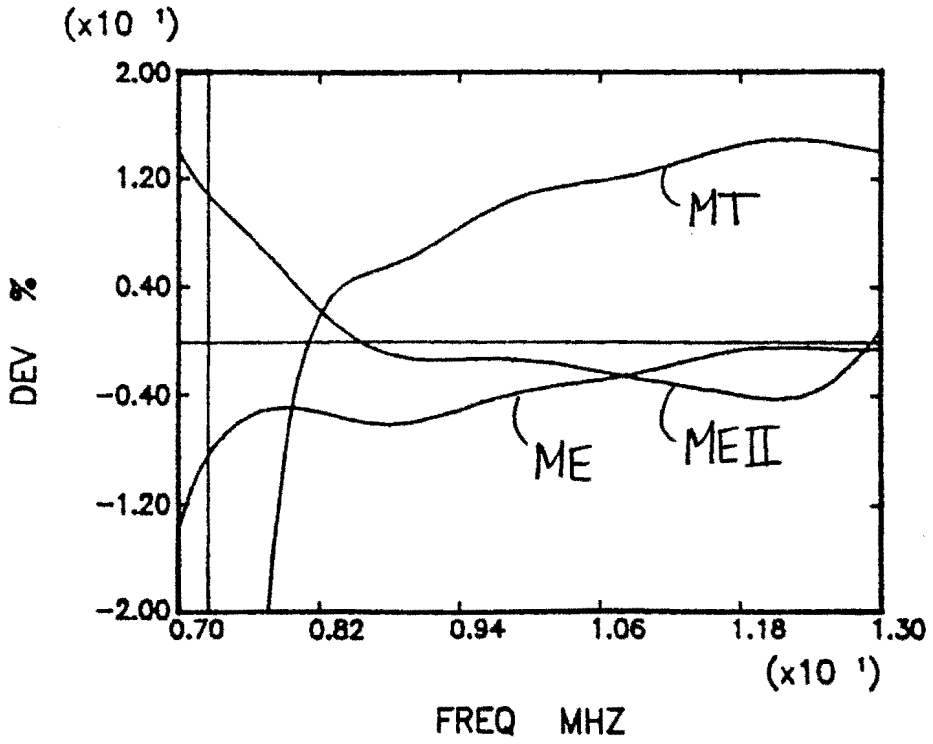

Figure 4.28: Deviation in the Measured Attenuation of 7075 Aluminum using the MT, ME, and MEII Attenuation Techniques with Transducer 2 with the Active Diameter (Transducer 3 Eliminated From the Results)

thesis have indicated:

1) The estimation of the diameter of the probe can have significant effects on the results of the attenuation measurements. This effect is especially evident in the MT attenuation measurement technique, where to make the effects of the diameter estimation similar to the effects of the diameter estimation in the ME and MEII techniques, measured at a water path distance of 3 cm, the test must be performed at a significantly larger water path distance of 8 cm.

2) By use of transducer characterization in the form of the active diameter, attenuation measurements became less transducer dependent.

3) Removing the transducer which behaved the least like a planar piston source decreased the deviations of the results of the attenuation measurements.

5 GENERAL CONCLUSIONS

When the measurement model is used to quantitatively interpret received signals from ultrasonic measurements, it is extremely important to have knowledge of the ultrasonic wave attenuation in the solid material and to know how closely the transducers behave as planar piston sources. By measuring the attenuation of ultrasonic waves in 7075 aluminum and A357 aluminum, and by examining the ultrasonic transducers by measuring their axial and radial profiles, the following conclusions follow from this research:

1) Attenuation of low attenuating materials can be measured consistently, however, transducer characterization needs to be improved to enable the correct calculation of diffraction corrections for a probe, which are required for obtaining transducer independent results.

2) In the case of higher attenuating materials or at higher frequencies, where the attenuation is higher, it is easier to measure the attenuation more consistently using the same methods because the diffraction of the beam is of less importance than the material's attenuation.

3) Axial profiles of transducers can be used to calculate active diameters for transducers, enabling characterization of probes as planar piston sources. This characterization reduces transducer dependence in ultrasonic attenuation measure-

ments.

4) Radial profiles of transducers seem to indicate that probes radiate beams that behave more like theoretical planar pistons near the center of their main axis, however, this agreement decreases with radial distance.

5) The active diameter can be effectively used to reduce transducer dependence in ultrasonic attenuation measurements providing the involved probe's radiation pattern obeys the rigid piston theory which is not true for all planar, non-focused, immersion transducers.

6 BIBLIOGRAPHY

[1] R.B. Thompson and T.A. Gray. "A Model Relating Ultrasonic Scattering Measurements Through Liquid-Solid Interfaces to Unbounded Medium Scattering Amplitudes." J. Acoust. Soc. Am. 74 (1983): 1279.

[2] E.P. Papadakis. "Revised Grain-Scattering Formulas and Tables." J. Acoust. Soc. Am. 37 (1965): 703.

[3] B. Kopec. "Ultrasonic Inspection of Grain Size in the Materials for Railway Wheel Sets." Ultrasonics. 13 (1975): 267.

[4] R.L. Roderick and R. Truell. "The Measurement of Ultrasonic Attenuation in Solids by the Pulse Technique and Some Results in Steel". J. Appl. Phys. 23 (1952): 267.

[5] E.P. Papadakis. "Ultrasonic Attenuation by Spectrum Analysis of Pulses in Buffer Rods." J. Acoust. Soc. Am. 53 (1973): 1336.

[6] E.P. Papadakis. "Absolute Measurements of Ultrasonic Attenuation using Damped Nondestructive Testing Transducers." J. Test. Eval. 12 (1984): 273.

[7] E.R. Generazio. "The Role of the Reflection Coefficient in Precision Measurement of Ultrasonic Attenuation." Material Evaluation. 42 (1985): 995.

[8] W.S. Burkle. "Measurement of Ultrasonic Longitudinal Wave Attenuation." Material Evaluation. 42(3) (1984): 262.

[9] R.A. Kline. "Measurement of Attenuation and Dispersion using an Ultrasonic Spectroscopy Technique." J. Acoust. Soc. Am. 76 (1984): 498.

[10] P.S. Stelkov. "Attenuation-Coefficient Measurement with Immersion." Sov. J. Nondestructive Testing.13(1) (1977): 115.

[11] D.D. Bennink. Multiple Thickness Technique. Unpublished. Engineering Science and Mechanics Department, Iowa State University, Ames, Iowa. 1986.

[12] L.E. Kinsler and A.R. Frey. "Fundamentals of Acoustics." John Wiley and Sons, Inc., New York, 1962.

[13] D.D. Bennink and A.L. Mielnicka-Pate. "Transducer Radiation Modeling for Ultrasonic Inspection Purposes." Review of Progress in Quantitative NDE. 6A (1986): 657.

[14] A.D. Pierce. "Acoustics: An Introduction to its Physical Principles and Applications." McGraw-Hill Book Company, New York, 1981.

$\mathcal{J}(f)$ = frequency dependent complex scale factor (measurement system efficiency factor)

$V_r(f,z)$ = the received frequency dependent voltage when the scatterer is at axial distance z

$\alpha(f)$ = the attenuation of the signal in water

and

$$|c(f,z)| = 2|\sin[\frac{1}{2}k(\sqrt{z^2+a^2(f)}-z]| \tag{3.4}$$

where

k= wave number

z= small scatter axial distance

$a(f)$ = active radius of the transducer

The parameter of variation between Equations 3.3 and 3.4 is the frequency dependent radius, $a(f)$, which can be varied until the least accumulated error between the theoretical and measured values of $c(f,z)$ is arrived at where the accumulated error is

$$\tilde{E}(f_j) = \frac{1}{N}\sqrt{\sum_{i=1}^{N}(V_{th}(f_j,z_i)-Vm(f_j,z_i))^2} \times 100 \qquad j=1,2.....M \tag{3.5}$$

where

N= number of positions included in the curve fitting procedure

M = the number of frequencies in the pressure spectrum

$V_{th}(f_j,z_i)$ = the theoretical pressure magnitude of the on axis profile at frequency, f_j, and distance, z_i

$Vm(f_j,z_i)$ = the scaled experimental pressure magnitude of the on axis profile at frequency, f_j, and distance, z_i

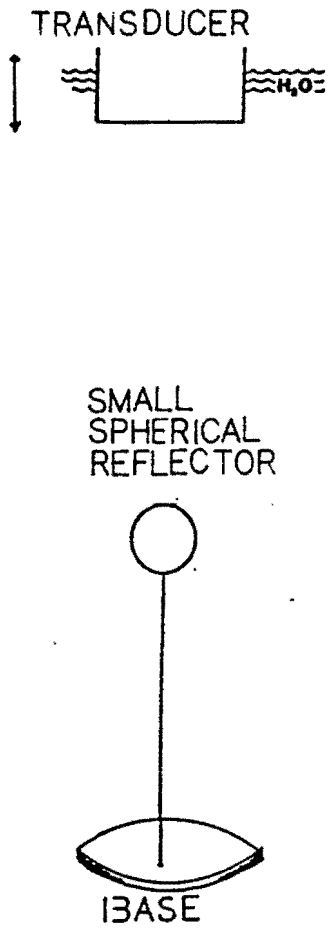

Figure 3.1: Schematic of the Set-up used for Axial Profile Measurements

In fitting the theoretical profile to the experimental profile, knowledge of the attenuation constant of the water is necessary. This value can either be entered as a known value or it can be calculated in the curve fitting procedure. Calculation of it takes place at the same time as the calculation of the frequency dependent complex scale factor, $\mathcal{B}(f)$, by a least squares fit of

$$\ln \frac{|V(f_j,z)|}{|c(f_j,z)|} = \ln \mathcal{B}(f_j) - \alpha(f_j)z \qquad j = 1,2,.....M \tag{3.6}$$

where $V(f_j,z)$ is measured, $c(f_j,z)$ is calculated from the choice of the diameter, and z is known. If the attenuation is entered as a textbook value, $\mathcal{B}(f)$ is calculated similarly by a least squares fit, however, in this case, the attenuation constant is known, so there is only one parameter to determine in the fitting procedure.

The frequency dependent radius arrived at by use of the least accumulated error is called the active radius which can be used for evaluating ultrasonic attenuation measurements in such a way that the results become less transducer dependent.

3.2.3 Experimental Apparatus

The electronic equipment used for the transducer characterization was the same as that previously used in the attenuation measurements. The schematic of the apparatus can be seen in Figure 2.7. The same equipment was used for all experiments making the measurements, with the exception of the transducers, independent of the equipment. Transducers used for the axial profile experiments include the same three, 10 MHz, .25 inch nominal diameter, model V312 unfocused, immersion probes which were used in the attenuation tests. The serial numbers and corresponding transducer numbers (which correlate to the numbers used in the attenuation tests) are shown in Table 3.1.

Table 3.1: Serial Numbers of the Transducers

Transducer Number	Serial Number
1	44689
2	58498
3	44686

3.2.4 Procedure

An approximately .2 cm spherical reflector was used (see Figure 3.1), and the impulse response at each location, from .5 cm to 11 cm at .5 cm intervals, was measured. The Fast Fourier Transform was performed on the time domain wave forms of the received voltage. The axial profiles were then extracted from the resulting frequency domain data within the range of 9 to 11 MHz with a spacing of 0.125 MHz. The external and internal attenuation values and time/division settings on the oscilloscope were kept constant throughout all measurements. By maximizing the output signal at the beginning of every experiment, the transducer was positioned so that it's acoustic axis was normal to the spherical reflector. The measurement was run twice per transducer.

3.2.5 Results and Discussion

The experimental versus theoretical results were examined in a number of different ways. First, the active diameter was found by fitting the experimental data with the theoretical data for all s values including both the nearfield and farfield data (Case 1). In doing this, the attenuation coefficient in water was both entered as a known value, and calculated in the fitting procedure. Second, the active diameter was found by fitting the theoretical data for s values greater than 1 thus including

Table 3.2: Active Diameters

Transducer Number	Active Diameter, a_1
1	.234
2	.237
3	.244

only the farfield data (Case 2). In this case, the attenuation was calculated in the fitting procedure. Finally, the active diameters were found by fitting the theoretical data for s values greater than 1, however, in this case, an assumed value of the attenuation was used in the fitting procedure (Case 3). From these three cases, three active diameters for three different ways of fitting the data were found which are denoted by a_i, where $i = 1, 2, 3$.

3.2.5.1 Case 1 The results were quite similar whether a text book value of .0265 $\frac{Np}{cm}$ was used for the attenuation or whether the attenuation was calculated during the fitting procedure. The resulting active diameters can be seen in Table 3.2 for the three transducers. The graphs of the axial profiles can be seen in Figures 3.2 through 3.4, and the ERMS, or accumulated error in percentage, can be seen for each transducer in Figures 3.5 through 3.7. As can be seen in these graphs, the fit between the experimental and theoretical data matches better for transducers 1 and 2 than for transducer 3. This leads to the assumption that transducer 3 does not follow the planar piston model as well as transducers 1 and 2, and in looking at the attenuation measurement results for aluminum, it can be noted that transducers 1 and 2 gave similar results while the results for transducer 3 were not as close.

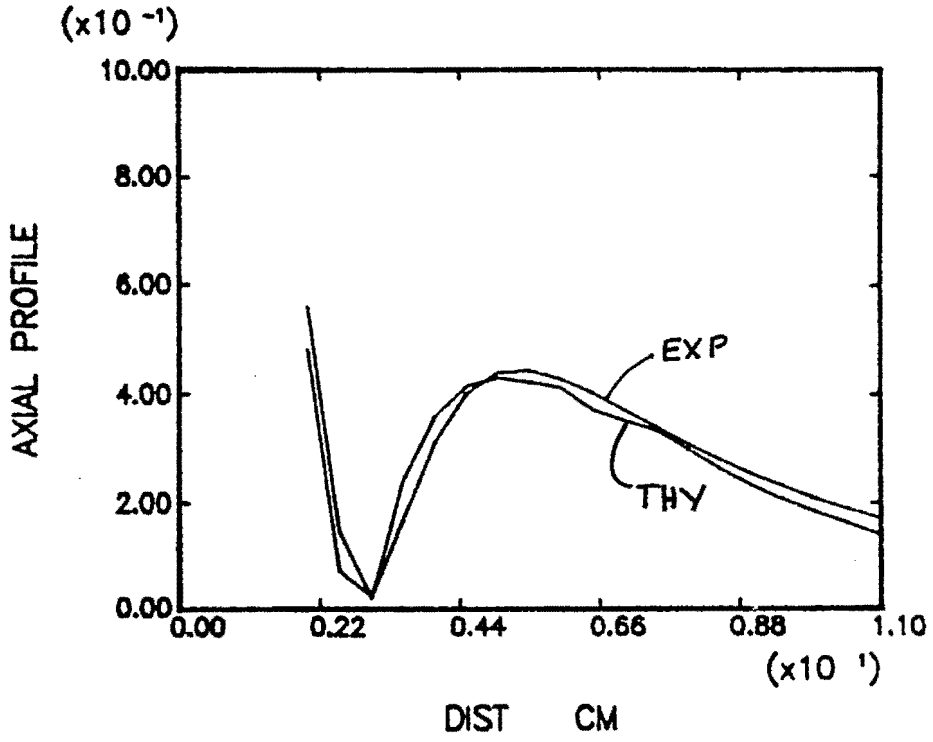

Figure 3.2: Axial Profile for Transducer 1 (Experimental and Theoretical)

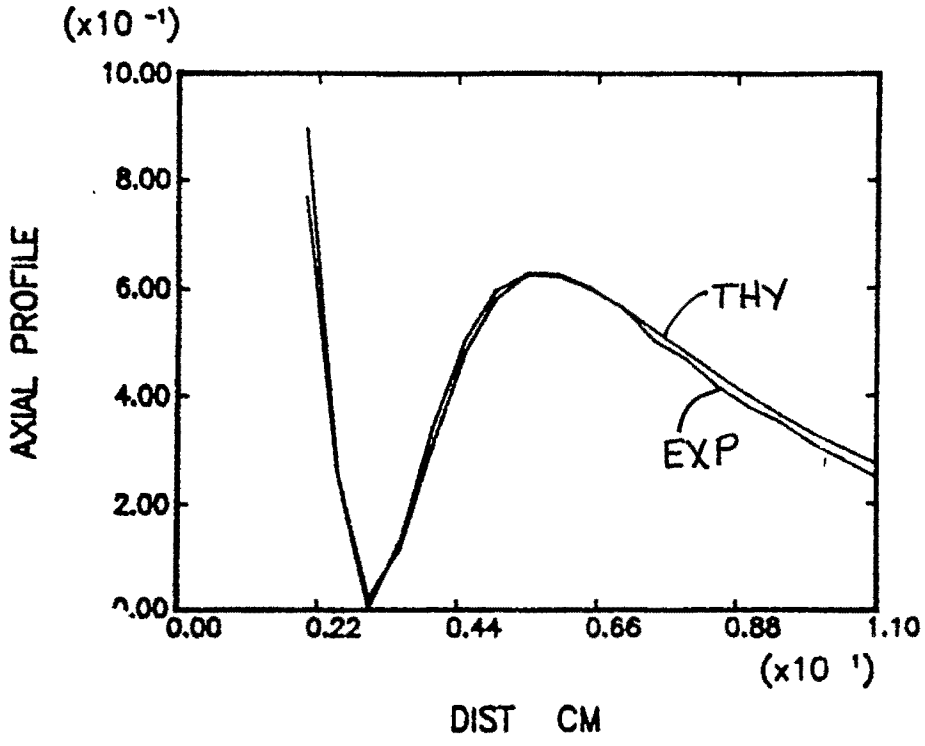

Figure 3.3: Axial Profile for Transducer 2 (Experimental and Theoretical)

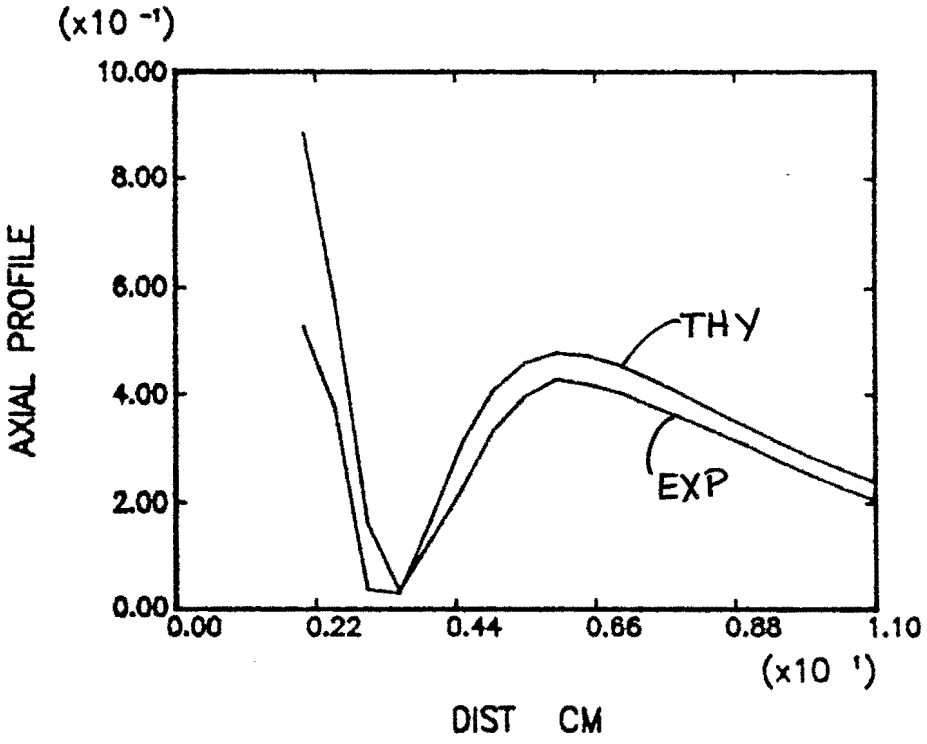

Figure 3.4: Axial Profile for Transducer 3 (Experimental and Theoretical)

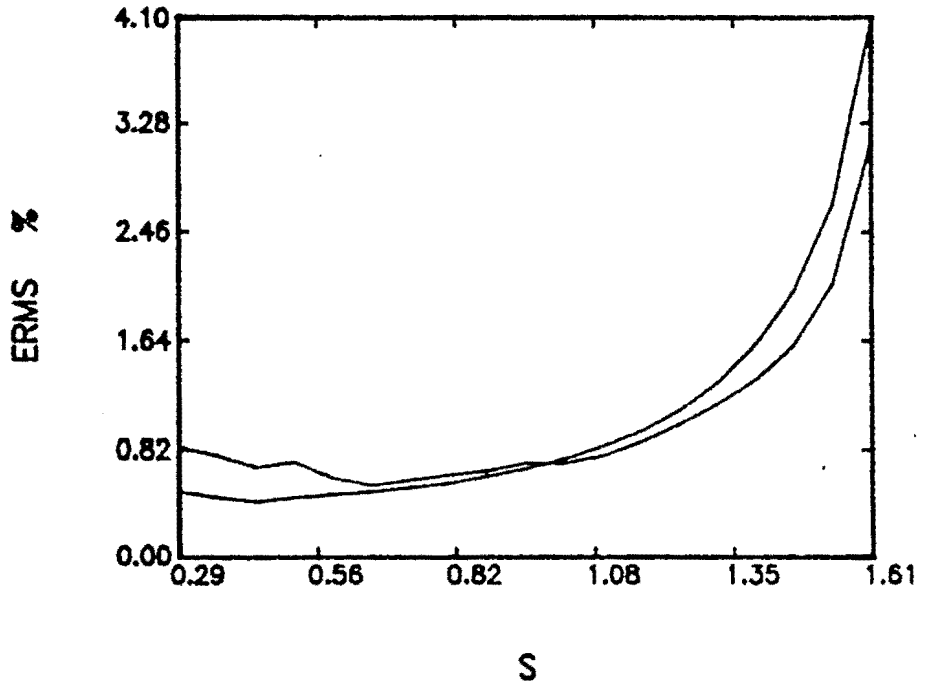

Figure 3.5: Accumulated Error Between Theoretical and Experimental Axial Profiles for Transducer 1

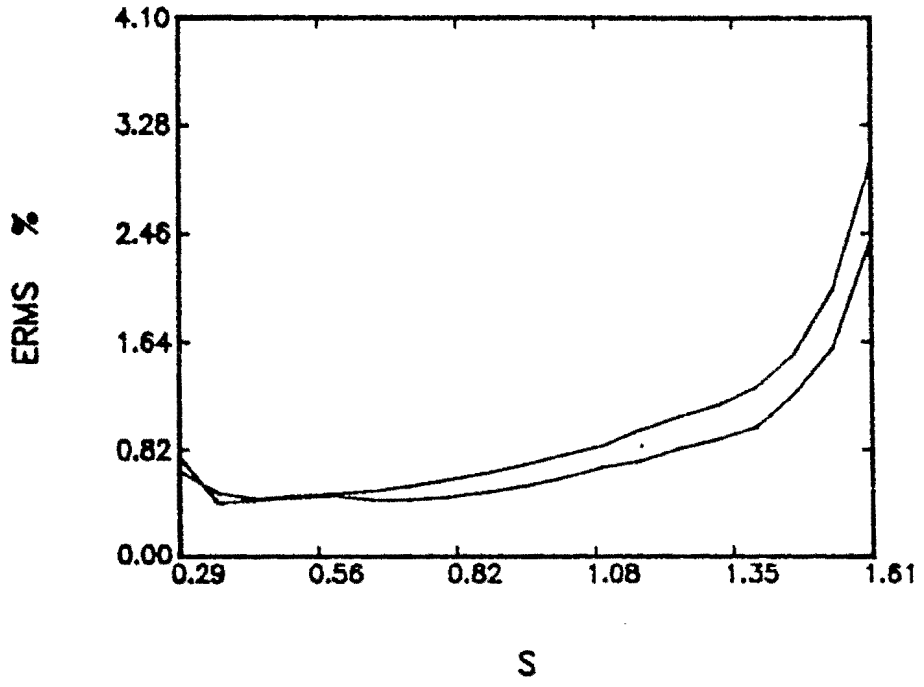

Figure 3.6: Accumulated Error Between Theoretical and Experimental Axial Profiles for Transducer 2

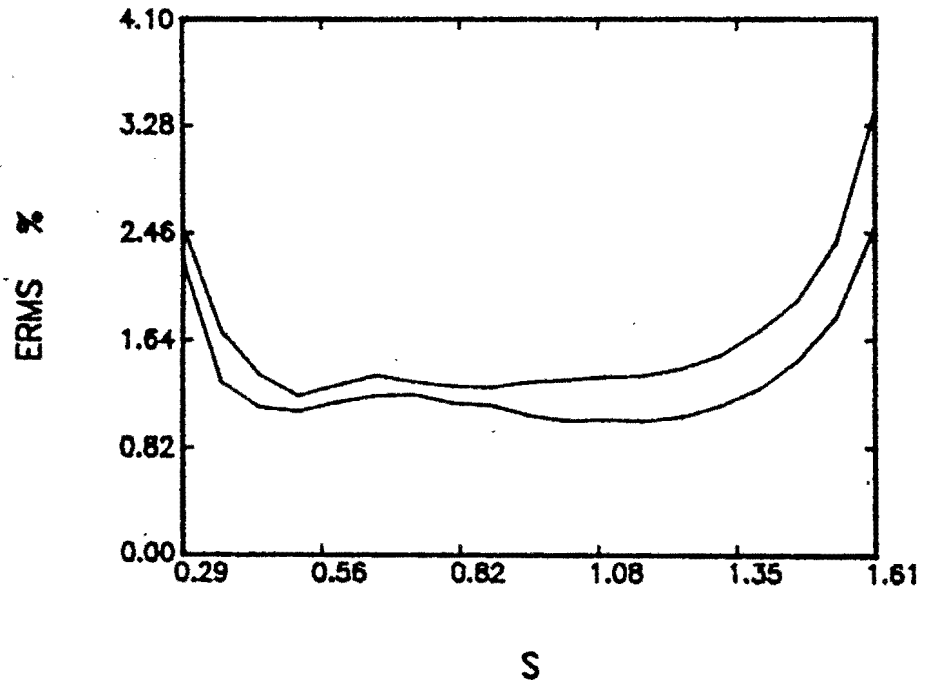

Figure 3.7: Accumulated Error Between Theoretical and Experimental Axial Profiles for Transducer 3

3.2.5.2 Case 2 Looking at the accumulated error for Case 1, it can be seen that the theoretical and experimental curves fit better in the nearfield. This is due to an evaluation of the data which has much more emphasis on the nearfield data than on the farfield data. Therefore, this section is devoted to seeing how the farfield emphasis effects the results.

The fitting procedure in Case 2 was designed such that the error over all data decreases as the s value increases, or in other words, the fit of theoretical to experimental data improves in the farfield. In this case, the fitting procedure calculated the water attenuation rather than assuming a known value. The results for fitting the data only over the farfield can be seen in Table 3.3. As can be seen from these results, fitting the data only over the farfield locations creates some difficulties especially for transducers 1 and 3. Both of these transducers obtain active diameters greater than the nominal diameters - a result which suggests error. Also, the calculated water attenuation, when this active diameter was used to evaluate the farfield and nearfield data, acquires values over 3.5 times the given textbook value, and the accumulated errors over the nearfields and farfields rise to extremely high values as compared to the previous case. Figures 3.8 through 3.10 show the the theoretical and experimental axial profiles for all three transducers. As can be seen by the graphs, the fits are not as good as in Case 1. This can also be seen by looking at the results of the accumulated errors in Figures 3.11 through 3.13.

3.2.5.3 Case 3 It can be observed that transducer 2 gives consistent results whether the data is fit over the nearfield and farfield (Case 1) or whether the data

Table 3.3: Results for Fitting Axial Data Over s>1 with a Calculated Attenuation Value being used for the Fit

Transducer Number	Active Diameter a_2	Calculated Attenuation (Np/cm)		Accumulated Error (%)	
		s>1	All s	s>1	All s
1	.269	.094414	.116854	.337202	36.279
1	.258	.079586	.101699	.325463	24.226
2	.238	.038407	.035561	.388188	1.883
2	.229	.030304	.029444	.437427	6.278
3	.256	.043579	.101270	.212050	17.665
3	.254	.042978	.128600	.190073	31.163

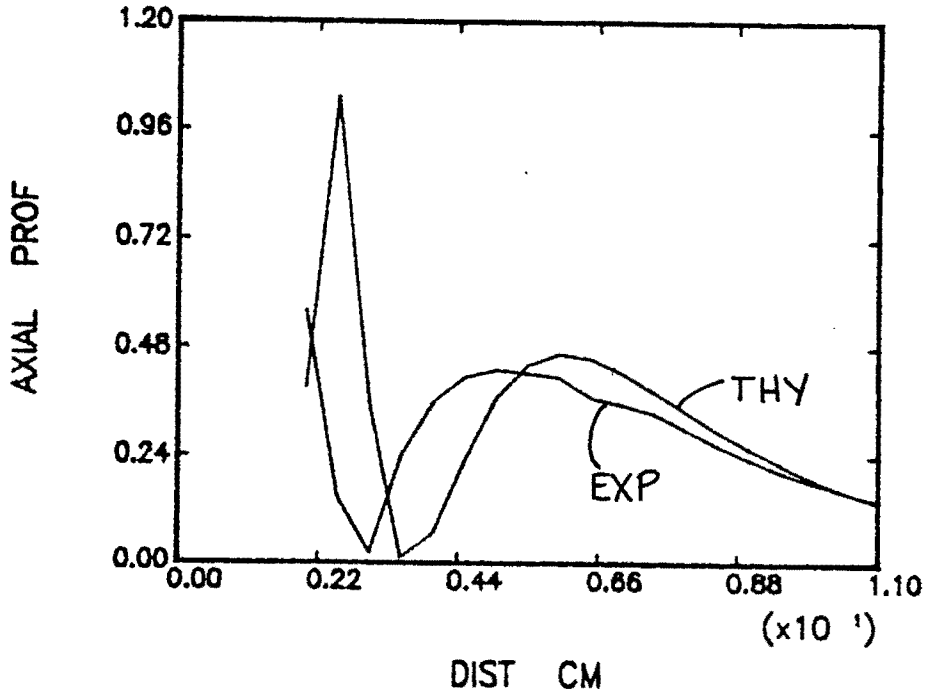

Figure 3.8: Axial Profile for Transducer 1 (Data Fit with Calculated Value of Water Attenuation for s > 1)

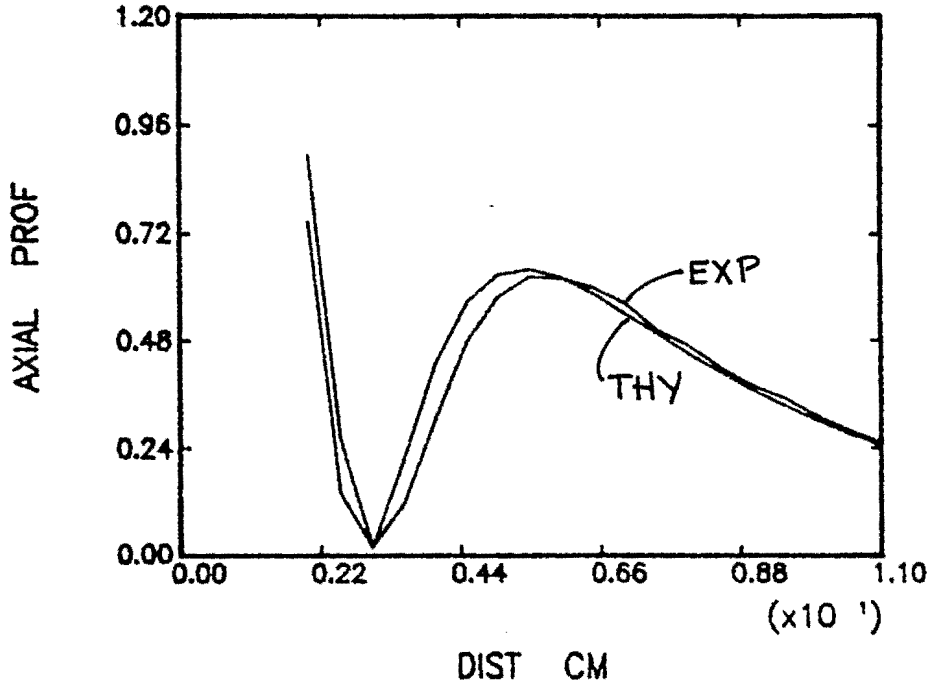

Figure 3.9: Axial Profile for Transducer 2 (Data Fit with Calculated Value of Water Attenuation for s > 1)

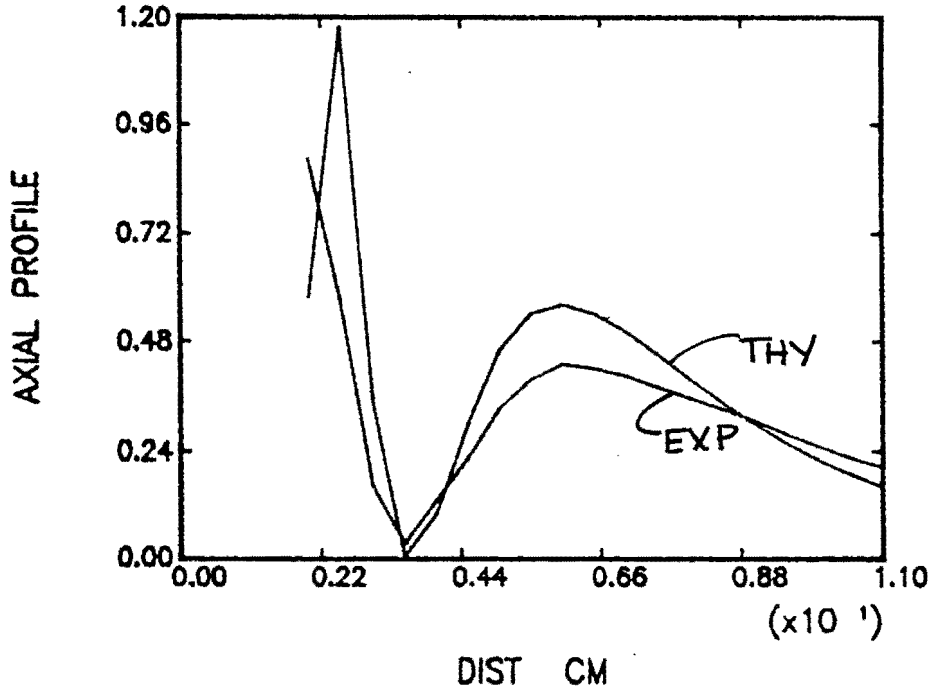

Figure 3.10: Axial Profile for Transducer 3 (Data Fit with Calculated Value of Water Attenuation for $s > 1$)

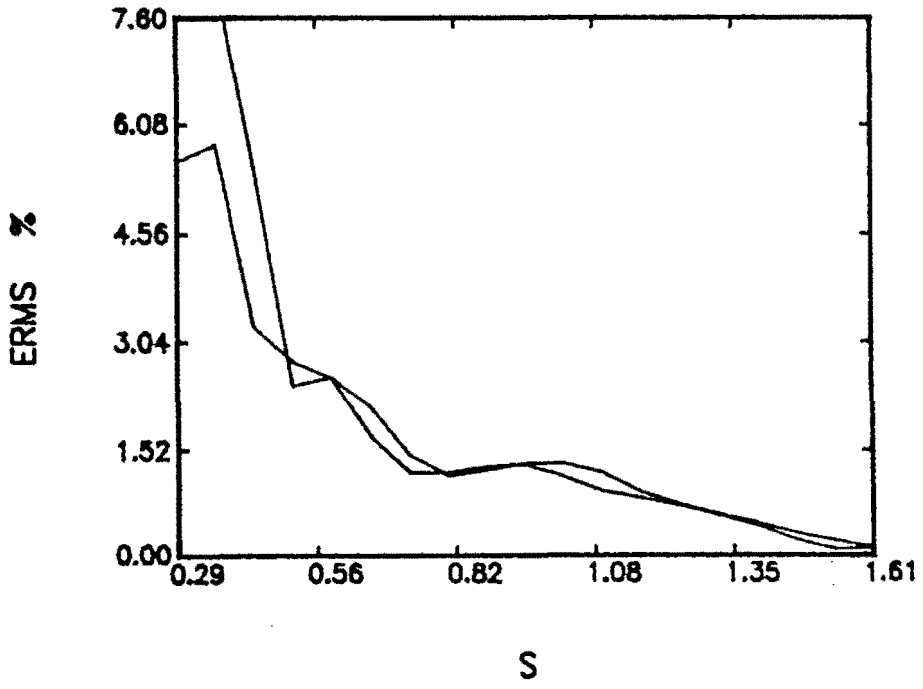

Figure 3.11: Accumulated Error Between Experimental and Theoretical Data Obtained with Transducer 1 (Data Fit with Calculated Value of Water Attenuation for $s > 1$)

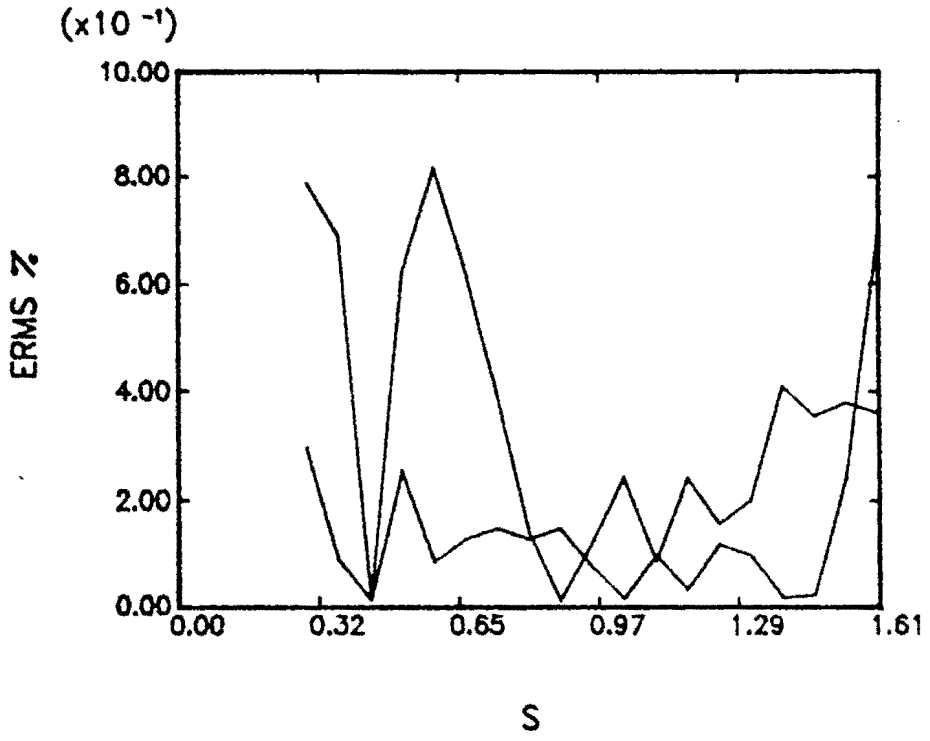

Figure 3.12: Accumulated Error Between Experimental and Theoretical Data Obtained with Transducer 2 (Data Fit with Calculated Value of Water Attenuation for s > 1)

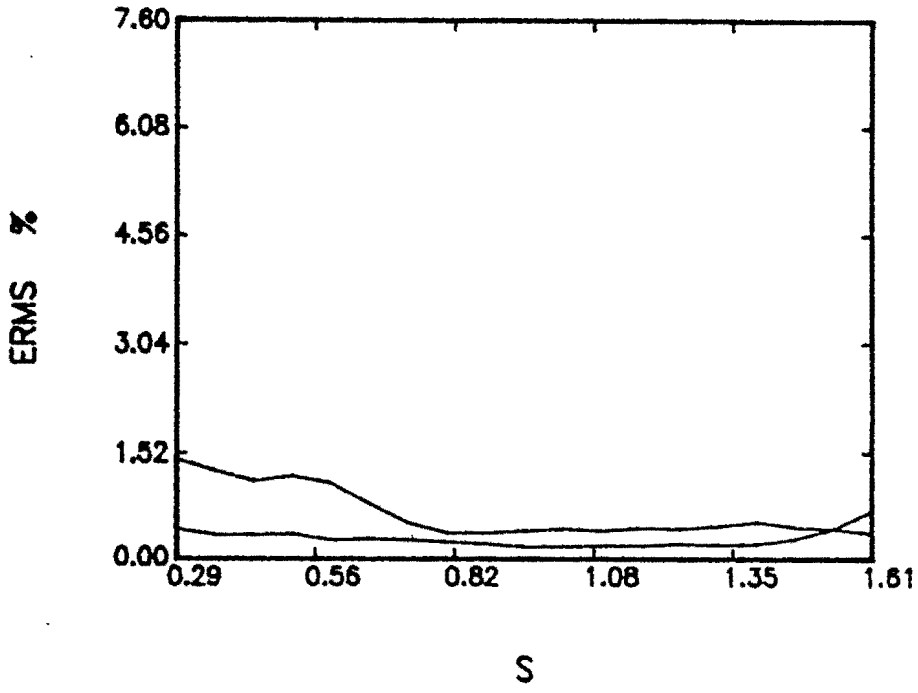

Figure 3.13: Accumulated Error Between Experimental and Theoretical Data Obtained with Transducer 3 (Data Fit with Calculated Value of Water Attenuation for $s > 1$)

Table 3.4: Results for Fitting Data Over s>1 with Attenuation equal to .038407 Np/cm

Transducer Number	Active Diameter, a_3	Accumulated Error (%)	
		s>1	All s
1	.227	.85539	4.3309
1	.222	.63015	4.1129
2	.238	.38818	1.2854
2	.237	.48916	2.2170
3	.252	.22767	11.7863
3	.251	.19815	11.9805

are just fit in the farfield (Case 2). In addition, the calculated water attenuation for this transducer stays very constant whether the data is run over all s values or only over s>1. Therefore, in Case 3, the attenuation value from the Case 2 results (.038407 Np/cm) was used in the fitting procedure and the data were fitted for s>1. These results can be seen in Table 3.4. Transducers 1 and 2 give reasonable results, but transducer 3 has slightly higher accumulated error, than transducers 1 and 2, and the calculated active diameters are larger than the nominal diameter by .8%. Table 3.5 shows the difference between the active diameters calculated in this case for s>1 and for all the data. The new active diameters calculated by this method are slightly smaller for transducers 1 and 2 and slightly larger for transducer 3.

The graphs of the axial profiles obtained for this case can be seen in Figures 3.14 through 3.16, and the accumulated error can be seen in Figures 3.17 through 3.19. As expected, in this case the accumulated error decreases as s increases showing the emphasis, in this fitting procedure, being placed more heavily on the farfield data in comparison to the nearfield data.

Table 3.5: Differences in Calculated Active Diameters for Case 1 and Case 3

Transducer Number	$\frac{a_1-a_3}{a_1} \times 100$
1	3.81%
1	2.20%
2	.85%
2	.85%
3	-3.28%
3	-4.15%

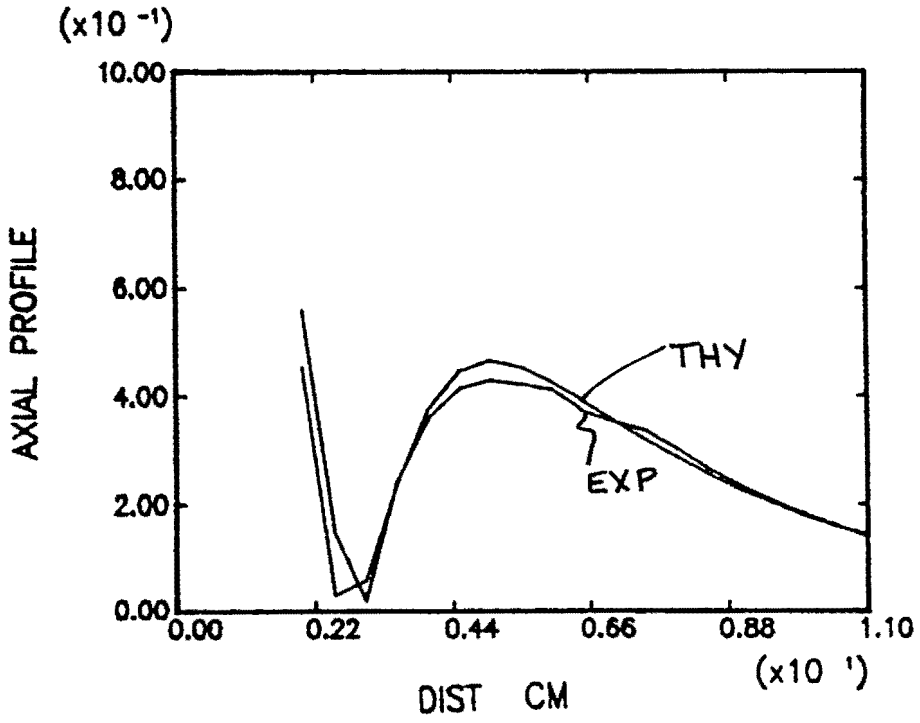

Figure 3.14: Axial Profile of Transducer 1 with Experimental and Theoretical Fit for s > 1 with Water Attenuation = .038407 Np/cm

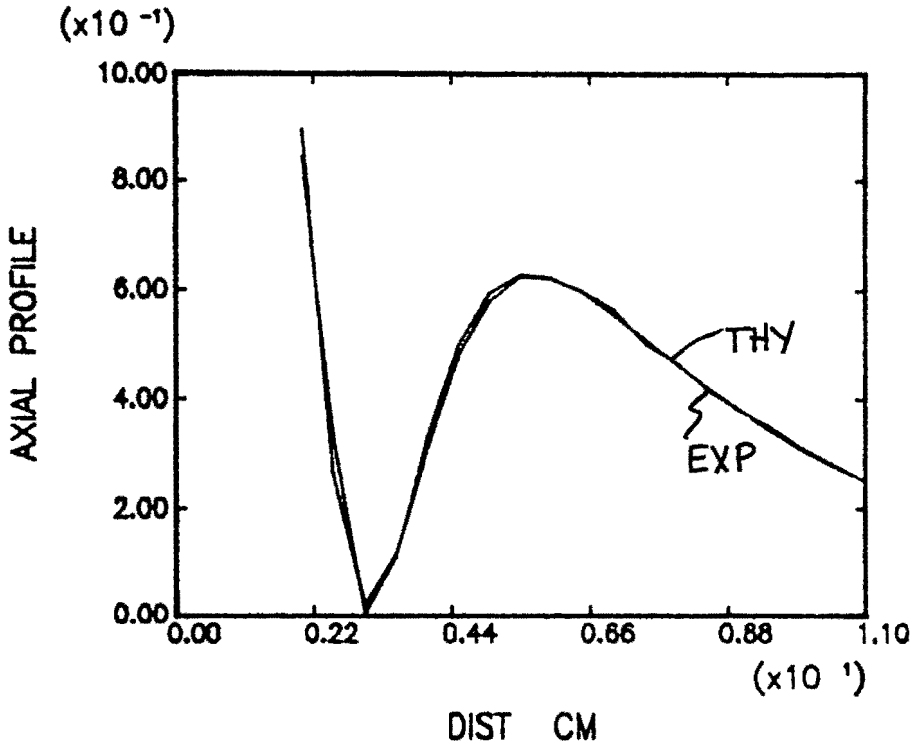

Figure 3.15: Axial Profile of Transducer 2 with Experimental and Theoretical Fit for s > 1 with Water Attenuation = .038407 Np/cm

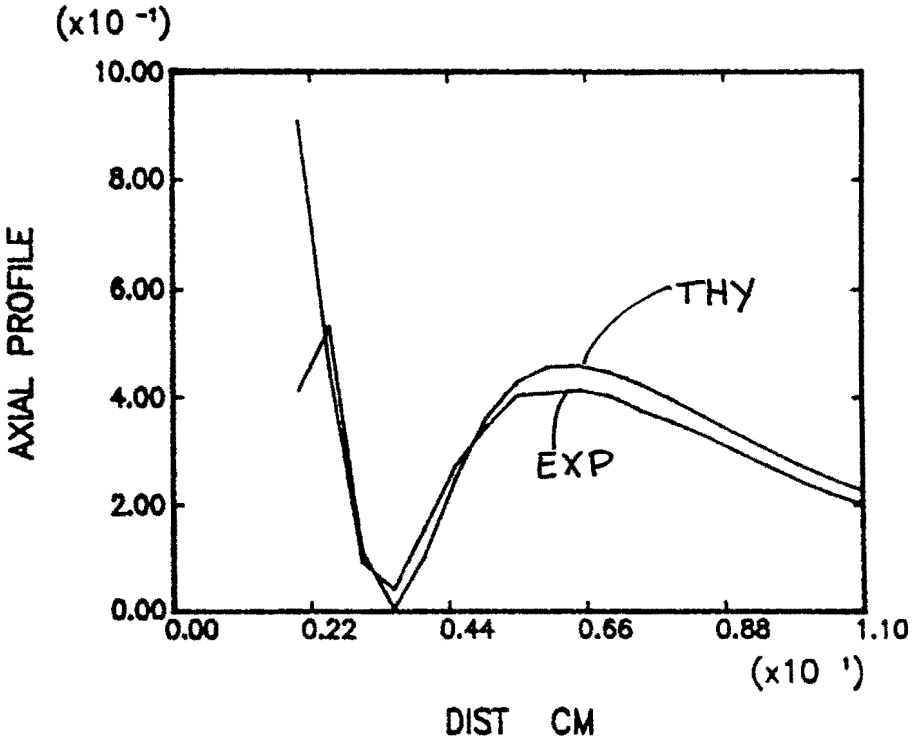

Figure 3.16: Axial Profile of Transducer 3 with Experimental and Theoretical Fit for s > 1 with Water Attenuation = .038407 Np/cm

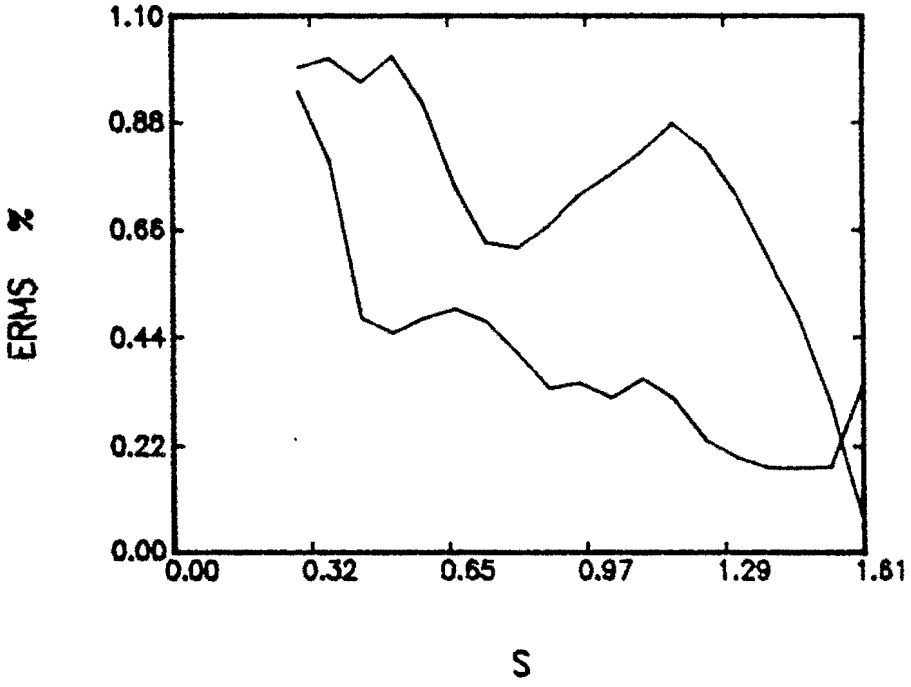

Figure 3.17: Accumulated Error in the Axial Profile of Transducer 1 when Fit for $s > 1$ with Water Attenuation = .038407 Np/cm

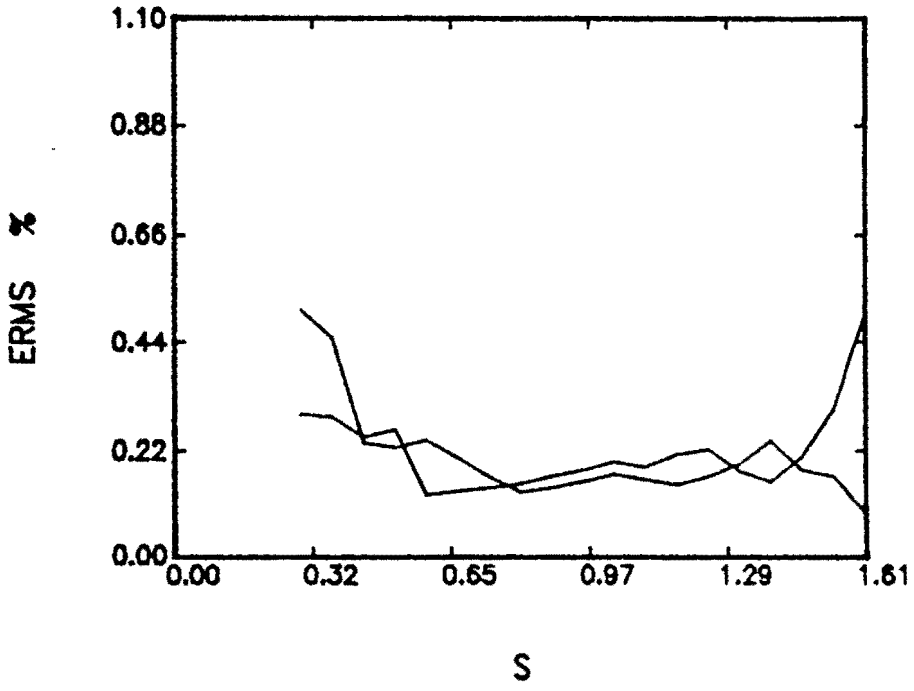

Figure 3.18: Accumulated Error in the Axial Profile of Transducer 2 when Fit for $s > 1$ with Water Attenuation = .038407 Np/cm

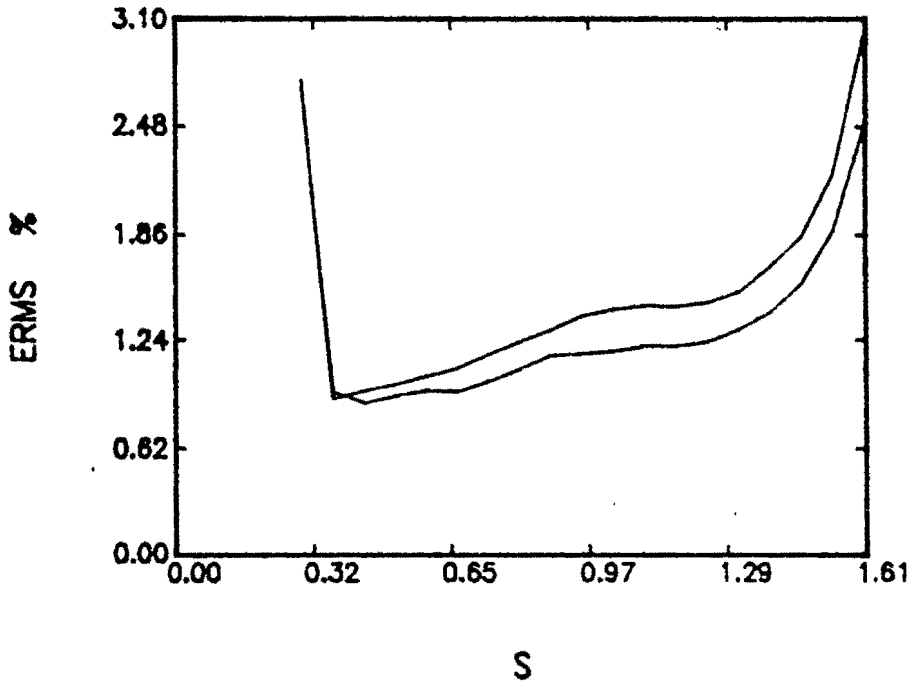

Figure 3.19: Accumulated Error in the Axial Profile of Transducer 3 when Fit for $s > 1$ with Water Attenuation = .038407 Np/cm

3.2.6 Conclusions

The axial profile can be used to characterize transducers as planar piston sources with the calculation of an active diameter. However, care must be taken when calculating these active diameters to 1) evaluate the effect of incorporating both the nearfield data and the farfield data in calculating the accumulated error necessary in finding the active diameter, and 2) to properly account for the attenuation of the ultrasonic wave in water during the calculations of the active diameters.

3.3 Radial Profiles

3.3.1 Theory

If the pressure amplitude is measured at a fixed distance, z, a c-scan of the transducer can be taken, enabling the radial profile of the transducer to be examined. The symmetry of the transducer can be evaluated by looking at the consistency of the pressure at a given radial distance. Also, the average radial pressure can be compared to the theoretical radial pressure which can be calculated by the Rayleigh integral performed over the surface of the transducer.

3.3.2 Radial Profile Measurements

In this measurement, the same method previously discussed for the axial profiles was used, and the impulse response at locations at a fixed distance, z, was measured using the setup shown in Figure 3.20.

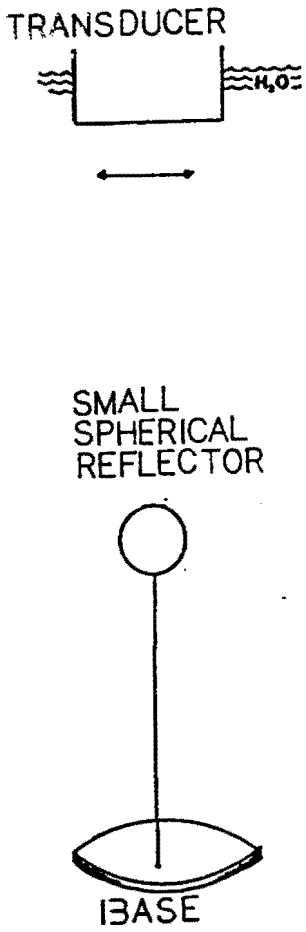

Figure 3.20: Set-up used for the Radial Profile Measurements

3.3.3 Experimental Apparatus

The experimental apparatus used in the radial profile measurements is the same as the equipment used in the axial profile measurements with the addition of an automated scanner. This scanner did cause some difficulty when attempting to find the maximum output signal (the center of the probe radiation), also the signal amplitude was noticeably decreased when the scanner was turned on for the measurement.

3.3.4 Procedure

An approximately .2 cm spherical reflector was used, and the data was taken for a frequency of 10 MHz. The measurements were taken at distances of 6 cm (s= .88) and 8 cm (s= 1.17). The scan was run in an .21 inch by .21 inch square grid of .015 inch intervals for the test run at 6 cm and a .27 by .27 inch square grid of .015 inch intervals for the test run at 8 cm. At the beginning of each scan, the transducer was normalized and centered above the spherical reflector by maximizing the output signal.

3.3.5 Results and Discussion

The results of the c-scans were examined for two features, 1) the symmetry of the profile, and 2) the agreement with the theoretical radial profile when s $<$ 1 and when s$>$ 1.

3.3.5.1 Symmetry The radial symmetry was calculated by

$$\mathrm{Dev}(r) = \frac{P(r_i, z_o)_{MAX} - P(r_i, z_o)_{MIN}}{P(r_i, z_o)_{AVG}} \tag{3.7}$$

where

$P(r_i, z_o)_{MAX}$ = maximum pressure magnitude at radius, r

$P(r_i, z_o)_{MIN}$ = minimum pressure magnitude at radius, r

$P(r_i, z_o)_{AVG}$ = average pressure magnitude at radius, r, which was calculated from

$$P(r_i, z_o) = \frac{1}{N} \sum_{j=1}^{N} P_j(r_i, z_o) \tag{3.8}$$

Figure 3.21 shows the points which would be used to calculate $P(r_i, z_o)_{MAX}$, $P(r_i, z_o)_{MIN}$, and $P(r_i, z_o)_{AVG}$ at $r = r_2$. The radial symmetry was calculated for $r = 1, 2, 3...N$, where N is the largest radial distance for which the pressure magnitude was measured. Figures 3.22 through 3.24 demonstrate the radial symmetry of the profiles which were measured in the nearfield. As can be seen by these figures, none of the three transducers have very good symmetry. In fact, the deviations were up to 1000 % at a radial distance equal to .80 of the radius of the probe. However, the high deviations at this distance could be due to noise contributions at the edge of the radiated field. The scans were much more symmetric near the center of the transducer with deviations less than 100 % for a radial distance equal to .20 of the radius of the probe. Figures 3.25 through 3.30 show the measured c-scans, which are also lacking symmetry, for the three 10 MHz transducers.

3.3.5.2 Nearfield Radial Profiles For z= 6 cm (s = .88), the radial profiles were compared with the theoretical profiles. The theoretical profiles were normalized to the radial profiles by minimizing the accumulated error between the theoretical and experimental profiles. When this was done, for all transducers, it was found that near the center of the transducer, there was more consistency with

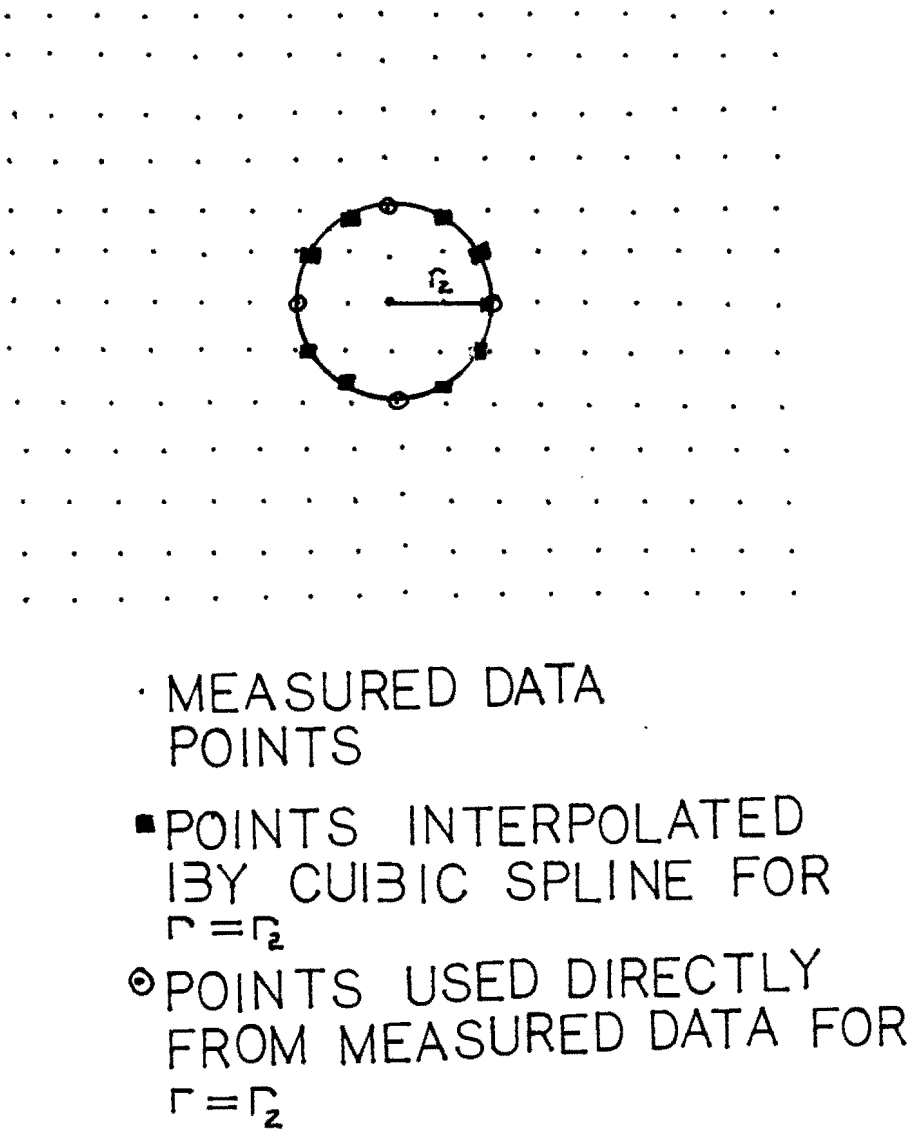

Figure 3.21: Points used to Calculate the Radial Symmetry for $r = r_2$

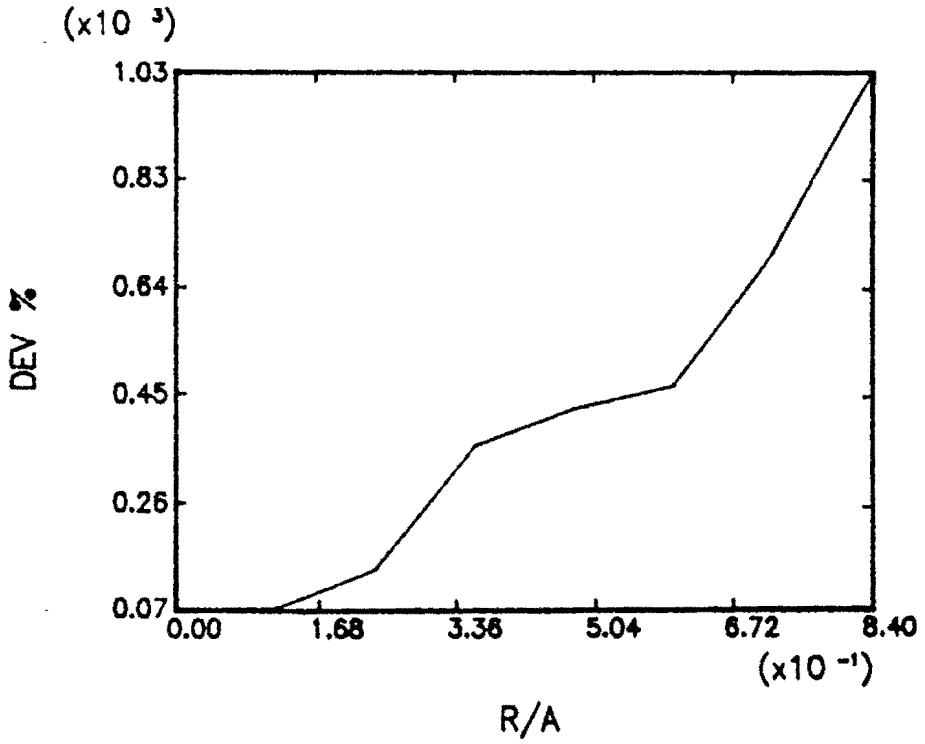

Figure 3.22: Radial Symmetry of the Transverse Pressure Profile Measured for Transducer 1 at 6 cm or s = .88

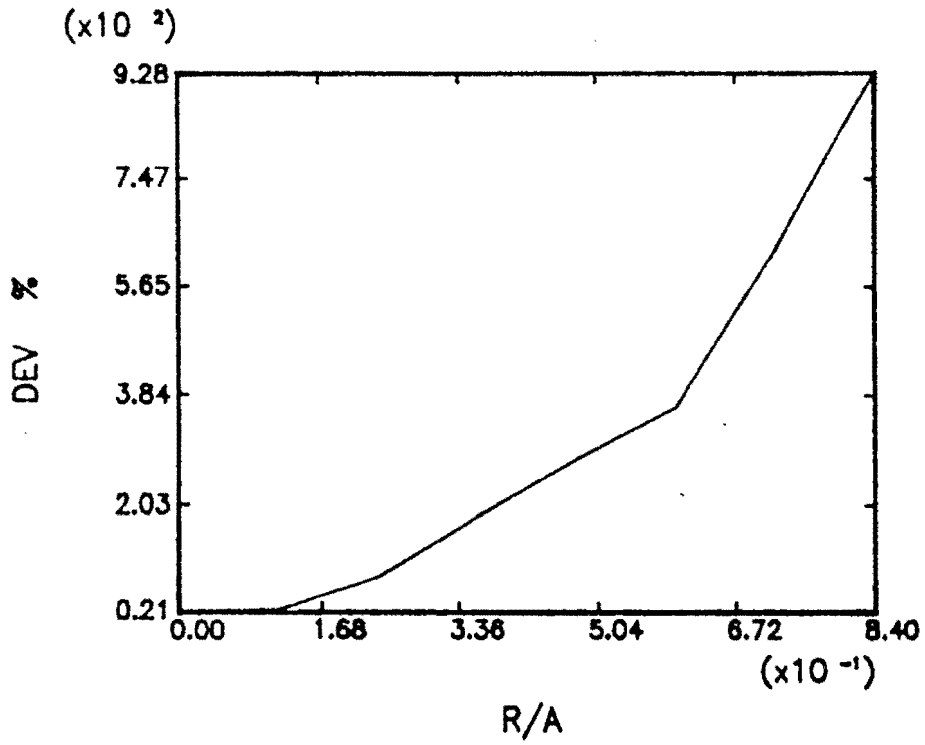

Figure 3.23: Radial Symmetry of the Transverse Pressure Profile Measured for Transducer 2 at 6 cm or s = .88

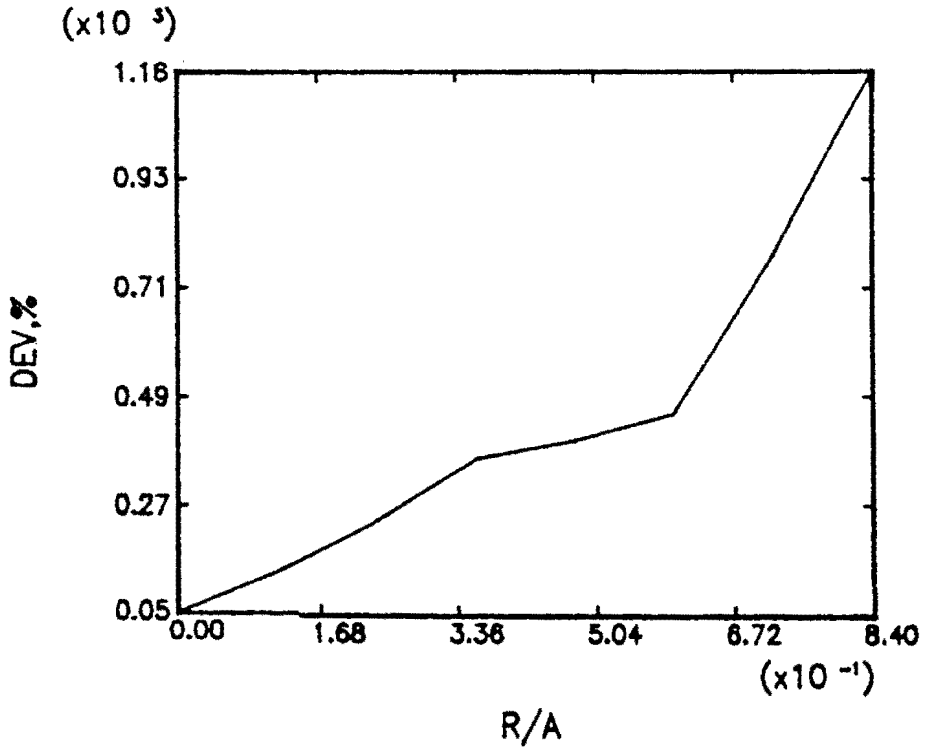

Figure 3.24: Radial Symmetry of the Transverse Pressure Profile Measured for Transducer 3 at 6 cm or s = .88

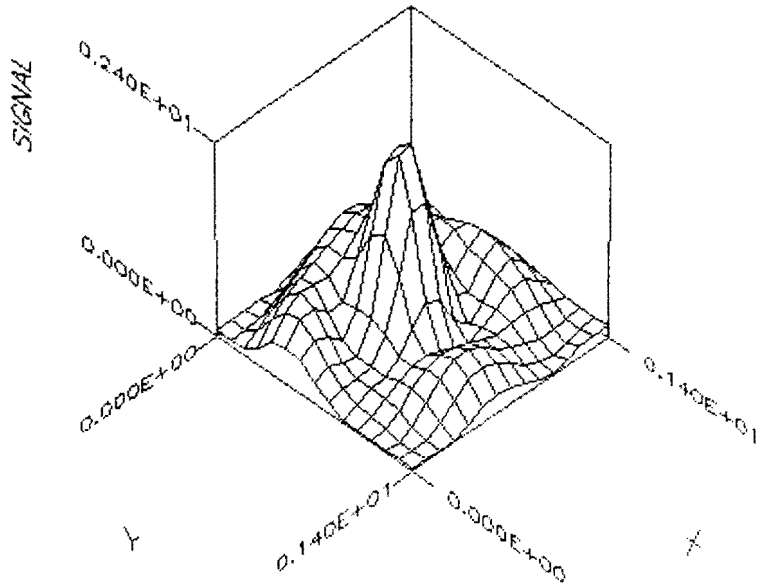

Figure 3.25: Radial Pressure Profile of Transducer 1 at 6 cm (s = .88)

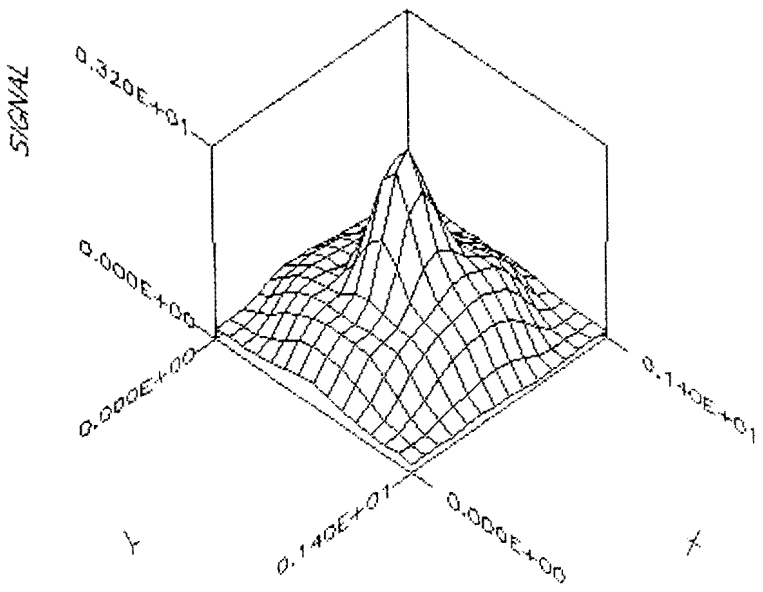

Figure 3.26: Radial Pressure Profile of Transducer 2 at 6 cm (s = .88)

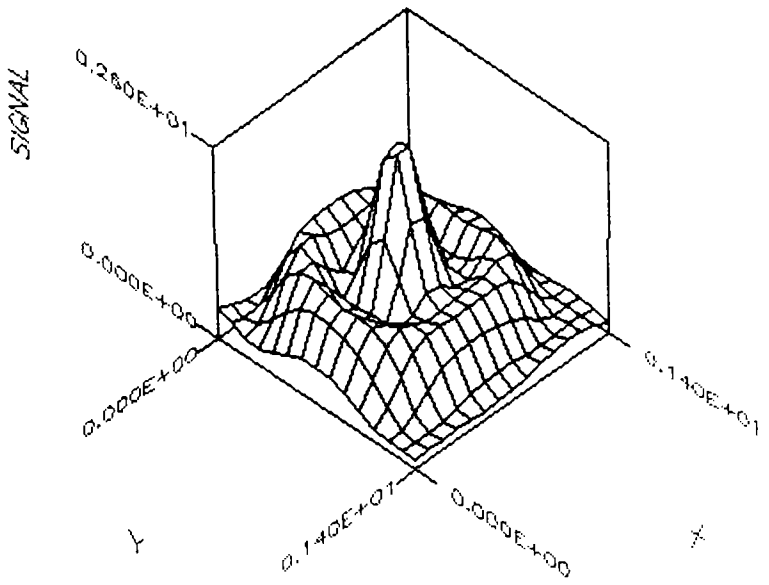

Figure 3.27: Radial Pressure Profile of Transducer 3 at 6 cm (s = .88)

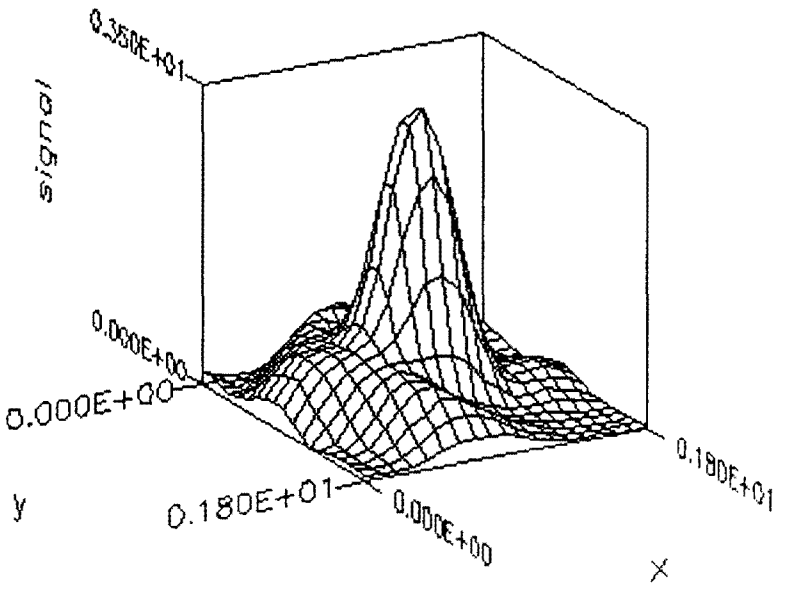

Figure 3.28: Radial Pressure Profile of Transducer 1 at 8 cm (s = 1.17)

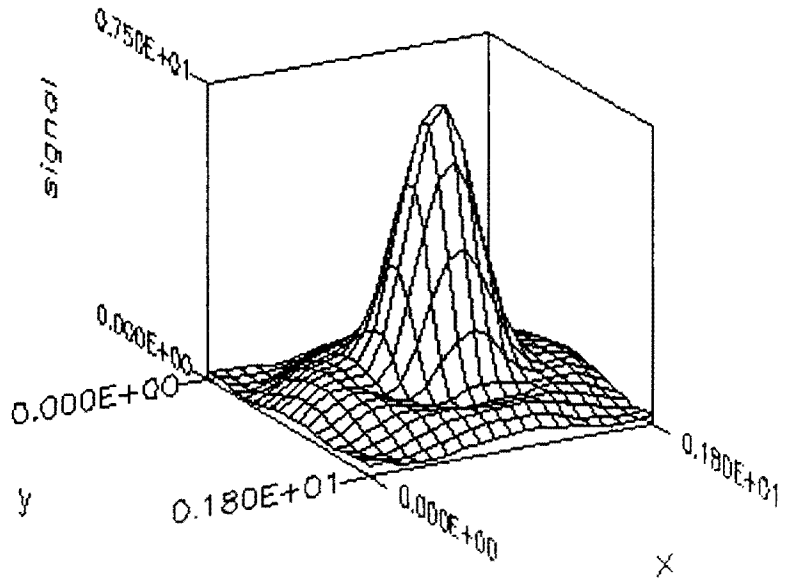

Figure 3.29: Radial Pressure Profile of Transducer 2 at 8 cm (s = 1.17)

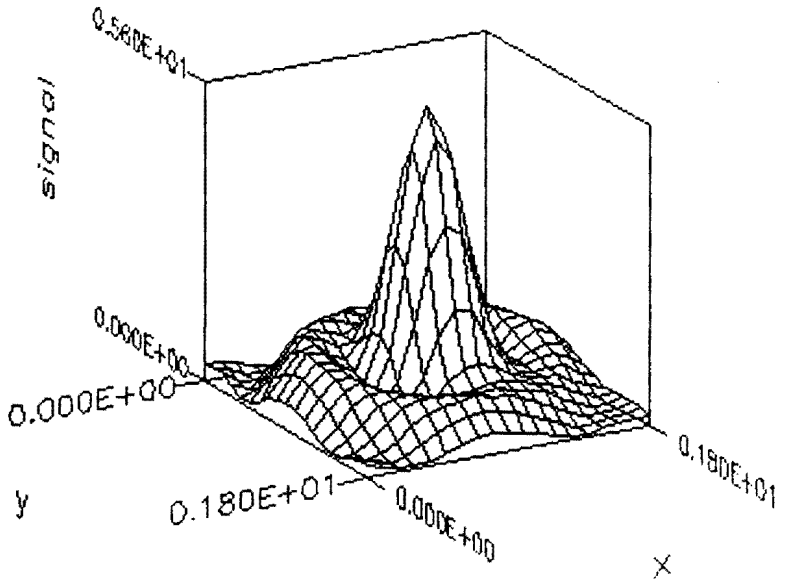

Figure 3.30: Radial Pressure Profile of Transducer 3 at 8 cm (s = 1.17)

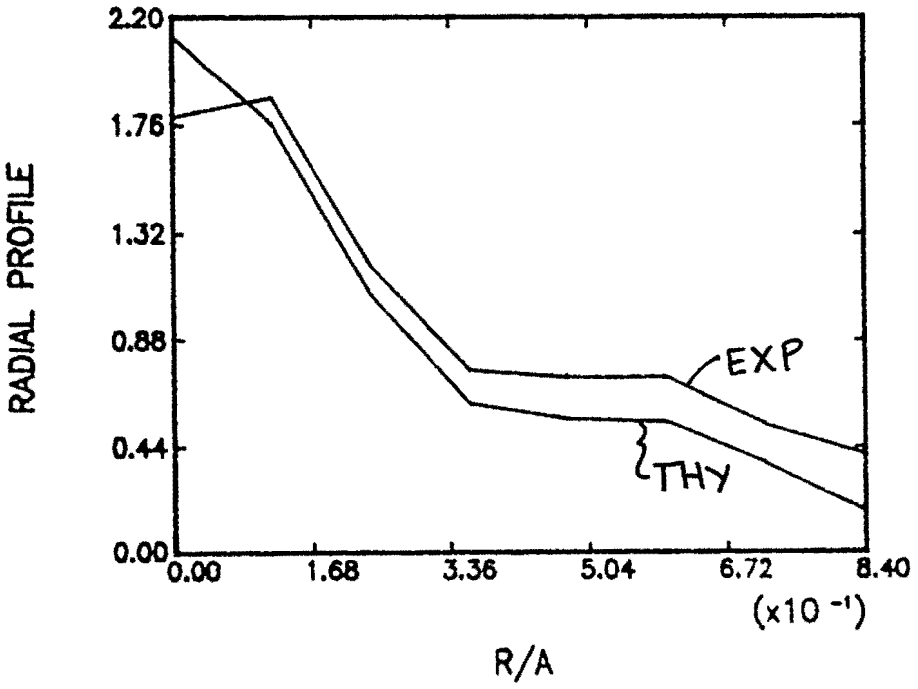

Figure 3.31: Radial Profile of Transducer 1 for s = .88; Theoretical and Experimental Data using Nominal Diameter

the theoretical profiles. Again, as in the axial profile case, transducer 3 had the greatest deviations from the theoretical profiles. These results are shown in Figures 3.31 through 3.33. Use of the active diameter in evaluation of the theoretical profile did not change results significantly. Figures 3.34 through 3.36 show this result.

3.3.5.3 Farfield Radial Profiles For z= 8 cm (s= 1.17), the theoretical profiles were again normalized to the experimental profiles by minimizing the accumulated error between the two. Again, in this case, for all transducers, there was more consistency with theory near the center of the transducer, and transducer 3

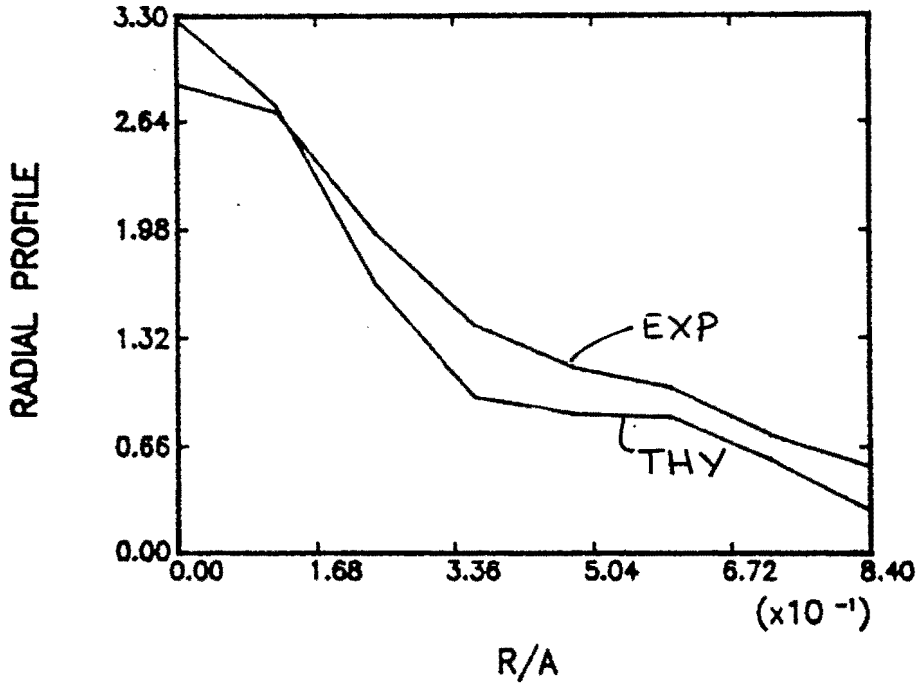

Figure 3.32: Radial Profile of Transducer 2 for s = .88; Theoretical and Experimental Data using Nominal Diameter

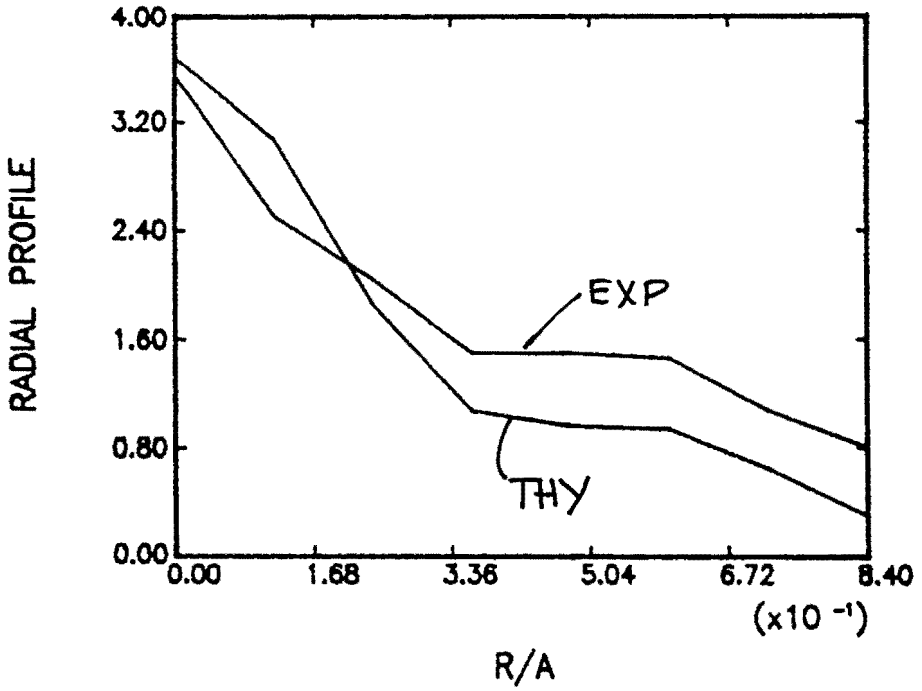

Figure 3.33: Radial Profile of Transducer 3 for s = .88; Theoretical and Experimental Data using Nominal Diameter

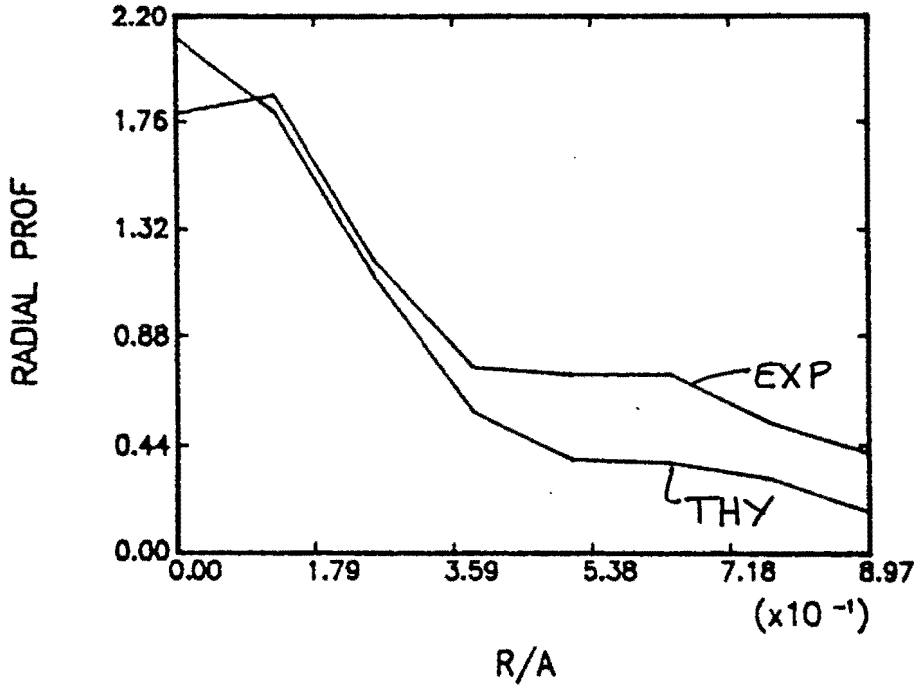

Figure 3.34: Radial Profile of Transducer 1 for s = .88; Theoretical and Experimental Data using Active Diameter

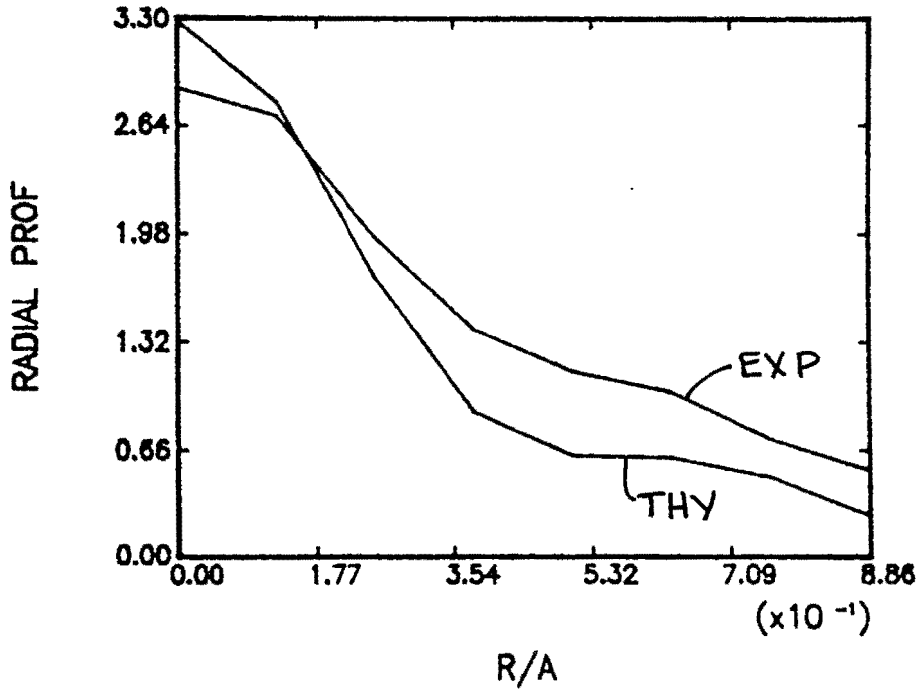

Figure 3.35: Radial Profile of Transducer 2 for s = .88; Theoretical and Experimental Data using Active Diameter

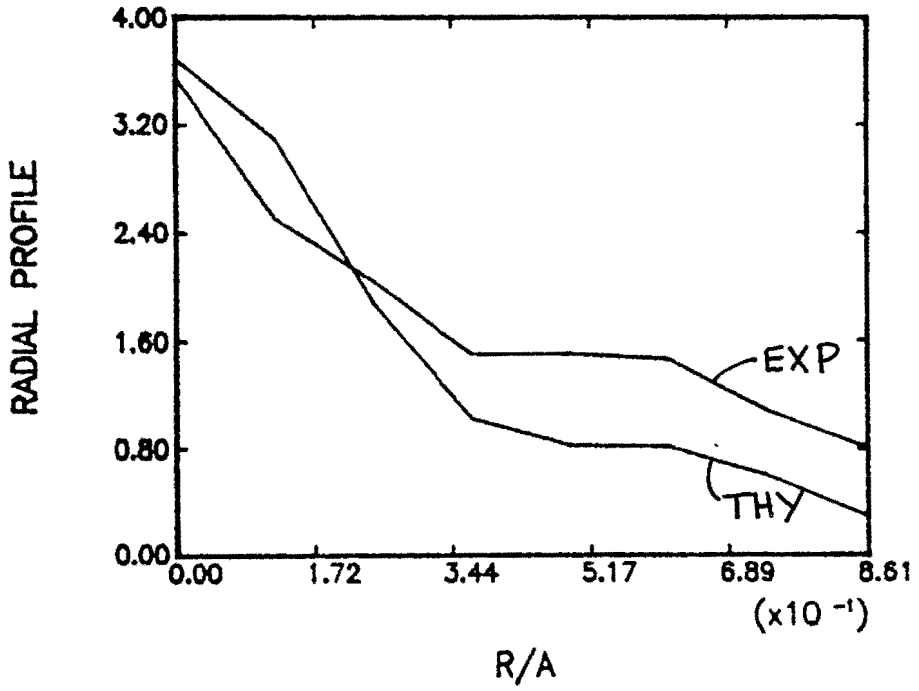

Figure 3.36: Radial Profile of Transducer 3 for s = .88; Theoretical and Experimental Data using Active Diameter

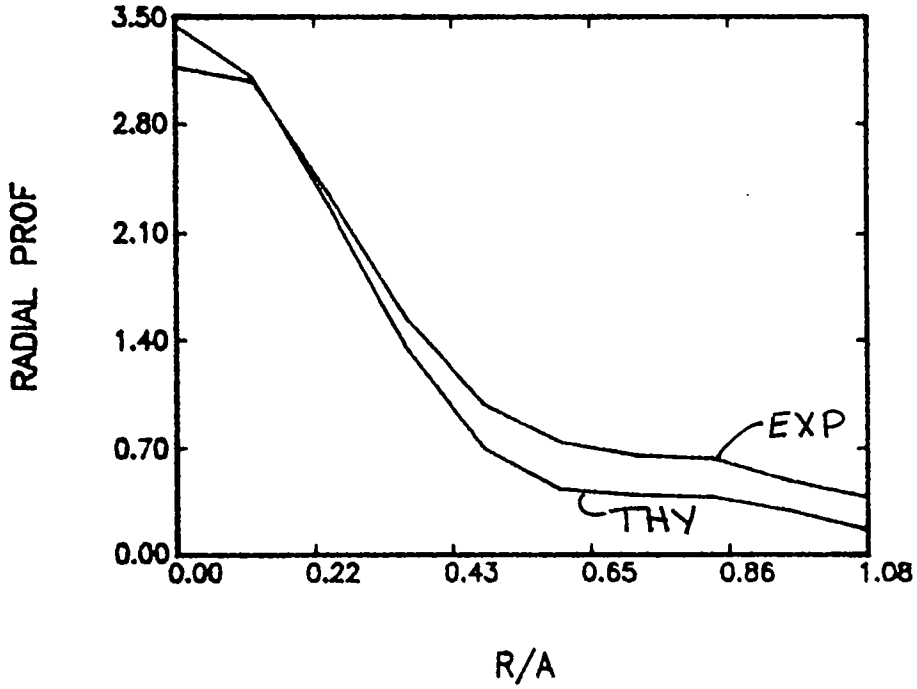

Figure 3.37: Radial Profile of Transducer 1 for s = 1.17; Theoretical and Experimental Data using Nominal Diameter

had the greatest deviations from theory. These results are graphed in Figures 3.37 through 3.39. Use of the active diameter had little significance. The results for active diameters can be seen in Figures 3.40 through 3.42.

3.3.6 Conclusions

The radial profile was used to analyze and compare the transducers for symmetry and agreement with planar piston theory. It was found that a) in general, the transducer profiles are not highly symmetric although symmetry is higher near the center of the transducer, b) the averaged radial profiles were very consistent

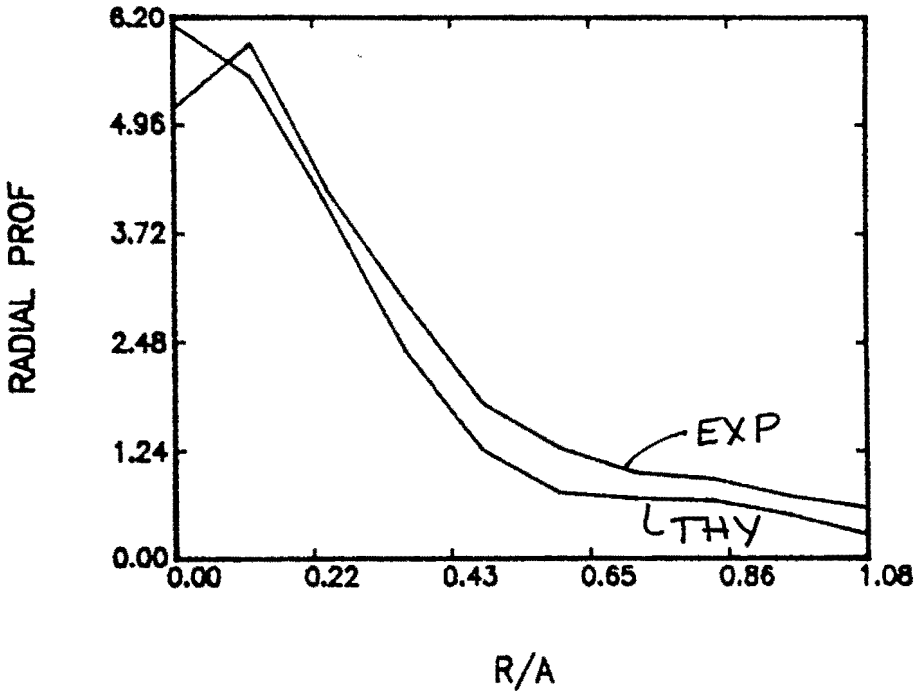

Figure 3.38: Radial Profile of Transducer 2 for s = 1.17; Theoretical and Experimental Data using Nominal Diameter

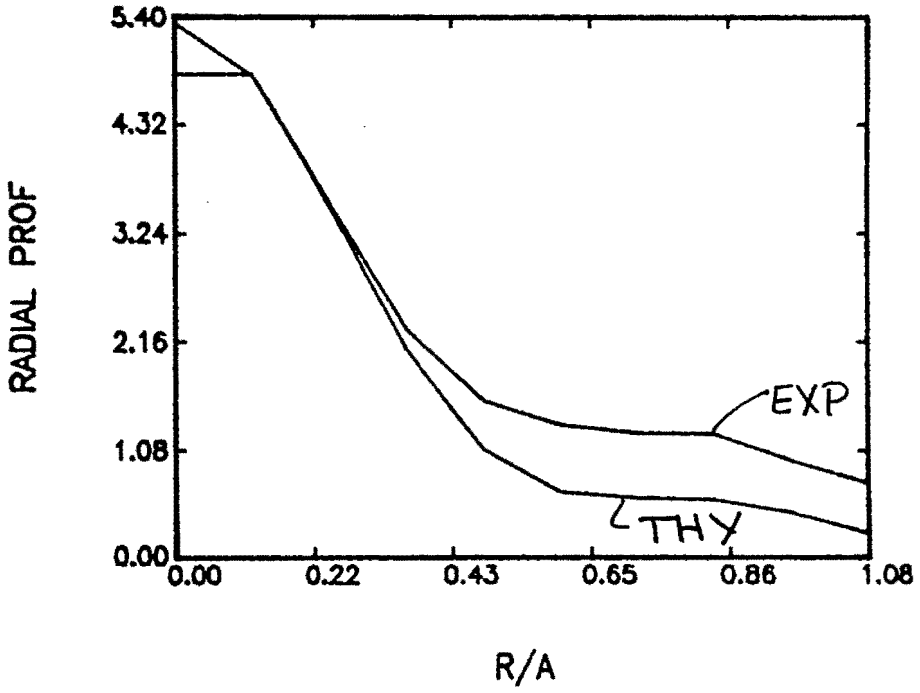

Figure 3.39: Radial Profile of Transducer 3 for s = 1.17; Theoretical and Experimental Data using Nominal Diameter

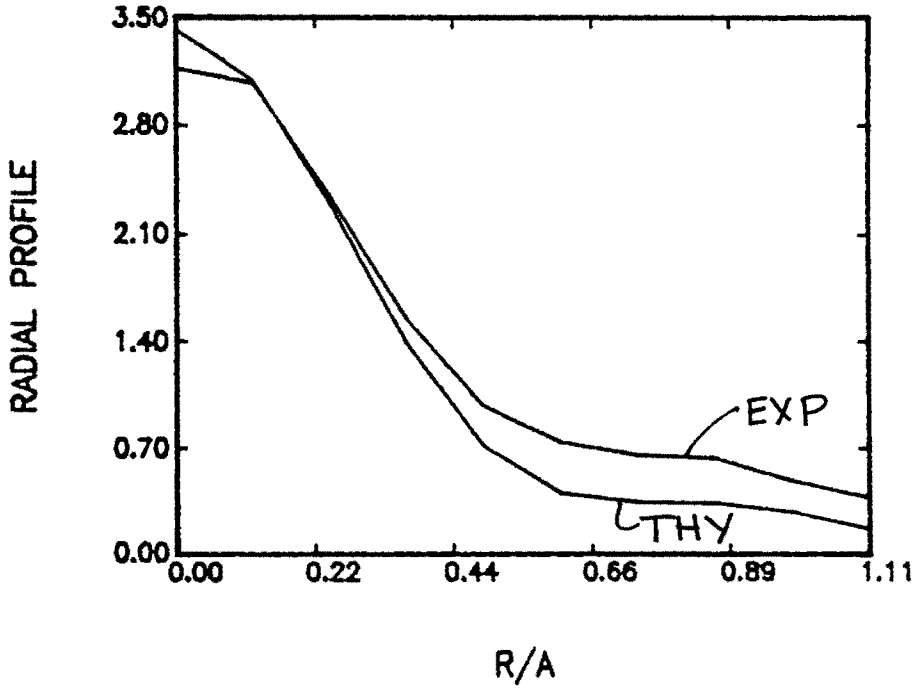

Figure 3.40: Radial Profile of Transducer 1 for s = 1.17; Theoretical and Experimental Data using Active Diameter

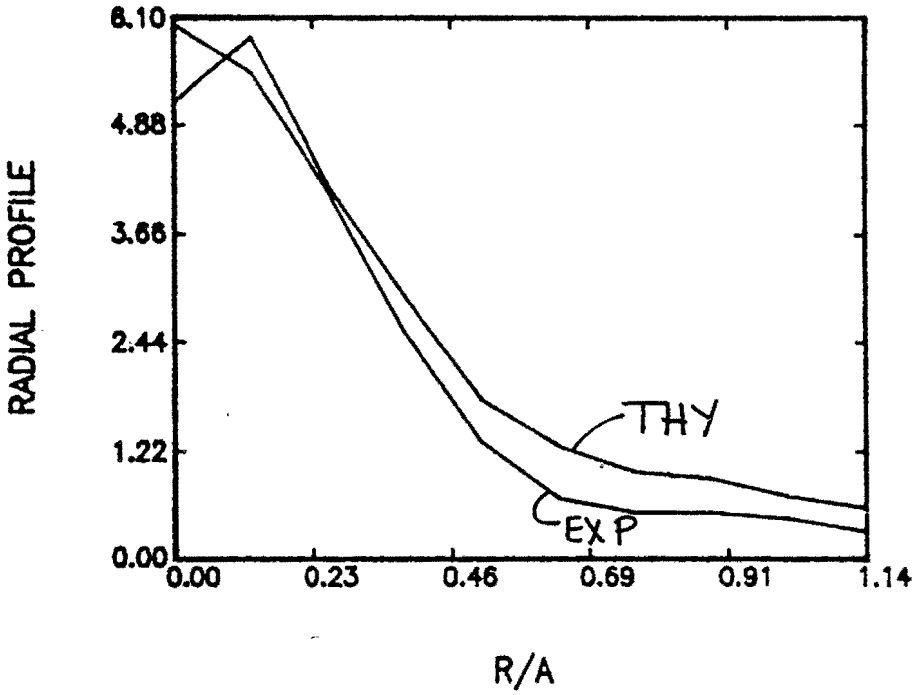

Figure 3.41: Radial Profile of Transducer 2 for s = 1.17; Theoretical and Experimental Data using Active Diameter

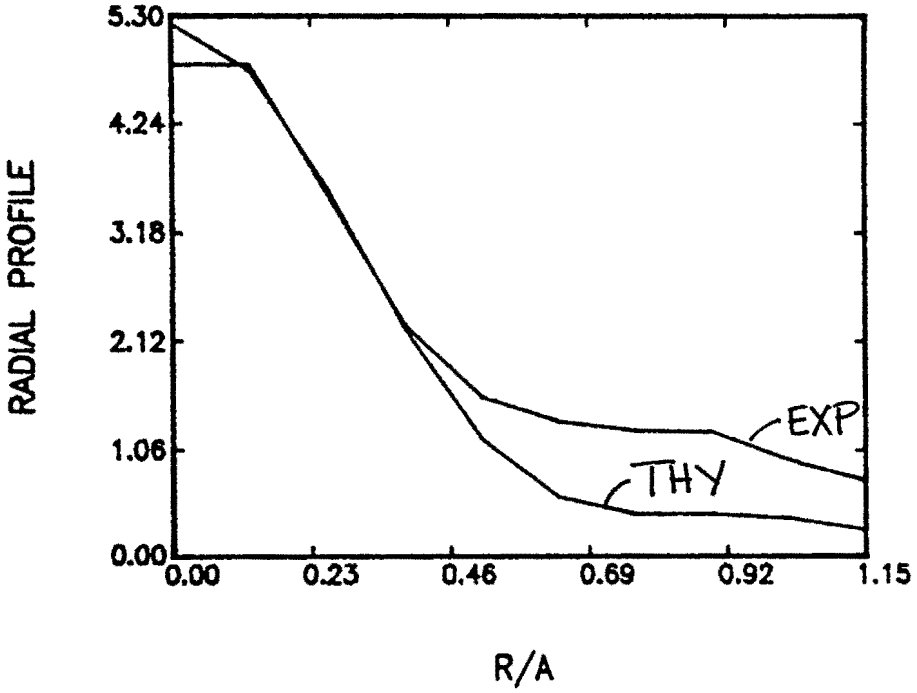

Figure 3.42: Radial Profile of Transducer 3 for s = 1.17; Theoretical and Experimental Data using Active Diameter

with the theory near the center of the transducer, c) both axial and radial profiles of transducers 1 and 2 are more similar to the rigid piston theoretical predictions than transducer 3, and d) use of the active diameter does not greatly influence the radial profiles.

3.4 Summary

The axial and radial profiles of a transducer can be used to analyze and compare transducer radiation patterns for their agreement with theory and for their over all symmetry. It was found, with the three 10 MHz transducers being used for the attenuation tests, that all involved transducer's behavior differed somewhat from theory, although transducers 1 and 2 followed theory more closely for both the axial profile and the radial profile results. In examining the symmetry of the transducers, it was found that the greatest symmetry occurred near the center of the transducer, with the outer edges of the radiation pattern being far from symmetric. The results of the transducer examination verify the results obtained for the attenuation measurements in that transducers 1 and 2 gave more similar results, and the results for transducer 3 were much different.

4 EFFECT OF TRANSDUCER CHARACTERIZATION ON ATTENUATION MEASUREMENTS

4.1 Introduction

The results of the previous chapter on transducer characterization can now be used to attempt to decrease the transducer dependence of the attenuation measurements which were presented in Chapter 2. The radial profile results can not be utilized at this time due to insufficient knowledge of how to use the information which was obtained, however the axial profile results (the active diameters) can be used directly in the calculation of the diffraction corrections, and therefore the attenuation measurements.

4.2 Effect of Errors in Diameter Estimation on Attenuation Measurements

The effect of error in the value for the probe's diameter on the results of the attenuation measurement was investigated for the three different methods. For a specific method, z_0 is the water path distance (constant) plus the distance to the first echo, and z is the water path distance (constant) plus the distance to the second or third echos necessary for the specific attenuation method in question. The received signal, $|V(z,f)|$, can be related to the system efficiency, reflection

coefficients, and transmission coefficients, $\beta(f)$, the diffraction corrections, $D(z,f)$, and the attenuation of the specimen, $\alpha(f)$, by [14]:

$$|V(z,f)| = |\beta(f)||D(z,f)|e^{-\alpha(f)z} \tag{4.1}$$

When a reference voltage is measured using the distance, z_o, one obtains,

$$|V(z_o,f)| = |\beta(f)||D(z_o,f)|e^{-\alpha(f)z_o} \tag{4.2}$$

The following ratios can then be written

$$e^{\alpha(f)(z-z_o)} = \frac{|D(z,f)|}{|D(z_o,f)|}\frac{|V(z_o,f)|}{|V(z,f)|} \tag{4.3}$$

and

$$\frac{V(z_o)|}{|V(z)|} = e^{\alpha(f)(z-z_o)}\frac{D(z_o,f)|}{D(z,f)|} \tag{4.4}$$

Using the incorrect value of the probe diameter, one obtains

$$e^{\alpha'(f)(z-z_o)} = \frac{|D'(z,f)|}{|D'(z_o,f)|}\frac{|V(z_o,f)|}{|V(z,f)|} \tag{4.5}$$

where the primed quantities refer to the quantities calculated with the incorrect value of the active diameters, and the corresponding unprimed quantities refer to the same quantities calculated with the correct probe diameters. Upon substitution of Equation 4.4 into Equation 4.5,

$$e^{\alpha'(f)(z-z_o)} = \frac{|D'(z,f)|}{|D'(z_o,f)|}\frac{|D(z_o,f)|}{|D(z,f)|}e^{\alpha(f)(z-z_o)} \tag{4.6}$$

and

$$\alpha'(f)(z-z_o) = \ln\frac{|D'(z,f)|}{|D'(z_o,f)|}\frac{|D(z_o,f)|}{|D(z,f)|} + \alpha(f)(z-z_o) \tag{4.7}$$

Therefore, the error in attenuation due to the error in transducer diameter is,

$$\Delta\alpha(f) = \alpha'(f) - \alpha(f) = \frac{1}{z - z_o} \ln \frac{|D'(z,f)|}{|D'(z_o,f)|} \frac{|D(z_o,f)|}{|D(z,f)|} \tag{4.8}$$

From Equation 4.8, it can be seen that the dependency of the experimental estimate of the attenuation constant on the probe diameter can be discussed in terms of the distance, $z - z_o$. The distance , $z - z_o$, is defined as the distance of travel between the first and second echo or the first and third echo. From Equation 4.8, it is evident that error in attenuation caused by errors in diameter estimation depends on: the distance, $z - z_o$, the diffraction correction at the true diameter and distance z_o and z, and the diffraction correction at the estimated diameter and distance z_o and z. From Figures 4.1 through 4.6, among all three attenuation measurement methods, the largest error in the diffraction correction occurs in the MT method for a given value of the error in the estimation of the probe's diameter. From this follows the largest error in measured attenuation. The second largest error occurs in the multiple echo II method.

Initially, z_o was 3 cm in the 10 MHz multiple thickness technique. However, if z_o is changed, the delta attenuation for a specific error in probe's diameter also changes. Therefore, a z_o can be found for the multiple thickness method which makes the attenuation error, $\Delta\alpha(f)$, approximately equal to the attenuation error in the results from the multiple echo and multiple echo II techniques at a 3 cm water path distance. The distance, z_o, which satisfies this condition is 8 cm (see Figure 4.7). The results across the three 10 MHz transducers obtained with the MT technique and the distance, z_o, equal to 8 cm can be seen in Figure 4.8.

The deviations of these results can be seen in Figure 4.9, and they are very

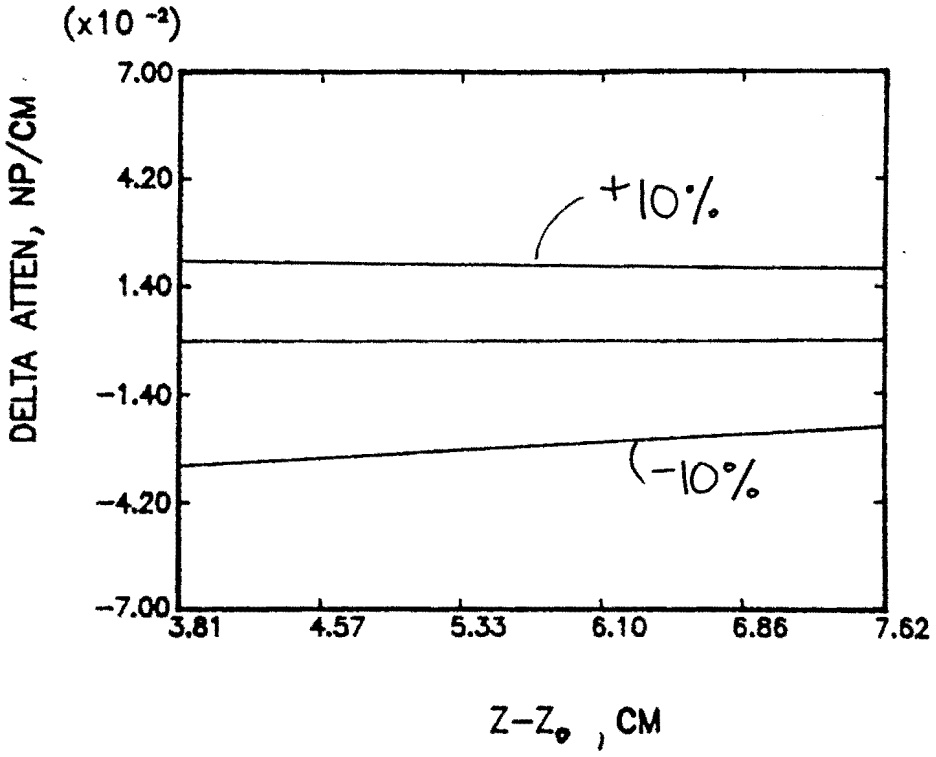

Figure 4.1: Change in Attenuation by the MT Attenuation Technique and a 10 MHz Probe Caused by $\pm$ 10 % Error in Probe Diameter Estimation

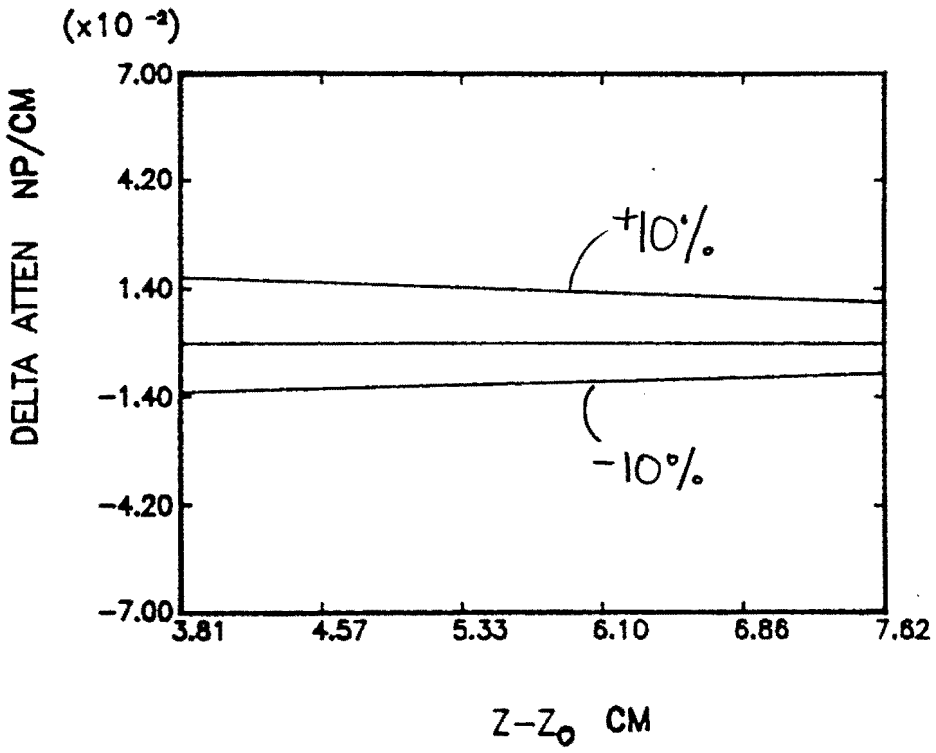

Figure 4.2: Change in Attenuation by the ME Attenuation Technique and a 10 MHz Probe Caused by $\pm$ 10 % Error in Probe Diameter Estimation

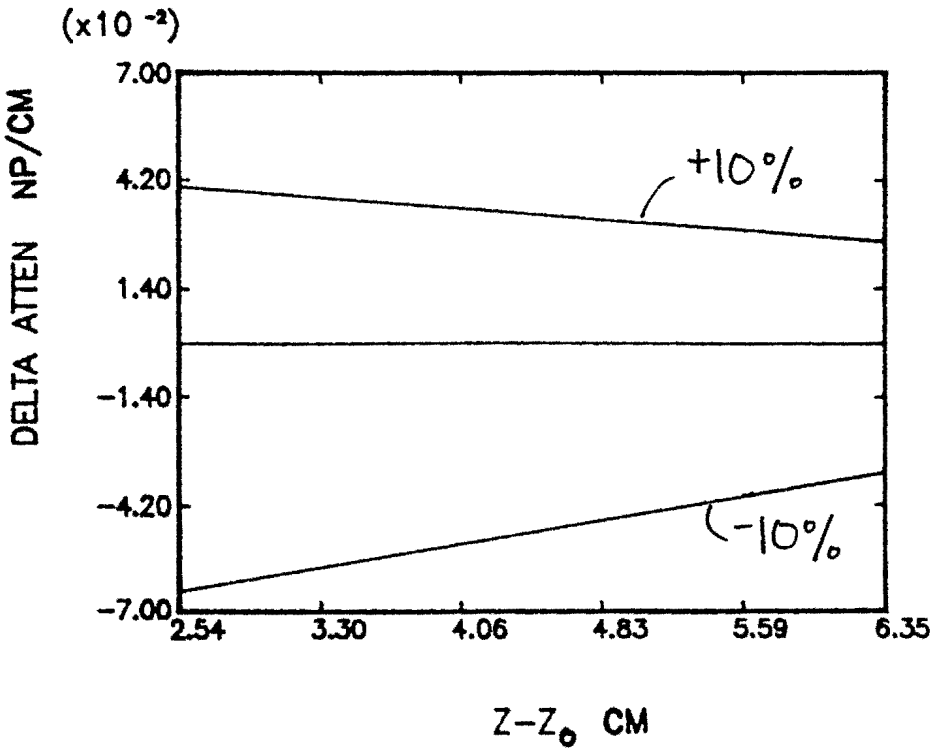

Figure 4.3: Change in Attenuation by the MEII Attenuation Technique and a 10 MHz Probe Caused by $\pm$ 10 % Error in Probe Diameter Estimation

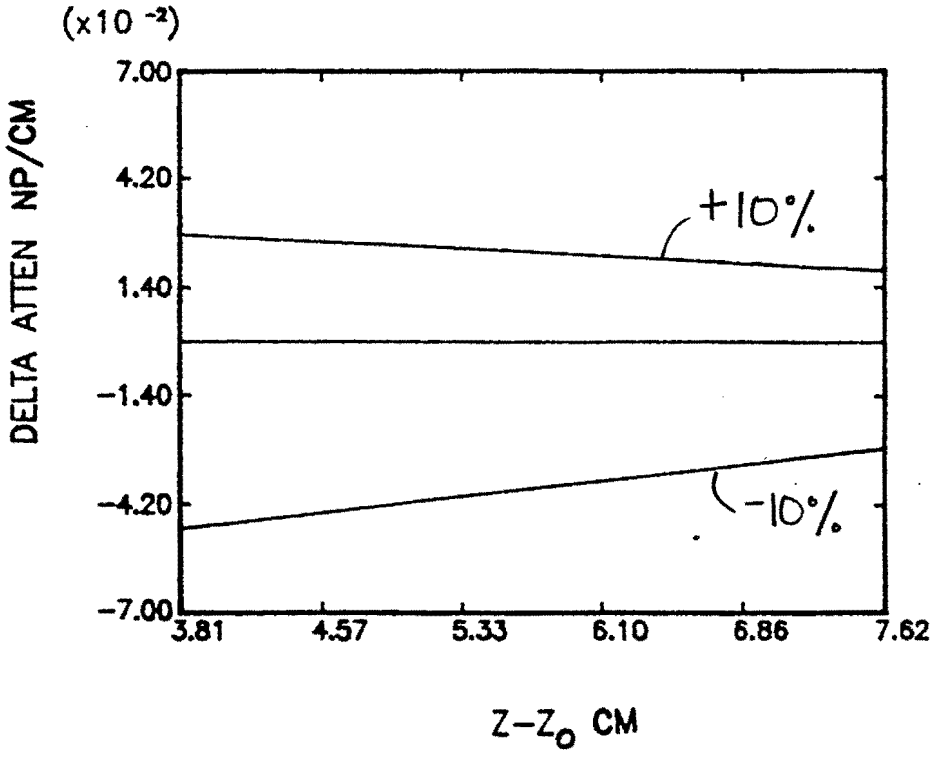

Figure 4.4: Change in Attenuation by the MT Attenuation Technique and a 15 MHz Probe Caused by $\pm$ 10 % Error in Probe Diameter Estimation

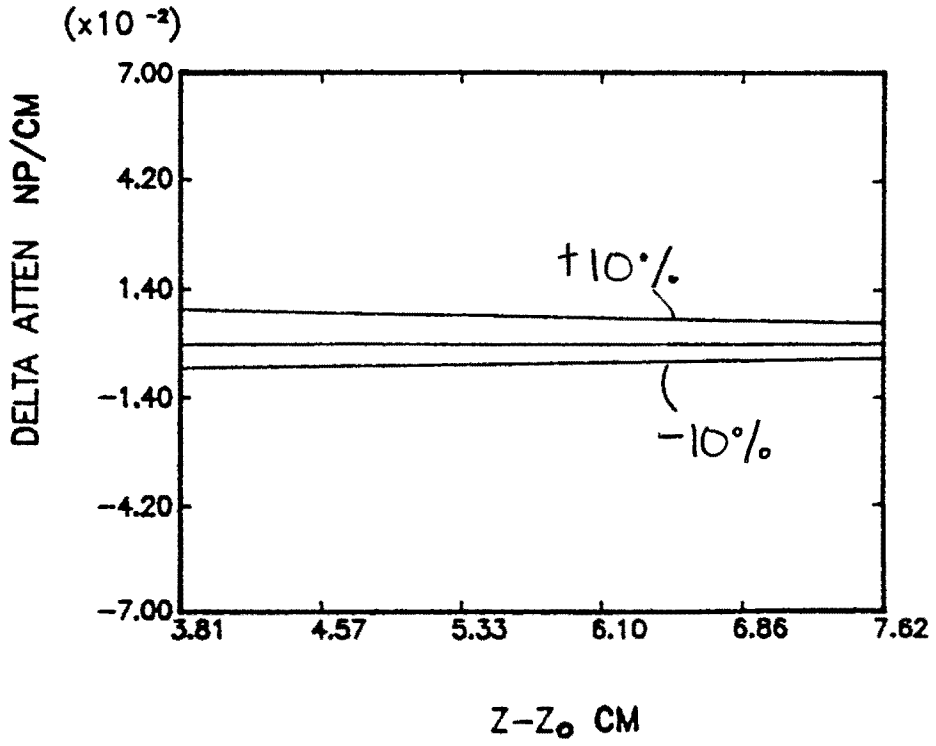

Figure 4.5: Change in Attenuation by the ME Attenuation Technique and a 15 MHz Probe Caused by $\pm$ 10 % Error in Probe Diameter Estimation

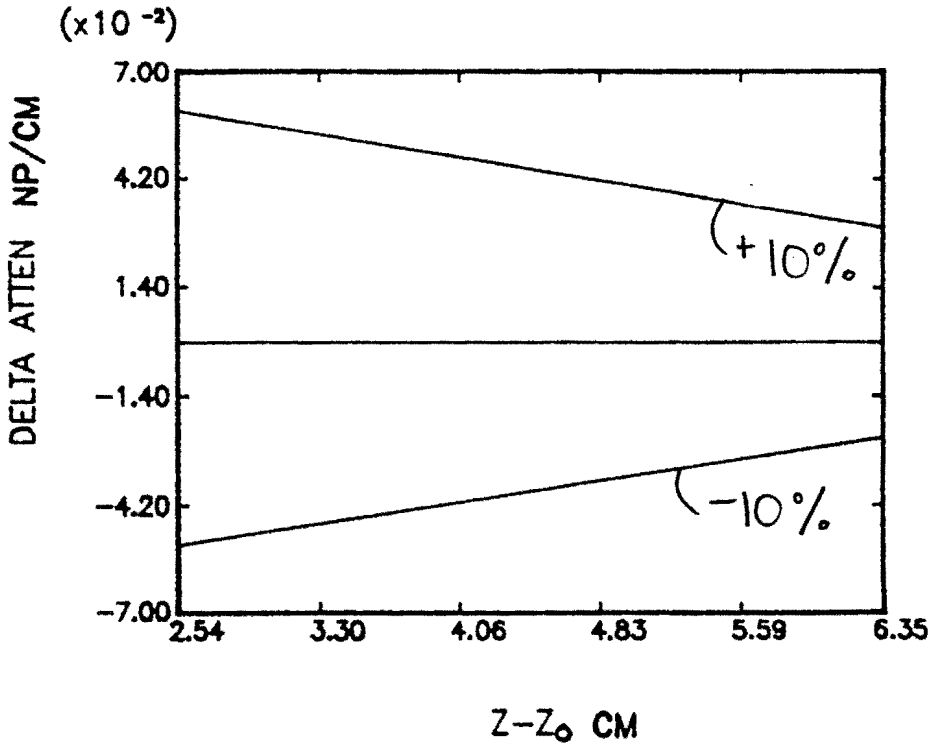

Figure 4.6: Change in Attenuation by the MEII Attenuation Technique and a 15 MHz Probe Caused by $\pm$ 10 % Error in Probe Diameter Estimation

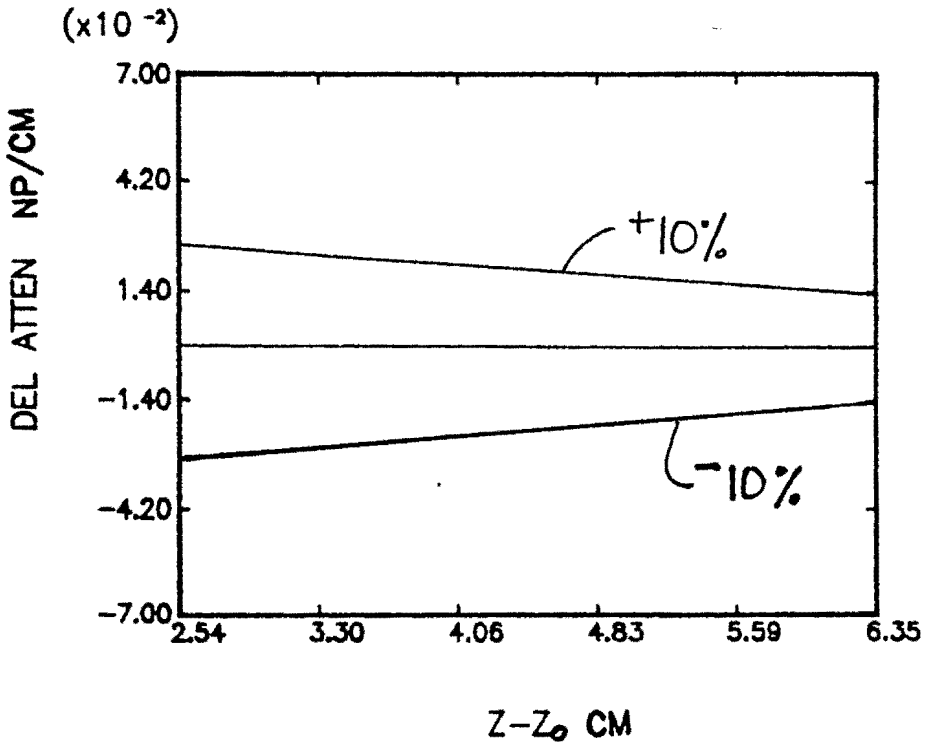

Figure 4.7: Change in Attenuation by the MT Attenuation Technique with z_o = 8 cm and a 10 MHz Probe Caused by a *pm* 10 % Error in Probe Diameter Estimation

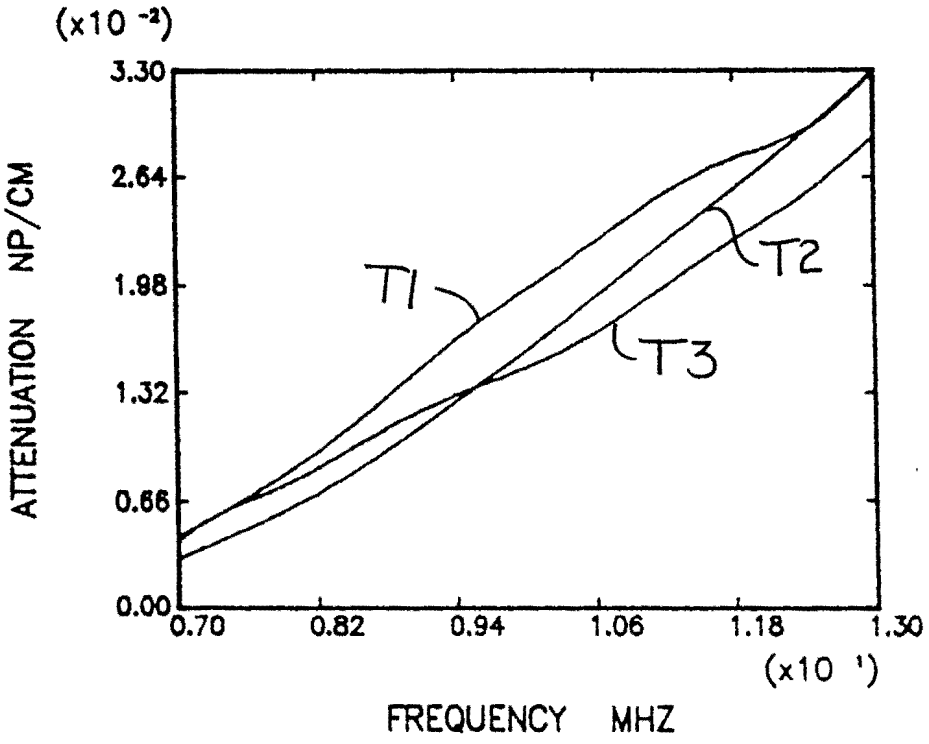

Figure 4.8: Attenuation in 7075 Aluminum Measured with the MT Technique at $z_o = 8$ cm using the Nominal Diameter (Transducers 1,2,3)

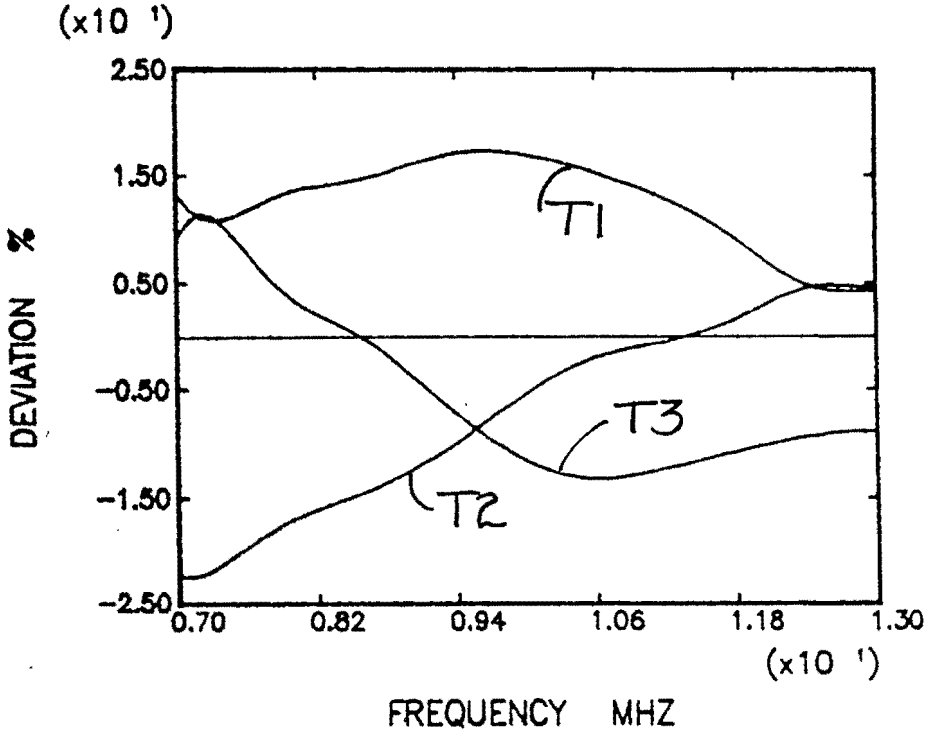

Figure 4.9: Deviation in Measured Attenuation for 7075 Aluminum with the MT Method at z_o = 8 cm using Transducers 1,2,3 with the Nominal Diameter

comparable to those for the multiple echo and the multiple echo II methods run at 3 cm. Figures 4.10 and 4.11 show the results when the active diameters are used, instead of the nominal diameters, and as expected, the deviations of the attenuation values between the transducers decrease. These results show the importance of the distance at which the measurement is performed in the attenuation measurement.

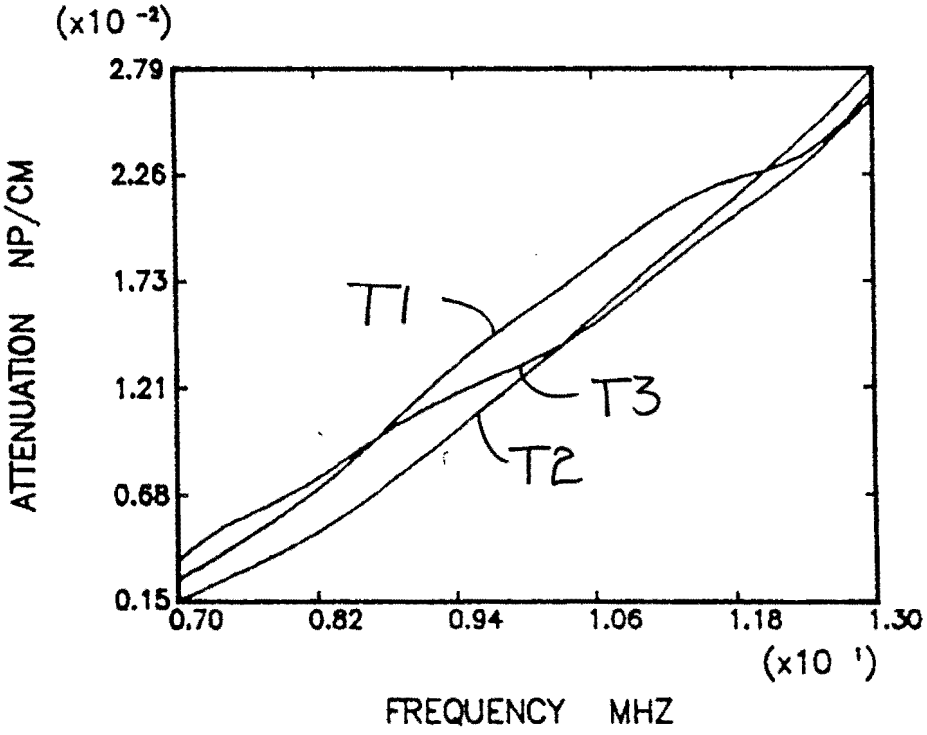

Figure 4.10: Attenuation in 7075 Aluminum with the MT Method at $z_o = 8$ cm using Transducers 1,2,3 and Their Respective Active Diameters

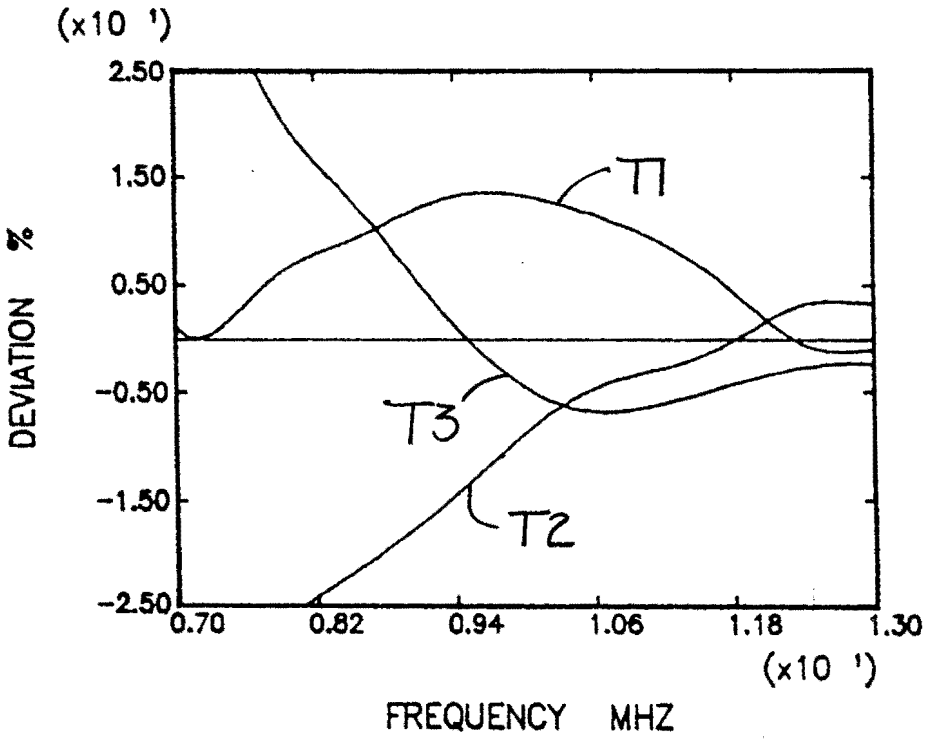

Figure 4.11: Deviation in Measured Attenuation for 7075 Aluminum with the MT Method at $z_o = 8$ cm using Transducers 1,2,3 with Their Respective Active Diameters

4.3 Attenuation Measurements of 7075 Aluminum with 10 MHz Transducers Using Active Diameters

In order to improve the consistency of the measurements across transducers, active diameters for each transducer were found assuming they behave as planar piston sources. These diameters were calculated based on measuring the backscattered signals from small spherical reflectors located along the main axis of the transducer, as described in detail in Chapter 3. In finding the active diameters, the fit between experimental and theoretical axial profiles was better with transducers 1 and 2, and active diameters of .234 inches and .237 inches, respectively were found. However for transducer 3, the fit between experimental and theoretical axial profiles was not as good leading to the conclusion that this transducer does not follow the planar piston model as well as the other two transducers. An active diameter of .244 inches was found for this transducer.

Bias of a particular method using the active diameters to calculate the attenuation can be seen in Figures 4.12 through 4.14. The multiple thickness method gives the lowest value for all transducers, and there is quite a bit of scatter across measurement techniques. The attenuation values obtained with the use of the active diameters are all lower than the results obtained with the nominal diameters. Deviations between transducers for each particular method stayed within $\pm$ 20 % with the MEII method giving the lowest deviations and the MT the highest. The deviations with the active diameters are lower than the values obtained with the nominal diameters for all methods. These results can be seen in Figures 4.15 through 4.17.

The consistency of the measurements across transducers can be examined by

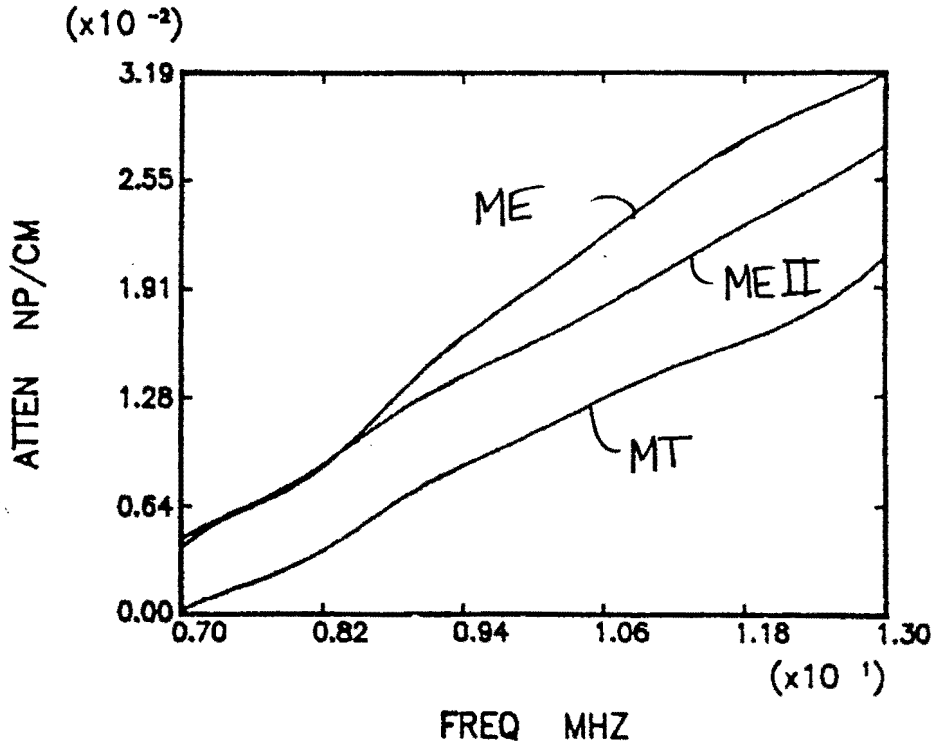

Figure 4.12: Attenuation in 7075 Aluminum with the ME, MT, and MEII Techniques using Transducer 1 with the Active Diameter

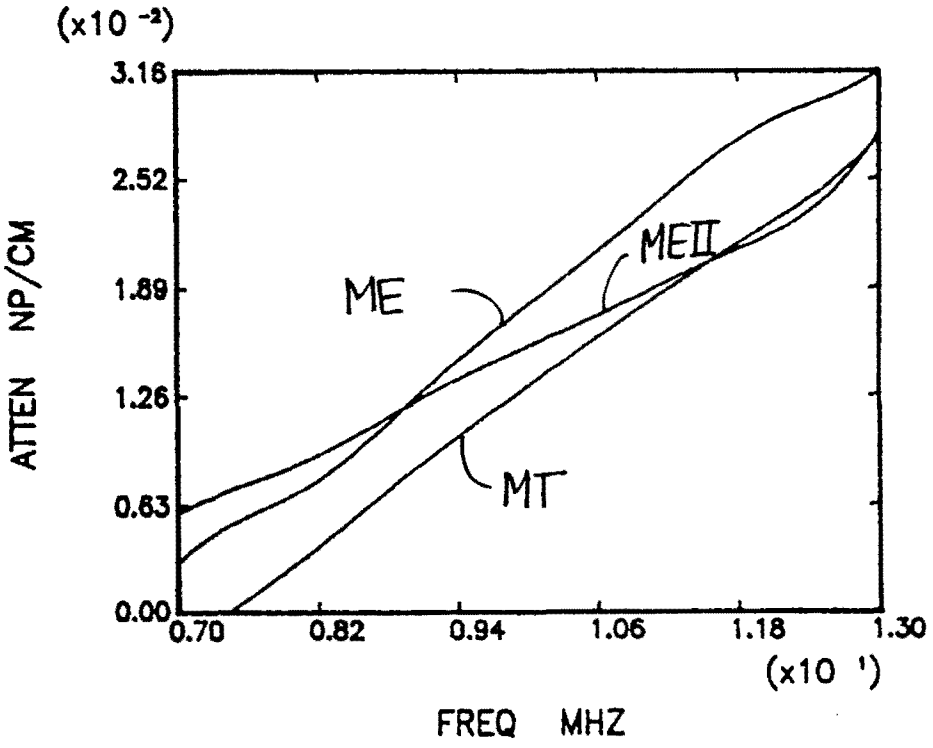

Figure 4.13: Attenuation in 7075 Aluminum with the ME, MT, and MEII Techniques using Transducer 2 with the Active Diameter

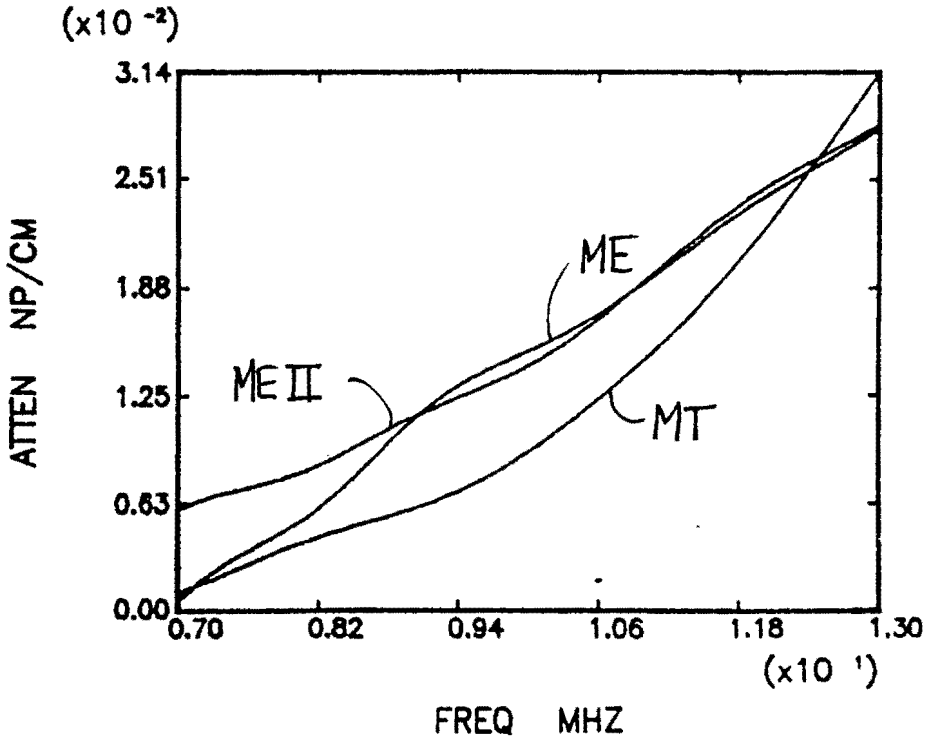

Figure 4.14: Attenuation in 7075 Aluminum with the ME, MT, and MEII Techniques using Transducer 3 with the Active Diameter

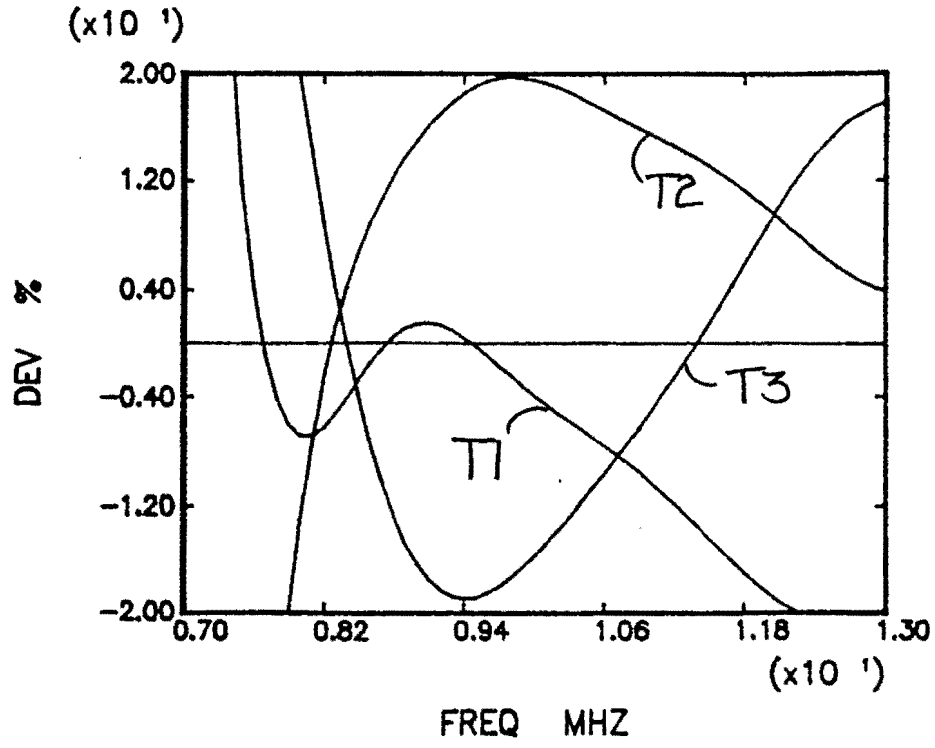

Figure 4.15: Deviation of the Measured Attenuation for 7075 Aluminum with the MT Method using Transducers 1,2,3

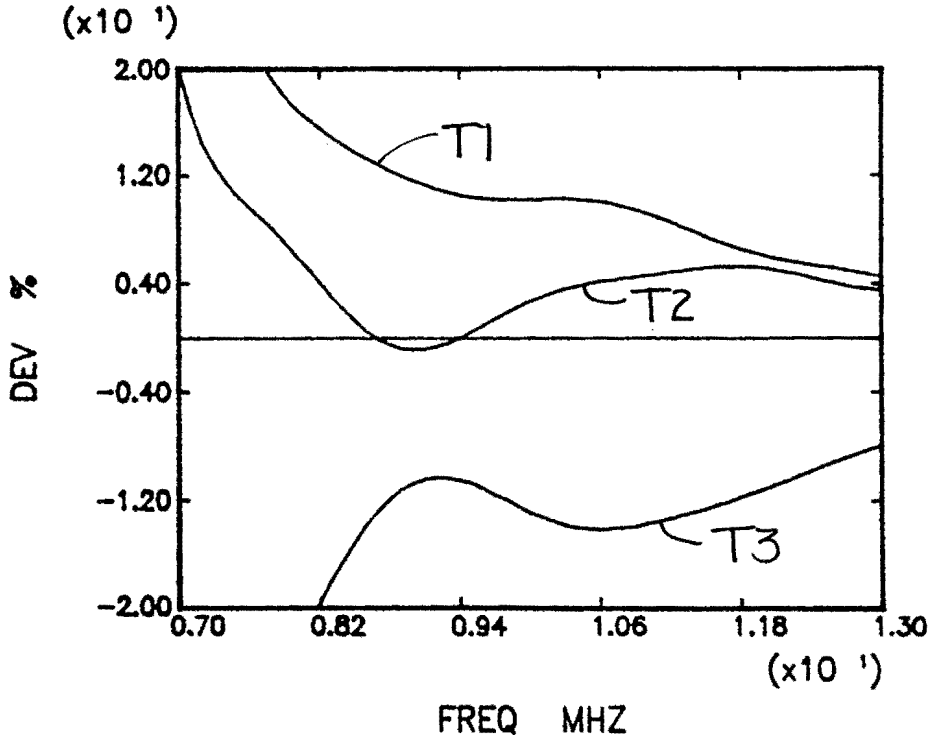

Figure 4.16: Deviation of the Measured Attenuation for 7075 Aluminum with the ME Method using Transducers 1,2,3 with the Active Diameters

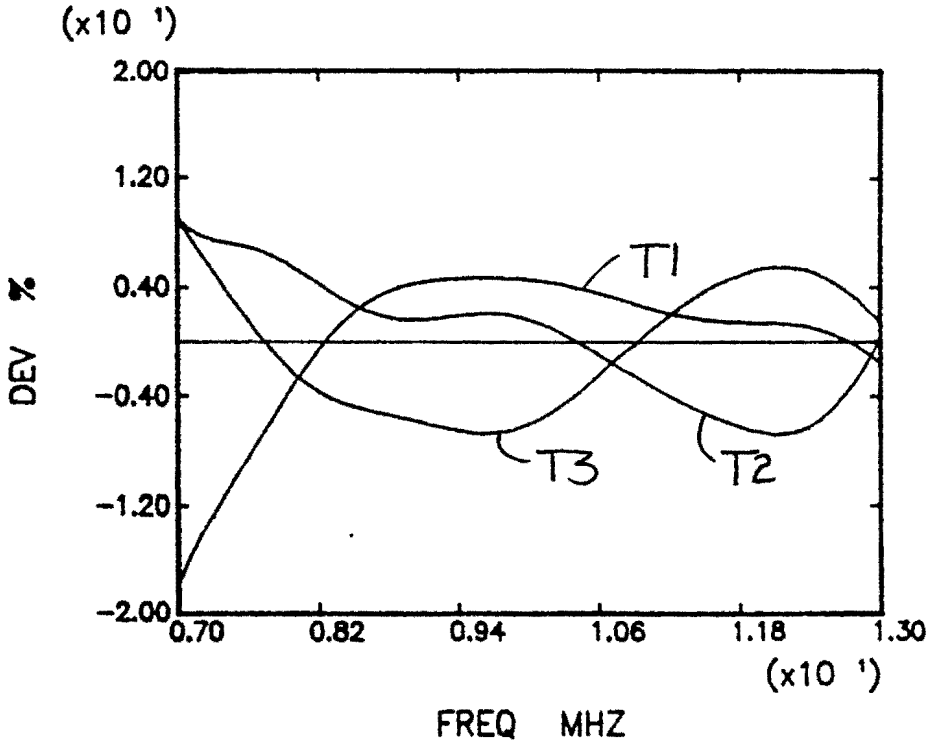

Figure 4.17: Deviation of the Measured Attenuation for 7075 Aluminum with the MEII Method using Transducers 1,2,3 with the Active Diameters

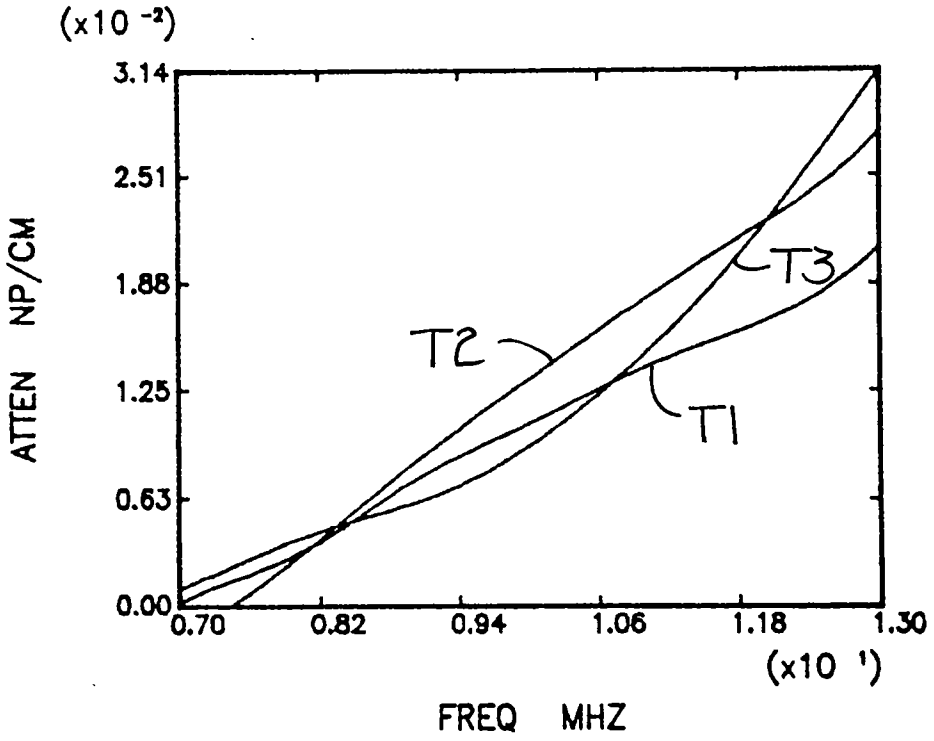

Figure 4.18: Attenuation of 7075 Aluminum with the Multiple Thickness Technique using Transducers 1,2,3 with the Active Diameters

looking at Figures 4.18 through 4.20. No one transducer shows bias with any particular method. Deviations are all within $\pm$ 20 % and are lower than the deviations for the nominal diameters. Results can be seen in Figures 4.21 through 4.23.

4.4 Scatter in Attenuation Results when Transducer not Obeying Piston Theory is Excluded

As was stated before, transducer 3 does not follow the planar piston model as well as transducers 1 and 2. Therefore, by eliminating transducer 3 from the

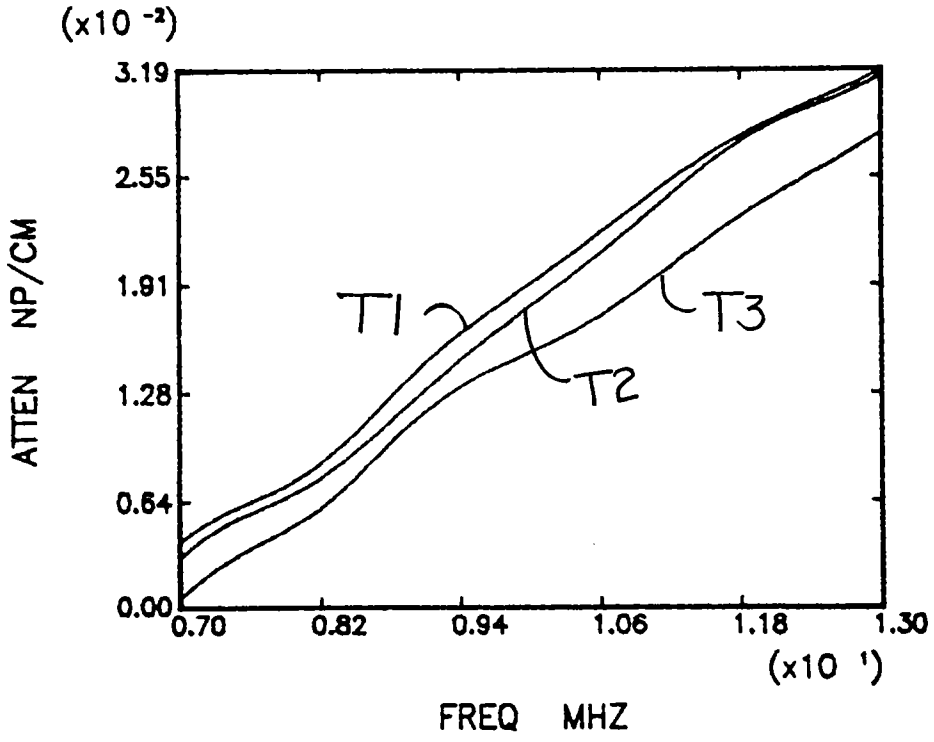

Figure 4.19: Attenuation of 7075 Aluminum with the Multiple Echo Technique using Transducers 1,2,3 with the Active Diameters

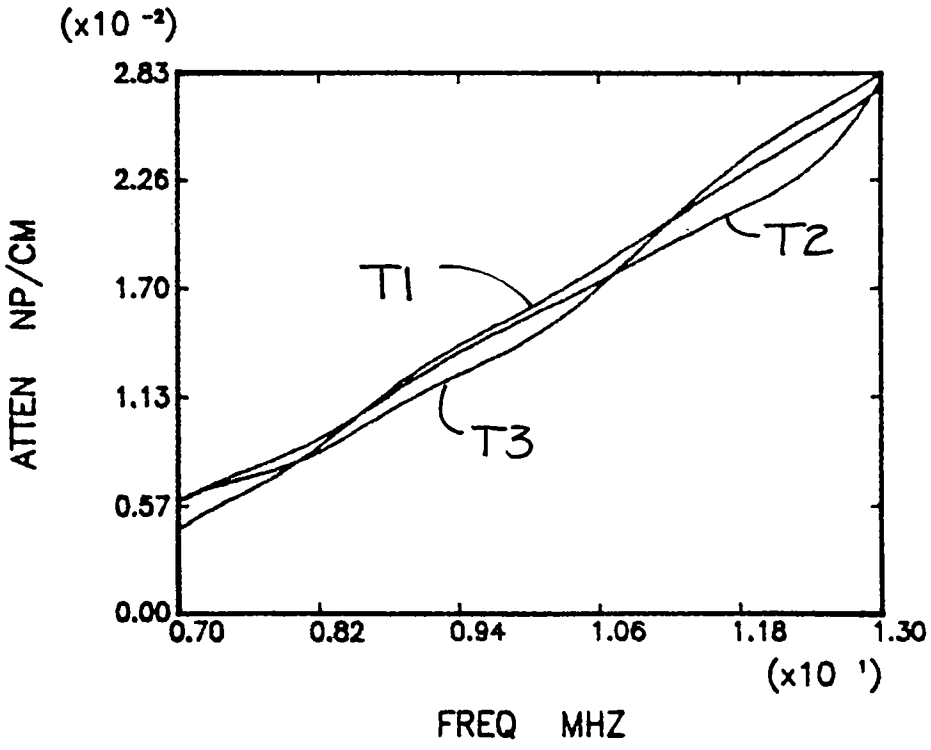

Figure 4.20: Attenuation of 7075 Aluminum with the Multiple Echo II Technique using Transducers 1,2,3 with the Active Diameters

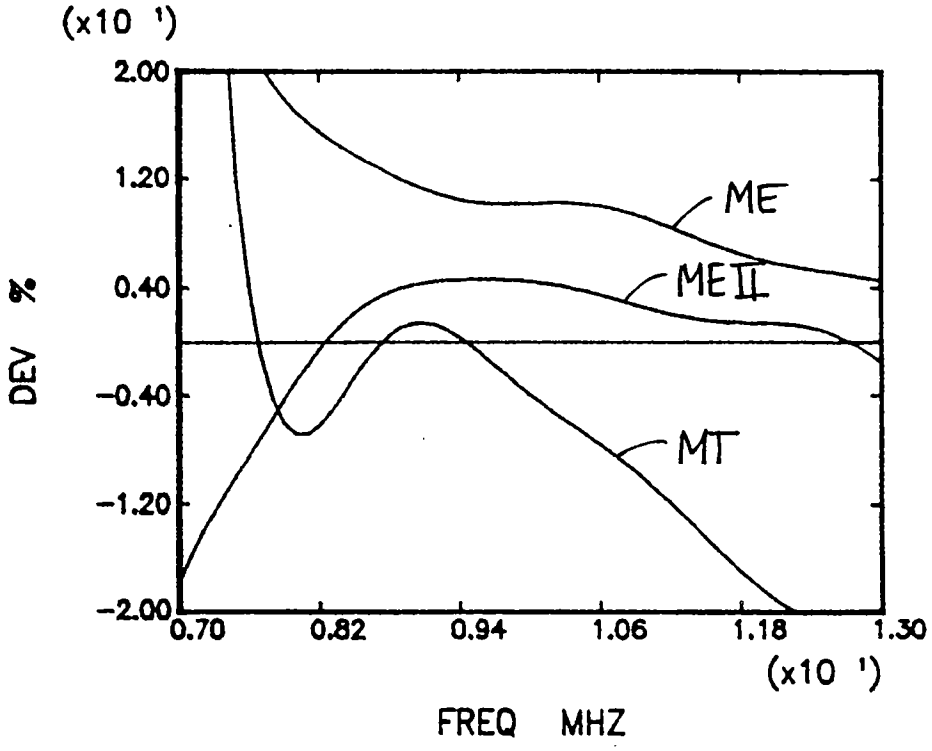

Figure 4.21: Deviation in the Measured Attenuation of 7075 Aluminum with the MT, ME, and MEII Techniques for Transducer 1 using the Active Diameter

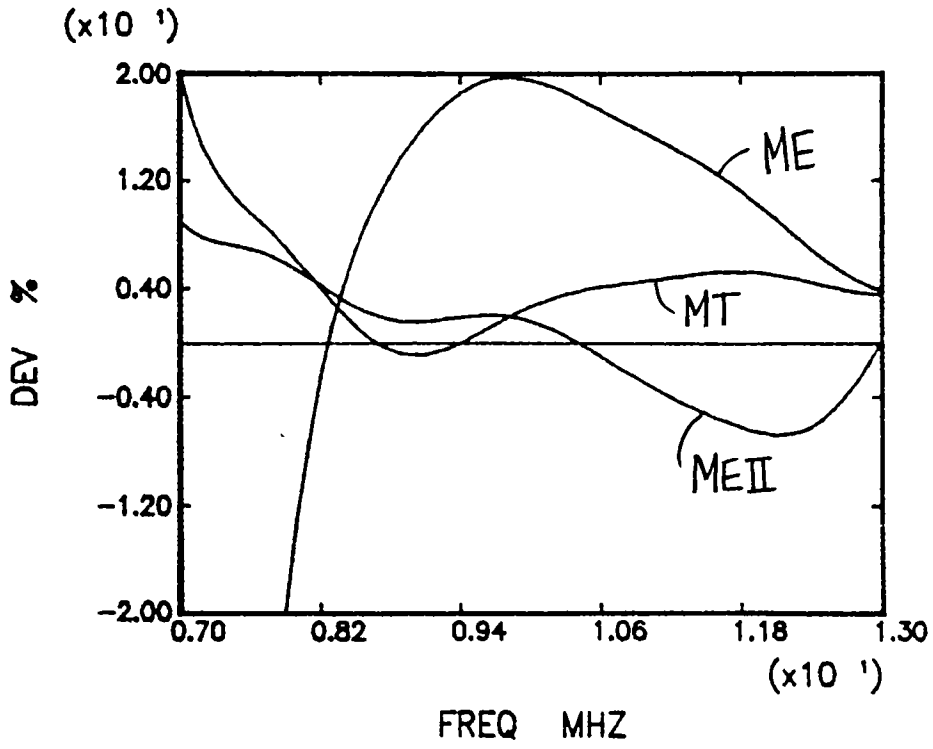

Figure 4.22: Deviation in the Measured Attenuation of 7075 Aluminum with the MT, ME, and MEII Techniques for Transducer 2 using the Active Diameter

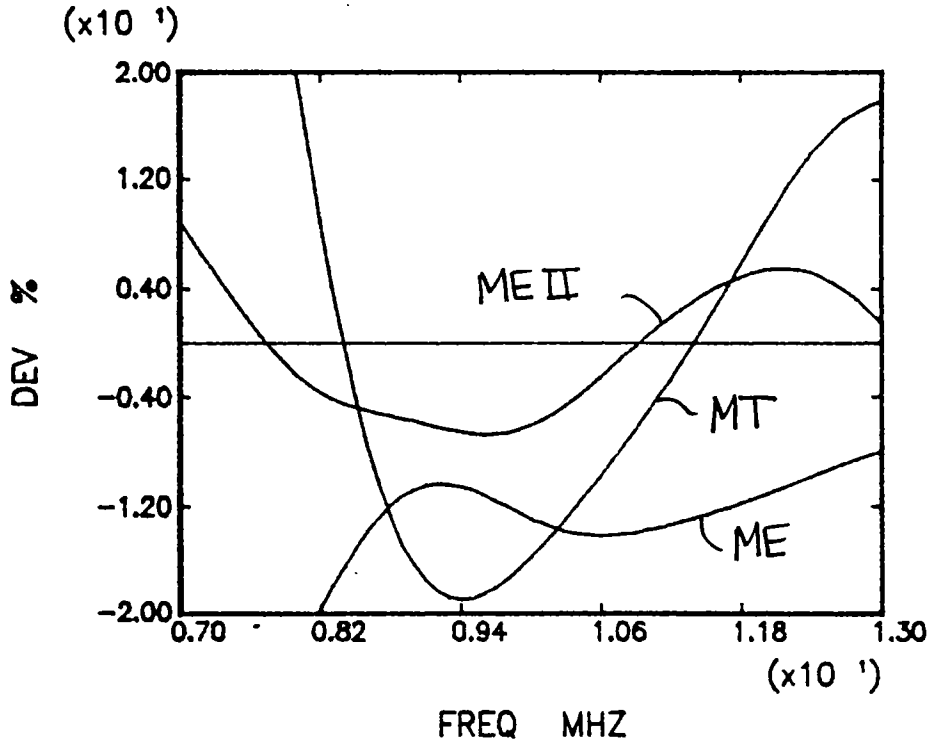

Figure 4.23: Deviation in the Measured Attenuation of 7075 Aluminum with the MT, ME, and MEII Techniques for Transducer 3 using the Active Diameter

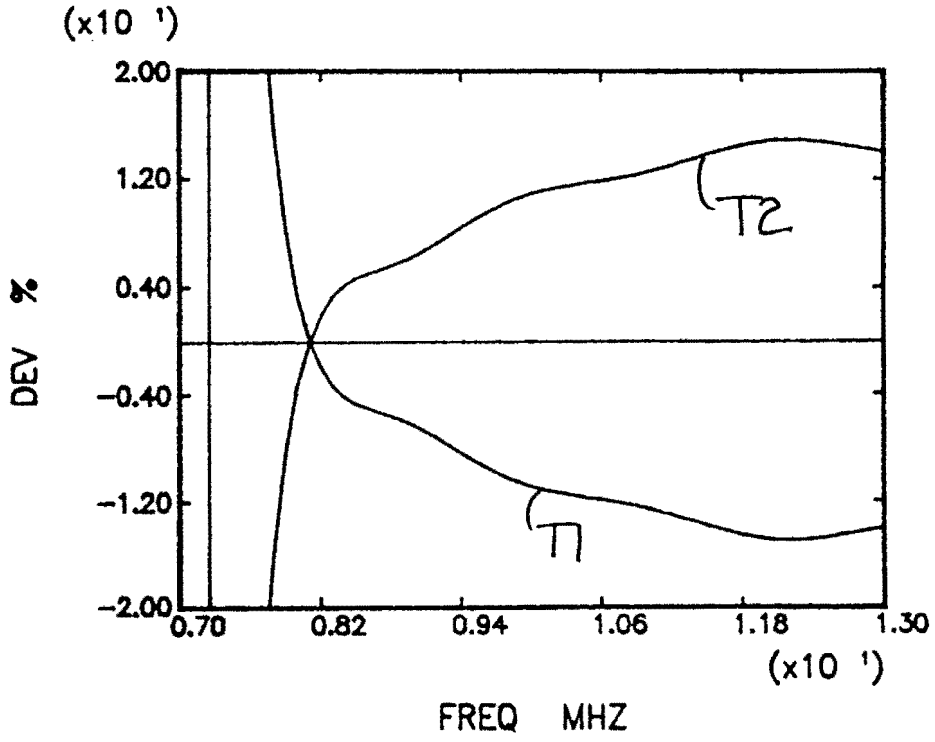

Figure 4.24: Deviation in the Measured Attenuation in 7075 Aluminum using the MT Attenuation Technique with Transducers 1 and 2 using Active Diameters (Transducer 3 Eliminated from the Results)

results, the deviations between the methods and the transducers should decrease. As can be seen by Figures 4.24 through 4.26, as predicted, the deviations between methods decrease, and, as seen in Figures 4.27 through 4.28, the deviations between transducers also decrease.

4.5 Conclusions

Transducer characterization by means of the active diameter can have significant effects on the attenuation measurements. The results of the research in this

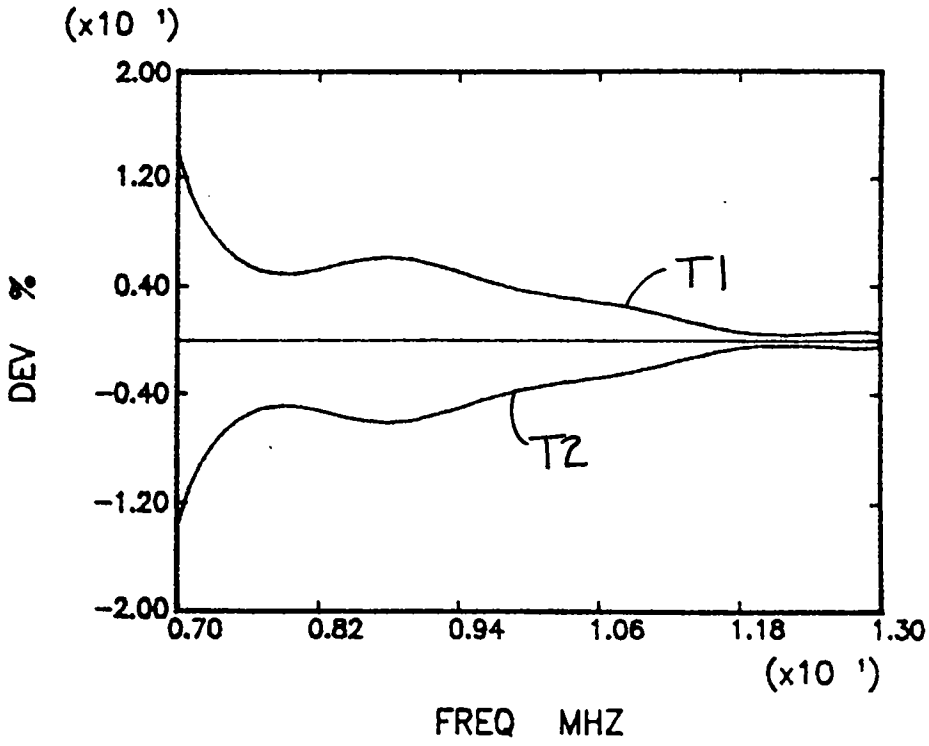

Figure 4.25: Deviation in the Measured Attenuation of 7075 Aluminum using the ME Attenuation Technique with Transducers 1 and 2 using Active Diameters (Transducer 3 Eliminated from the Results)

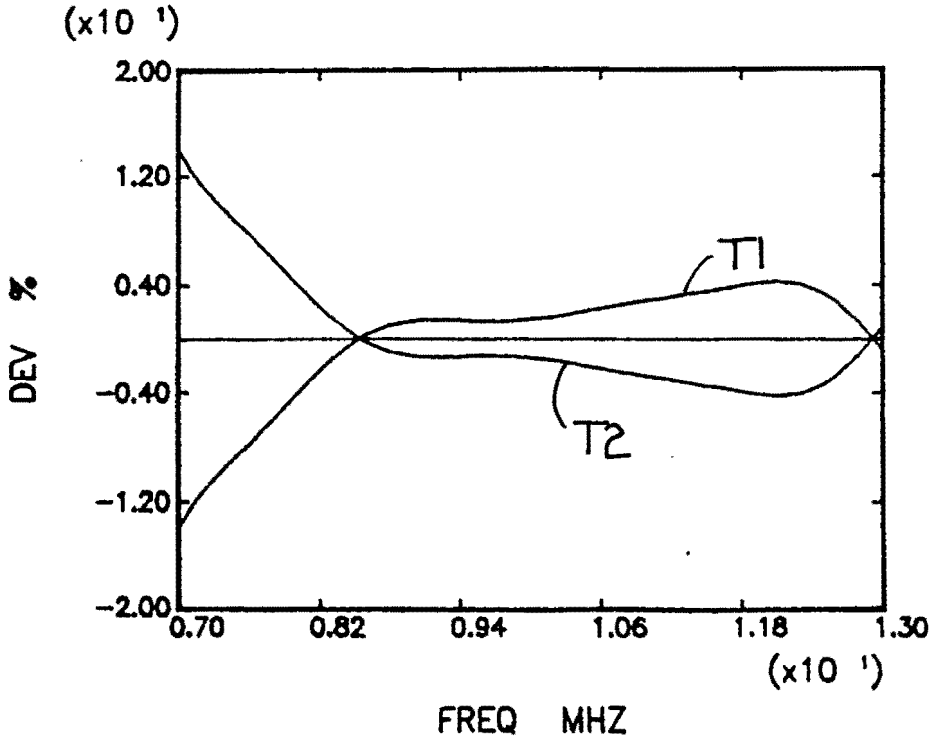

Figure 4.26: Deviation in the Measured Attenuation of 7075 Aluminum using the MEII Attenuation Technique with Transducers 1 and 2 using Active Diameters (Transducer 3 Eliminated from the Results)

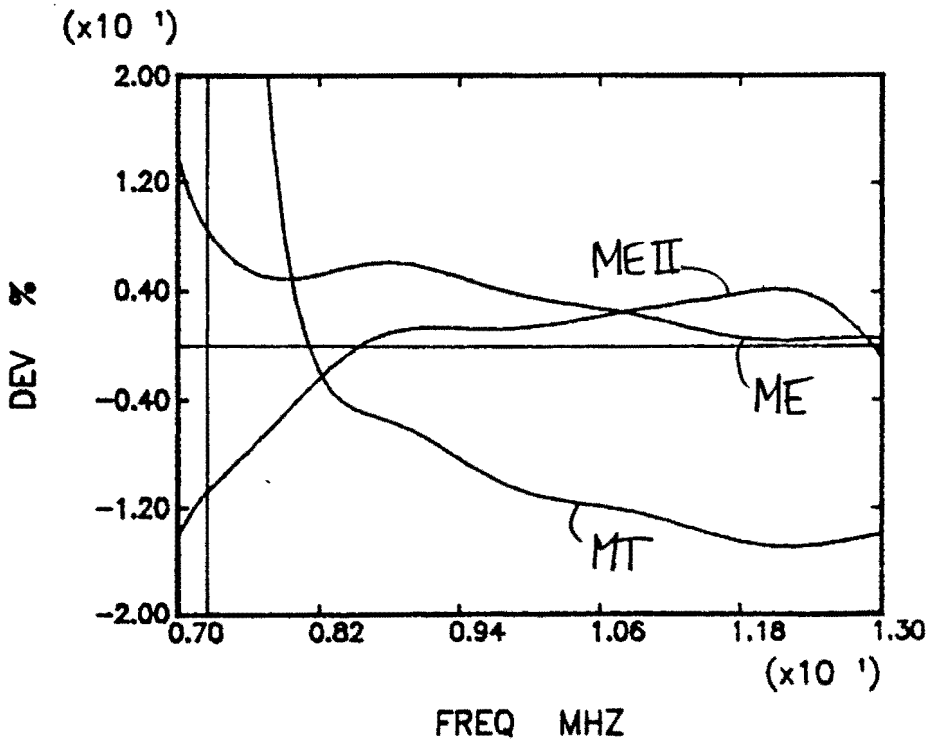

Figure 4.27: Deviation in the Measured Attenuation of 7075 Aluminum using the MT, ME, and MEII Attenuation Techniques with Transducer 1 with the Active Diameter (Transducer 3 Eliminated from the Results)

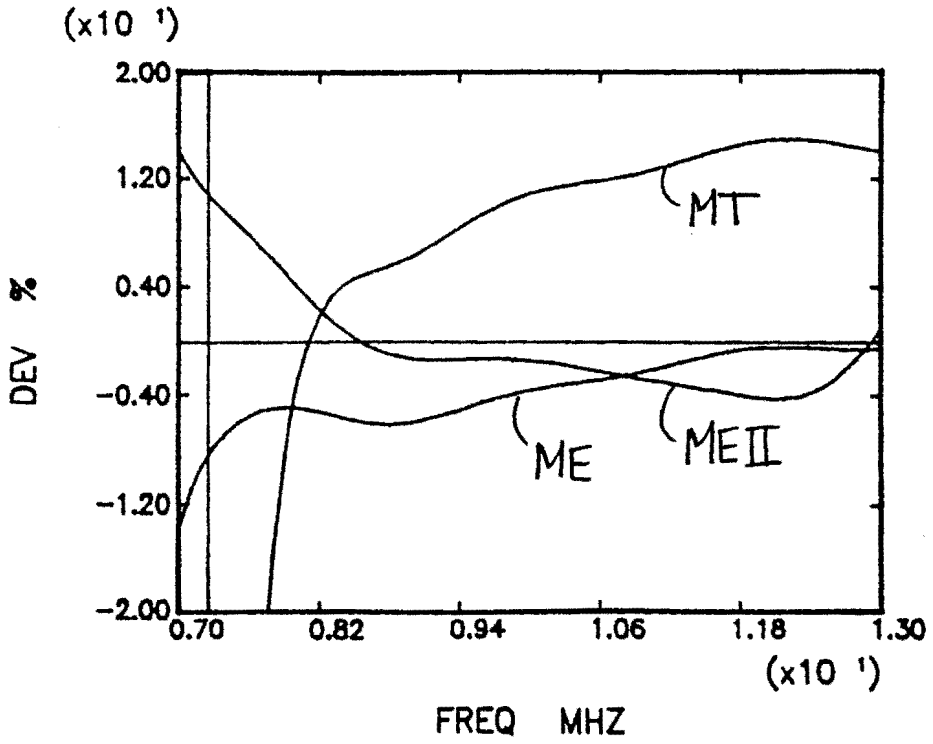

Figure 4.28: Deviation in the Measured Attenuation of 7075 Aluminum using the MT, ME, and MEII Attenuation Techniques with Transducer 2 with the Active Diameter (Transducer 3 Eliminated From the Results)

thesis have indicated:

1) The estimation of the diameter of the probe can have significant effects on the results of the attenuation measurements. This effect is especially evident in the MT attenuation measurement technique, where to make the effects of the diameter estimation similar to the effects of the diameter estimation in the ME and MEII techniques, measured at a water path distance of 3 cm, the test must be performed at a significantly larger water path distance of 8 cm.

2) By use of transducer characterization in the form of the active diameter, attenuation measurements became less transducer dependent.

3) Removing the transducer which behaved the least like a planar piston source decreased the deviations of the results of the attenuation measurements.

5 GENERAL CONCLUSIONS

When the measurement model is used to quantitatively interpret received signals from ultrasonic measurements, it is extremely important to have knowledge of the ultrasonic wave attenuation in the solid material and to know how closely the transducers behave as planar piston sources. By measuring the attenuation of ultrasonic waves in 7075 aluminum and A357 aluminum, and by examining the ultrasonic transducers by measuring their axial and radial profiles, the following conclusions follow from this research:

1) Attenuation of low attenuating materials can be measured consistently, however, transducer characterization needs to be improved to enable the correct calculation of diffraction corrections for a probe, which are required for obtaining transducer independent results.

2) In the case of higher attenuating materials or at higher frequencies, where the attenuation is higher, it is easier to measure the attenuation more consistently using the same methods because the diffraction of the beam is of less importance than the material's attenuation.

3) Axial profiles of transducers can be used to calculate active diameters for transducers, enabling characterization of probes as planar piston sources. This characterization reduces transducer dependence in ultrasonic attenuation measure-

ments.

4) Radial profiles of transducers seem to indicate that probes radiate beams that behave more like theoretical planar pistons near the center of their main axis, however, this agreement decreases with radial distance.

5) The active diameter can be effectively used to reduce transducer dependence in ultrasonic attenuation measurements providing the involved probe's radiation pattern obeys the rigid piston theory which is not true for all planar, non-focused, immersion transducers.

6 BIBLIOGRAPHY

[1] R.B. Thompson and T.A. Gray. "A Model Relating Ultrasonic Scattering Measurements Through Liquid-Solid Interfaces to Unbounded Medium Scattering Amplitudes." J. Acoust. Soc. Am. 74 (1983): 1279.

[2] E.P. Papadakis. "Revised Grain-Scattering Formulas and Tables." J. Acoust. Soc. Am. 37 (1965): 703.

[3] B. Kopec. "Ultrasonic Inspection of Grain Size in the Materials for Railway Wheel Sets." Ultrasonics. 13 (1975): 267.

[4] R.L. Roderick and R. Truell. "The Measurement of Ultrasonic Attenuation in Solids by the Pulse Technique and Some Results in Steel". J. Appl. Phys. 23 (1952): 267.

[5] E.P. Papadakis. "Ultrasonic Attenuation by Spectrum Analysis of Pulses in Buffer Rods." J. Acoust. Soc. Am. 53 (1973): 1336.

[6] E.P. Papadakis. "Absolute Measurements of Ultrasonic Attenuation using Damped Nondestructive Testing Transducers." J. Test. Eval. 12 (1984): 273.

[7] E.R. Generazio. "The Role of the Reflection Coefficient in Precision Measurement of Ultrasonic Attenuation." Material Evaluation. 42 (1985): 995.

[8] W.S. Burkle. "Measurement of Ultrasonic Longitudinal Wave Attenuation." Material Evaluation. 42(3) (1984): 262.

[9] R.A. Kline. "Measurement of Attenuation and Dispersion using an Ultrasonic Spectroscopy Technique." J. Acoust. Soc. Am. 76 (1984): 498.

[10] P.S. Stelkov. "Attenuation-Coefficient Measurement with Immersion." Sov. J. Nondestructive Testing.13(1) (1977): 115.

[11] D.D. Bennink. Multiple Thickness Technique. Unpublished. Engineering Science and Mechanics Department, Iowa State University, Ames, Iowa. 1986.

[12] L.E. Kinsler and A.R. Frey. "Fundamentals of Acoustics." John Wiley and Sons, Inc., New York, 1962.

[13] D.D. Bennink and A.L. Mielnicka-Pate. "Transducer Radiation Modeling for Ultrasonic Inspection Purposes." Review of Progress in Quantitative NDE. 6A (1986): 657.

[14] A.D. Pierce. "Acoustics: An Introduction to its Physical Principles and Applications." McGraw-Hill Book Company, New York, 1981.